



HAL
open science

Thermosensitive macroporous hydrogels for cells encapsulation and delivery

Phuong Anh Dang

► **To cite this version:**

Phuong Anh Dang. Thermosensitive macroporous hydrogels for cells encapsulation and delivery. Mechanics [physics]. Université Paris sciences et lettres, 2022. English. NNT : 2022UPSLM087 . tel-04226939

HAL Id: tel-04226939

<https://pastel.hal.science/tel-04226939>

Submitted on 3 Oct 2023

HAL is a multi-disciplinary open access archive for the deposit and dissemination of scientific research documents, whether they are published or not. The documents may come from teaching and research institutions in France or abroad, or from public or private research centers.

L'archive ouverte pluridisciplinaire **HAL**, est destinée au dépôt et à la diffusion de documents scientifiques de niveau recherche, publiés ou non, émanant des établissements d'enseignement et de recherche français ou étrangers, des laboratoires publics ou privés.



THÈSE DE DOCTORAT
DE L'UNIVERSITÉ PSL

Préparée à MINES ParisTech - PSL et ESPCI Paris - PSL

**Hydrogels thermosensibles macroporeux pour
l'encapsulation et la délivrance de cellules**

**Thermosensitive macroporous hydrogels for
cells encapsulation and delivery**

Soutenue par

Phuong Anh DANG

Le 12 janvier 2022

École doctorale n° 621

**Ingénierie des Systèmes,
Matériaux, Mécanique,
Énergétique**

Spécialité

**Sciences et génie des
matériaux**

Encadrants

Sophie, NORVEZ	Co-encadrante
Emmanuel, PAUTHE	Co-directeur
Laurent, CORTÉ	Directeur de thèse

Composition du jury :

Jean-François, JOANNY Professeur, Collège de France	<i>Président</i>
Florence, AGNÉLY Professeure, Université Paris-Saclay	<i>Rapporteuse</i>
Anne, DES RIEUX Maître de recherche, FNRS	<i>Rapporteuse</i>
Joëlle, AMÉDÉE Directrice de recherche, INSERM	<i>Examinatrice</i>
Sophie, NORVEZ Maître de conférences, ESPCI Paris-PSL	<i>Examinatrice</i>
Emmanuel, PAUTHE Professeur, CY Cergy Paris Université	<i>Co-directeur</i>
Laurent, CORTÉ Professeur, MINES ParisTech-PSL	<i>Directeur de thèse</i>

THÈSE DE DOCTORAT
DE L'UNIVERSITÉ PSL

REMERCIEMENTS

Je souhaite remercier chaleureusement ici toutes les personnes grâce à qui cette thèse a été un chapitre magnifique de ma vie.

J'adresse d'abord mes remerciements à l'ensemble des membres du jury, qui m'ont fait l'honneur d'évaluer avec attention mes travaux de thèse et pour les échanges enrichissants lors de la soutenance. Je remercie Dr. Florence Agnely et Dr. Anne des Rieux pour leurs rapports très détaillés et constructifs. Je remercie chaleureusement Dr. Joëlle Amédée d'avoir été examinatrice et pour m'avoir donnée l'opportunité d'être membre du bureau des Jeunes Chercheurs BIOMAT et pour m'avoir aidée dans cette fonction. Enfin, je remercie Pr. Jean-François Joanny pour m'avoir fait l'honneur d'être président de ce jury et également pour son cours à l'ESPCI durant mes études et pour ses cours au Collège de France que je continue à suivre chaque année.

Je tiens à remercier chaleureusement mes encadrants de thèse : Pr. Laurent Corté, Dr. Sophie Norvez et Pr. Emmanuel Pauthé. Je vous remercie pour m'avoir donnée l'opportunité de réaliser cette thèse, pour votre confiance et pour votre présence.

Laurent, tu as été l'initiateur et le soutien de beaucoup d'idée durant ces années de travail commun. Tu m'as donnée de la confiance mais en même temps, tu étais présent quand j'avais besoin des conseils avisés sur comment bien analyser les données ou même bricoler un porte-échantillon express ☺

Sophie, je te connais depuis mes premiers jours à l'ESPCI, ce qui fait presque 8 ans maintenant. Tu es une professeure formidable, très pédagogue et à l'écoute. Les TPs avec toi ont toujours été très agréables et dynamiques. Ensuite, j'ai eu la chance de t'avoir comme encadrante de stage et de thèse. Le jour où j'avais frappé à ton bureau pour redemander un stage sur le projet, tu m'as toute de suite accueillie avec beaucoup de gentillesse et de bienveillance et tu es restée comme ça pendant toutes ces années.

Emmanuel, j'ai découvert un nouveau monde, celui des cellules, et tu as été un superbe guide. Tu as toujours su m'accompagner dans cette découverte avec ta pédagogie et ta bonne humeur. Merci également d'avoir créé un environnement stimulant en tant que directeur du laboratoire ERRMECe.

Vous avez tous les trois énormément contribué à ce que ce projet se déroule dans d'excellentes conditions, scientifiques et humaines. Merci à vous pour m'avoir toujours encouragée à aller plus loin, à saisir des opportunités et à devenir la scientifique que je suis aujourd'hui.

Je tiens à remercier Dr. Michel Cloître, directeur du laboratoire C3M pour m'avoir accueillie au sein du laboratoire pour le stage et ensuite pour la thèse. Merci également pour avoir transmis vos connaissances et votre passion sur la Physique de la matière molle lors de vos cours à l'ESPCI et à la Sorbonne. Merci pour toutes les discussions scientifiques très enrichissantes autour de la rhéologie et la dynamique des polymères. Je vous remercie également pour votre soutien à mes différents projets.

Mes remerciements s'adressent également à tous les membres permanents du laboratoire C3M : François Tournilhac, Renaud Nicolaÿ, Corinne Soulié-Ziakovic et Nathan Van Zee pour des discussions scientifiques enrichissantes notamment en séminaire interne. Merci à Mickaël Pomes-Hadda pour m'avoir aidé sur la rhéologie et la viscosimétrie. Merci à Isabelle Marlart pour ton aide précieuse en informatique, Arould Radja pour votre aide concernant les commandes et les démarches administratives. Merci à Gaëlle Carré de Lusancay pour des moments passés ensemble au microscope confocal mais surtout pour ta bonne humeur.

J'adresse ensuite mes remerciements aux différentes personnes avec qui j'ai eu la chance de collaborer durant ce projet. Merci à Stefano Aime (C3M) pour ton aide et les discussions sur la diffusion de la lumière. Merci à Carla Palomino-Durand (ERRMECe) pour ta disponibilité, ta gentillesse et ton aide sur les manip. Merci à Lamia El-Guermah et Rémy Agniel pour m'avoir beaucoup appris sur les cellules. Merci à Etienne Descencière (Centre Morphologie Mathématiques) pour vos conseils sur le traitement d'images. Je remercie Piotr Topilko, Laure Lecerf et Gaspard Gerschenfeld pour m'avoir accueillie dans votre laboratoire (anciens et nouveaux locaux) et pour m'avoir aidée à faire des expériences avec les cellules neuronales ou les cellules cancéreuses. Je remercie Rachel Auzély-Velty, Sonia Ortega et Raphaël Michel (CERMAVE Grenoble) pour vos aides sur la GPC et la viscosimétrie.

Je remercie les stagiaires avec qui j'ai eu la chance de collaborer durant ce projet. Merci à Louison Blivet, grâce à toi nous avons pu explorer les effets des différents chitosans. Merci à Pierre Marquaille pour ton travail de qualité sur les algorithmes de traitement et d'analyse d'images ; je te souhaite beaucoup de succès pour la suite du projet et je n'ai aucun doute que tu vas si bien le mener (merci au passage pour ton talent incroyable de scénariste et ton implication pour animer la vie du labo). Thanks to Andrey Kolosov for your good work on hydrogel characterization.

J'adresse maintenant mes remerciements aux membres non-permanents du MMC/C3M. C'est avec eux que j'ai passé les moments les plus inoubliables, de fous rire mais aussi des débats sur des sujets très sérieux durant la pause déjeuner. Sans eux, cette aventure n'aurait sûrement été pas si belle. J'espère que nous allons nous recroiser très vite pour des futurs bons moments, autour des sushis un midi ou des pichets de Margarita un soir.

Je vais commencer par les anciens doctorants et post-docs pour m'avoir accueillie et pour nous avoir laissés tant de bonnes traditions. Merci Maddalena Mattiello pour ta bonne humeur sans faille et tes convictions sur la vraie carbonara. Merci Sarah Goujard pour ton aide précieux sur la DLS et pour nos petites discussions au labo. Merci Maïssa Farroux pour tes conseils tout aussi pertinents sur la dialyse que sur les adresses de restaurants. Merci Antoine Breuillac pour m'avoir convertie en écolo grâce aux débats du midi et c'est grâce à toi que je mange des légumes de saison maintenant, pour ton initiative des soirées WWT et pour le super weekend à Montpellier (merci aussi à Lucie !). Merci Quentin Nozet pour ta générosité dans la vie et pour nous avoir accueillis chez toi pour différentes occasions. Un grand

merci aux anciens post-docs : Florent Caffy, Ralm Ricarte, Chirine Ben Osman, Raphaël Michel (je te remercie pour avoir pris du temps à discuter avec moi sur mon projet personnel), Mohamad Maaz, Iurri Antoniuk, Bodgan Tarus, Esther Cazares, Marta Abellan (merci pour la soirée espagnole !), Emeline Placet, Jaroslav Minar (merci à toi et à ta femme pour l'organisation de la soirée Tchèque !). Merci également aux anciens stagiaires avec qui j'ai passé de superbes moments pendant mes 6 mois de stage : Louise Breloy, Élodie Llusar, Chloé Seyrig, Margarita Bosmi (merci pour m'avoir si bien accueillie à Athènes !), Naima Orra. Vous avez tous créé une superbe ambiance, qui a joué considérablement dans ma décision de rester encore 3 ans au MMC.

Merci à ceux et celles qui sont encore présents au laboratoire. Merci aux post-docs : Georges Formon (que je remercie au passage pour son aide sur la GPC), Paolo Edera (pour les discussions intéressantes autour de la DLS), Estelle Palierse (pour des bons moments partagés à Bourg Saint-Maurice et pour des chouettes discussions au labo) et aussi Quentin Poutrel, Camille Bakkali-Hassani, Noushin Hasanabadi.

Un très très grand merci aux doctorants ! Je vais commencer par le bureau France – Italie : Merci à Arnaud Chaub, aka Daruxan, pour tes excellentes blagues et pour ton talent exceptionnel de montage de vidéo et pour les raccourcis dans Mario Kart ; Merci à Bruno Di-dio pour ta bonne humeur et pour ton aide à plusieurs reprises pour la rhéo ; Merci Chiara Maraffa, toujours dynamique et souriante, ton énergie est vraiment contaminant ! Au tour du bureau des « Zg » : Merci à Alexi Riba-Bremerch, aka Ribou, pour ta bonne humeur, ta gentillesse, et ta volonté d'aider les autres ; Merci à Imed Ben Tarcha, aka Mimi, pour avoir été à mes côtés depuis presque le début, pour les débats et pour les moments « histoire géopolitique avec Mimi » mais je ne te remercie pas de m'avoir mise dans un carton ; Merci à Deyo Maeztu-Redin, toujours souriant et si gentil, ton gâteau basque est vraiment à tomber ! J'arrive maintenant au bureau des J : Merci à Henrique Trevisan pour ta positive attitude ta dynamique qui égaye toujours mes journées au labo quand je te vois ; Merci à Jacob Langenbach, pour avoir été là depuis presque le début de mes premiers jours au labo et pour les supers moments passés ensemble ; Merci à Violette Mohring pour ta gentillesse, ta générosité et pour les discussions très intéressantes autour du féminisme, on compte sur toi pour maintenir le bon niveau des débats du midi ; Un spécial merci à Maïlie Roquart, aka Lilie la reine des J, pour avoir toujours été à mes côtés durant ces 3 dernières années, de l'expédition à Évry, les réunions de crise le vendredi ou samedi soir jusqu'à la soirée de feu à Bourg Saint-Maurice en passant par le catamaran à la Grande Motte, je n'oublierai jamais ces moments ! J'arrive maintenant au 4^{ème} étage, à commencer avec le bureau des BG : Merci à Thomas Vialon, aka Tote, pour ton expertise en RMN et pour ta volonté à toujours aider les autres. Merci à Maxime Beaugendre pour nous avoir organisé plein de sorties surtout le sushi à volonté. Merci à Clément Desvaux pour les discussions super intéressantes autour de l'écologie. Merci à Larissa Hammer, avec qui j'ai partagé la totalité de ma thèse et des moments très forts dès le début (#onfire), merci pour la soirée allemande qui était trop géniale ! Merci à Olivia Kool pour son sourire et son énergie, tu es

vraiment la reine du dance floor ! Merci aussi à Ibrahim Gode et Alvaro Quinteros pour les bons moments.

Mon bureau des poussins. Alexis Brastel et Sélène Chappuis, aka Xixis et Sésé, vous êtes surement les personnes avec qui j'ai passé le plus de temps durant ces 3 dernières années et quelques mois. Nous avons commencé la thèse à une semaine d'écart chacun et nous avons vraiment vécu tous les moments forts, des hauts et des bas ensemble. Merci d'avoir toujours été présents et à l'écoute quand j'avais besoin. J'apprécie tellement comment on peut débattre sur tout et n'importe quoi en activant le mode sans filtre et sans jugement. Ce que j'ai appris avec vous à travers de nos discussions est tout aussi important que ce que j'ai appris scientifiquement dans ma thèse. Merci à Diego Ciardi, qui nous a rejoint l'année dernière, pour ta bonne humeur, ton énergie et ton sourire qui égayaient le bureau avec trois thésards en dernière année !

Durant ce projet, j'ai eu la chance d'être accueillie dans un deuxième laboratoire, ERRMECe. J'adresse mes remerciements chaleureux à tous les membres permanents pour les discussions scientifiques enrichissantes autour du déjeuner ou pendant les ateliers scientifiques. Merci à Michel Boissière, Adeline Gand, Damien Sayer, Agnès Mihajlowski, et Violetta Rodriguez (BIOSAN) pour les échanges constructifs. Merci à Ambroise Lambert pour m'avoir appris à faire une transfection de cellules. Un spécial merci aux doctorants avec qui j'ai partagé des bons moments au labo et dehors : Maxime Gobin (merci encore pour la raclette !), Solène Rota, Rosa Caldéron, Carla Palomino-Durand, Amel Houaoui, Amel Benabdi, Mathilde Recipon – Le Dinh, Carine Laurent-Issartel, Audrey Deraine.

Mes amis de l'UPMC : Mickaëlla Courjol, Hervé Chan, Antoine Dahi, Murad Abuzarli et Hoang Phuong Thinh. Vous êtes mes premiers amis en France. Merci d'avoir toujours été à mes côtés et pour votre soutien sans faille durant toutes ces années et bien sûr durant ma thèse !

Con xin gửi lời cảm ơn tới gia đình ở Việt Nam và ở Pháp đã luôn yêu thương và ủng hộ. Con cảm ơn bố mẹ đã luôn dành cho con những điều tốt đẹp nhất, cảm ơn những sự hy sinh của bố mẹ để chấp cánh cho con bay xa như ngày hôm nay. Cảm ơn sự tin tưởng và ủng hộ của bố mẹ trong những quyết định của con. Em cảm ơn anh chị đã nâng đỡ em từ những ngày đầu nhiều bỡ ngỡ em bước chân sang Pháp. Cô cảm ơn Ivy và Zoé, hai chuột nhỏ đã mang lại cho cô thật nhiều niềm vui và xua tan mọi căng thẳng. Con yêu cả nhà rất nhiều.

Enfin, merci à toi, Lionel Plancher, d'avoir partagé ma vie depuis plus de 5 ans maintenant. Merci pour ton soutien au quotidien, merci d'avoir été à mes côtés pendant des moments heureux tout comme des moments difficiles. 5 ans, 2 thèses, 2 déménagements et d'innombrables aventures, le bilan est plutôt riche ! Merci d'être un super compagnon de vie, qui m'accompagne et qui me soutient toujours dans mes projets. Je me rends compte que j'ai tellement évolué en tant que personne depuis notre rencontre et ta présence a été décisive. J'ai si hâte de notre vie après-thèse et pour nos prochains projets !

TABLE OF CONTENTS

Introduction.....	8
--------------------------	----------

Chapter I

Literature review.....	15
-------------------------------	-----------

I.1. Requirements for designing injectable matrices for cell delivery.....	17
I.2. Strategies for engineering macroporosity in injectable cell-laden matrices.....	25
I.3. Thermosensitive chitosan/salt mixtures.....	45
References	79

Chapter II

Rational formulation design of injectable thermosensitive chitosan-based hydrogels for cell encapsulation and delivery	97
---	-----------

Résumé en français.....	99
II.1. Introduction.....	100
II.2. Materials & Methods.....	101
II.3. Results & discussion	105
II.4. Conclusion.....	120
References	121

Chapter III

Molecular and microscopic mechanisms of the sol/gel transition in Chitosan/salt mixtures	125
---	------------

Résumé en français.....	127
III.1. Introduction.....	128
III.2. Materials.....	128
III.3. Molecular mechanisms of the sol/gel transition in CS/ β GP/AHP mixtures.....	129
III.4. Microscopic mechanisms of macropore formation in CS/ β GP/AHP mixtures	145
III.5. Conclusions.....	158
References	159

Chapter IV

The microstructure in CS/ β GP/AHP hydrogels..... 163

Résumé en français	165
IV.1. Introduction.....	167
IV.2. Quantitative analysis of the microstructure of CS/ β GP/AHP hydrogels	168
IV.3. Effect of CS characteristics on the properties of CS/ β GP/AHP hydrogels	175
IV.4. Effect of the presence of cells on the microstructure of CS/ β GP/AHP hydrogels ..	187
IV.5. Conclusions.....	194
References	195

Chapter V

Bio-functionalization of CS/ β GP/AHP hydrogels..... 199

Résumé en français	201
IV.1. Introduction.....	202
IV.2. Encapsulation of MPNST cancer cells in CS/ β GP/AHP hydrogels	203
IV.3. Bio-functionalization of CS/ β GP/AHP hydrogels	210
IV.4. Conclusion.....	220
References	221

Conclusion 225

Perspectives 230

Appendices 235

A. Determination of the dissociation constants of β GP and AHP	235
B. Viscometric study on various CS grades.....	236
C. DLS measurements	239
D. Effect of various characteristics of CS on the microstructural and mechanical properties of CS/ β GP/AHP hydrogels	240
E. Staining of cell membrane by Membright 560 (MB560).....	242

INTRODUCTION

Living organisms are composed of one or more cells, which are considered as the most basic structural and functional units of life (*Cell theory, 1839* by Schleiden and Schwann). In the human body, over two hundred different cell types ensure specialized functionalities and the proper running of every organ. In many cases, like injury, disease or aging, cells might die or become dysfunctional and their renewal can be difficult or even impossible, therefore causing an impairment or a threat for the organism. In such situations, cell therapy, or cell-based therapy, might be a promising strategy. This type of therapy consists in delivering progenitor, primary or stem cells into the patient in order to facilitate the regeneration of lost or damaged cell and thus the reparation of the organ or tissue.¹ Tremendous efforts have been made during the last decades in the development of cell-based therapy.^{2,3} In particular, the discovery of induced pluripotent stem cells in 2006 has been a breakthrough in the field and has raised a lot of hopes for the treatment of many diseases.

The success of such therapies strongly depends on the viability and the behavior of cells after transplantation. Unfortunately, it is well-known that direct injection of cell suspensions in culture media or buffers into tissues results in poor retention and very low survival rate.⁴ These unsatisfactory results are attributed to the shear stress forces applied on cells during the injection and to an inadequate microenvironment post-injection. Therefore, there is a growing need for injectable matrices able to support cell survival and retention. These matrices should both provide a protection for the cells during injection through the needle, allowing minimally invasive delivery, and offer a suitable environment for the correct upcoming behavior of the injected cells.

Cell viability, proliferation and migration are governed by a complex, spatiotemporally integrated set of mechanisms that are influenced not only by the biochemistry but also by the biophysics of the extracellular environment.⁵ Therefore, the ideal matrix should possess adequate mechanical, biochemical and microstructural properties, which are adapted to the application. Matrices should possess multi-scale porosity involving both micro- and macro-porosity with a good interconnectivity to ensure the adequate diffusion of molecular biochemical signals, nutrients and waste products and to enable the cellular proliferation and migration that is needed for tissue vascularization.⁶ Despite many efforts and progress, elaborating injectable systems that remain liquid at room temperature and form a macroporous matrix in the presence of cells at body temperature is still a challenge.

In this thesis, I propose to investigate the design of macroporosity in injectable cell-laden matrices. For that, I have studied a particular system composed of a thermosensitive hydrogel in which the sol/gel transition is induced by a phase-separation of aqueous polymer solutions at body temperature. With this research, I have explored how this process results in the formation of a

macroporous network and how this strategy can be adjusted to make relevant matrices for cell encapsulation and delivery.

As of today, the injectable cell-laden matrices that have been proposed can be divided into two main classes: *in situ* forming matrices which are injected in a liquid form and solidify in the targeted site, and preformed matrices which are fabricated prior to cell seeding and then injected into the targeted site. The studied approach in this project belongs to the *in situ* forming matrices class. In such systems, cells can be easily dispersed in the liquid which then becomes a gel at physiological temperature, thus filling in the defect and maintaining cells at the targeted site. Among different studied materials, hydrogels have been widely investigated thanks to their similarities to the native extracellular matrix (ECM). However, most studied injectable hydrogels are characterized by macromolecular networks having nanoscale mesh sizes well below 1 μm , which is much smaller than the average cell size of about 10 μm . Hence, injected cells are trapped in a tight macromolecular network, which compromises their mobility and function. Although many efforts have been made in the recent years, the default of macroporosity remains a bottleneck limiting the efficiency of injectable cell-laden hydrogels.

We investigated here a system composed of chitosan and phosphate salts. Chitosan (CS) is a biosourced polysaccharide obtained by partial deacetylation of chitin, a primary component of cell walls in fungi and crustacean shells. CS possesses beneficial biological properties like low toxicity and biodegradability. CS can be considered as a copolymer with a random distribution of D-glucosamine units (bearing the amine functional group) and *N*-acetyl-glucosamine units (bearing the acetamide group). Amine groups of CS have an apparent $\text{p}K_{\text{app}}$ in the vicinity of 6.2, making CS a polyelectrolyte soluble in acidic conditions. Near neutral pHs where CS is mostly deprotonated, the strong tendency of the CS chains to self-associate through H-bonding and hydrophobic interactions dominates, giving rise to the formation of a hydrated gel-like precipitate.

The poor solubility of CS at physiological pHs has long been a limitation for biomedical uses, until the pioneering work by Chenite *et al.* in 2000.⁷ They demonstrated that adding an organic phosphate salt, beta-glycerophosphate (βGP), allows to raise the pH of CS solution to neutral values without inducing precipitation. This mixture can stay liquid at room temperature but turns into a gel upon heating, in particular at physiological temperature, 37°C. Most interestingly, this gelation results from a phase separation which produces interconnected pores which size can go up to tens of microns. The CS/ βGP system has been the subject of numerous researches to investigate its biocompatibility and its relevance as injectable carrier for drugs and cells. For the use as cell vehicles, this system has a major limitation. It was reported that typical βGP concentrations needed for ensuring physiological pHs and adequate gelation kinetics lead to a hypertonic level of osmolarity, thus inducing cytotoxicity.

My PhD project had multiples objectives. The main goal was to design injectable hydrogels having controlled macroporosity for cell encapsulation and delivery based on thermosensitive chitosan/phosphate salt mixtures. In a more fundamental aspect, it was interesting to gain a deeper understanding on the molecular and microscopic mechanisms involved in this sol/gel transition and on the emergence of the macroporous microstructure in this peculiar system. Moreover, another objective was to explore the possible effects of the presence of cells on the gelation and the formation of the microstructure.

Our strategy was as follows:

Firstly, a rational formulation approach was developed for designing cytocompatible injectable formulations in which the pH and the osmolarity can be adjusted independently. *In vitro* encapsulation studies demonstrated the cytocompatibility of these formulations. Gelation kinetics was investigated to ensure injectability/gelation of these solutions in operating conditions.

Secondly, a study on several CS/salt systems including physiological formulations was performed to investigate the mechanisms of the sol/gel transition in thermosensitive CS/salt mixtures, at both the molecular and microstructural levels.

Thirdly, the microstructure of these systems was studied in depth and quantitatively. The possibility to tune the porosity and the pore size distribution was explored by playing with different parameters, such as the CS concentration and the CS characteristics.

Finally, strategies aiming to improve the bioactivity of these formulations were explored.

This manuscript is organized into five chapters:

Chapter I: This chapter is a literature review organized into three sections. The first section aims at giving a quick overview on the requirements to design injectable cell-laden matrices. The second section exposes several recent progresses to engineer macroporosity in such materials. The third section is devoted to the description of the thermosensitive system composed of chitosan and salt.

Chapter II: Given that the standard system composed of CS and β GP presents a cytotoxic hyperosmolarity, a rational formulation approach to make cytocompatible CS solutions was developed. This approach consists in partially replacing β GP by ammonium hydrogen phosphate, AHP. Using this second salt, the pH and the osmolarity of the formulation can be independently and finely controlled whatever the CS concentration. CS concentration is a key parameter governing the viscoelastic, microstructural and degradation properties of the hydrogels. The cytocompatibility of

one CS/ β GP/AHP formulation was evaluated by *in vitro* encapsulation of pre-osteoblastic MC3T3-E1 cells and primary human gingival fibroblasts. *This study is published in Carbohydrate Polymers, <https://doi.org/10.1016/j.carbpol.2021.118836>.*

Chapter III: The mechanisms of the sol/gel transition at the molecular and microscopic levels were investigated. By exploring CS solutions in the presence of bases having different natures and chemical structures, we demonstrated that the sol/gel transition is strongly governed by the interactions between CS chains and the base. The formation of a macroporous structure in CS/ β GP/AHP formulations was observed combining time-resolved direct observations and light scattering measurements. We demonstrated that this macroporous structure originates from the percolation of CS colloidal-like particles. Based on these results and observation, a model for the mechanisms of the sol/gel transition in the CS/ β GP/AHP system is proposed.

Chapter IV: This chapter is devoted to the microstructure of CS/ β GP/AHP hydrogels. Firstly, we developed methods and tools for a quantitative microstructural characterization of these gels. Secondly, these tools were employed to investigate the effect of the molar mass distribution and the origin of CS on the microstructure. We showed that the porosity and the pore size distribution of CS/ β GP/AHP hydrogels can be tuned while maintaining the physiological conditions by varying CS characteristics. Finally, the effect of the presence of cells on the gelation and the microstructure of the resulting hydrogel was quantitatively studied, which is a key question as the microstructure is formed *in situ* and in the presence of cells.

Chapter V: In this last chapter, we explored the possibility to use CS/ β GP/AHP hydrogels as a 3D encapsulation matrix that could be used to study the development of specific cancer cells *in vitro* and *in vivo*. In collaboration with Dr. Piotr Topilko's team (Institut Mondor de Recherche Biomédicale), the behavior of cancer cells, which are involved in malignant peripheral nerve sheath tumors, was investigated in *in vitro* 2D culture or 3D encapsulation experiments. Cells remained alive up to 6 days of incubation, however very few were able to attach, to spread and to proliferate. These exploratory results highlight the need to improve the bioactivity of CS/ β GP/AHP hydrogels. Accordingly, strategies for functionalizing the formulations with peptide sequences or proteins were explored.

References

- (1) Buzhor, E.; Leshansky, L.; Blumenthal, J.; Barash, H.; Warshawsky, D.; Mazor, Y.; Shtrichman, R. Cell-Based Therapy Approaches: The Hope for Incurable Diseases. *Regen. Med.* **2014**, *9* (5), 649–672. <https://doi.org/10.2217/rme.14.35>.
- (2) Mount, N. M.; Ward, S. J.; Kefalas, P.; Hyllner, J. Cell-Based Therapy Technology Classifications and Translational Challenges. *Philos. Trans. R. Soc. B Biol. Sci.* **2015**, *370* (1680). <https://doi.org/10.1098/rstb.2015.0017>.
- (3) Aly, R. M. Current State of Stem Cell-Based Therapies: An Overview. *Stem Cell Investig.* **2020**, *7* (May), 1–10. <https://doi.org/10.21037/sci-2020-001>.
- (4) Li, J.; Hu, S.; Zhu, D.; Huang, K. Retention and Outcomes From Various Delivery Routes of Cell Therapy Products to the Heart. **2021**, 1–17. <https://doi.org/10.1161/JAHA.120.020402>.
- (5) Chang, H.-I.; Wang, Y. Cell Responses to Surface and Architecture of Tissue Engineering Scaffolds. *Regen. Med. Tissue Eng. - Cells Biomater.* **2011**. <https://doi.org/10.5772/21983>.
- (6) Loh, Q. L.; Choong, C. Three-Dimensional Scaffolds for Tissue Engineering Applications: Role of Porosity and Pore Size. *Tissue Eng. Part B Rev.* **2013**, *19* (6), 485–502. <https://doi.org/10.1089/ten.teb.2012.0437>.
- (7) Chenite, A.; Chaput, C.; Wang, D.; Combes, C.; Buschmann, M. D.; Hoemann, C. D.; Leroux, J. C.; Atkinson, B. L.; Binette, F.; Selmani, A. Novel Injectable Neutral Solutions of Chitosan Form Biodegradable Gels in Situ. *Biomaterials* **2000**, *21* (21), 2155–2161. [https://doi.org/10.1016/S0142-9612\(00\)00116-2](https://doi.org/10.1016/S0142-9612(00)00116-2).

CHAPTER I

LITERATURE REVIEW

TABLE OF CONTENTS

I.1.	Requirements for designing injectable matrices for cell delivery.....	17
I.1.1.	Cytocompatibility.....	18
I.1.2.	Injectability.....	19
I.1.3.	Surface scaffold bio-functionalization.....	19
I.1.4.	Mechanical properties.....	20
I.1.5.	Degradation properties.....	22
I.1.6.	Microstructural properties.....	23
I.2.	Strategies for engineering macroporosity in injectable cell-laden matrices.....	25
I.2.1.	Preformed macroporous matrices.....	25
2.1.a.	Macroporous microcarriers.....	25
2.1.b.	Polymeric cryogels.....	27
2.1.c.	Emulsion templating.....	30
I.2.2.	In situ forming macroporous matrices.....	32
2.2.a.	<i>In situ</i> crosslinking of hydrogels.....	32
2.2.b.	<i>In situ</i> assembly of microbuilding blocks.....	35
2.2.c.	<i>In situ</i> void formation using porogens or foaming agents.....	38
2.2.d.	High-speed shearing treatment.....	40
I.3.	Thermosensitive chitosan/salt mixtures.....	45
I.3.1.	Chitosan and chitin.....	45
3.1.a.	Chemical structure.....	45
3.1.b.	Solubility.....	49
3.1.c.	Biological properties.....	51
I.3.2.	Thermosensitive mixture of chitosan and salts.....	54
3.2.a.	Mixture of chitosan and beta-glycerophosphate (CS/ β GP).....	54
3.2.b.	Mechanisms of the thermoresponsivity in CS/ β GP mixtures.....	59
3.2.c.	Biological properties and application of CS/ β GP gels as <i>in situ</i> forming carriers.....	76
	References.....	79

This literature review is composed of three sections. In the first section, a brief overview on the specific requirements for designing injectable cell-laden matrices is exposed. In this project, we focus on the design of macroporosity in injectable cell-laden matrices while keeping in mind that all of these requirements need to be satisfied for ensuring the survival and activity of cells. Recent progresses and strategies to engineer macroporosity in injectable cell-laden matrices are presented in the second section. Among the proposed strategies, we chose to explore thermosensitive mixtures composed of chitosan and salts. A state-of-the-art about this system, from the physico-chemical to biological properties, is exposed in the last section.

I.1. Requirements for designing injectable matrices for cell delivery

The success of cell-based therapy depends strongly on the viability and the behavior of cells after transplantation. It has been reported that direct injection of suspensions of cells in culture media or specific buffers into tissues results in significant cell loss and death. Very few cells remain in the targeted site with retention rates of the order of 1–10%,^{1–3} and up to 80% of them die within a few days.^{4,5} Such a low survival rate is attributed to the shear forces exerted on the cells during injection and to the absence of a proper microenvironment. As a result, the therapeutic effect of injections of cells alone is very unsatisfactory. For these reasons, there is a growing need for injectable matrices able to support cell retention and survival. Ideally, these matrices would provide a protection for cells during injection through a needle, therefore allowing to deliver the cells in a minimally invasive manner. These cell-loaded matrices should fill the targeted site and act as a temporary physical and chemical support for cell survival and growth until the formation of new tissues. As of today, the injectable cell-laden matrices that have been proposed can be divided into two main classes: *in situ* forming matrices which are injected in a liquid form and solidify in the targeted site, and preformed matrices which are fabricated prior to cell seeding and then injected into the targeted site. These two concepts are illustrated with some corresponding examples in **Figure I - 1**, and will be described in more detail in the second part of this review.

Facing the needs to address numerous requirements, which moreover are application dependent, the design of an ideal injectable matrix for cell delivery remains a challenge. In addition to general requirements in designing cell scaffolds, specific criteria must be taken into account for injectable cell-laden matrices. Among several reviews on the topic,^{5–8} Guyot & Lerouge provided an extensive list of specifications for the design of injectable scaffold for cell delivery.⁵ Firstly, the matrix must be cytocompatible, and secondly must possess adequate complementary characteristics, such as injectability, suitable surface functionality, mechanical properties, adequate degradation rate and

microstructural features. This literature review does not claim to be exhaustive but to provide an overview on these criteria.

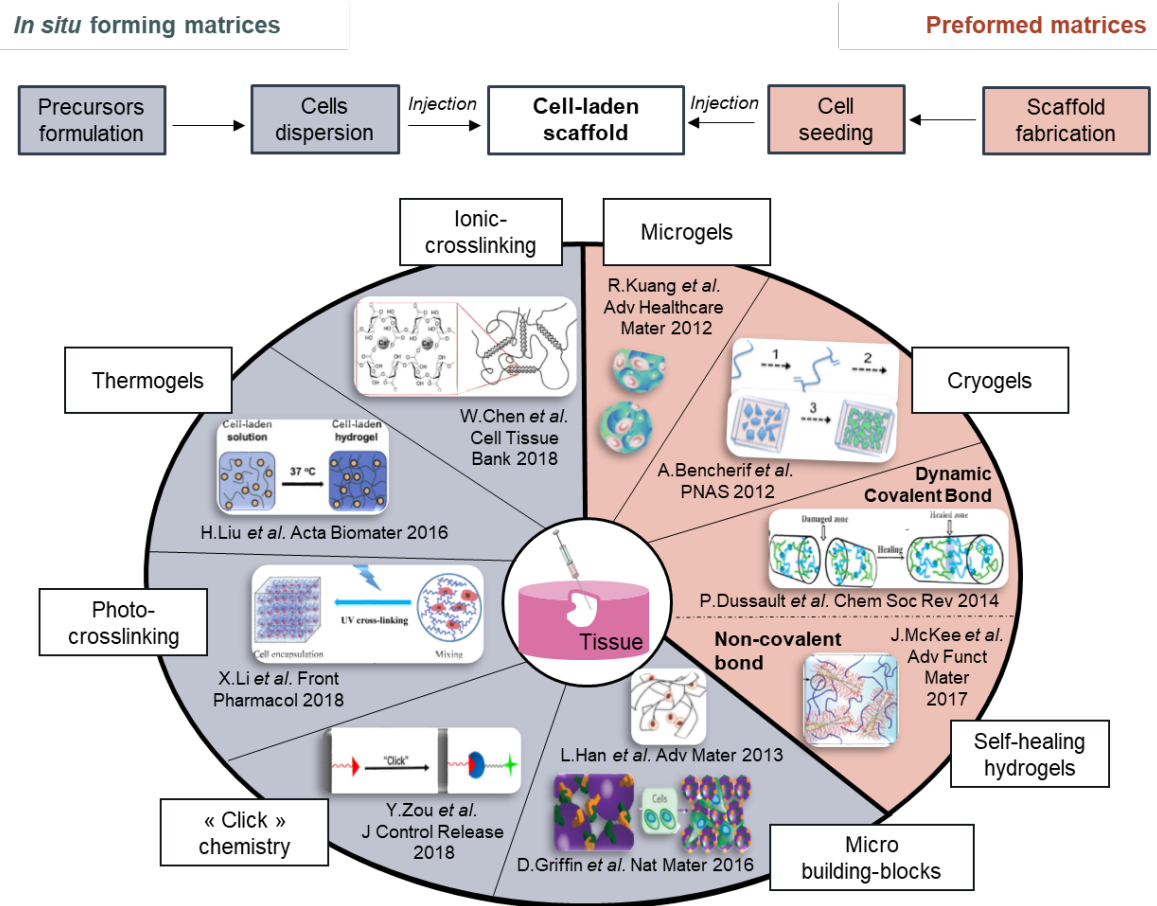


Figure I - 1. Principles and examples of the two main classes of injectable cell-laden matrices

I.1.1. Cytocompatibility

The cytocompatibility must be considered over all the transplantation process: pre-injection, injection and post-injection phases. During the pre-injection and the injection steps, cells should be maintained in physiological conditions, at neutral pH (7.0–7.4), with an osmolarity in the vicinity of 300 mOsm.kg⁻¹.⁵ Moreover, care should be taken not to expose cells to cytotoxic chemical products or reactions. For preformed scaffolds, all residues of solvent or chemical reagents should be eliminated before cell seeding. For *in situ* forming scaffolds, the solidification process occurring *in vivo* must not involve products or reactions toxic to the cells and surrounding tissues. In that respect, naturally derived materials usually provide a better cytocompatibility than synthetic materials.⁹ the literature of cell-laden

systems, the material is usually considered as non-cytotoxic when the cell viability is equal or greater than 70% after at least 24 h.

I.1.2. Injectability

The material should be injectable through a needle, which size depends on the targeted tissue and is typically in the range of 20 to 27 G.¹⁰ In the class of preformed scaffolds, some examples of strategies to achieve injectability are: i) the micrometric size of the scaffold (microspheres)¹¹, ii) the self-healing property (dynamic covalent networks, supramolecular interactions)¹²; or iii) the elasticity at large strains (cryogel).¹³ For *in situ* forming scaffolds, stimuli-responsive hydrogels are usually used in which the gelation can be triggered by different stimuli such as pH¹⁴, temperature¹⁵, light¹⁶ or ionic strength.¹⁷ In these systems, the gelation kinetics must be controlled to permit the injection: the system must be able to flow or be extruded during injection and must solidify rapidly to ensure cell retention. For example, for cell injections into brain, typical injection rate ranges from 60 to 300 $\mu\text{L}\cdot\text{min}^{-1}$ and injection volume varies from tens to hundreds μL .^{10,18} Independently of the cell survival, it was reported that an infusion rate of 3 $\text{mL}\cdot\text{min}^{-1}$ led to complications such as stroke lesions in mouse model.¹⁹ Therefore, it is important that the formulation stays liquid during the dispersion of cells, followed by the injection operation. To the best of our knowledge, the ideal minimal gelation time, after injection, is not clearly defined in the literature and is application dependent, however, it is generally in the order of a couple of seconds to few minutes.

I.1.3. Surface scaffold bio-functionalization

All normal tissue-derived cells (except those derived from the haematopoietic system) are anchorage-dependent cells, *i.e.* they need to attach to a surface to ensure a normal proliferation.²⁰ By contrast, cells derived from the hematopoietic system, and transformed cells such as tumoral cells, are able to proliferate in suspension and do not need any surface for cell growth. For anchorage-dependent cells, the biochemical properties of the scaffold surface must promote cell adhesion. Considerable research and progress have been done in the past decades to functionalize materials surfaces and promote cell adhesion. For example, extracellular matrix (ECM) proteins such as collagen,²¹ fibronectin²² or laminin²³ can be used to enhance cell-scaffold interactions. Peptide sequences containing the arginine-glycine-aspartate (RGD) moiety, the principal integrin-binding site within ECM proteins, has also been extensively explored as a strategy to improve cell attachment.^{22,24-27} Recent advances in application of RGD-functionalized biomaterials are well summarized in the review of Alipour *et al.*²⁸ The use of synthetic peptide sequences containing RGD has the advantages of minimizing the risk of immune reactivity or pathogen transfer, as compared to ECM proteins. Moreover, the conjugation of small

peptide sequences onto biomaterials can be more precisely controlled than for proteins due to the complex conformations of the latter. However, a major advantage of proteins over small peptide sequences is the presence of multiple cell binding sites, which firstly can be recognized by a larger number of integrins and secondly, can have synergic effect to improve cell functions.²⁹

Hence, each strategy has its advantages and limitations. It was reported that both proteins and small peptide sequences were successfully conjugated onto chitosan.³⁰⁻³² In this PhD project, the incorporation of fibronectin and RGD-containing peptide sequences has been explored for improving the bioactivity of thermosensitive CS/salt mixtures.

I.1.4. Mechanical properties

Like the biochemical properties of the surface, the mechanical properties of the scaffold have been shown to significantly influence cell behaviors such as adhesion, growth and differentiation, and to affect their bioactivity.³³ Human tissues present a remarkable spectrum of stiffness. Their elastic moduli range from 10 Pa (intestinal mucus) to 20 GPa (cortical bone).³⁴ Central nervous system tissues and most abdominal organs are considered as the softest tissues while tendons and bones are the stiffest tissues of the human body. Several studies have reported that dynamic changes of surface stiffness were dominant for cell differentiation over environmental factors as temperature or pH.³⁵⁻³⁷ The effect of elastic modulus of the substrate on the phenotype and differentiation of mesenchymal stem cells (MSCs) has been widely studied in 2D cultures.³⁸⁻⁴⁰ For instance, a soft matrix with brain-like stiffness can incite MSCs to undergo neurogenic differentiation while a rigid matrix can incite MSCs to undergo osteogenic differentiation, as shown in **Figure I - 2a**.

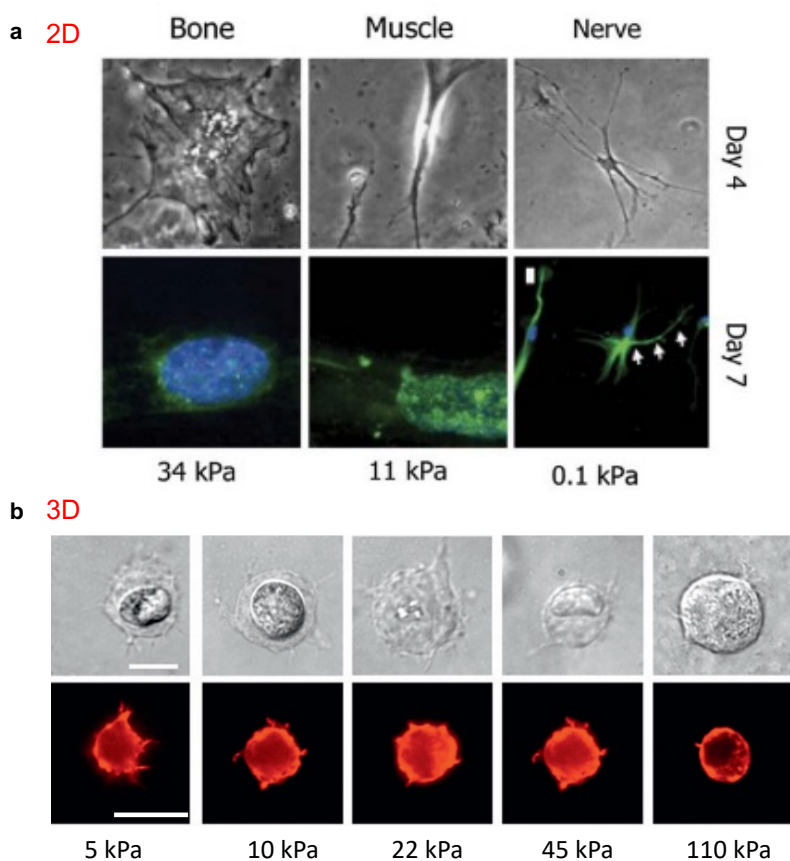


Figure I - 2. The sensitivity of MSCs differentiation to matrix elastic modulus: **a)** in 2D cell culture, blue = nuclei, green = actin cytoskeleton, reproduced from Reilly & Engler⁴¹ and **b)** in 3D cell culture, red = F-actin, scale bar = 10 μm , adapted from Huebsch *et al.*⁴²

Nevertheless, the behavior of cells is much more complex when they are encapsulated or embedded in a 3D environment as compared to a 2D culture. Huebsch *et al.* reported that the elastic modulus has no significant effects on murine MSC morphology in 3D alginate matrices, even after one week of culture (**Figure I - 2b**).⁴² It is also important to note that biological tissues and extracellular matrices are not purely elastic but viscoelastic materials, as they exhibit stress relaxation in response to a deformation.⁴³ Recent studies have revealed exciting findings showing that the viscoelastic properties of the matrix have strong effects on cell behavior.⁴⁴⁻⁴⁷ **Figure I - 3** shows a simplified picture on the dependence of the cellular behavior on the mechanical properties of the matrix, as proposed by Chaudhuri *et al.*⁴⁷ Accordingly, embedded cells exert strains on the matrix which amplitude are determined by the matrix stiffness. In a purely elastic matrix, these mechanical forces applied by cells cannot induce the remodeling of the matrix and the cells remain confined if the pores are too small. Therefore, to facilitate cell spreading, the matrix should have stress-relaxation properties which timescales are comparable with those related to cell behaviors. It has been reported that cells respond to force oscillations over seconds, to traction forces over minutes and cell spreading occurs over minutes to hours.⁴⁷⁻⁵⁰ For instance,

Chaudhuri *et al.* reported that cell spreading, proliferation and osteogenic differentiation of MSCs are all enhanced for encapsulated cells within alginate hydrogels which the stress relaxation timescale decreased from 3300 s to 70 s.⁵¹

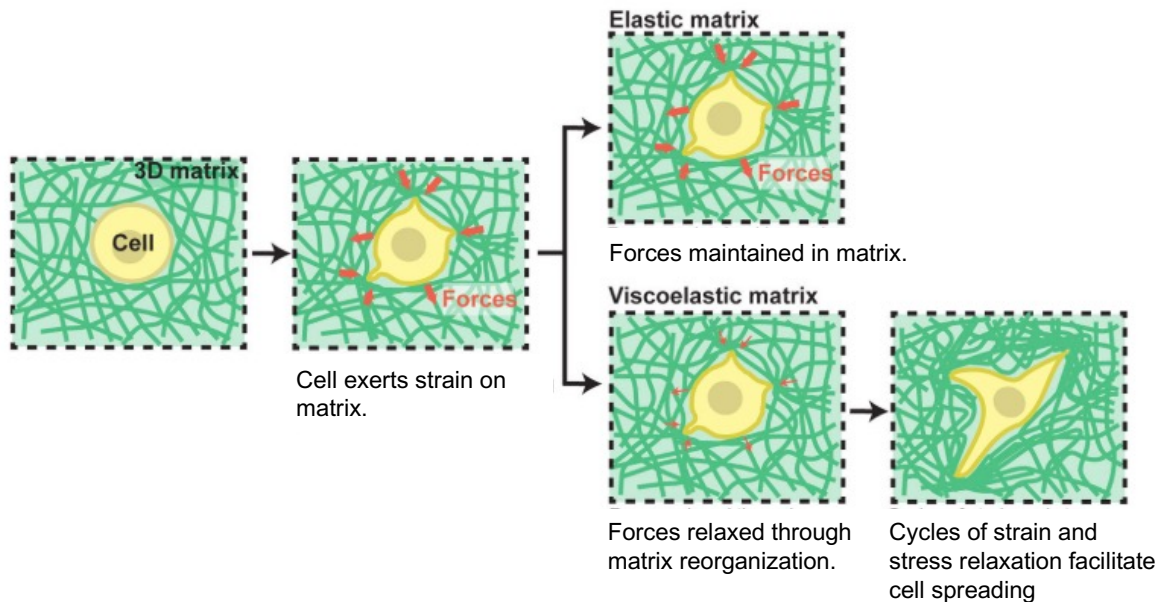


Figure I - 3. Schematic representation of the effect of the elastic modulus and the stress relaxation properties of the matrix on the cellular behavior when cells are encapsulated or embedded within the matrix. Adapted from Chaudhuri *et al.*⁴⁷

1.1.5. Degradation properties

In vivo degradation commonly occurs by hydrolysis or enzymatic processes. The desired kinetics for scaffold degradation depends on the targeted application. For tissue engineering, it is considered that the conditions for isomorphous tissue replacement should be preferred, when the rate of scaffold degradation is comparable to the rate of new tissue formation.⁵² Indeed, if the degradation of the scaffold is much slower than the regeneration process, the prolonged presence of the scaffold may hinder the growth of new tissue and induce an inflammatory response.⁵³ On the contrary, scaffolds that degrade too quickly can fail to support the cell activity until the complete tissue replacement and may create an accumulation of degradation products that induces an inflammatory reaction. Moreover, in the context of cell-laden matrices, the degradation of the matrix is an important parameter that directly affects the cell behavior. Madl *et al.* studied the behavior of neural progenitor cells encapsulated in a hydrogel and reported that increasing the hydrogel degradation promoted the proliferation and the stemness maintenance of neural progenitor cells.⁴⁵

The degradation kinetics of injectable matrices can be tailored by playing with different parameters, such as the solid content, the concentration in degradable functions or component and the crosslinking density. The degradation rate is also a function of the polymer properties, such as chemical composition, crystallinity and molar mass.⁵⁴

I.1.6. Microstructural properties

Scaffolds should possess multi-scale porosity involving both micro- and macro-porosity with a good interconnectivity to ensure the adequate diffusion of nutrients and waste products within the scaffold and to enable the cellular proliferation and migration that is needed for tissue vascularization.^{55,56} The porosity of scaffolds must be adapted to the application as each tissue has its own characteristics.^{56,57} Moreover, specific cells require different pore sizes for optimal attachment, growth and mobility.⁵⁸⁻⁶¹ It was reported in the literature a very wide spectrum of optimal pore sizes, not only as a function of the cell type, but also of the composition and properties of the material. In porous silicon nitride scaffolds, endothelial cells bind only to pores smaller than 80 μm while fibroblasts preferentially bind to pores larger than 90 μm .⁶⁰ In poly(L-lactide) scaffolds, vascular smooth muscle cells bind to pore having sizes ranging from 63 to 150 μm while fibroblasts bind to a wider range from 38 to 150 μm .⁶¹ It has also been demonstrated that vascularization requires pores larger than 300 μm .⁶²

Interestingly, the mechanical behavior of cells greatly depends on how their size is compared to the pore size. This effect was investigated in several studies and was nicely summarized in the literature review of Reilly & Engler.⁴¹ In particular, the cellular contractility appears to be directly regulated by the pore size, as illustrated in **Figure I - 4**. When pores are much larger than cells, the mechano-transduction mechanisms are similar to those on planar substrates. When pores and cells have similar sizes, cells are able to attach tri-dimensionally to the scaffold and the force they apply is smaller than in the 2D configuration. Hence, when varying the pore size, there may exist a continuous transition from highly spread cells onto planar substrates to rounded cells that attach to the scaffold in all dimensions. In addition, we should also keep in mind that cells continuously remodel their environment.

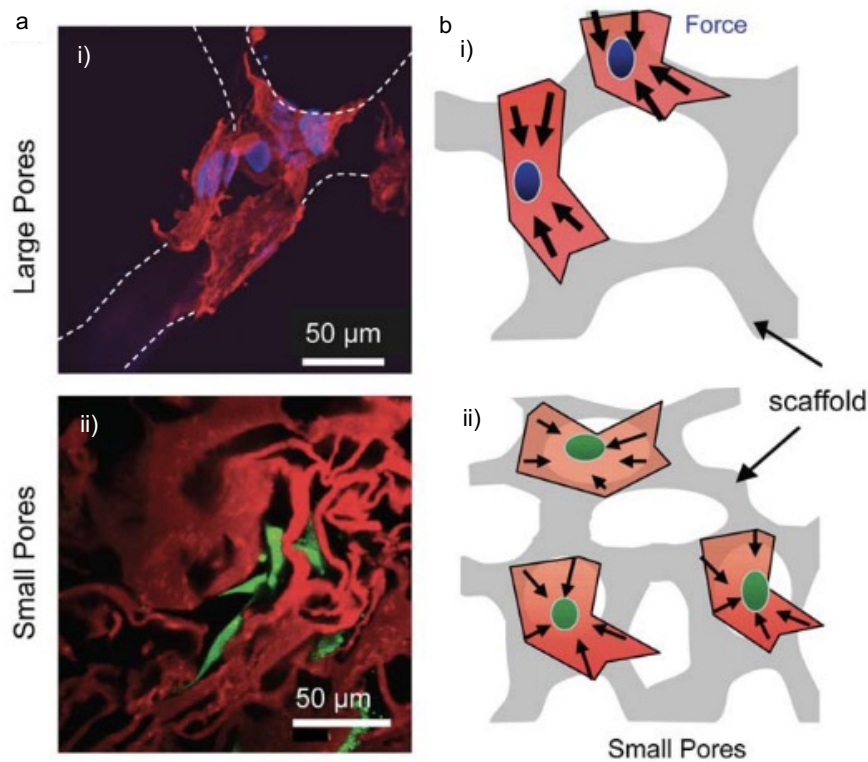


Figure I - 4. Influence of the pore size on cells contractility. **a)** Confocal micrographs of i) stained MSC (blue = nuclei, red = actin cytoskeleton) showing the flat and spread morphology of the cells on the walls of the scaffold (dotted lines) having pores $> 100 \mu\text{m}$; and ii) stained osteoblasts (green) embedded within a scaffold (red) having pores $< 50 \mu\text{m}$; **b)** Scheme illustrating how cells “feel” their environment: i) when the pore size is much larger than the cell size, the force is large (thick arrows) and ii) when the pore size is comparable to cell size, the force is smaller (thin arrows). Reproduced from Reilly and Engler.⁴¹

Despite many efforts and progresses, addressing all the criteria mentioned above still remains a challenge in the development of efficient injectable cell-laden matrices. The cellular behavior in 3D is a complex function depending on many variables including the cellular specificities, and biochemical, mechanical and architecture properties of the matrix.

In this project, we focus on the design of macroporosity in injectable cell-laden matrices while keeping in mind that an overall control of the material properties is needed. In the next section, several recent approaches to elaborate injectable macroporous cell-laden matrices are presented.

I.2. Strategies for engineering macroporosity in injectable cell-laden matrices

Few literature reviews focus on the strategies to develop macroporous injectable cell-laden matrices. We can cite the review by Tong & Yang (2018),⁹ that provides a brief overview of the recent strategies for improving the performance of injectable cell-laden matrices including the specific progress to engineer macroporosity. The following section proposes an up-to-date review on this topic. It is structured in two parts, which correspond to the two main classes of cell-laden injectable matrices, as defined in section 1: preformed *vs in situ* forming matrices.

I.2.1. Preformed macroporous matrices

Three recent approaches are exposed in this section: macroporous microcarriers, polymeric cryogels and emulsion templating.

2.1.a. Macroporous microcarriers

Microcarriers have been widely developed for the last 20 years for minimally invasive delivery of cells. They are generally spherical in shape, referred to as microspheres or microbeads. Polymeric materials, both synthetic (poly(lactic acid),^{63–68} poly(ϵ -caprolactone, PCL),^{69–73} poly(ethylene glycol), PEG⁷⁴) and naturally-derived (collagen,⁷⁵ chitosan,⁷⁶ silk fibroin⁷⁷) have been largely investigated. Inorganic materials such as bioactive glass and ceramic microspheres have also been studied for hard tissue repair.^{78,79} The fabrication technique depends on the type of material. For example, polymer-based microspheres are usually prepared via emulsion-solvent evaporation and phase separation technique.^{66,72,76} For a low dispersity in the size of microspheres, microfluidics and extrusion techniques are preferable over emulsion.⁸⁰ Microcarriers present the advantage of injectability owing to their microscopic size (usually few hundreds of micrometers in diameter). Moreover, their porosity can be controlled using well-known fabrication techniques of preformed 3D scaffolds such as particle leaching or gas foaming. However, these systems have a major limitation: the lack of control on the distribution of the microspheres post-injection. Indeed, microcarriers can easily migrate away from the targeted site under the effect of the physiological stresses. To overcome this problem, the possibility of incorporating microspheres into injectable hydrogels^{73,81} or an excipient⁷⁸ have been recently explored, as described hereafter.

Matamoros-Veloza *et al.* studied porous calcium phosphate glass microspheres along with various viscosity modifiers (xanthan gum, methyl cellulose and carboxyl methyl cellulose) as a potential platform for cell delivery for hard tissue engineering.^{78,79} Resulting microspheres possess interconnected pores with average pore size around 50 μm , which favors the migration of human mesenchymal stem cells within the microspheres in a direct cell culture experiment *in vitro* (**Figure I - 5a,b**). The mixing of these calcium phosphate glass microspheres with xanthan gum at a specific proportion gives a paste

that exhibits shear-thinning behavior and can be injected with a clinically relevant pressure, as shown in **Figure I - 5c**. Liao *et al.* developed an injectable alginate hydrogel loaded with biodegradable porous microspheres containing calcium gluconate.⁷³ The microspheres are based on a block copolymer composed of PEG and PCL, into which the porosity is induced by the foaming of ammonium bicarbonate and can be controlled by the molecular weight of the copolymer. These highly porous microspheres were loaded with calcium gluconate and once mixed with alginate solution, the microspheres released Ca^{2+} ions leading to gelation within 3 minutes *in vitro* and *in vivo*. This approach is interesting because cells, here chondrocytes, can be suspended in the alginate solution together with the microspheres. The resulting injectable composite hydrogel gives rise to a 3D scaffold in which the porosity can be modulated by tuning the degradation rate of the microspheres. *In vivo* subcutaneous injection in rats demonstrated that this system loaded with chondrocytes is efficient for cartilage repair.

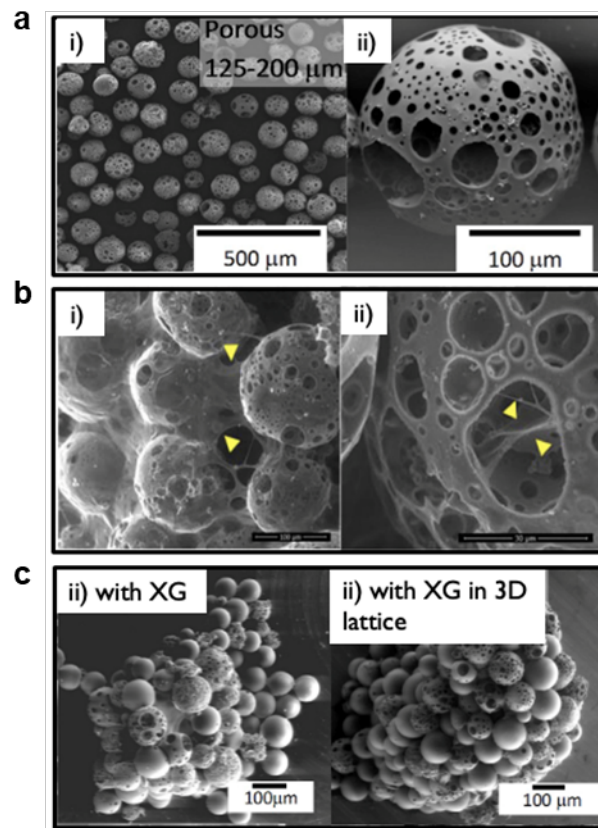


Figure I - 5. *a*) Scanning Electron Microscopy (SEM) images showing the morphology of calcium phosphate-based microspheres (i) and the detailed of the interconnected porosity (ii); ESEM images showing: *b*) stem cell-microsphere aggregates, the yellow arrows indicate cells attached and bridging across several microspheres (i) and yellow arrows indicate colonization of stem cells within the pore of microspheres (ii)⁷⁹; *c*) extruded pastes through a 3 mL syringe and 14 G needle of microspheres with xanthan gum (XG) (i) and with XG using a 3D osteoporotic lattice (ii).⁷⁸

2.1.b. Polymeric cryogels

Cryogels are defined as a class of hydrogels prepared by a process called cryogelation.¹³ In general, cryogelation is produced from a polymer solution and involves three steps as described in **Figure I - 6a**: 1) phase separation with the formation of solvent crystals at subzero temperatures, 2) crosslinking/polymerization of precursors (that can be monomeric or polymeric) in the liquid phase and 3) thawing of solvent crystals leading to an open and interconnected macroporous polymer network.⁸² In a similar manner to conventional hydrogels obtained by crosslinking in solution, the crosslinking/polymerization can be achieved by covalent reaction of monomers or pre-polymers (chemically-crosslinked cryogels) or by weak interactions such as ionic or hydrophobic interactions between polymer chains (physically-crosslinked cryogels). This process gives the possibility to elaborate a 3D cell scaffold with precise and controlled porosity by playing with adjustable parameters such as the crosslink type, the cryogelation temperature, the nature and concentration of the precursor and solvent, the cooling rate, etc.⁸² Both natural polymers (gelatin,^{83–86} alginate,⁸⁷ starch⁸⁸, etc.) and synthetic polymers (PEG,^{84,89,90} PCL,⁹¹) have been intensively studied to make cryogels for biomedical applications.

The first injectable 3D scaffold in the form of an elastic sponge-like matrix prepared by cryogelation was reported by Bencherif *et al.* in 2012.⁸⁷ Using methacrylated-alginate grafted RGD, these authors prepared a preformed cryogel by a free-radical crosslinking mechanism. The average pore size determined by SEM images was between 150–200 μm . Unlike a conventional hydrogel obtained by crosslinking in solution, their cryogel exhibits large and interconnected macropores (**Figure I - 6b,c**). Thanks to the reversible collapse of the pores, this cryogel has an excellent elasticity up to very large compressive strains (> 80%) (**Figure I - 6d**) thus the ability of being squeezed through conventional needle-syringe injection (16 gauge) and rapidly recovering its original structure. This alginate-based cryogel showed great potential to be used as an injectable cell delivery vehicle. Clonally-derived murine mesenchymal stem cells were loaded into the cryogel and showed good cell retention (80%) and cell viability (92%) after *in vitro* injection (**Figure I - 6e**). In *in vivo* dorsal injection into mice, the cryogel maintained cells at the introduction area up to 15 days after injection.

More recently, Kim *et al.* developed an injectable heparin/gelatin-based cryogel for the treatment of the *in vivo* hind-limb ischemia model.⁹² The formation of the cryogel is based on two levels of crosslinking using the carbodiimide reaction: intramolecular crosslinking of gelatin (type A) and intermolecular conjugation of heparin to gelatin. The resulting cryogels have an interconnected macroporous structure with pore diameters around 100 μm . The gelatin concentration determines various properties of the resulting cryogel including porosity, elasticity and swelling property while the heparin concentration controls the release of growth factors. By playing with the composition of the cryogel, the authors

succeeded in preparing an optimized cryogel and demonstrated with an *in vivo* ischemic hind-limb mouse model that NIH3T3 fibroblasts-loaded cryogels allowed an improvement of neovascularization.

In spite of the great potential of cryogels for minimally invasive delivery, as demonstrated in the last two examples, these systems cannot offer freeform fabrication in order to fill-in usually complex wound sites. To overcome this problem, 3D printing with cryogel ink has been developed.^{93,94} Serex *et al.* used carboxymethyl cellulose as cryogel ink to create printed cryogel having a controlled porosity and a complex geometry (**Figure I - 6f**).⁹⁴ The pore size can be tuned from 4 μm to over 20 μm by simply changing the probe temperature. NOR-10 cells seeded on the printed cryogel exhibit good viability. By tuning the pore size, cells can be guided and seeded in specific places in the printed cryogel as cells can only spread in large pores (25 μm), as shown in **Figure I - 6g**. With the same concept, the same group prepared soft free-form scaffolds with shape memory that could endure partial dehydration-rehydration deployment for minimally invasive delivery.⁹⁵

The cryogelation technique was also used to elaborate microcarriers for cell delivery.^{84-86,89} The first demonstration of fabrication and application of microscale cryogels as cell carriers was reported by Liu *et al.*⁸⁴ They fabricated ready-to-use array chip containing microcryogels that enable homogeneous and automatic loading of tailored cellular niches. The PEG-derived microcryogels have an interconnected macroporous structure with pore sizes ranging from 20 to 80 μm and a great elasticity under compression. Suspensions of cells can be automatically and homogeneously loaded into the microgels via physical absorption. NIH3T3 fibroblasts and human mesenchymal stem cells encapsulated in alginate-loaded microcryogels show good viability after 7 days. *In vivo* subcutaneous injection of NIH-3T3 alginate-loaded microcryogels in mice showed induction of angiogenesis 2 weeks after injection, demonstrating the potential of this system for therapeutic application in ischemia treatment. As compared to bulk cryogels, microcryogels have the advantage of being injectable through smaller needles (16 G for bulk cryogels vs 27 G for microcryogels). Nevertheless, they provide a lower level of control over the post-injection distribution.

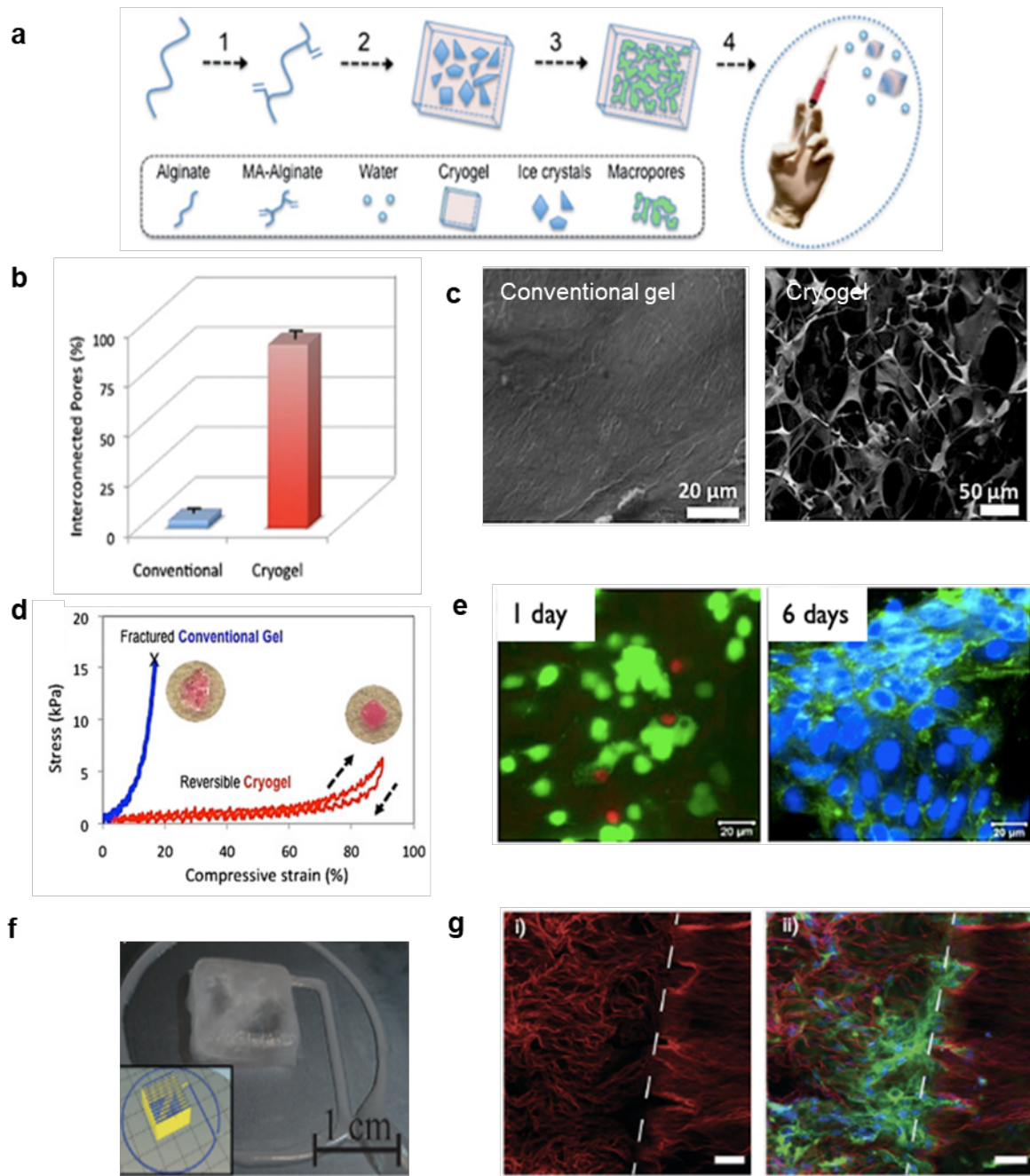


Figure I - 6. *a)* Scheme illustrating the cryogelation process; *b-d)* Comparison of the structural and mechanical properties between conventional nanoporous gels vs cryogels both fabricated with 1 %w/v MA-alginate: *b)* the pore connectivity, *c)* SEM images, *d)* stress vs strain curves of compression tests; *e)* Confocal microscopy images of live/dead staining of MSCs seeded into RGD-modified MA-alginate cryogels at 1 day and 6 days post-injection (green: live cells, red: dead cells, blue: nuclei). Adapted from Bencherif et al.⁸⁷ *f)* Photograph of a 3D printed cryogel; *g)* Confocal microscopy images highlighting the possibility to choose specific seeding areas based on the pore size: (i) the transition from 25 μm to 5 μm pores form a cell barrier; (ii) cells spread well in the large pores but cannot migrate into the small pores region. Red: cryogel, green: actin, blue: nuclei. Adapted from Serex et al.⁹⁴

2.1.c. Emulsion templating

Emulsion templating techniques has emerged into the field of tissue engineering in the 80s. Nonetheless, their use to fabricate *in situ* forming macroporous cell-laden scaffolds remains relatively new compared to other approaches.⁹⁶ This technique is based on emulsions or foams where the dispersed phase (internal phase) behaves like a template that will be removed following solidification leading to a porous structure. The term “High Internal Phase Emulsion” (HIPE) is used when the internal phase presents at least 74% of the emulsion volume.⁹⁶ Above this volume fraction, the dispersed phase droplets deformed into polyhedra. The main advantage of this approach for fabricating 3D scaffolds is the high tunability of the porosity and the interconnectivity of the structure by playing with parameters such as internal phase content, surfactant nature and content, stirring speed,...⁹⁷ Nevertheless, this process requires a freeze-drying or a washing step to remove the liquid phase and to eliminate residues of chemical precursors and surfactants. Nowadays, only few studies have reported injectable HIPE processes that can be served as cell carrier, examples are presented hereafter.

Oh *et al.* designed a dual thermoresponsive gelatin-graft-PNIPAM copolymer that can be emulsified with large amount of oil to form HIPE thanks to its amphiphilicity.⁹⁸ The fabrication process is illustrated in **Figure I - 7a**. At 4°C, the gelatin backbone solidifies while at 40°C the PNIPAM side chains become insoluble and form physical crosslinks. In a systematic study, the authors explored the effect of the oil fraction, the gelation type (at 4°C or 40°C) and the grafted PNIPAM chains fraction on the porosity of the freeze-dried hydrogel. They showed that the average pore diameter can be tuned from 10 to 160 µm by varying these parameters (**Figure I - 7b**). However, a characterization of the final structure of the hydrogel in physiological conditions at 37°C is missing. Using human foreskin fibroblasts, cell-laden hydrogels were prepared and an injection assay through a hypodermic needle was performed. The hydrogels broke up into pieces but retained their bulk structure and the cells remained alive right after injection (**Figure I - 7c**).

Zhou *et al.* synthesized alginate-based ion-responsive macroporous hydrogels using oil-in-water HIPE templating.⁹⁹ The authors combined covalently crosslinked methacrylate-modified alginate HIPE hydrogels giving these hydrogels permanent porosity with the well-known ion-responsiveness of alginate to Ca²⁺ ions. Upon extrusion through a hypodermic needle, the covalently crosslinked hydrogel broke up into small fragments which were then recombined together thanks to the complexation of unmodified alginate and Ca²⁺ ions. *Ex vivo* injection assays into pork muscle demonstrated that the interconnected macroporous structure could be observed in the reformed scaffold without apparent pore size change as compared to the hydrogel before injection. The pore size characterized using SEM was found to be in the range 14–31 µm. In a direct contact cytotoxicity test, human pneumocyte-like A549

cells showed extensive colonization on the surface and inside the hydrogel as well as better proliferation compared to the positive control.

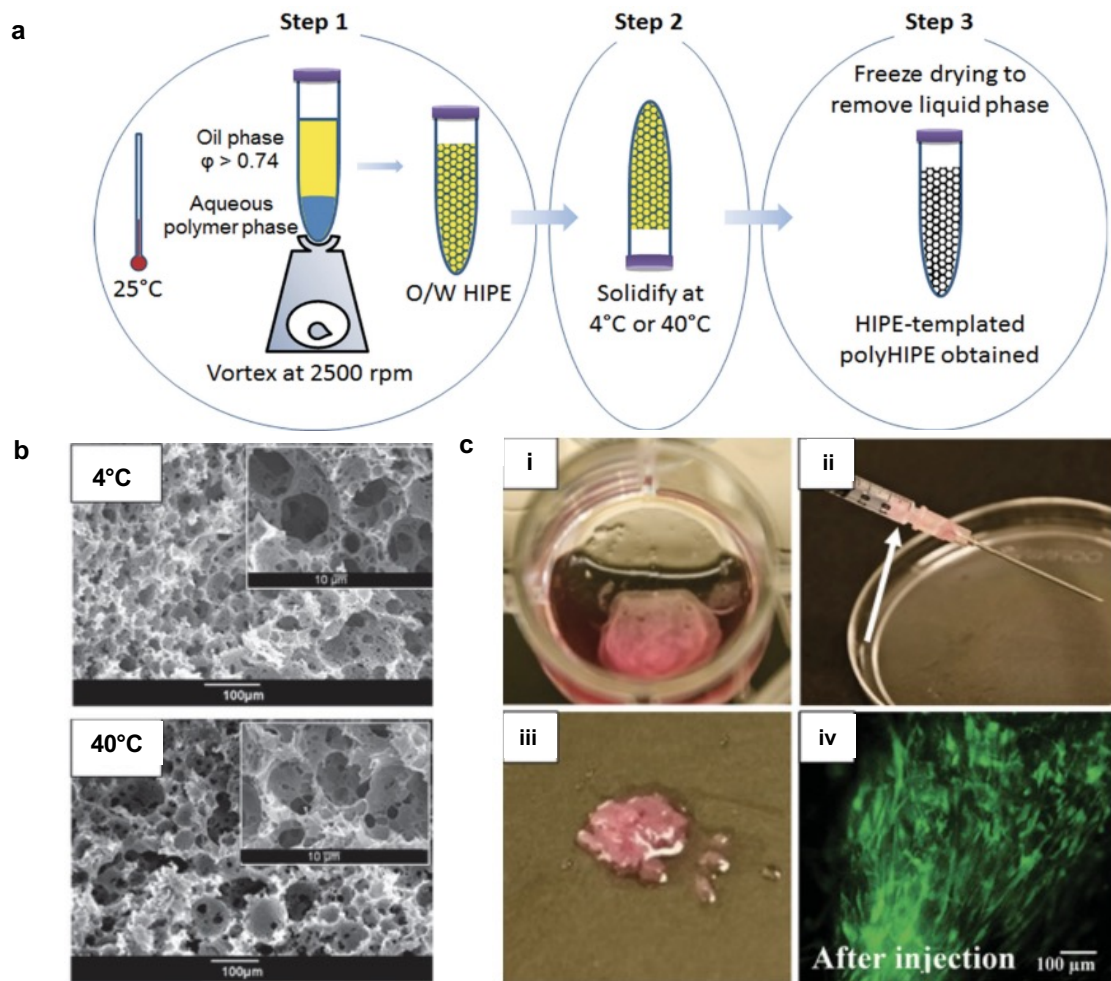


Figure I - 7. **a)** Scheme presenting the fabrication process of poly(gelatin)HIPE; **b)** SEM images of poly(gelatin)HIPE gelled at 4°C or 40°C; **c)** Photographs illustrating cell loading and injection: Cell-laden poly(gelatin)HIPE in culture media (i), loaded into a syringe (ii) and after being extruded (iii), fluorescence image of cells after the injection (iv) (green = live cells). Adapted from Oh et al.⁹⁸

1.2.3. *In situ* forming macroporous matrices

Four recent *in situ* approaches are reported in this section: crosslinking of hydrogels, assembly of micro-building blocks, use of porogens or foaming agents and high-speed shearing treatment.

2.3.a. *In situ* crosslinking of hydrogels

In situ forming hydrogels are very popular materials in tissue engineering thanks to their similarities to the extracellular matrix.¹⁰⁰ Composed of a physically and/or chemically cross-linked network of polymers swollen in water, the properties of the hydrogel can be tuned to match a wide range of physical, mechanical, chemical and biological properties. However, most of existing injectable hydrogels are characterized by cross-linked molecular networks having a nanoscale mesh size of the order of 1–100 nm, thus a porosity not compatible with cell development.^{101,102} Still, some studies have recently reported *in situ* forming hydrogels presenting a macroporous structure, using adjustment of crosslinking density and polymer concentration.^{103–106} Examples will be given in the following paragraphs.

In situ chemical crosslinking can be achieved using a variety of reactions, for example Schiff base reactions,^{81,103,104,107} click chemistry^{108–111} or photo-initiated crosslinking^{16,112–116}. In particular, the Schiff base reaction between amine or hydrazide groups and aldehyde allows a gelation without any chemical crosslinking agents and without releasing toxic by-products. Here are two examples of recently reported systems. Yan *et al.* reported an injectable hydrogel using modified poly(L-glutamic acid) with dihydrazide (PLGA-ADH) and aldehyde (PLGA-CHO) functions (**Figure I - 8a,b**).¹⁰³ The gelation time around ten seconds is very rapid, which might complicate the cell dispersion and injection. These authors showed that the pore size of the resulting hydrogel can be tuned from 20 to 100 μm by changing the solid content, the ratio between dihydrazide and aldehyde groups and the oxidation degree of PLGA-CHO (**Figure I - 8c-f**). **Figure I - 8g** shows fluorescence micrographs of encapsulated chondrocytes in PLGA hydrogels stained using Live/Dead assay, at different times of culture. The cells survived up to a long period of 21 days (viability = 75%). Using the same chemistry, Li *et al.* developed a system based on two polysaccharides, pullulan and chondroitin sulfate.¹⁰⁴ Large pores up to 300 μm could be obtained. Encapsulated rabbit articular chondrocytes in the gel showed good viability (> 80%) and a normal morphology after 14 days culture. It is surprising to see such large pores in these chemically cross-linked hydrogels. No explanation on the origin of the porosity was given in both articles. Two possible explanations can be proposed. The first explanation is that the macropores might arise from a phase separation due to the possible presence of aggregates. In the second explanation, the macropores might come from an artifact of the freeze-drying step prior to SEM observations. Indeed, ice crystals are created during this step and acts like porogens. This process has been previously used to generate porosity in preformed scaffolds.^{117,118}

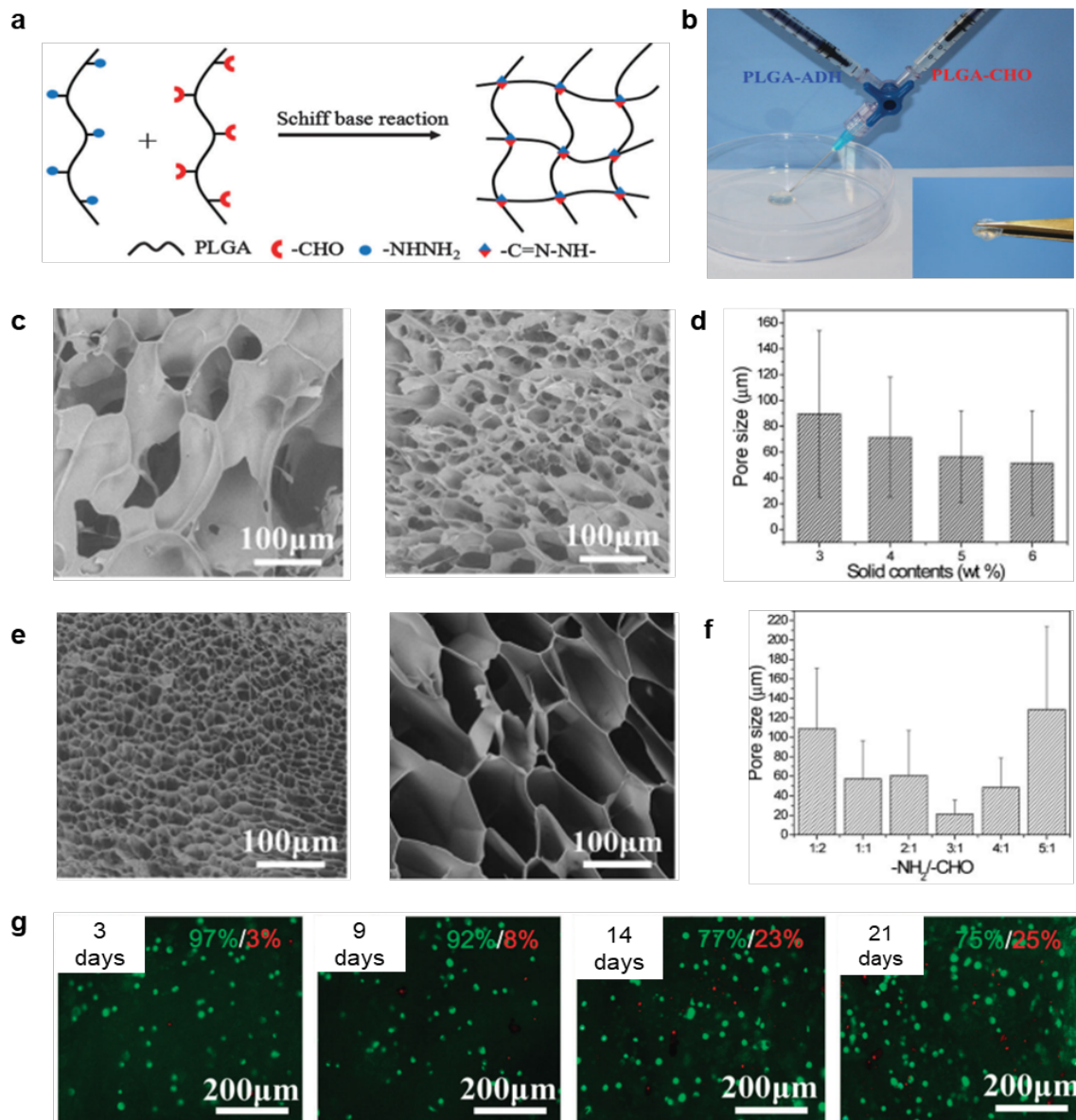


Figure I - 8. *a)* Schematic of in situ hydrogel crosslinking by Schiff base reaction. *b)* Photographs of the in situ formation of the hydrogel using dual syringes. *c)* SEM images of lyophilized hydrogels with solid contents of 3 or 6 wt%. *d)* Effect of the solid content on the pore size. *e)* SEM images of lyophilized hydrogels with $\text{-NH}_2/\text{-CHO}$ molar ratio of 3:1 or 5:1. *f)* Effect of the $\text{-NH}_2/\text{-CHO}$ molar ratio on the pore size. *g)* Fluorescence micrographs of encapsulated chondrocytes in PLGA hydrogel at 6 wt% of solid content (green = live cells, red = dead cells). Adapted from Yan et al.¹⁰³

In situ physical crosslinking can be achieved using a variety of interactions such as electrostatic interaction, hydrogen bonding, hydrophobic interaction, etc. Among the different systems, thermosensitive injectable hydrogels (or thermogels) are the most studied for cell encapsulation and delivery because of the mild processing condition.^{15,119–127} In these systems, cells can be dispersed in a liquid at room temperature which then becomes quickly a gel at physiological temperature. To the best

of our knowledge, very few studies have characterized the microstructure and the porosity of thermogels for cell encapsulation and delivery.

Some studies have reported thermosensitive hydrogels in which the sol/gel is induced by a phase-separation process resulting in a macroporous network.^{105,106,128,129} In particular, Lü and coworkers reported an injectable hydrogel based on chondroitin sulfate grafted poly(*N*-isopropylacrylamide) (PNIPAAm).¹⁰⁵ Possessing a low critical solution temperature around 32°C, PNIPAAm exhibits a phase transition under physiological conditions. SEM observation of lyophilized gels showed interconnected porous structure with an average pore size of 25 µm. The viability of encapsulated cancer HeLa cells was good up to 4 days (90 %) but drops to 50% at the 7th day.

Another example is the thermosensitive injectable cell-carrier designed by Yeon *et al.*, which is based on diblock copolymer poly(ethylene glycol)-poly(L-alanine) (PEG-PA).¹⁰⁶ In solution, the copolymer chains auto-assemble into micelles. When the temperature increases, PA undergoes a helix-to-random-coil transition, along with the dehydration of PEG, inducing aggregation of the micelles, as shown in **Figure I - 9a**. The authors stated that the pore size distribution is a complex function of the polymer composition and concentration. By playing with these two parameters, they obtained macroporous hydrogels with pores up to 50 µm (**Figure I - 9b**). *In vitro* 3D culture of adipose-derived stem cells (ADSCs) showed comparable viability and proliferation as in Matrigel (cell proliferation of 300-400% at 14 days) but the morphology of the cells remained rounded and no sign of fibroblastic morphological changes was observed. *In vivo* study in mice showed chondrogenic differentiation of ADSCs in the gel implanted in the subcutaneous layer.

This concept was also applied to chitosan, a pseudo-natural cationic polysaccharide. Chenite *et al.* reported a thermosensitive hydrogel composed of chitosan and β-glycerophosphate, an organic phosphate salt. Interestingly, this system can stay liquid at 20°C at neutral pH and turns quickly into a gel when temperature increases to 37°C.¹²⁹ Briefly, upon heating, chitosan chains tend to aggregate through H-bonds and hydrophobic interactions, thus inducing a phase separation resulting in the formation of a macroporous gel. *In vitro* encapsulation of several cell lines (cos-7, L929 and Rat-1) showed > 80% of cell viability over 3 weeks. *In vivo* chondrocytes transplantation in mice indicated several areas of remodeling chondrocytes secreting a matrix characteristic of normal cartilage 3 weeks later.

Such thermosensitive chitosan/salt mixtures form the core of this PhD work. The mechanisms of their sol/gel transition and the biological properties of these peculiar systems will be detailed in the third section: Thermosensitive chitosan/salt mixtures.

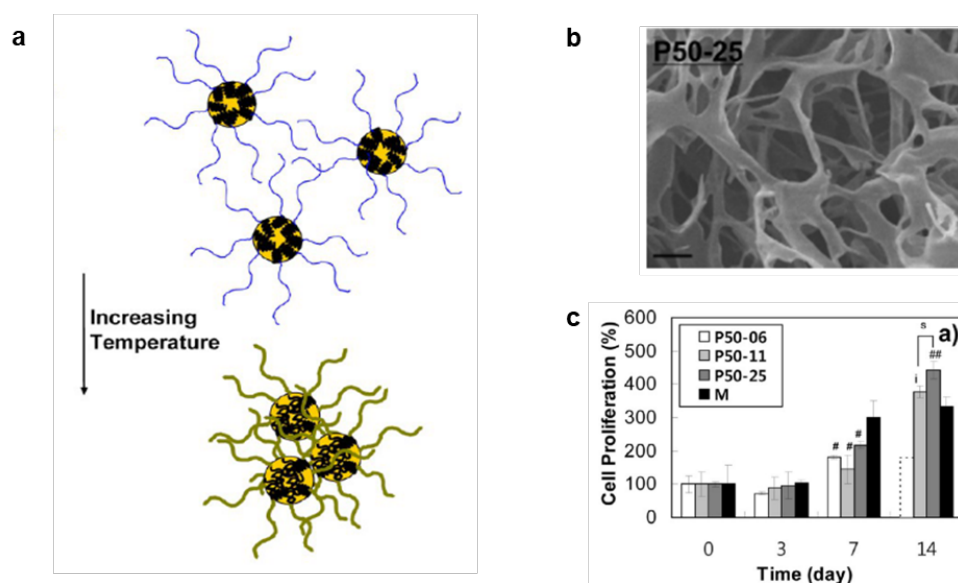


Figure I - 9. a) Schematic presentation of temperature-sensitive conformational changes of PEG-PA micelles in water: PEGs dehydration (hydrated state: thin blue curves, dehydrated state: thick yellow curves), PA phase transition from α -helix to random coil (black curves) and micelles aggregates as the temperature increases; b) SEM images of typical lyophilized hydrogel, scale bar = 10 μ m. c) Proliferation rate of encapsulated ADSCs in PEG-PA hydrogels prepared with three different molar masses of PA, as compared to Matrigel (M). Reproduced from Yeon *et al.*¹⁰⁶

2.3.b. *In situ* assembly of microbuilding blocks

Instead of forming a gel from a molecular solution, another type of approach consists in the *in situ* assembly of microscopic building blocks to fabricate large and complex tissue construct. This class of biomaterial has the advantage of having an enhanced pore interconnectivity and a fine tuning materials property through the design of preformed microbuilding blocks. Two major types of microbuilding blocks (microgels and microribbons) were investigated and resulting scaffolds showed remarkable success as cell culture platforms.

When the microbuilding blocks are microgels, these materials can be defined as “granular hydrogels”.¹³⁰ These macroporous scaffolds are formed by interlinking of microgels through various mechanisms: weak interactions,^{131,132} enzymatic^{133–137} or chemical crosslinking^{138,139} or cell-bridging through cell-particle adhesion.^{140–142} These microgels are self-assembled into a fully percolated network which inherent pore size is the interstitial space among the particles, followed by an annealing using surface functionalities to create an interconnected porous scaffold (**Figure I - 10a**). The first injectable granular hydrogel, termed “microporous annealed particle (MAP) hydrogels” was reported by Griffin *et al.*¹³⁷ The PEG-based microgels surface was functionalized with peptides moieties and could be directly injected into the wound site and *in situ* “annealed”, *i.e.* solidified, via enzymatic crosslinking. By using

a microfluidic approach, the microgels building blocks size could be finely tuned from 30 to 150 μm . The MAP hydrogel supported 3D cellular network formation and proliferation of encapsulated cells within 48 hours *in vitro*. More recently they demonstrated that *in vivo*, mesenchymal stem cells delivery within MAP scaffold largely enhanced the cell proliferation compared to cell delivery in PBS or in an *in situ* crosslinked PEG-based hydrogel, presenting no macroporosity (**Figure I - 10b**).¹³⁴ The same research group also explored the possibility to prepare MAP scaffolds based on hyaluronic acid building blocks and investigated three different annealing approaches without any additional modification of the microgels: enzymatic crosslinking as previous, light induced radical polymerization and carbodiimide chemistry.¹³⁸ Interestingly, they observed that differences in porosity fraction and characteristic pore size with changing the annealing method followed a common trend: radical polymerization > carbodiimide chemistry > enzymatic crosslinking. This was explained by the difference in packing prior to gelation depending on the settling time, which varied within the three approaches. Hence, the pore diameter could be finely tuned by controlling the packing prior to gelation.

Another microbuilding blocks forming 3D scaffold are the microribbons. Inspired by preformed microfiber-based scaffolds, this concept has been explored in order to overcome the poor cell infiltration and distribution that is encountered in original method, as cells are usually seeded onto preformed scaffold. All existing microribbons-based hydrogels were fabricated using photo-crosslinking with microribbons made of natural polymer (exclusively gelatin¹⁴³⁻¹⁴⁷) and synthetic polymers (PEG)¹⁴⁸, poly(lactide-co-glycolide)^{149,150}). Han *et al.* developed microribbon-like, injectable hydrogels for fabricating *in situ* macroporous and highly flexible scaffolds in the presence of cells.¹⁴³ The microribbons were made from gelatin by a wet-spinning process and modified with methacrylate or hydroxyl groups. The so-obtained microribbons were then cross-linked by exposure to light and formed a microporous gelatin network (**Figure I - 10c**). The space among microribbons formed interconnected macropores. The porosity fraction and the median pore size can be tuned by controlling the density of microribbons (**Figure I - 10d**). Typically, increasing the density in microribbons from 2.5 to 10% w/v led to a decrease in pore size from 250 μm to 50 μm . By investigating the effect of the pore size on the morphology of encapsulated adipose-derived stromal cells, these authors showed that no difference was observed by Day 6, however, by Day 20, cells adapted a rounder morphology when encapsulated in smaller pores of 50 μm and more spindle shapes in larger pores of 250 μm by day.

One advantage of the microribbon-based scaffold is its ability to decouple easily the “microenvironment stiffness” (determined by the individual microribbon rigidity) that the cell senses, from the “scaffold bulk stiffness” (determined by the density of the microribbons). The individual microribbon rigidity can be tuned by varying the PEG end-group chemistry while the scaffold bulk stiffness can be tuned by varying the microribbon density, as shown in **Figure I - 10e,f**. However, the synthesis of these microribbons is complicated and time-consuming. Indeed, it is a long process including the formation

of the microribbons by wet-spinning, the pre-crosslinking process and multiple drying and washing steps involving the use of organic solvents.

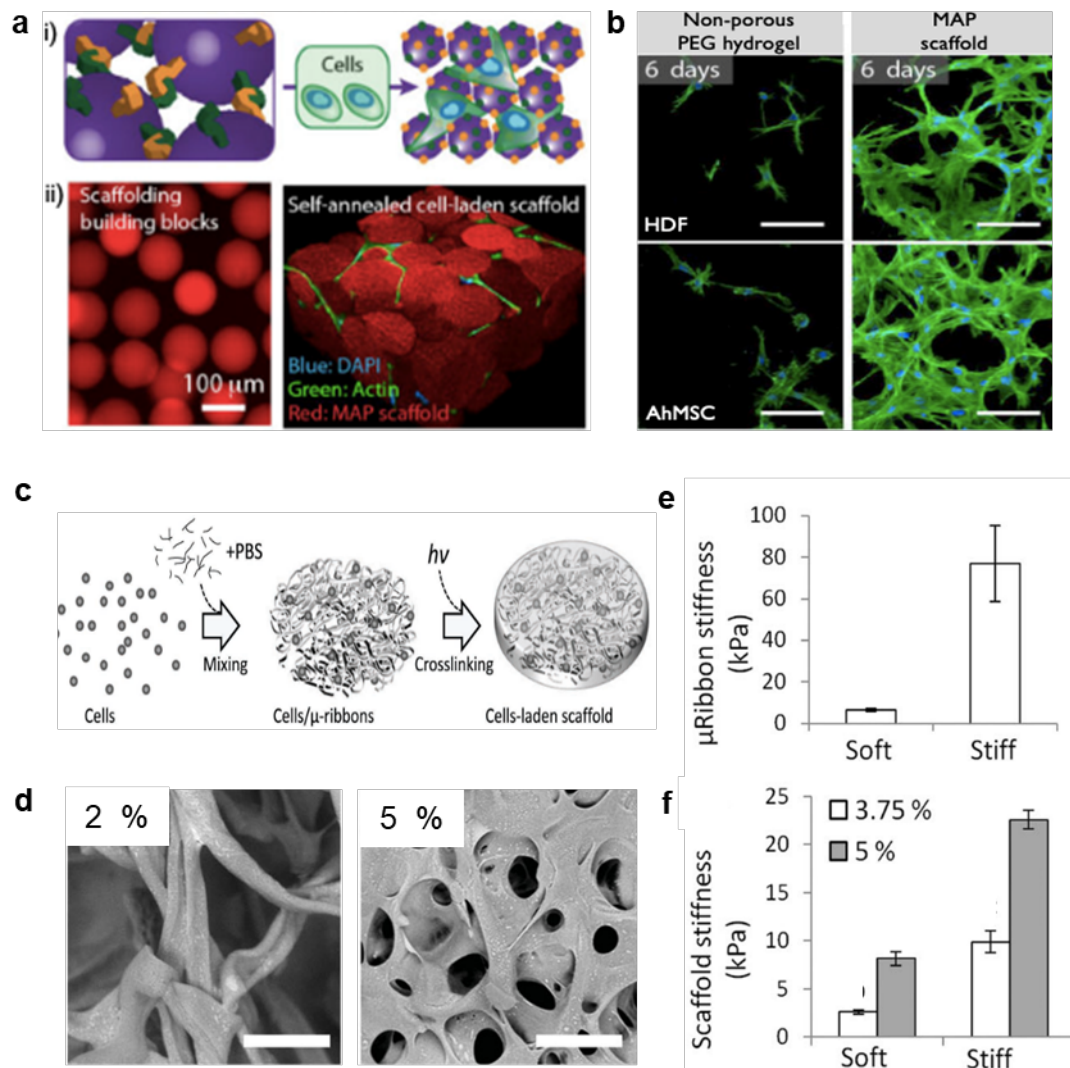


Figure 1 - 10. *a*) Annealing of the microgels using enzymatic cross-linking between peptide moieties (yellow and green hooks) into porous scaffold, either as a pure scaffold or in presence of cells (*i*) and confocal microscopy images showing individual microgel building blocks and subsequent cell-laden MAP scaffold (*ii*); *b*) MAP scaffold facilitates in vitro cell growth and the formation of 3D cellular network compared to non-macroporous scaffold for human dermal fibroblasts HDF and adipose-derived mesenchymal stem cells AhMSC. Adapted from Griffin et al.¹³³ *c*) Scheme of the encapsulation process of cells within photo-crosslinkable microribbon-based scaffold. Adapted from Han et al.¹⁴³ *d*) SEM images of the morphology of microribbon-based scaffolds prepared with different microribbon densities (2 or 5%). *e*) Tuning the individual microribbon stiffness by varying the PEG end-group chemistry. *f*) Tuning the macroscopic stiffness by varying microribbon density. Adapted from Han et al.¹⁴⁸

2.3.c. *In situ* void formation using porogens or foaming agents

Inspired by porogen leaching and gas foaming which are two well-known methods employed in the fabrication of conventional scaffolds, recent studies have reported the use of degradable and biocompatible porogens or foaming agents to induce macroporosity *in situ* under physiological conditions. This approach is convenient as the porosity and the pore size can be simply controlled by the concentration and the size of porogens and by the concentration of foaming agents.

Various natural-based polymers and hydrogels were investigated as porogen agents.^{151–157} Porogen agents can be degraded via thermosensitive, enzymatic or chelating processes, which needs to be cell-friendly. For example, Hwang *et al.* prepared injectable alginate hydrogels having macropores which diameter ranging from 150 to 300 μm . These macropores are generated by the instantaneous dissolution of gelatin microbeads at physiological conditions (**Figure I - 11a**).¹⁵⁶ Huebsch *et al.* developed a macroporous hydrogel by encapsulating oxidized, hydrolytically labile alginate beads into a bulk slowly degradable alginate hydrogel.¹⁵¹ The sacrificial microbeads of diameter around 150 μm degraded within a week leaving macropores in the bulk hydrogel. The interconnectivity of the pores, which is a major parameter in cell migration and mass transport, could be achieved with a minimum porogen fraction near 50%. *In vitro*, encapsulated mesenchymal stem cells showed good proliferation. Interestingly, the kinetics of deployment and overall number of released cells could be controlled by the kinetics of degradation of the porogen, which is itself controlled by fabrication parameters. Han *et al.* further developed an injectable hydrogel with tunable dynamic macroporosity by combining three different types of porogen corresponding to different degradation mechanisms.¹⁵⁵ They showed the possibility of a sequential macropore formation that led to a controlled porosity in order to facilitate desirable cellular fate. Another geometry of porogen, microfiber, was also explored.¹⁵³ The use of microfibers resulted in interconnected microchannel-like pores, as shown in **Figure I - 11b**. This system is promising for cell delivery as the cells can be successfully encapsulated into alginate-based microfibers, which are dissolved by ethylenediaminetetraacetic acid (EDTA), within photo-cross-linkable alginate bulk hydrogels. The authors used human embryonic kidney cells as a model but this approach may be applied to other cell types, in particular smooth muscle cells and endothelial cells to engineer tubular tissues.

In situ formation of macropores can also be performed by gas foaming. Monette *et al.* used sodium hydrogen carbonate, NaHCO_3 , to induce porosity in chitosan-based thermosensitive hydrogels.¹⁵⁸ At the same time as the chitosan forms a hydrogel, the ion HCO_3^- reacts with H^+ protons present in the acidic chitosan solution, generating CO_2 gas bubbles thus creating porosity. The concentration of NaHCO_3 is a key parameter to tune the porosity of the forming hydrogel. Hydrogels with interconnected macropores of few hundreds of microns were achieved. T-cells were successfully encapsulated inside the hydrogel and remained viable for at least 24 days demonstrating the therapeutic potential of this system in tumors treatment. However, one might wonder about the stability of these gas bubbles during cell manipulation

and injection. Moreover, the release of CO₂ might induce some important changes in the pH of the mixture.

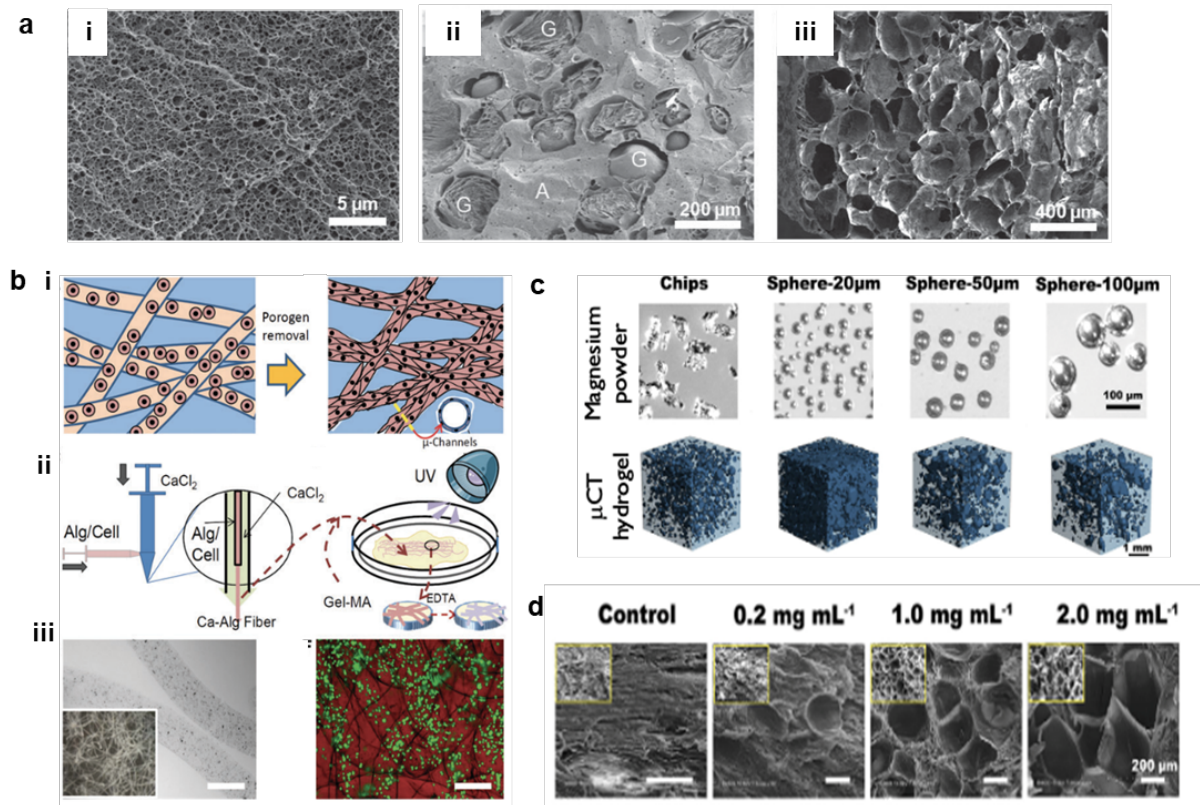


Figure I - 11. a) SEM micrographs showing the non-macroporous alginate hydrogel at 2% w/v (i), alginate hydrogel at 2% w/v with 50% volume fraction of gelatin beads before (ii) and after (iii) pore generation. Adapted from Hwang *et al.*¹⁵⁶ **b)** Formation of microchannels and releasing of cells when the microfibers are degraded (i); Fabrication of alginate microfibers with a co-axial needle set and encapsulation of the microfibers within photo-cross-linkable methacrylated gelatin hydrogel and dissolution of the microfibers by EDTA (ii); Micrograph showing the morphology of alginates microfibers, the inset shows a network-like bundle of microfibers and Live/Dead staining of human embryonic kidney cells encapsulated within alginate microfibers (green: live cells, red: dead cells)(iii). Scale bar = 200 μm. Adapted from Hammer *et al.*¹⁵³ **c)** Various sizes and morphologies of Mg particles (imaged by stereo light microscopy) lead to alginate/gelatin hydrogels with different porosities (scanned by micro-CT); **d)** SEM images of alginate/gelatin hydrogels prepared with different concentrations of spherical Mg particles. Adapted from Tang *et al.*¹⁵⁹

More recently, Tang *et al.* explored the capacity of magnesium particles as foaming and porogen agents at the same time to generate interconnected pores *in situ*.¹⁵⁹ These particles are soluble in water producing H₂ gas and Mg²⁺ ions which are also osteogenic. The macroporous network was successfully formed by the degradation of Mg particles in different stimuli-responsive hydrogels composed of alginate (ionic), collagen I (pH-sensing), thermal (gelatin) or enzyme-mediated cross-linking (silk

fibroin). **Figure I - 11c,d** shows the effect of different shapes and sizes of Mg particles and revealed that the atomized spherical Mg powder with an average size of 20 μm has the highest foaming ability due to its high specific surface area. *In vitro*, murine embryo fibroblasts were encapsulated in gelatin/alginate hydrogel containing pores formed by Mg particles. They exhibited significantly better viability and proliferation as compared to cells in a non-macroporous hydrogel. Rat bone marrow mesenchymal stem cells showed good viability and osteogenic differentiation when encapsulated in such hydrogels implanted in an *in vivo* femur defect model.

2.3.d. High-speed shearing treatment

High-speed shearing treatment has been recently used as a new technique for fabricating macroporous structure.¹⁶⁰ In this technique, the porosity is basically created by blending air bubbles into the precursor mixture before solidification. To our knowledge, Wang and coworkers¹⁶⁰ were the first and only one until now to use this method to prepare *in situ* forming macroporous hydrogels. They applied high-speed shearing treatment to gelatin (GE)/oxidized sodium alginate (OSA)/adipic acid dihydrazide (ADH) hydrogels. This mixture is able to form a gel after 5 min at 37°C through the formation of imine and acylhydrazone bonds (**Figure I - 12a**). These bonds are dynamic, which allows the system to be injected. In a systematic study, the authors investigated the effects of the shearing frequency and of the precursor composition on the resulting gel structure. They found that the porosity and the pore size increase with increasing shearing speed, and reach a plateau when operating at 30000 rpm during 30 s. At this frequency, by playing with the composition in precursors, pore sizes can be tuned from 150 to 380 μm , as shown in **Figure I - 12b,c**. *In vitro* encapsulation study was performed for two cell types: L929 fibroblasts and NIH3T3 cells. Cells were dispersed into the precursor solution, which was previously treated with high-speed shearing, and cell-encapsulated hydrogels were formed at 37°C. They found a cellular viability of about 80% up to 48 h. *In vivo* dorsal subcutaneous injection of one composition without cells into a rat model was also evaluated and no signs of inflammation or tissue damage were observed for up to 4 weeks. This approach, which does not require any porogen or foaming agent but offers a high tunability of the porosity, shows great potential for the fabrication of 3D cell-laden scaffolds. However, a potential limitation of this approach might be the stability of the air bubbles during manipulation including cell dispersion and loading of the system into a syringe during the injection. The reproducibility of this approach might hence be arguable.

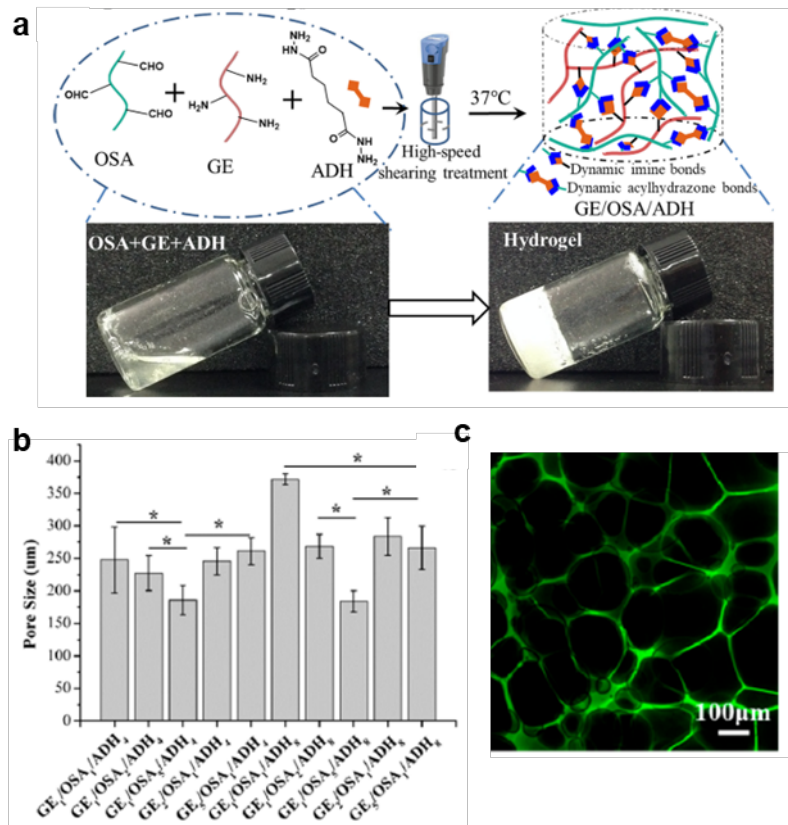


Figure I - 12. a) Construction of macroporous GE/OSA/ADH hydrogels with high-speed shearing treatment based on imine bonds and acylhydrazone bonds; **b)** Pore size of lyophilized hydrogels as measured by scanning electron microscopy; **c)** Confocal microscopy image of isolated hydrogel formed after *ex vivo* injection. Adapted from Wang et al.¹⁶⁰

In summary, many efforts have been made in order to engineer adequate macroporous injectable scaffold able to support cell development. In our opinion, each approach has advantages and drawbacks, as illustrated in the summary table (**Table I-1**). Overall, further studies and optimizations are required to fabricate injectable scaffolds with adequate properties for specific applications. Interestingly, one might think that some approaches can be combined together for a better control of the properties of the scaffold. For example, the high-speed shearing treatment could be applied to composites of microcarriers/hydrogel to better homogenize the microcarriers as well as introduce porosity that is useful for the diffusion of nutrients and wastes in the hydrogel.

For this PhD research, we were interested in physical hydrogels where the macroporosity originates from thermally induced phase separation. To the best of our knowledge, this effect was still little considered in the context of cell-laden injectable gels. In particular, the thermosensitive system composed of chitosan and phosphate salts presents interesting features for this application. Indeed, chitosan is one of the few representatives of biodegradable and biocompatible polymer approved for clinical use. Moreover, the porosity of this system might be tuned by playing with different parameters, such as the concentration and the characteristics of chitosan. In the next section, a literature review devoted to this peculiar system is presented.

Table I - 1. Summary of different strategies to engineer macroporosity in injectable cell-laden scaffolds

Class	Approaches	Materials	Major advantages	Major limitations
Preformed macroporous matrices	Macroporous microcarriers	Composite microcarrier/hydrogel or excipient	Resolving of the lack of control on the distribution of microcarriers Control of the porosity by well-known techniques	Inhomogeneity of the microcarriers dispersion
	Polymeric cryogels	Bulk cryogel	Interconnected macropores High flexibility	Incapacity to fill in complex wound shape
		3D printed cryogel	Free-from scaffold adaptable to wound shape	Complexity of the 3D printing technique
		Micro-cryogels	Precise control of the microstructure Injectability through smaller needle Possibility of automatic cell loading	Poor control on the distribution post-injection and risk of cell loss
	Emulsion templating	High Internal Phase Emulsion hydrogel	High porosity can be achieved	Use of oil and surfactant
In situ forming macroporous matrices	<i>In situ</i> crosslinking of hydrogels	Chemical hydrogel	Diversity of existing systems	Poor control on the interconnectivity and the size of pores
		Physical hydrogel by phase separation	Tunability of the porosity by varying polymer properties, crosslinker or precursor content	
	<i>In situ</i> assembly of microbuilding blocks	Microporous annealed particle (MAP) scaffold	High tunability of the porosity and other properties (biochemical, mechanical, ...) Ensured interconnectivity of pores	Complex and time-consuming synthesis of the microbuilding blocks
Microribbon-based scaffold		Decoupling of the "microenvironment stiffness" from the "scaffold bulk stiffness" Interconnected macroporous channels		

<i>In situ</i> void-formation using porogens or foaming agents	Degradable microgels as porogen	High tunability of the porosity fraction and pore size Possibility of sequential degradation of porogen leading to dynamic macroporosity	Poor control on the interconnectivity of pores
	Degradable microfibers as porogen	Ensured interconnectivity of pores	
	Magnesium particles as porogen and foaming agent	High tunability of the porosity fraction and pore size Compatibility with various responsive hydrogels	Poor control on the interconnectivity of pores
	Inorganic salt as foaming agent	Moderate tunability of porosity fraction and pore size	Dependence of the pH and osmolarity of the hydrogel on salt concentration
High-speed shearing treatment	Chemical crosslinked hydrogel	Simple technique Tunability of the porosity	Poor control of the stability of the air bubbles

I.3. Thermosensitive chitosan/salt mixtures

This section, organized into two parts, presents the characteristics and properties of thermosensitive mixtures of chitosan and salts. The first part is devoted to chitosan (CS) and chitin. CS production process, chemical and biological properties, as well as its behavior in solution will be detailed. The second part exposes the state-of-the-art of thermosensitive systems composed of chitosan and salts. We focus on the current understanding of the sol/gel transition mechanisms, and report on studies investigating biocompatibility and application of this thermosensitive system as an *in situ* injectable hydrogel for cell encapsulation and delivery.

I.3.1. Chitosan and chitin

Chitosan is a biosourced polysaccharide obtained by partial deacetylation of chitin, a primary component of cell walls in fungi and crustacean shells.^{161,162} During the process of deacetylation of chitin, the acetamido group $-\text{NHCOCH}_3$ is replaced by the amino group $-\text{NH}_2$ (**Figure I - 13**). CS can be considered as a copolymer with a random distribution of D-glucosamine units (bearing amine group) and N-acetyl-glucosamine units (bearing acetamido group). The deacetylation degree, *DD*, defined as the proportion of the D-glucosamine monomer, varies from 50% to 100% (when *DD* < 50%, the polysaccharide is referred to as chitin). The *DD* can be controlled by the duration, the temperature and the concentration of NaOH during the alkaline treatment of chitin.¹⁶² The *DD*, together with the molar mass, M_w , and the distribution of each monomer type, are the parameters that govern most of the physical and biological characteristics of CS including crystallinity, solubility, mechanical properties, degradation kinetics, and immunogenicity.

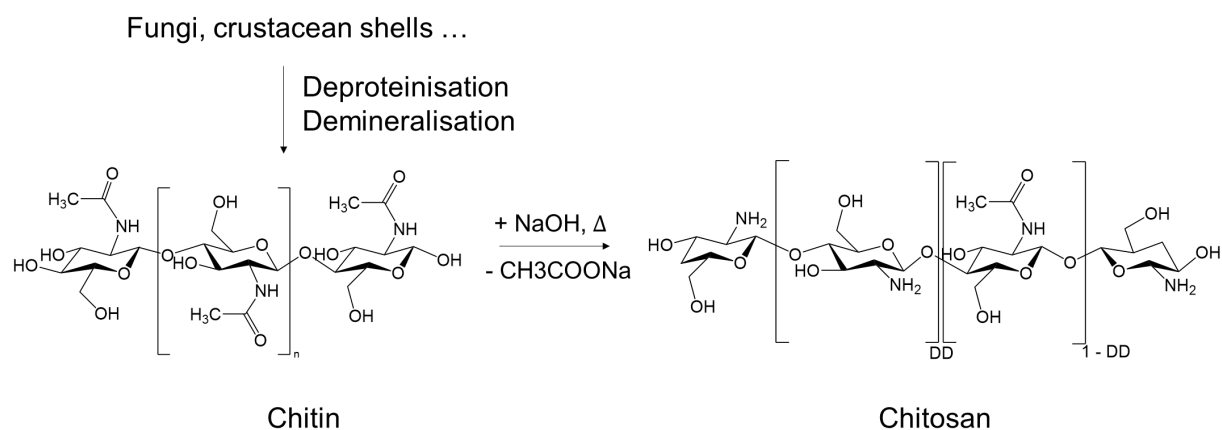


Figure I - 13. General steps for chitosan production from natural vegetal or animal sources

3.1.a. Chemical structure

CS possesses three functional groups: hydroxide $-\text{OH}$, amine $-\text{NH}_2$ and acetamide $-\text{NHCOCH}_3$. Various techniques have been proposed to characterize the chemical structure, in particular the average *DD*, and can be divided into three groups: conventional (potentiometric or conductometric titration,

ninhydrin assay), spectroscopies (NMR including ^1H , ^{13}C , ^{15}N ; IR and UV) and destructive methods (elemental analysis, HPLC, DSC).¹⁶³ The two most widely used methods are NMR^{164–166} for its precision and IR^{167–170} for its simplicity. Typical spectra for each technique are shown in **Figure I - 14**.

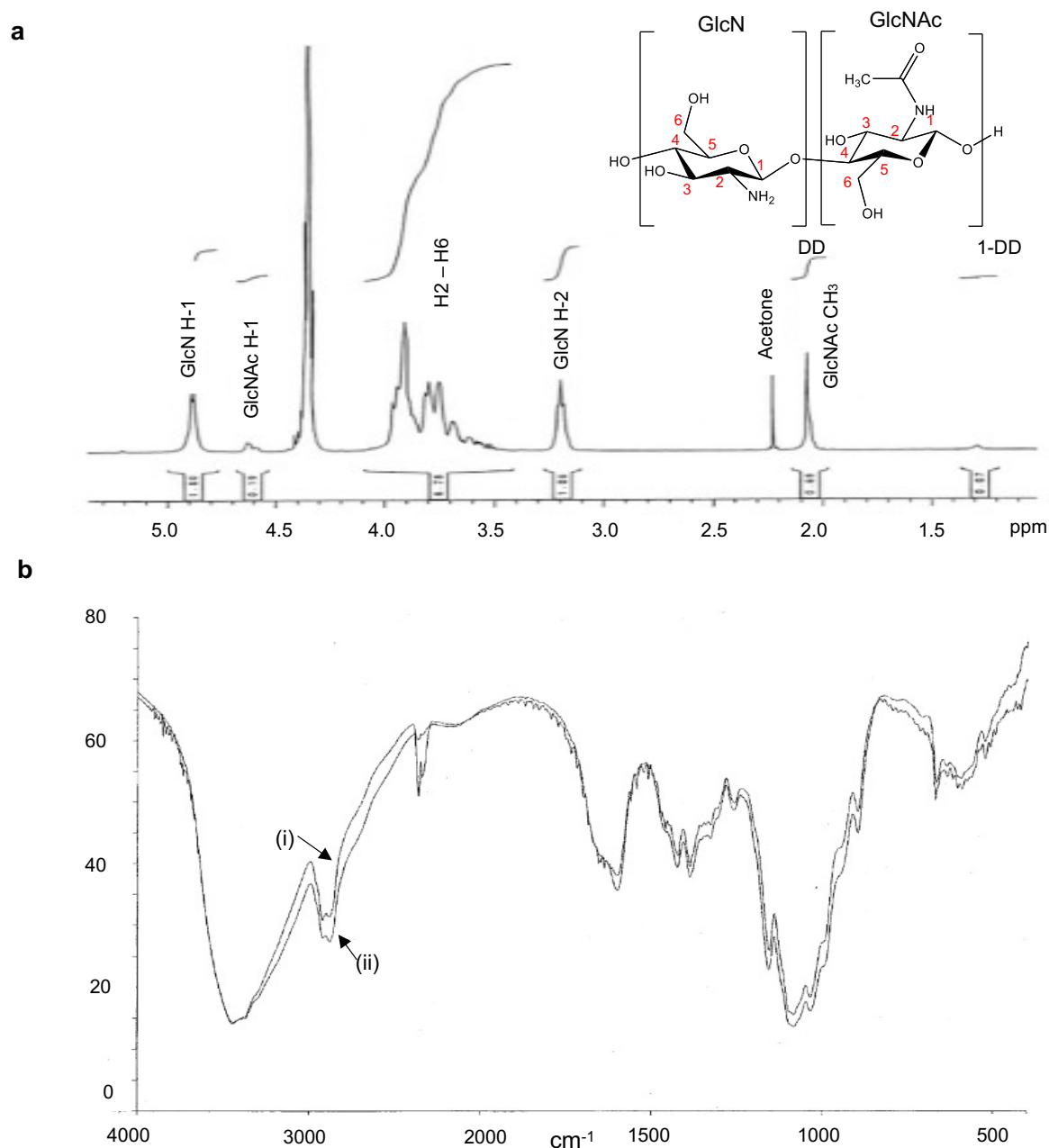


Figure I - 14. a) ^1H NMR spectrum of CS sample in $\text{DCl}/\text{D}_2\text{O}$ measured at 600 MHz and 65°C , adapted from Yang & Montgomery.¹⁶⁵ **b)** IR spectrum for fully deacetylated chitosan: dried state (i) or hydrated sample (ii), adapted from Brugnerotto et al.¹⁶⁸

Like its parent chitin, chitosan is a semicrystalline polymer. The crystallography of both chitosan and chitin has been widely studied.^{171–176} Chitin has three polymorphs: α -chitin has antiparallel chains, β -chitin has parallel chains and γ -chitin is a combination of both forms (**Figure I - 15**).^{177,178} α -chitin,

commonly found in shrimp and crab shells, is more abundant than β -chitin, found in squid pens. Both conformations possess an organization in sheets where the chitin chains exhibit intra-sheet hydrogen bonds $\text{CO}\cdots\text{NH}$ and $\text{CO}\cdots\text{OH}$. The *N*-acetyl glycosyl moiety is the independent crystallographic unit in both allomorphs.¹⁷⁸ Chitin chains are maintained at a distance of about 0.48 nm.^{179,180} The crystallographic parameters also reveal that there are two antiparallel molecules per unit cell in α -chitin while there is only one in β -chitin. Moreover, inter-chain hydrogen bonds were observed only for the α conformation.

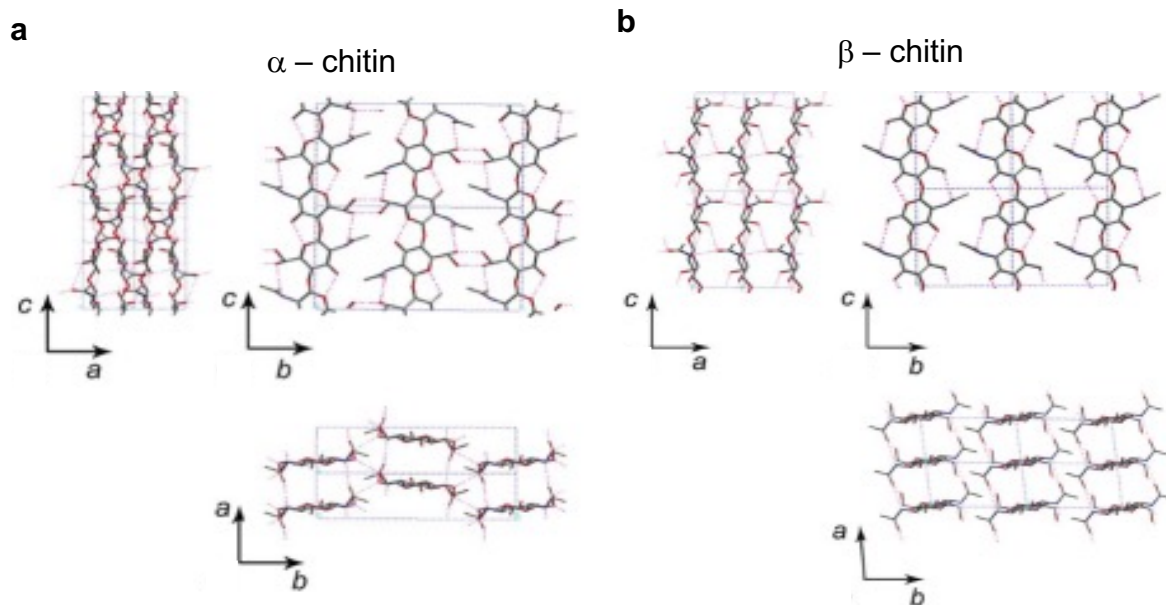


Figure I - 15. Representation of the crystal structure of α -chitin (a) and β -chitin (b), reproduced from Rinaudo¹⁷⁸ who draw the structures using coordinates of Minke *et al.*¹⁸⁰ and Gardner *et al.*¹⁷⁹

In the case of CS, crystals result from the crystallization of residual chitin monomers but also of CS monomers. Taking into account the difference between chitin polymorphisms, CS from diverse origins certainly have different properties. Many polymorphisms have been reported for CS, which correspond to either CS alone or complexation of CS with small molecules (water, acid or salt).¹⁷⁶ In particular, Okuyama *et al.* described that a unit cell of hydrated CS contains four chains and eight water molecules.¹⁸¹ These chains are assembled into a sheet structure, which results from direct H-bonds $\text{H}_2\text{N}\cdots\text{OH}$ between adjacent chains. H-bonds between sheets are ensured by H_2O bridges and contribute to stabilize the structure, as shown in **Figure I - 16a**. Cartier *et al.* reported the preparation and characterization of single CS crystals.¹⁷¹ The crystals take the form of micrometer-sized platelets with a square-like shape having a diagonal ranging from 0.2 to 0.5 μm and a thickness around 12 nm, as shown in **Figure I - 16b**. Typical X-ray powder diagram of CS single crystals is shown in **Figure I - 16c**. The CS unit cell contains two antiparallel chains and can be indexed in the orthorhombic system with $a = 0.807$ nm, $b = 0.844$ nm and $c = 1.034$ nm.

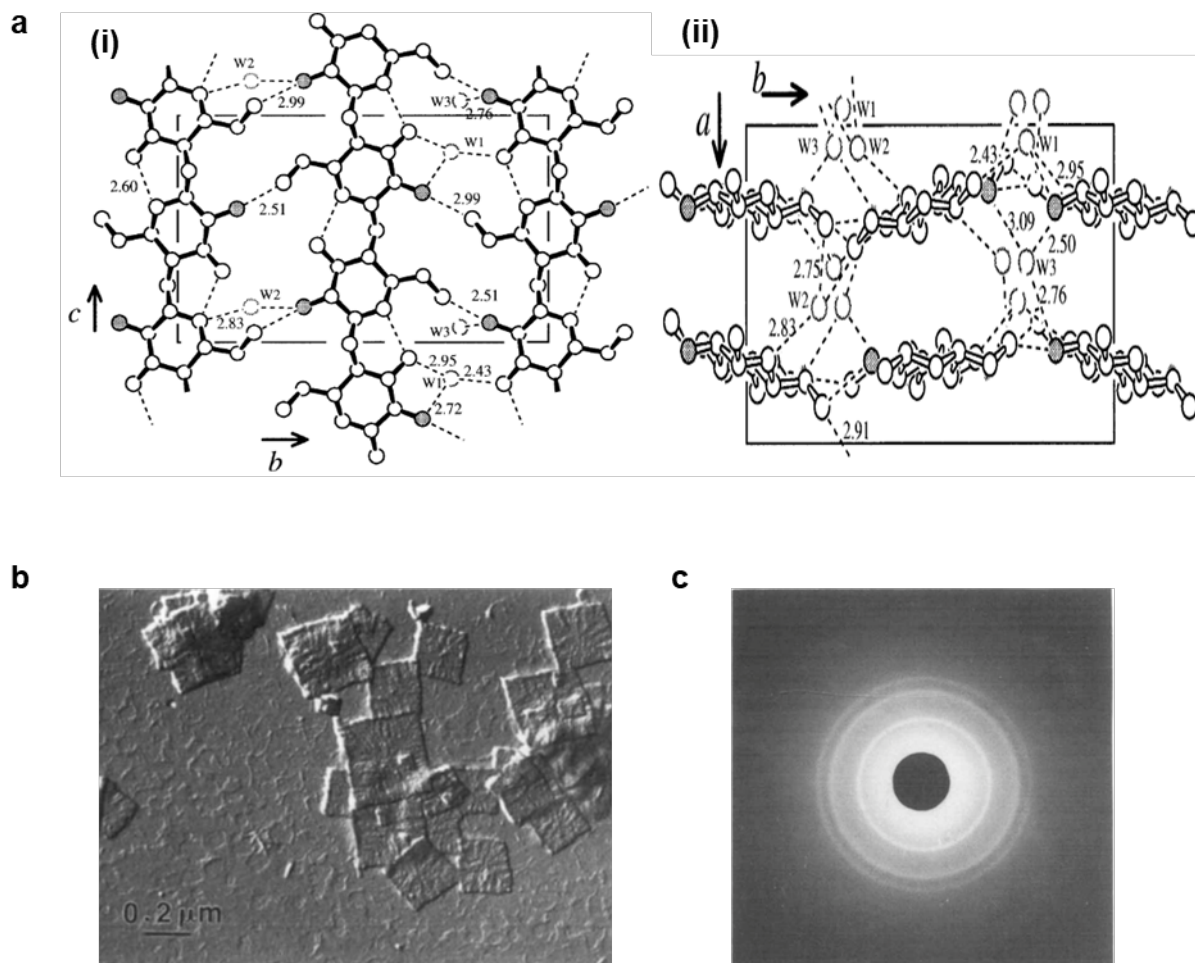


Figure I - 16. a) Scheme illustrating structure of hydrated CS projected along the *a*-axis (i) and along the *c*-axis (ii). Reproduced from Okuyama *et al.*¹⁸¹ **b-c)** Characterization of single crystals of CS: electron micrograph (b) and x-ray powder diagram (c). Reproduced from Cartier *et al.*¹⁷¹

The crystallinity of chitin and chitosan strongly depends on its origin,¹⁸² the production process,¹⁷² the degree of deacetylation *DD* and the molar mass M_w .¹⁷⁵ Jaworska *et al.* reported that the crystal size depends on the origin of CS in this following order: shrimp > fungal ~ squid.¹⁸² It is important to notice that the procedure of CS production, which can be homogeneous or heterogeneous, strongly influences the crystallinity of the resulting CS. Ogawa *et al.* characterized chitin/chitosan samples prepared by two different procedures: partial deacetylation of chitin by heterogeneous process in solid state, and partial reacetylation from a fully deacetylated chitin (pure chitosan) by homogeneous process in swollen state.¹⁷² They demonstrated that for the same *DD*, more crystals were observed for partially deacetylated chitin as compared to partially reacetylated chitosan. This can be explained by the fact that in the homogeneous procedure to obtain reacetylated chitosan, *N*-acetyl groups are expected to be randomly distributed, thus resulting in a lower level of crystallinity. As regards the *DD*, it has been reported that the crystallinity is maximum for chitin (*DD* = 0%) and fully deacetylated chitosan (*DD* = 100%) and decreases for intermediate *DD*.^{183,184} Indeed, partially deacetylated chitins with a low *DD* would

crystallize in a chitin polymorph and those with high *DD* would crystallize in a chitosan polymorph. For M_w , it was demonstrated that the crystallinity decreases with decreasing CS chain length.¹⁷⁵

3.1.b. Solubility

CS is soluble in dilute acidic medium while chitin is insoluble in most organic acids and regular solvents.¹⁷⁷ The CS solubility behavior is explained by the presence of amino groups which have a $pK_{a,app}$ in the vicinity of 6.2 at 25°C. At $pH < pK_{a,app}$, CS behaves as a cationic polyelectrolyte bearing protonated amino groups. Near neutral pHs where CS is mostly deprotonated, the strong tendency of the CS chains to self-associate through H-bonding and hydrophobic interactions dominates, giving rise to the formation of a hydrated gel-like precipitate. Rinaudo and coworkers examined the role of the protonation of CS on its solubility in the presence of a strong acid, HCl¹⁸⁵ or a weak acid, AcOH¹⁸⁶. They demonstrated that complete solubilization is obtained when the ionization degree of CS is at least 0.5 and that the amount of acid needed is at least equal to the concentration of NH_2 groups. CS solubility also depends on the ionic strength of the solution. When the ionic strength is high, for example when HCl concentration is larger than 1 mol.L⁻¹, salting out occurs leading to a phase separation and precipitation of CS chains. Hence, the use of AcOH or another weak acid is more favorable to CS solubility as weak acids have a low dissociation degree. A solvent mixture composed of AcOH 0.3 M/AcONa 0.2 M was reported as a good solvent for CS and has been widely used for CS characterization.¹⁸⁷

The solubility of CS is very difficult to control, as a complex function of many variables: *DD*, M_w , ionic strength, the nature of the acid, the distribution of *N*-acetyl units. Several studies reported a discrepancy in the behavior of CS at the same *DD*, which can be explained by the difference in the distribution of *N*-acetyl units. On the one hand, Kubota & Eguchi reported the preparation of reacetylated CS from fully deacetylated chitin in swollen state. They found that CS having *DD* = 50% and M_w below 20 kg.mol⁻¹ were soluble in water, as shown by transmittance measurements in **Figure I - 17a**.¹⁸⁸ Interestingly, there is a maximum of the water-solubility with *DD* in the vicinity of 50%, regardless of the molar mass (**Figure I - 17b**). This observation was supported by other studies.^{189,190} For example, Varum *et al.* also reported increased solubility of reacetylated CS having the *DD* varying from 0.99 to 0.40.¹⁹⁰ Similarly, Philippova *et al.* showed that bigger aggregates were observed for CS having higher *DD* (**Figure I - 17c**).¹⁸⁹ On the other hand, Ottoy *et al.* reported that the aggregation of CS in AcONa 0.02 M/NaCl 0.1 M/NaN₃ 0.02 % w/v solvent at pH 4.5 is more pronounced when *DD* decreases.¹⁹¹ Using size exclusion chromatography combined with low angle laser light scattering (LALLS), these authors detected higher aggregate peak for CS having lower *DD* when comparing three different CS at the same concentration and at about the same molar mass (**Figure I - 18**). This discrepancy in the behavior of CS at the same *DD* can be explained by the difference in deacetylation/reacetylation process which can affect the

distribution of *N*-acetyl units. Homogeneous process results in a more random distribution of *N*-acetyl groups along the CS backbone, thus lowering the crystallinity and increasing the solubility.

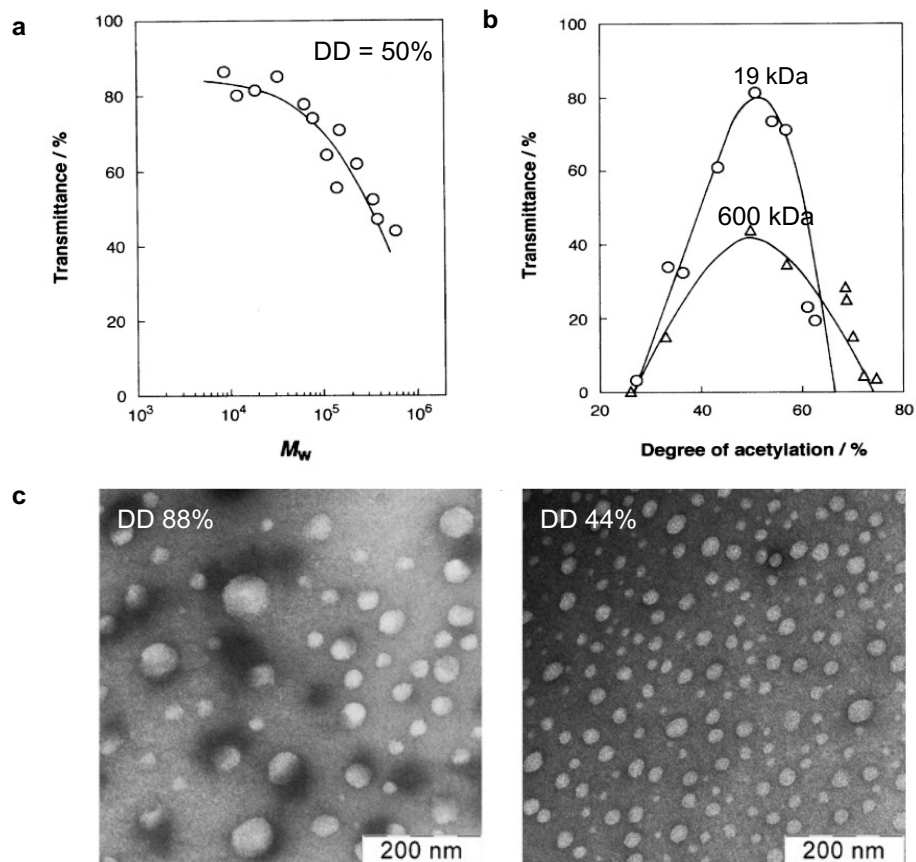


Figure I - 17. Dependence of the water-solubility on: **a)** the M_w (fixed DD = 50%) and **b)** the DD for two different M_w (19 and 600 $\text{kg}\cdot\text{mol}^{-1}$); adapted from Kubota & Eguchi.¹⁸⁸ **c)** TEM micrographs of aggregates of two chitosan grades having DD = 88% and DD = 44%; adapted from Philippova et al.¹⁸⁹

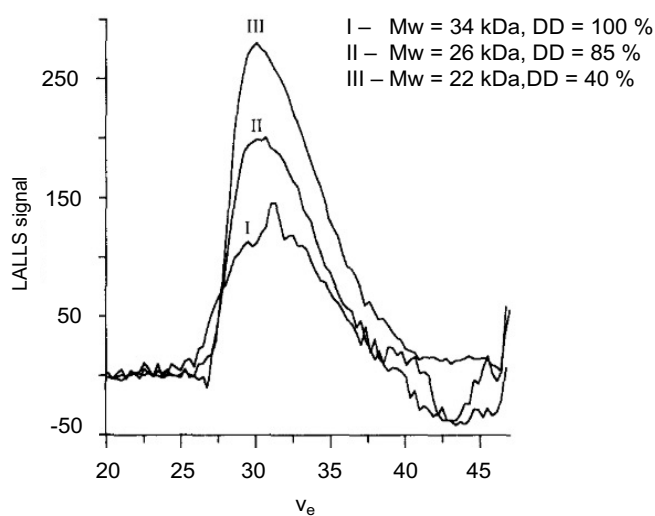


Figure I - 18. LALLS signals for three different CS having molar mass of 34, 26, 22 $\text{kg}\cdot\text{mol}^{-1}$ and DD 100, 85, 40 %, respectively, at concentration of 0.125 $\text{mg}\cdot\text{mL}^{-1}$. Adapted from Ottoy et al.¹⁹¹

3.1.c. Biological properties

CS is considered as a non-toxic polymer and is approved by the FDA for use in wound dressing.¹⁹² As the only pseudo-natural cationic polymer, CS offers remarkable biological properties. Positively charged amine groups can bind to negatively charged surfaces such as mucosal membranes (bioadhesive property)¹⁹³ and with bacterial DNA leading to the inhibition of RNA synthesis (antimicrobial property).¹⁹⁴ Moreover, CS, especially at high *DD*, exhibits a hemostatic effect by activating platelets.¹⁹⁵

CS is biodegradable by enzymatic processes (chitinases, chitosanases and lysozymes) or by acid catalyzed hydrolysis (for example in the stomach or in an inflammatory environment).¹⁹⁶ In the human body, CS is most likely degraded by the activity of lysozyme and bacterial enzymes in the colon.^{197,198} An *in vitro* study of the degradation of CS in human serum at pH 5 showed that the degradation rate increases strongly when *DD* decreases from 0.6 to 0.4 (**Figure I - 19a**).¹⁹⁹ Same trend was lately observed by Yang *et al.* on CS fibers in both *in vitro* and *in vivo* studies.²⁰⁰ Hirano *et al.* studied *in vitro* enzymatic hydrolysis for chitosan with *DD* ranging from 0.8 to 0.2 (**Figure I - 19b**).²⁰¹ They found that higher degradation levels were reached for intermediate *DD* (0.6–0.8) as compared to *DD* close to 1 or 0. All these observations are in line with the evolution of CS crystallinity as a function of *DD* as the more crystalline the system is, the less accessible the degradable functions are. The crystallinity is at the lowest level for intermediate *DD* values. As regards the molar mass, it is well established that low M_w grades of CS are more degradable than high M_w grades.^{54,202}

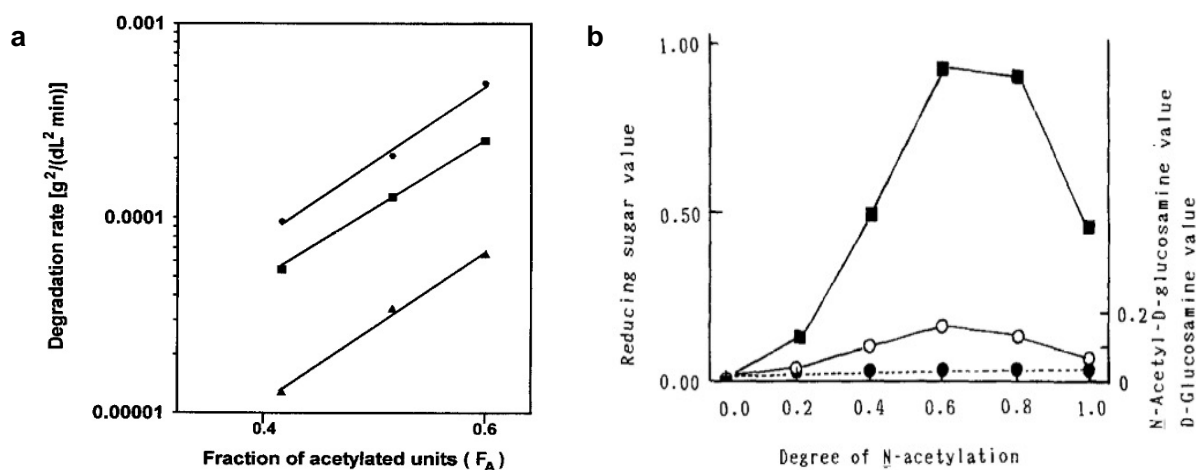


Figure I - 19. Enzymatic degradation as function of the fraction of *N*-acetyl groups (= 1 - *DD*) using lysozyme (**a**) or chitinase (**b**). In figure **b**: squares = reducing sugar value ($\mu\text{mol}\cdot\text{mL}^{-1}$), filled circles = *N*-acetyl-*D*-glucosamine ($\mu\text{mol}\cdot\text{mL}^{-1}$) and empty circles = *D*-glucosamine ($\mu\text{mol}\cdot\text{mL}^{-1}$). Reproduced from Vårum *et al.*¹⁹⁹ and Hirano *et al.*²⁰¹

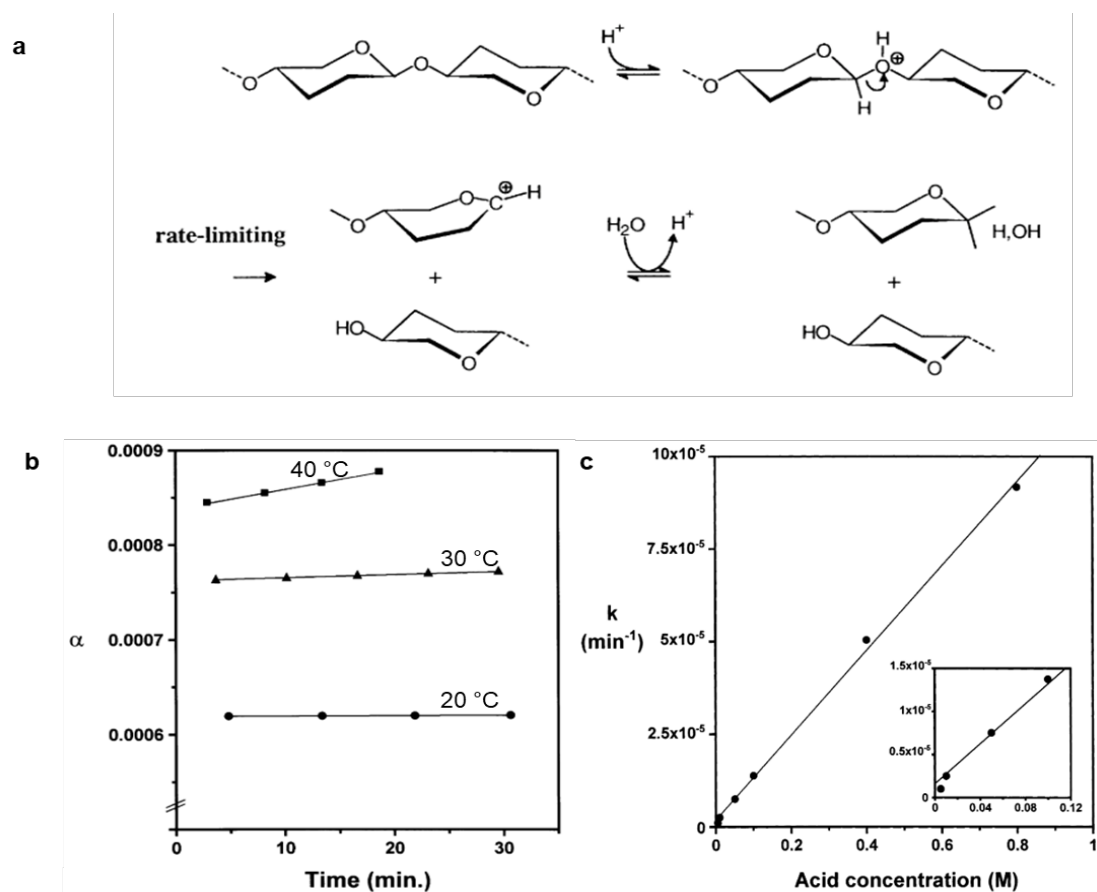


Figure I - 20. a) Proposed mechanism for hydrolysis of the glycosidic linkages; b) The degree of scission (α) overtime at different temperatures, c) Degradation rate constants (k) as a function of HCl concentration, the inset is a zoom on the range of HCl concentration from 0 to 0.12 M. Reproduced from Vårum *et al.*²⁰⁵

Characterization of the degradation of CS in the presence of a strong acid HCl was reported by Vårum *et al.*²⁰³ In this case, depolymerization of CS occurred through acid-catalysed cleavage of the glycosidic linkages, as shown in **Figure I - 20a**. These authors found that the reaction rate strongly depends on the temperature, as shown in **Figure I - 20b**. Moreover, the degradation rate was found to increase linearly with the acid concentration (**Figure I - 20c**). In the presence of weak acids, such as acetic acid or formic acid (the pH was not given), it was reported that the molar mass distribution of CS barely changed up to 7 days at 20 °C (**Figure I - 21**).²⁰⁴ Hence, to limit the degradation of the CS chains, one should use weak acids for the solubilization.

Accordingly, in this project, CS is solubilized at room temperature ($21 \pm 1^\circ\text{C}$) using acetic acid.

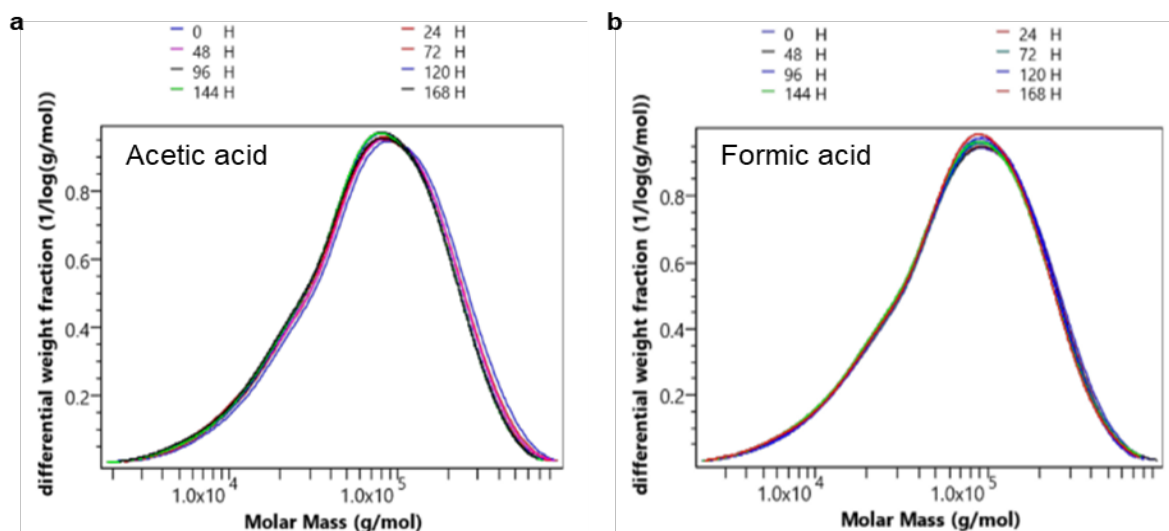


Figure I - 21. Molar mass distribution for CS in acetic acid (a) or formic acid (b); The concentration in CS is 5 wt% and in acid is 3 wt%. Reproduced from Sikorski et al.²⁰⁴

CS is generally considered as being non-toxic.¹⁹² The toxicity of CS was found to depend on the *DD* and the M_w , which strongly govern the crystallinity and thus the degradation rate. CS with low *DD* is more susceptible to degrade, causing an important accumulation of sugars and oligosaccharides in the implantation site, thus inducing a stronger inflammatory reaction as compared to CS with high *DD*.²⁰⁶ Moreover, it has been reported that highly deacetylated CS are more favorable for cell adhesion.²⁰⁷

For these reasons, we have chosen to work with highly deacetylated CS grades ($DD > 90\%$) in this project.

For all of these interesting properties, CS is a popular biomaterial for pharmaceutical and biomedical applications including as a vehicle for cells or therapeutic molecules.^{196,208–211} In particular, thermosensitive chitosan-based hydrogels have been extensively explored in that context and will be discussed in detail in the following section.

1.3.2. Thermosensitive mixture of chitosan and salts

This section presents a state-of-the-art about thermosensitive mixtures composed of chitosan and salt(s). Firstly, the pioneering work of Chenite *et al.* in 2000 on the first system using beta-glycerophosphate is presented. Secondly, we expose different studies that we considered important to the understanding of the mechanism of the sol/gel transition in these systems. Finally, studies investigating the biocompatibility and the potential of these systems for cell encapsulation and delivery is reported.

3.2.a. Mixture of chitosan and beta-glycerophosphate (CS/ β GP)

The poor solubility of CS in physiological pHs has long limited the use of CS in biomedical applications until the pioneering work of Chenite *et al.*^{129,212} After the addition of an organic phosphate salt, the beta-glycerophosphate β GP, to an acidic solution of CS, the system remains soluble until neutral pH (6.8 to 7.2) and more interestingly, the mixture rapidly turns into a gel around 37°C. Practically, the use of glycerophosphate is relevant. Indeed, β GP is an organic compound naturally found in the body which is involved in the generation of adenosine triphosphate.²¹³ Intravenous administration of glycerophosphate has been approved by the FDA for the treatment of unbalance of phosphate metabolism.²¹⁴ Glycerophosphate possesses two conformations, α -glycerophosphate and β -glycerophosphate, which structures are shown in **Figure I - 22**. In the study reported by Chenite *et al.*, β GP was used but lately, α GP and mixture of both conformations were also successfully used to prepare thermosensitive CS mixtures.²¹⁵

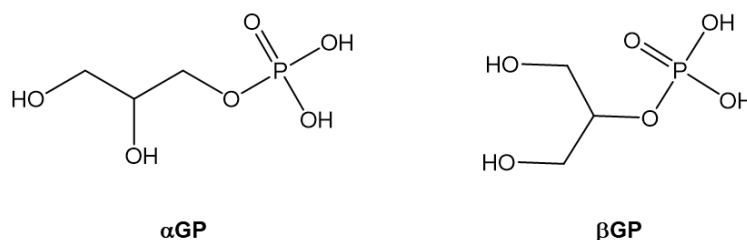


Figure I - 22. Chemical structure of the two conformations of glycerophosphate.

The pH of CS solutions can be raised to neutral values using β GP without inducing immediate precipitation at room temperature, though above the pK_{app} of CS. **Figure I - 23a** shows the evolution of the pH of a solution of CS at 2 wt% as a function of the β GP concentration. While incubating the mixture at 37°C, CS/ β GP solutions gelate at pH 7.2, which is visualized by an increase in turbidity, as shown in **Figure I - 23b**. Chenite *et al.* made an analogy with the well-known stabilizing effect of polyols on proteins over thermal denaturation and suggested that the thermosensitivity of CS/ β GP mixtures would be a result of the effect of the polyol moiety on the hydration structure of CS: (i) at low temperature, CS chains are stabilized by interactions with water molecules; (ii) when the temperature increases, the water molecules are removed by the glycerol moiety, allowing association of CS chains through hydrophobic

interactions. In this proposed mechanism, the role of the polyol part and the removal of water molecules upon heating seem however unclear.

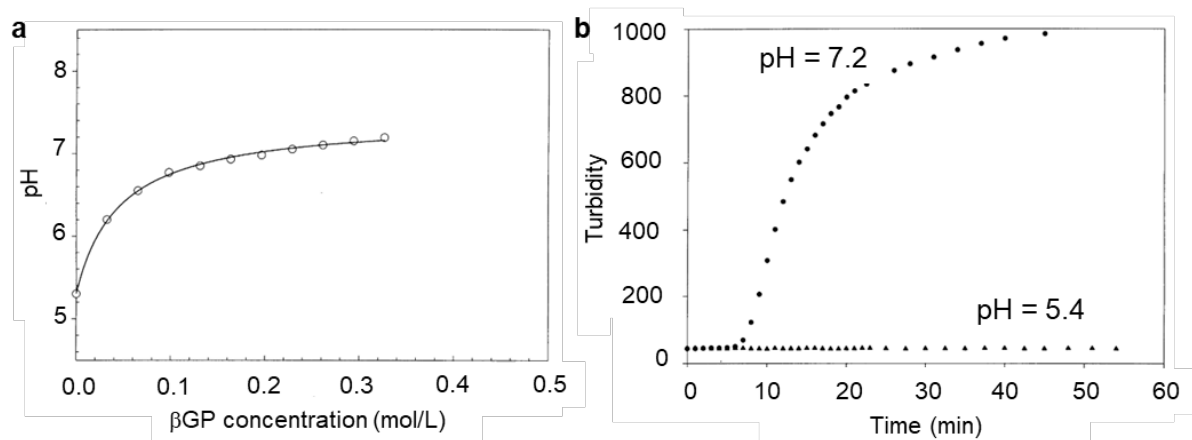


Figure I - 23. **a)** pH variation of CS solution (2 wt%) as a function of β GP concentration at room temperature; **b)** Change in turbidity with time of CS solutions (2 wt%) incubated at 37°C in the presence of β GP at pH 7.2 and in the absence of β GP at pH 5.4.

Gelation kinetics of thermosensitive CS/ β GP mixtures

The gelation kinetics of these mixtures was studied by temperature ramp experiments at different pHs. The elastic modulus G' of a CS/ β GP solution having pH 7.15 was found to increase sharply when the temperature reached 40°C (**Figure I - 24a**). The gelation temperature, as measured by temperature ramp rheological experiments, was found to strongly decrease with increasing pH (**Figure I - 24b**). During a heating/cooling cycle, these mixtures showed a thermoreversible behavior with a large hysteresis, as shown in **Figure I - 24c**. The hysteresis is larger when pH increases. In the accessible temperature ranges from 4 to 70°C, a mixture having pH 6.85 shows a complete thermoreversibility while a mixture at pH 7.15 only shows partial thermoreversibility.

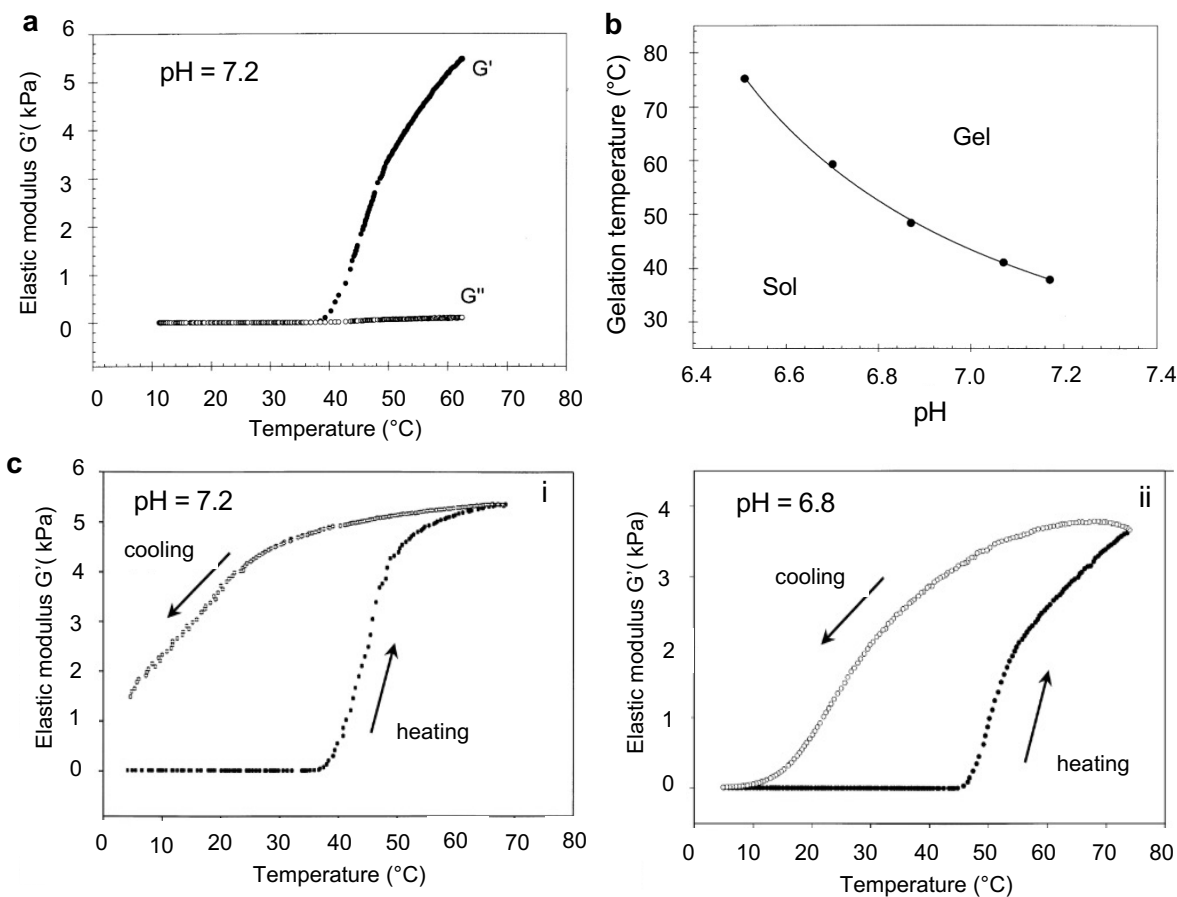


Figure I - 24. Rheological study of the gelation kinetics in dynamic conditions for CS/ β GP mixtures at CS 2 wt% and $[\beta\text{GP}] = 0.262 \text{ mol}\cdot\text{L}^{-1}$ in which the pH is varied by altering $[\text{HCl}]$: **a**) Evolution of the elastic modulus upon heating from 4 to 70°C at $1^{\circ}\text{C}\cdot\text{min}^{-1}$; **b**) Evolution of the gelation temperature as a function of the pH; **c**) Evolution of the elastic modulus during a heating/cooling cycle for mixtures having pH = 7.2 or 6.8. Reproduced from Chenite *et al.*^{129,212}

Rheological measurements were also performed in isothermal conditions. Chenite *et al.* reported that the gelling time decreases exponentially with temperature, varying from 13 min at 32°C to 2 min at 42°C for a formulation having pH 7.2 (**Figure I - 25**). However, one might think that their exponential fit is not relevant as the gelling time covers only two decades.

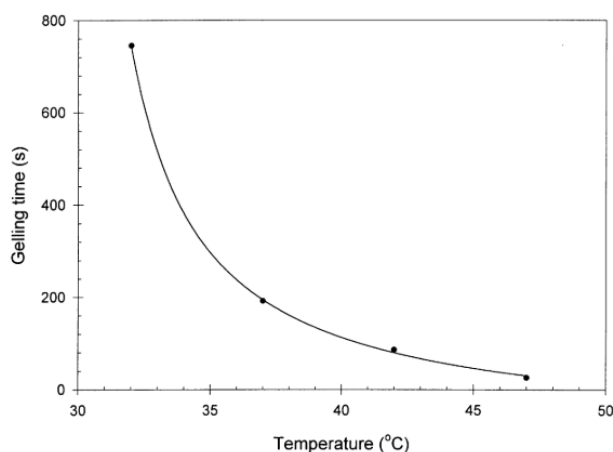


Figure I - 25. Evolution of the gelling time as a function of temperature for a CS/βGP mixture prepared with 2 wt% of CS, $[\beta\text{GP}] = 0.262$ and $\text{pH} = 7.2$. Reproduced from Chenite *et al.*¹²⁹

In our study, the gelation kinetics of these thermosensitive systems will be investigated in depth on a wide range of gelling time that covers five decades.

Influence of the DD and M_w

Chenite *et al.* also studied the effects of DD and M_w on the properties of CS/βGP mixtures. They reported that the gelation temperatures increased from 37 to 66°C when the DD decreases from 91 to 70%. For a given DD equal to 81%, no significant effect on the gelation temperature was observed for M_w varying from 120 to 840 kg.mol⁻¹. However, from my point of view, a very important information, the pH, was missing, making the interpretation of these results complicated.

Biological evaluation

In this seminal study, Chenite *et al.* performed *in vitro* encapsulation of several cell lines (cos-7, L929, Rat-1) as well as freshly isolated primary cells (bovine and human chondrocytes) and found 80% of cell viability over extended period (data not shown). In an *in vivo* experiment, they also demonstrated the injectability of a formulation prepared with CS 2wt% having $\text{pH} = 7.2$. Volumes of 0.2 mL were subcutaneously injected into the dorsal of adult rats through 22 G needle. **Figure I - 26a** shows the bean-like shapes of the formed hydrogels that remained morphologically intact for up to 7 days. This mixture was also shown to be efficient for delivering bone-inducing growth factor. Differentiating cartilage and bone tissue were observed after 4 weeks, as characterized by histological staining (**Figure I - 26b**).

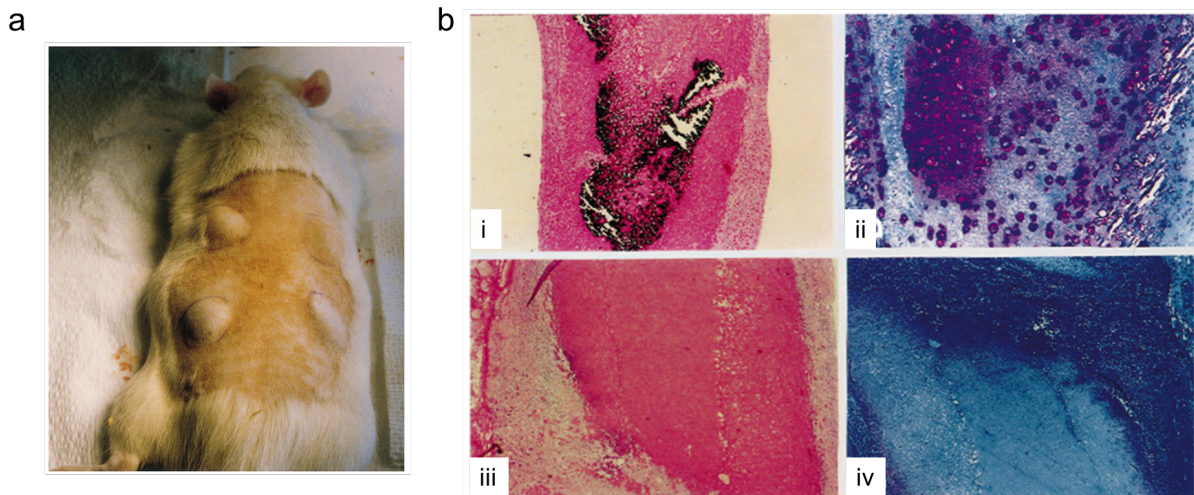


Figure I - 26. a) Photograph showing the subcutaneous gels formed after injection. **b)** An osteoinductive mixture of proteins (BP) delivered from CS/ β GP induces bone and cartilage formation in the rodent ectopic model: (i) Von Kossa stain of CS/ β GP + BP showing immature, mineralized bone and cartilage; (ii) Toluidine blue stain of CS/ β GP + BP showing an abundance of chondrocytes encompassed by a territorial cartilaginous matrix; (iii) Von Kossa stain of CS/ β GP gel showing fibrous and unmineralized tissue; (iv) Toluidine blue stain of CS/ β GP gel showing fibrous and no cartilaginous tissue. Reproduced from Chenite et al.¹²⁹

As a summary, this thermosensitive system composed of CS and β GP exhibits interesting features for use as an injectable vehicle for cell therapy or drug administration. Many studies have been carried out to investigate the mechanism of this peculiar sol/gel transition and to explore the biocompatibility and the relevance of CS/salt systems as injectable carriers for drugs and cells. Important elements that contribute to the understanding of the sol/gel transition in CS/ β GP solutions are detailed in the following section.

3.2.b. Mechanisms of the thermoresponsivity in CS/ β GP mixtures

To better understand the thermosensitive gelation of CS/ β GP solutions, it is important to note that the gelation of CS solutions in presence of salts can appear through different mechanisms. In particular, CS solutions can form gels in the presence of polyphosphates through ionotropic crosslinking. This phenomenon has been used with tripolyphosphate (TPP) for the fabrication of micro-vehicles for drug encapsulation and delivery.^{216–221} Such ionogelation is utterly different from the one observed in CS/ β GP mixtures and does not exhibit the same thermosensitivity. This system is briefly presented in the following section, before going to our main topic about thermoresponsive CS/ β GP mixtures.

Ionotropic crosslinking of chitosan and polyphosphates

TPP is a non-toxic polyanion having five dissociation constants which are 1.0, 2.0, 2.8, 6.5, 9.2 (25°C). This polyanion can form either intermolecular or intramolecular bonds with the positively charged amino groups on CS, as shown in **Figure I - 27**, leading to the formation of a gel within seconds at acidic pHs, at room temperature or even at low temperature (2–4°C).^{216,222}

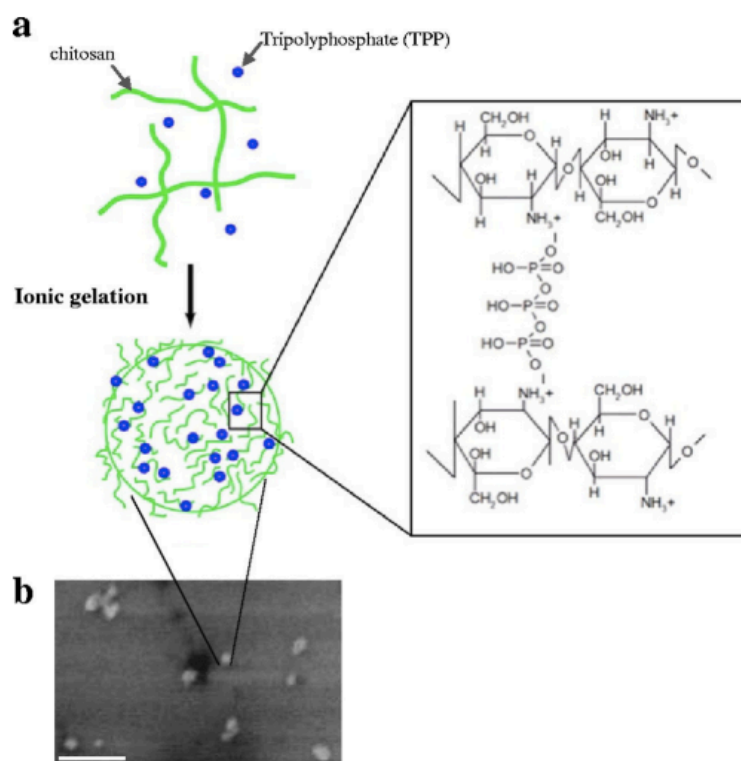


Figure I - 27. **a)** Scheme illustrating the formation of CS-TPP complex by ionotropic gelation. **b)** SEM image, scale bar = 200 nm. Reproduced from de Paz et al.²²⁰

Yuan & Huang reported the existence of a critical molar ratio TPP:glucosamine for the formation of CS/TPP complexes.²²³ They demonstrated for three different grades of CS having *DD* ranging from 82 to 96%, that the same molar ratio TPP:glucosamine was required for a given pH. The pH is a crucial

parameter which affects the ionization state of both CS and TPP and thus the crosslinking density. The critical ratio TPP:glucosamine decreased with increasing pH. Indeed, increasing the pH induces deprotonation of CS and reduction of available binding sites for TPP, thus lowering the TPP:glucosamine ratio necessary for particle formation. This observation was in agreement with a previous study reported by Fan *et al.*²²²

CS/TPP particles are usually prepared at acidic pHs around 4.0. The behavior of CS/TPP particles as a function of the pH was investigated by López-León *et al.*²²⁴ They demonstrated that the diameter of the particles decreases when pH increases from 4 to 7 (**Figure I - 28**). When pH increases, CS chains tend to lose their charges, thus becoming less extended, giving rise to a diminution of the particle size. Later, Mazancová *et al.* studied the stability of CS/TPP microparticles at physiological pH.²²⁵ They found that when the pH of the suspension of CS/TPP microparticles was adjusted to 7.4 using NaOH, 90% of the TPP amount was released into the solution, indicating the partial dissolution of CS/TPP particles. The complexation between CS and TPP is unstable at neutral pHs. This is a fundamental difference with the CS/ β GP system, which can be exploited in physiological conditions.

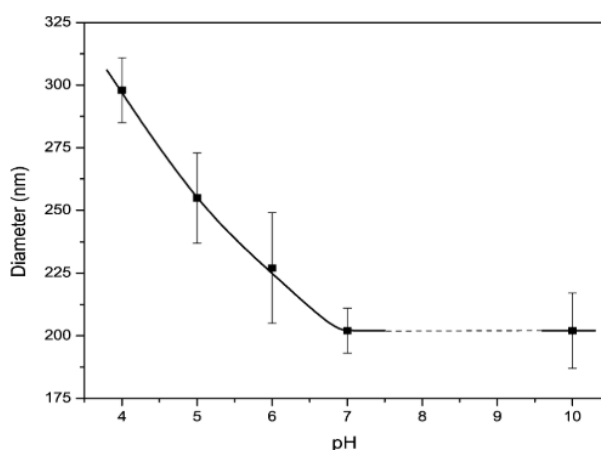


Figure I - 28. Evolution of the diameter of CS/TPP microparticles as a function of the pH. Reproduced from López-León *et al.*²²⁴

To the best of our knowledge, the effect of temperature on the stability of CS/TPP particles was little investigated. For instance, Morris *et al.* studied the size distribution of CS/TPP particles at pH 4.3, at different storage temperatures (4°C, 25°C, 40°C).²²⁶ They found that the particle size distribution remained unchanged after 12 months storage at 4°C and 25°C while there were very little particles remaining after 6 months at 40°C. Combining with size exclusion chromatography measurements, they found that the disintegration of the particles was due to acid hydrolysis causing scission of CS chains. Indeed, the kinetics of the hydrolysis reaction of CS is strongly accelerated at 40°C, as previously discussed in the section 3.1.c.

The use of another polyvalent salt, dibasic sodium phosphate (DSP), to prepare CS gels was reported by Li *et al.*²²⁷ They showed that CS solutions formed a gel at 4°C at pH ~ 7 in presence of DSP. DSP is a divalent phosphate salt having two pKa which are 7.2 and 12.6 at 25°C. These authors speculated that this gel was formed by hydrogen bonds between CS chains. However, this might not be the unique explanation. By making analogy with the CS/TPP system, we propose that this gel was formed through ionotropic crosslinking. At 4°C, the pK_{app} of CS is around 7.1,²²⁸ thus the CS chains are still charged at near neutral pHs, making the ionotropic crosslinking possible. The dependence of the pK_{app} of CS with temperature will be discussed in detail later in the section **The role of the ionization degree of CS in the thermosensitivity of CS/βGP mixtures.**

Li *et al.* also showed that upon heating, the gel becomes liquid, then exhibits a re-entrant transition to a gel. They suggested that this second gel is formed by hydrophobic interactions. One might think that this gel formed upon heating is actually very similar to CS/βGP. This hypothesis will be investigated in detail in this PhD project (chapter III).

The role of the polyol moiety in CS/βGP gelation

Chenite *et al.* assumed that although βGP forms divalent anions, the thermogelling of CS/βGP mixture could not be explained by ionic crosslinking. This hypothesis was lately confirmed by an experimental study reported by Filion *et al.*, showing the diffusion of βGP out of the gel after the gel formation.²²⁹ Chenite *et al.* suggested that the polyol part influenced the hydration state and the solubilization of CS chains. Indeed, hydration and water structuring are well known phenomena governing the behavior of polysaccharides and proteins in solution.^{230,231} In particular, in the case of CS, each monomer binds in average 2 water molecules, forming a first layer on which more water molecules can bind.²³²

The behavior of CS/βGP mixtures shows similar features with the one of proteins in solution. Water molecules interact with the hydrophilic moieties on amino of proteins, and play important roles in the dynamics of proteins.²³³ It has been suggested that the protein structure is stabilized thermodynamically in the presence of some polyols.²³⁰ This can be explained by the fact that the denaturation process must extensively exclude polyol molecules that bind to the protein surface, which requires more energy. More recent studies using molecular dynamics simulation proposed that the stabilization effect of polyol is more likely due to indirect interaction of water structure around polyol molecules, as the polyol have only few direct H-bonds with the protein.^{234,235} When the side chain length and/or the concentration of the polyol increases, the stabilizing effect is reinforced. For instance, Na *et al.* provided evidence of the stabilizing effect of glycerol on collagen solution.²³⁶ They studied the effects of glycerol on both the kinetics and the equilibrium of *in vitro* collagen fibril assembly and found that increasing glycerol concentration leads to a slow-down of the reaction rate and an increase of the critical concentration for fibril formation.

Back to CS/ β GP mixtures, Supper *et al.* reported in 2013 a study on the effect of the polyol part on their thermosensitive behavior.²³⁷ β GP was compared to two other polyols having different chemical structures, glucose-1-phosphate (G1-P) and glucose-6-phosphate (G6-P) and to a polyol-free phosphate salt, Na_2HPO_4 (**Figure I - 29a**). The authors reported that all the CS/polyol systems form transparent, clear and homogenous solutions with pH ranging from 7.2 to 7.5. The CS/ Na_2HPO_4 system prepared with the same range of salt concentration formed an inhomogeneous white dispersion with higher pH ranging from 7.6 to 7.9. They concluded that the polyol part was necessary to maintain CS in solution up to pH 7.5. However, one must be careful when comparing these systems, CS solution with or without polyols, because the pHs were not in the same range. This might have an important effect. According to Chenite *et al.*, the gelation time of CS/ β GP exhibited a strong dependence on the pH of the solution.²¹² Nevertheless, the results reported by Supper *et al.* on the three systems CS/polyol-phosphate brought valuable insights into the mechanism of this thermogelation. Using oscillatory rheology, they monitored the gelation both for isothermal experiment at 37°C, the time to reach the gel point (defined as the crossover of storage G' and loss G'' moduli) increased in the following order: β GP < G1-P < G6-P (**Figure I - 29b**). From temperature sweep experiments, they found that the sol/gel transition temperature, $T_{S/G}$, also evolved in the same order. Using ^{31}P NMR, they found that the chemical shift of the ^{31}P atom in CS/G1-P and CS/G6-P mixtures showed first a linear deshielding with increasing temperature, like for polyol solutions, then a decrease in a second part reflecting the decrease of the interactions between CS and the polyols (**Figure I - 29c**). The linear deshielding was not observed for CS/ β GP mixtures due to the very fast gelation. The temperature corresponding to the transition, observed in the ^{31}P chemical shift, shows a similar trend as the $T_{S/G}$ determined by rheology.

These results collectively suggested that the stabilizing effect of polyol salts on CS at neutral pHs is enhanced when the polyol size increases, in a similar way to protein/polyol systems. Supper *et al.* proposed a molecular picture where the polyol-phosphates moieties create a hydrated shell around CS chains by interacting with positively charged amino groups on one side and by forming H-bonds with water molecules on the other side. This shell remains stable at neutral pH and low temperature, therefore reducing the self-interactions between CS chains and maintaining the chains in solution. When heating, this hydrated shell is disrupted, hydrophobic interactions between CS chains become possible, leading to aggregation then gelation. A schematic illustration of this mechanism is shown in **Figure I - 30**. This proposed mechanism was recently supported by a thermodynamic study by Grinberg *et al.*²³⁸ From calorimetric analyses, they concluded that at low temperature, the β GP binding induces the formation of a highly ordered water clusters hydrating the polysaccharide chains. Due to the large entropic stress caused by this molecular complex, the hydration shell melts at higher temperature, thus triggering the phase separation of CS (**Figure I - 31**).

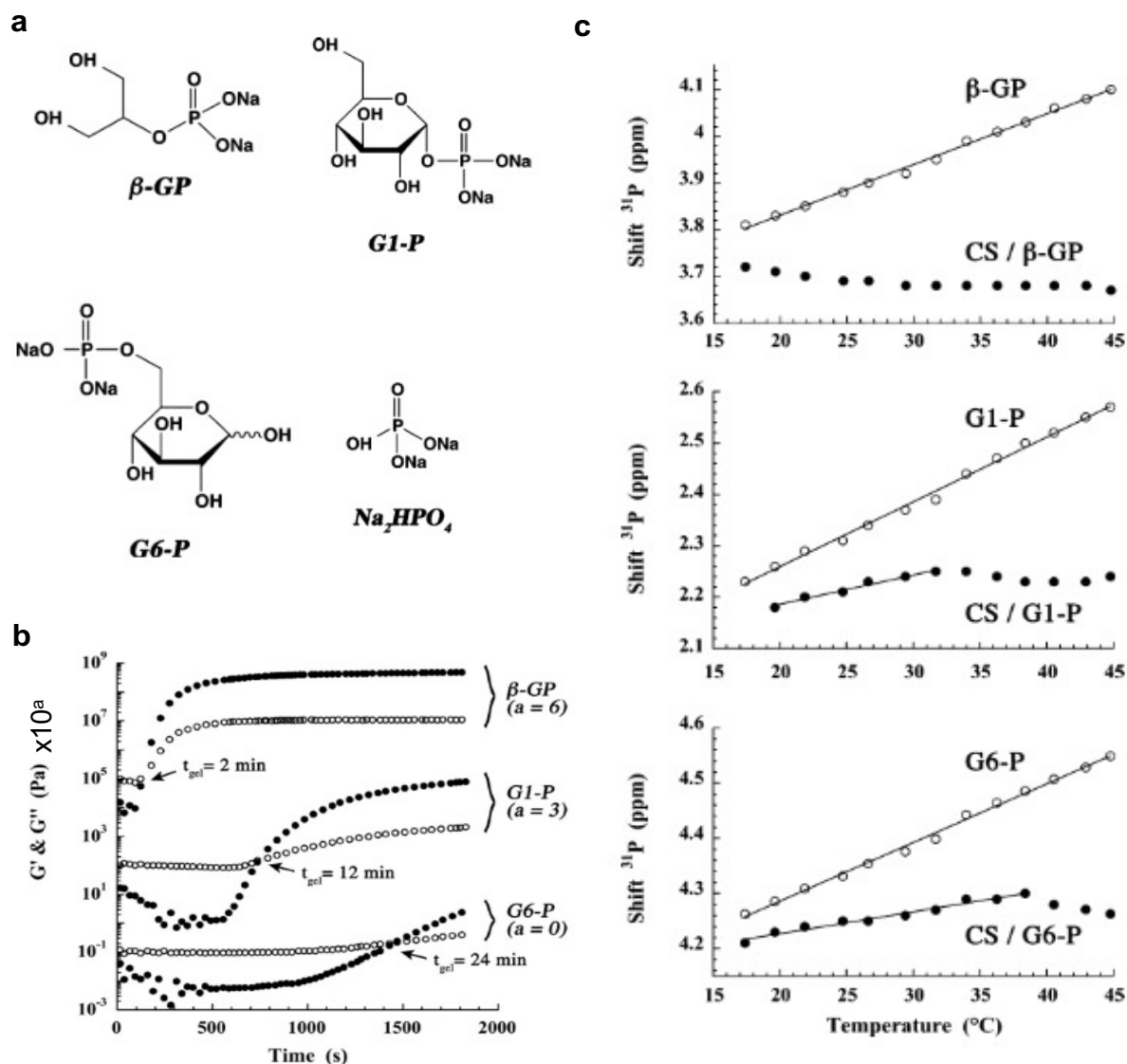


Figure I - 29. a) Chemical structure of different phosphate salts studied by Supper et al.; b) Time dependence of storage (G' , filled circles) and loss (G'' , empty circles) moduli of CS/ β GP, CS/G1-P and CS/G6-P for a fixed concentration of salt at 0.43 mmol.L^{-1} , at 37°C ; c) Temperature dependence of the chemical shift of ^{31}P nuclei from 17°C to 45°C of polyol solutions and CS/polyol mixtures. Adapted from Supper et al.²³⁷

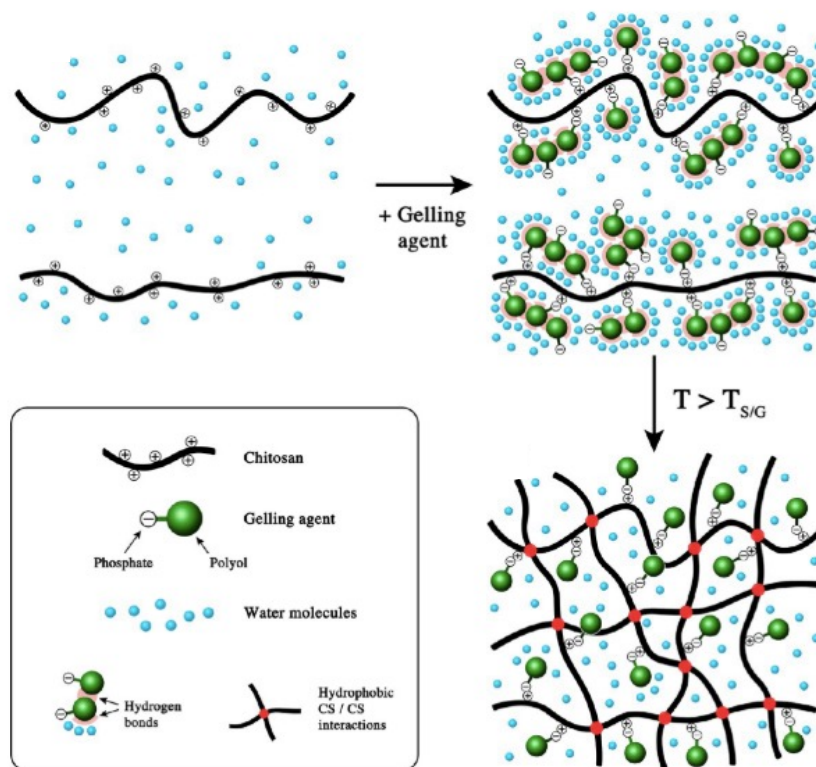


Figure I - 30. Schematic illustration of the gelation mechanisms of CS/polyol-phosphate solutions from Supper et al.²³⁷

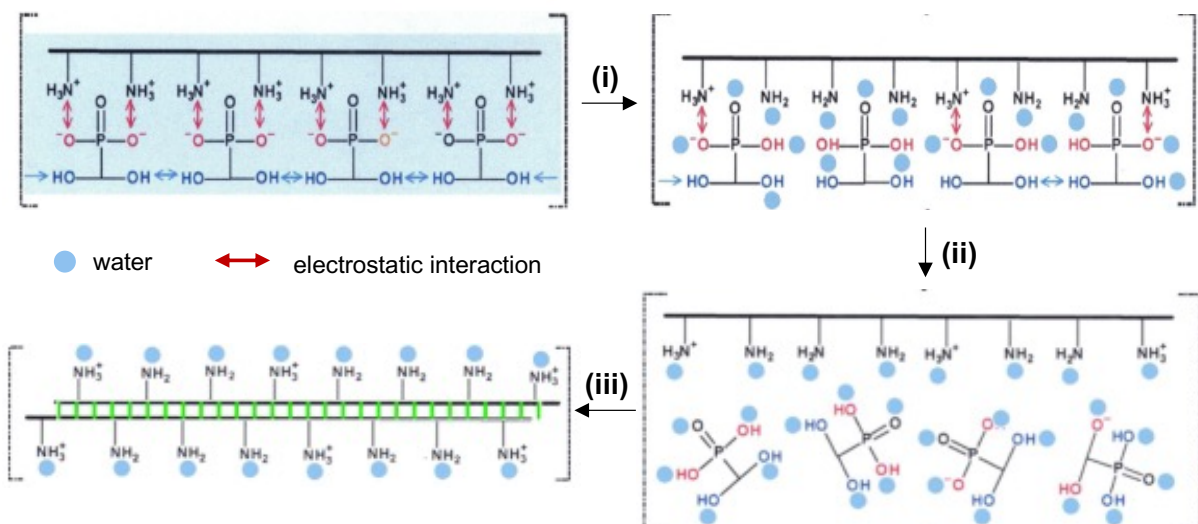


Figure I - 31. Proposed mechanism of the structural evolution of CS/βGP upon heating: (i) Melting of cooperative hydrate structure accompanied by dissociation of βGP-CS ionic pairs as a result of decreasing the pK_{app} and the subsequent transfer of protons from CS to GP; (ii) Release of primary bound βGP anions and (iii) formation of local aggregates (green bars). Adapted from Grinberg et al.²³⁸

The role of the ionization degree of CS in the thermosensitivity of CS/ β GP mixtures

As a cationic polyelectrolyte, the behavior of CS in solution is a complex function of its own characteristics (M_w and DD , *i.e.* number of amino groups, concentration) and of its environment (pH, ionic strength, temperature and other species present in solution). Filion *et al.* examined the temperature-dependent ionization of both the monomer (glucosamine) and the polymeric form of CS to investigate the gelation mechanism of CS/ β GP mixture.²²⁸ They designed an experimental setup in which the temperature, the pH and the relative light transmittance were simultaneously recorded (**Figure I - 32a**). They found that the dissociation constant of the glucosamine monomer, pK_0 , is about 6.6, which is very close to the pK_a of β GP, 6.67 at 25°C. Most interestingly, while the pK_a of β GP was very insensitive to temperature (**Figure I - 32b**), they showed that the dissociation constants pK_0 and pK_{app} of the CS chains have a very similar temperature dependence. Both pK decrease significantly with increasing temperature at a rate of -0.023 and -0.027 pK units per °C, respectively (**Figure I - 32b**). In other words, when the temperature increases, CS chains tend to deprotonate until reaching a critical ionization degree α_p at which electrostatic repulsion between ionized CS chains can no longer counteract attractive interchain forces, thus inducing precipitation.

The value of α_p was determined experimentally by monitoring the relative light transmittance during a pH titration experiment of acidic solution of CS in HCl with NaOH, as shown in **Figure I - 32c**. The decrease in the light transmittance (circle in **Figure I - 32c**) corresponds to CS aggregation. The value of α_p was calculated using the equation (I-1) knowing the concentration of all species in the solution.

$$\alpha = \frac{c_{Cl} - c_{Na} - \frac{10^{-pH}}{\gamma_+}}{f_D c_p} \quad (I - 1)$$

where c_{Cl} , c_{Na} and c_p are the concentrations of Cl^- , Na^+ ions and CS monomer respectively; f_D is the deacetylation degree and γ_+ the mobile ion activity coefficient.

Similarly, the temperature of precipitation, T_p , was determined from temperature ramp experiment, as shown in **Figure I - 32d**.

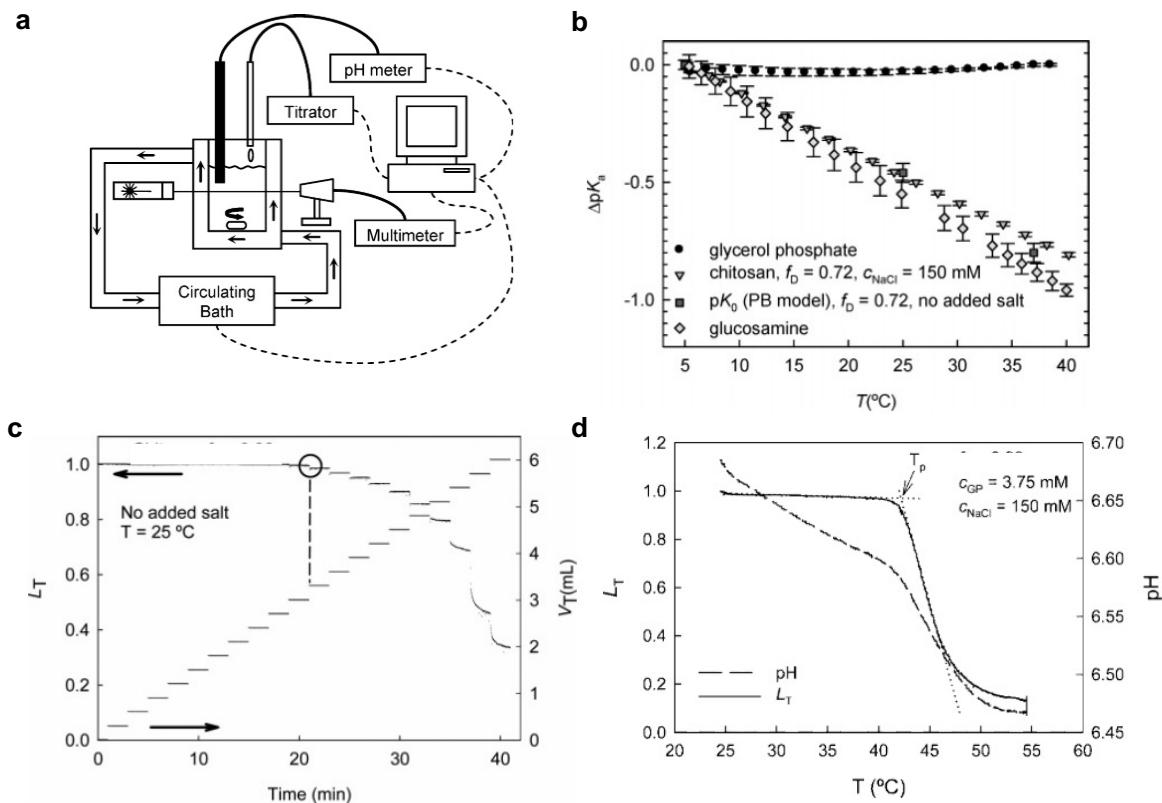


Figure I - 32. **a)** Custom experimental apparatus for temperature-controlled titration with simultaneous recording of temperature, pH, and relative light transmittance L_T of chitosan solutions; **b)** Temperature-dependence of pK_a of β GP, glucosamine, pK_{app} of CS (experimental and theoretical); **c)** Relative light transmittance L_T , and cumulative volume of added NaOH, V_T versus time illustrating the first step decrease in L_T due to chitosan precipitation (circle); **d)** Evolution of L_T and pH during a temperature ramp experiment. CS having DD = 98 % was used in these measurements. Reproduced from Filion, Lavertu et al.^{228,239}

They developed a theoretical model to calculate the ionization degree α_p as a function of temperature. For that, they proposed a polyelectrolyte model taking into account the thermosensitivity of the dissociation constant of the glucosamine monomer. Using this model, they predicted T_p , the temperature at which a given CS/ β GP mixture reaches the critical ionization degree α_p (**Figure I - 33a**). These calculations were in good agreement with their experimental values, as shown in **Figure I - 33b,c**.

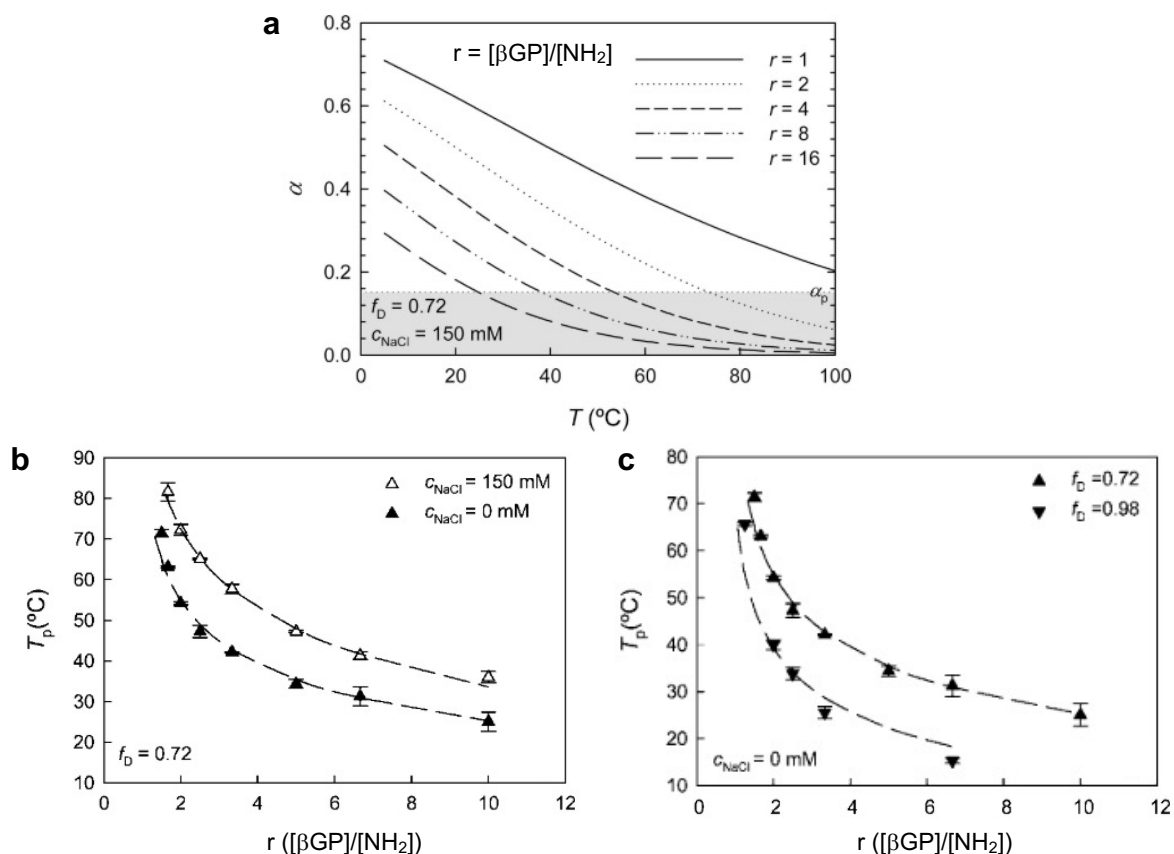


Figure I - 33. **a)** Calculations of CS ionization, α , versus temperature for CS/ β GP mixtures at $[\text{NH}_2] = 1.5 \text{ mM}$ and various $[\beta\text{GP}]/[\text{NH}_2]$ molar ratios; **b-c)** Comparison of experimental (symbols) and calculated (dashed lines) values of T_p as a function of the $[\beta\text{GP}]/[\text{NH}_2]$ molar ratio for CS/ β GP mixtures prepared with or without added NaCl (**b**) or with CS having different degrees of deacetylation (f_D) (**c**). Reproduced from Filion, Lavertu et al.^{228,239}

The effect of the presence of NaCl and the DD (noted f_D in this paper) on α_p and T_p was investigated. Experimental results for α_p are shown in **Table I - 2**.

Table I - 2. Average values of α_p for CS/ β GP mixtures prepared with CS having different DD and with or without added NaCl. Reproduced from Lavertu et al.²³⁹

	α_p (mean \pm sd, $n = 7$)	
	$c_{\text{NaCl}} = 0 \text{ mM}$	$c_{\text{NaCl}} = 150 \text{ mM}$
$f_D = 0.72$	0.12 ± 0.01	0.15 ± 0.01
$f_D = 0.98$	0.18 ± 0.02	0.28 ± 0.02

For a given DD, α_p was found to be higher with added salt because electrostatic screening reduce repulsive interactions between CS chains and allow precipitation at higher ionization state. Quite counterintuitively, the corresponding T_p was found to be higher as well (**Figure I - 33b**). This

contradiction was explained by the fact that the dissociation constant of β GP decreased from 6.58 to 6.21 when 150 mM of NaCl was added, therefore enhancing the thermal stability of the CS/ β GP complex.

In the absence of added NaCl, α_p slightly decreases from 0.18 to 0.12 (**Table I - 2**) and when *DD* decreases from 98 to 72%. T_p increases with decreasing *DD* for a given $[\beta\text{GP}]/[\text{NH}_2]$ ratio (**Figure I - 33c**). These results suggest that precipitation is more favorable for highly deacetylated CS. The authors explained this trend by the fact that the solubility decreases with increasing *DD*, as reported by Varum *et al.*¹⁹⁰ However, one might think that this explanation may not be the only one. Indeed, Varum *et al.* reported on reacylated CS, whereas in the studies by Lavertu, Filion and coworkers, two commercial CS grades were used, which are generally produced by a deacetylation process from chitin. It has been well established that the process strongly affects the distribution of N-acetyl groups and thus the crystallinity of the resulting CS (see 3.1.b). Hence, one might also explain the decrease of α_p with increasing *DD* by the relationship between the *DD* and the crystallinity of CS. In particular, CS with a *DD* as high as 98% has a high-level crystallinity, thus the precipitation is facilitated.

The same group also explored the possibility to replace β GP by either a strong base, NaOH or other polyol-free buffer, as 4-morpholineethanesulfonic acid (MES) and disodium phosphate.²³⁹ When titration of an acidic CS solution was done using NaOH at 25°C, chitosan precipitates quickly appeared around pH 6 due to the high local pH created at the point of titrant injection. A second decrease of the transmittance was observed around pH 7 when the α_p was reached, which is similar to the titration experiment with β GP (**Figure I - 34a,b**). The two other buffers, MES and Na₂HPO₄, have a pK_a similar as the one of CS and are relatively insensitive to temperature change, thus allowing the proton transfer from CS to buffers while heating. Like with β GP, precipitation of CS was observed in a temperature ramp experiment after the addition of a mixture of NaOH/MES or a solution of disodium phosphate (**Figure I - 34c**). However, the pH of the mixtures, a crucial parameter governing the gelation kinetics, was not given. The authors concluded that the glycerol moiety of β GP is non-essential and that temperature induced chitosan precipitation can be achieved using other buffers than β GP as long as they satisfy the requirements for proton transfer.

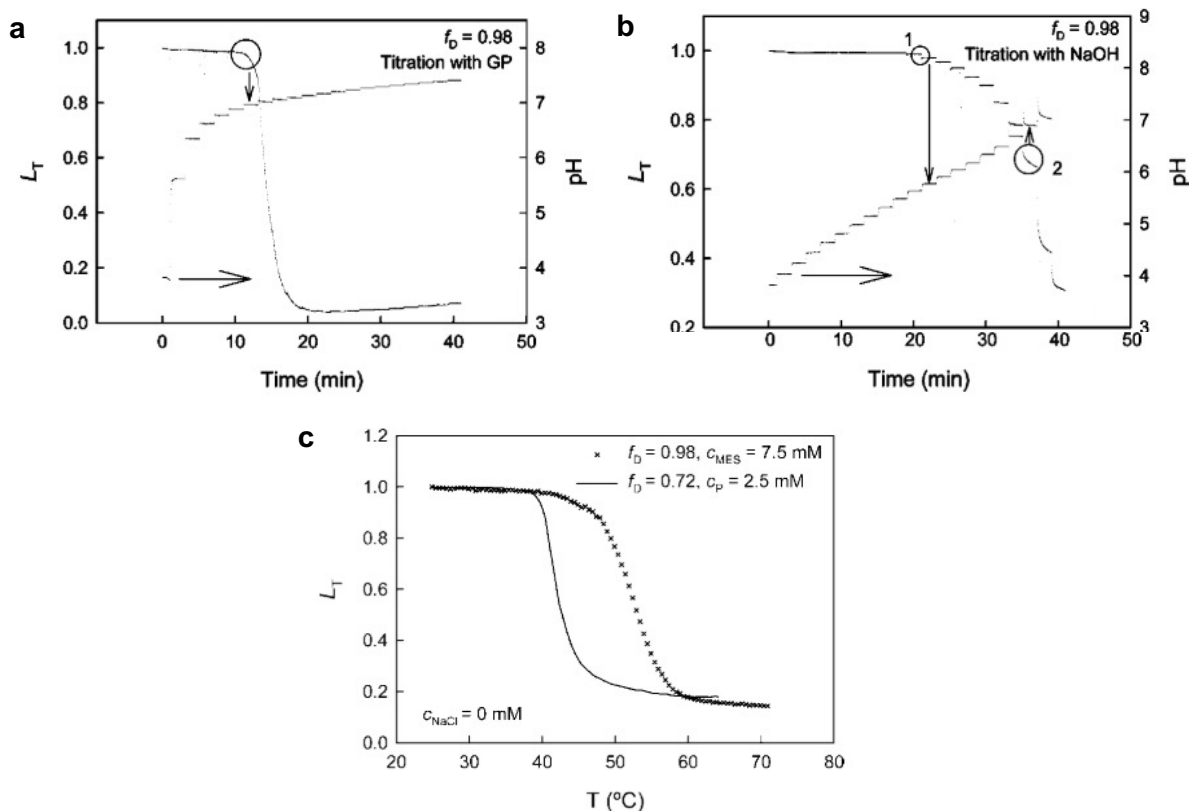


Figure I - 34. **a-b)** Evolution of L_T and the pH during titration experiments of CS solutions prepared with $[NH_2] = 1.5 \text{ mM}$ with βGP (**a**) and NaOH (**b**), at 25°C . **c)** Evolution of L_T as a function of temperature for CS/buffer mixtures prepared with $[NH_2] = 1.5 \text{ mM}$: MES/NaOH mixture with $[\text{MES}] = [\text{NaOH}] = 7.5 \text{ mM}$ (continuous line) or disodium phosphate solution at 2.5 mM (cross symbols). Reproduced from Lavertu *et al.*²³⁹

From these studies, one wonders if the thermosensitive phase separation of CS in aqueous solution is an intrinsic property of CS, or if its kinetics would depend on the pH of the solution and on the nature of the added salt/base. This question will be explored and debated in this PhD project. The corresponding results and discussions are presented in the chapter II.

Interactions involved in the sol/gel transition of CS/ βGP mixtures

It has been suggested in many studies that hydrophobic interactions are the main attractive forces involved in the thermogelation process of CS/ βGP mixtures.^{129,212,237,240–242} For instance, Cho *et al.* investigated the effect of urea, which is known to break H-bonds and weaken hydrophobic interactions.²⁴⁰ Using temperature ramp experiments, they found that the presence of urea hindered the gelation of CS/ βGP mixtures: when urea concentration increases, the gelation temperature increases and the storage modulus decreases (**Figure I - 35a**) and at a given temperature, the gelation time, as measured by rheology in temperature-ramp experiments, increases with increasing urea concentration

(Figure I - 35b). They proposed that hydrophobic interactions are more susceptible to be the driving force of the gelation process than H-bonds because H-bonds weaken rapidly with increasing temperature. However, this explanation is arguable because CS does not contain groups having a high hydrophobicity: the only clearly hydrophobic group is the $-\text{CH}_3$ moiety of the *N*-acetyl units.

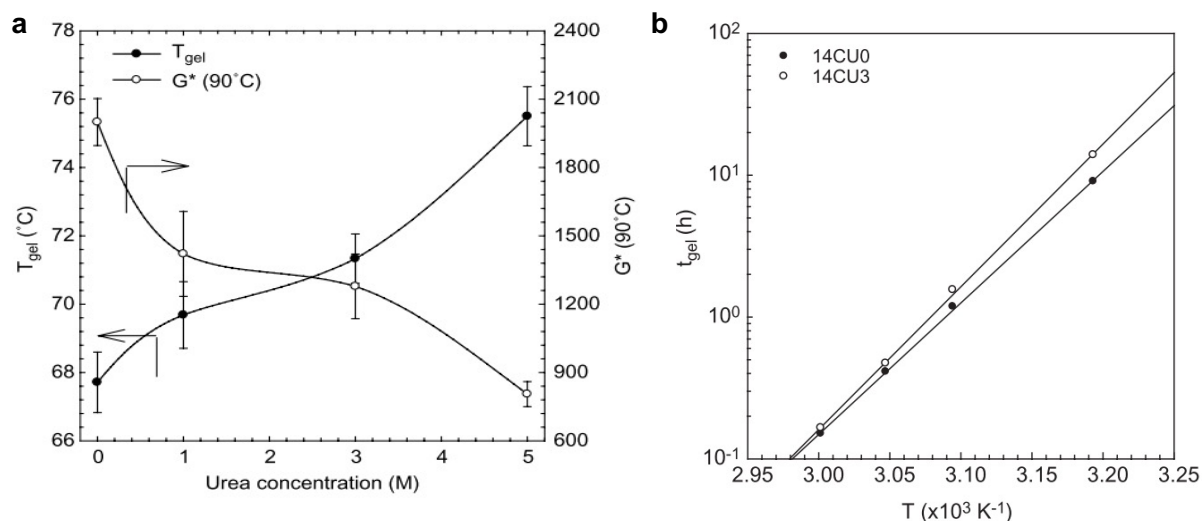


Figure I - 35. a) Effect of urea on the gelation temperature, T_{gel} , and the storage modulus of gels formed at 90°C; **b)** Evolution of gelling time, t_{gel} , as a function of temperature, for CS/ β GP mixtures without (14CU0, filled symbols) or with added urea (14CU3, open symbols). Reproduced from Cho *et al.*²⁴⁰

Philippova *et al.* studied the aggregation of CS in acidic aqueous solution using fluorescence spectroscopy with pyrene as a hydrophobicity probe.²⁴³ The concentration of hydrophobic domains was estimated from the polarity parameter of pyrene which is sensitive to the polarity of the medium. They found that the concentration of hydrophobic domains increased with increasing CS concentration. As there is no obvious hydrophobic interaction based on the chemical structure of CS, they suggested that the “hydrophobic domains” sensed by pyrene were rather due to cooperative H-bonds between glucosamine and *N*-acetyl units. Interestingly, they also found that heating led to a slight decrease in the polarity parameter of pyrene, which suggested an intrinsic temperature-dependence of CS solubility (Figure I - 36a). In a more recent study, using DLS combined with fluorescence spectroscopy and TEM, the same group showed that aggregation occurred even in water-soluble derivatives of chitin and in the absence of *N*-acetyl units (Figure I - 36b). Adding urea hindered the formation of aggregates, pointing out the contribution of H-bonds and/or hydrophobic interactions.¹⁸⁹ However, adding urea did not prevent the aggregation completely, which might be due to the presence of micro-crystallites, making the H-bonds inaccessible to urea. From these studies, it appears that H-bonds are the most likely interactions governing CS aggregation. However, depending on parameters such as DD , M_w and the distribution of *N*-acetyl units, other interactions like hydrophobic interactions or crystallization may also come into play.

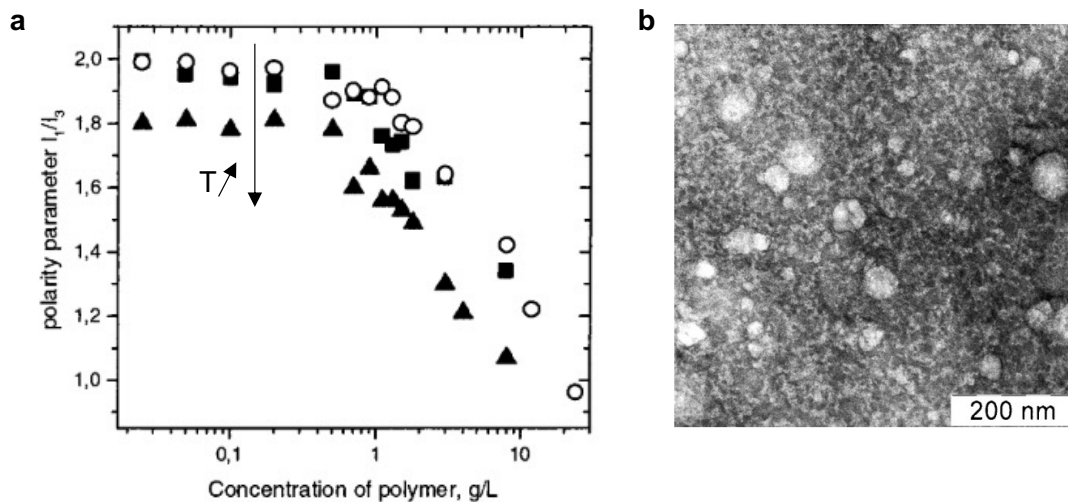


Figure I - 36. **a)** Evolution of the polarity parameter of pyrene in acidic aqueous solutions of CS as a function of CS concentration at different temperatures: 15°C (empty circles), 25°C (filled squares) and 40°C (filled triangles); **b)** TEM micrographs of aggregates of di-N,N-carboxymethylchitosan. Reproduced from Philippova *et al.*^{189,243}

Microstructural characterization of the thermosensitive CS/ β GP system

The morphology of CS/ β GP hydrogels was observed by Crompton *et al.* using confocal microscopy.²⁴⁴ The confocal micrographs shown in **Figure I - 37a** revealed a heterogeneous structure combining a polymer-rich phase and a polymer-poor phase, which can be interesting for hosting cells, as the polymer-poor phase may be qualified of pores. As expected, the polymer-rich phase increases with increasing CS concentration. It was found that the polymer-rich phase area increases linearly from 7% for CS 0.25 wt% to 33% for CS 1.5 wt% (**Figure I - 37b**). By analyzing the power spectra of confocal micrographs, Crompton *et al.* found a fractal dimension $D_f = 2.5$, indicating a fractal-like structure (**Figure I - 37c**). This value of D_f was later confirmed by a rheological study which found $D_f = 2.4$,²⁴² indicating a reaction-limited cluster-aggregation model.

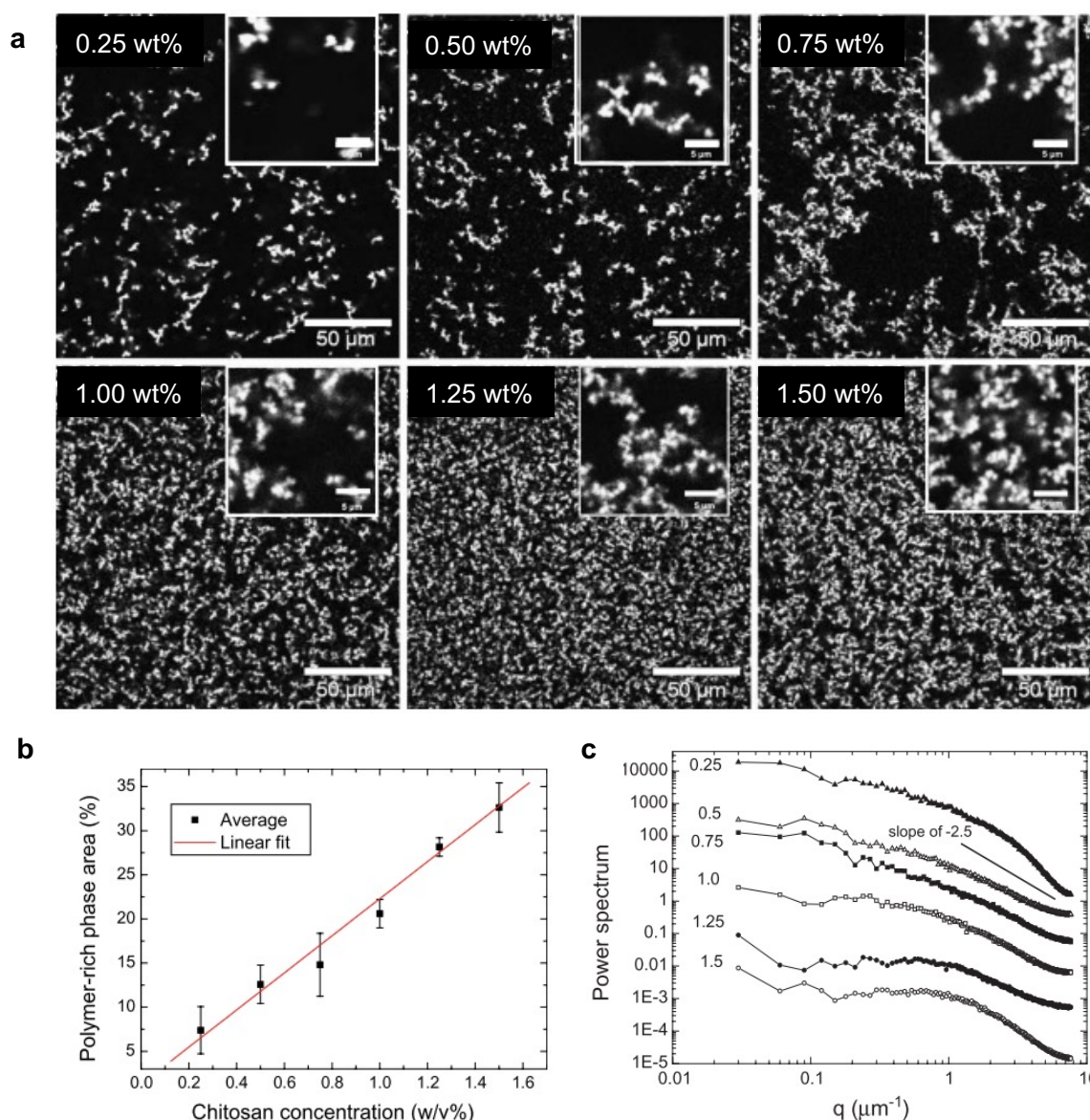


Figure I - 37. a) Confocal micrographs of CS/ β GP hydrogels prepared with various CS concentrations from 0.25 to 1.50 wt% and supplemented with fluorescein isothiocyanate after 2 min at 37°C (polymer-rich phase: bright, polymer-poor phase: dark); **b)** Linear fit of the polymer rich phase area as a function of CS concentration; **c)** Power spectra obtained from confocal micrographs. Reproduced from Crompton *et al.*²⁴⁴

The evolution of the microstructure of CS/ β GP mixtures both in the sol and in the gel states was studied in detail by Crompton *et al.* using small angle neutron scattering (SANS) and ultra-SANS (USANS).²⁴⁵ For that, they compared the $I(Q)$ profile from SANS of an acidic CS solution (pH \sim 3) to the one of a CS/ β GP solution ($[\beta\text{GP}]/[\text{NH}_2] = 12$, unknown pH). When the temperature increased from 10°C to 40°C, the $I(Q)$ profile of the CS/ β GP solution changed significantly while the one of the acidic CS solution did not change, indicating that the gel structure was only formed in the presence of β GP (**Figure I - 38a**).

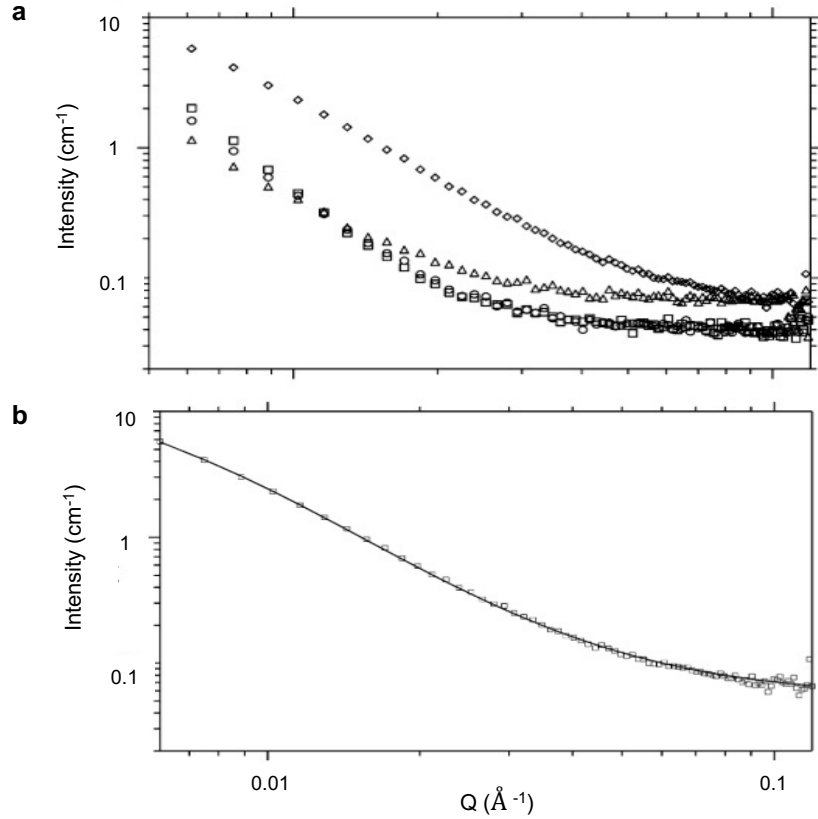


Figure I - 38. **a)** SANS profile of 1 w/v% CS solution at 10°C (circles) and 40°C (squares), CS/βGP solution at 10°C (triangles) and 40°C (diamonds); **b)** Fitting of $I(Q)$ profile for 1 w/v% CS solution at 40°C. Adapted from Crompton et al.²⁴⁵

The $I(Q)$ profile was fitted with a model derived from the description of semi-crystalline blends and swollen gels, as follows:

$$I(Q) = \frac{I_{0,y}}{(1 + \xi^2 Q^2)} + \frac{I_{0,x}}{(1 + \Xi^2 Q^2)} + \text{background} \quad (I - 2)$$

The first term represents the local concentration fluctuations of the liquid phase with a characteristic thermal blob dimension ξ , which increases proportionally with the polymer concentration. The second term originates from the solid inhomogeneity with a characteristic size Ξ , which is inversely proportional to the polymer concentration. The experimental $I(Q)$ profile nicely fits with the model, as shown in **Figure I - 38b**.

Figure I - 39a shows the $I(Q)$ profiles for CS/βGP hydrogels having %CS ranging from 0.25 to 1.50 wt% and reveals that the intensity increases with increasing CS concentration, suggesting changes in the parameters of equation (I - 2). On the one hand, the characteristic length ξ was found to slightly increase from 115 Å for CS 0.25 %wt to 135 Å for CS 1.5 wt%, as shown in **Figure I - 39b**. Such an increase in ξ with increasing CS concentration can be explained by the fact that the mobility and rotation

of each bond within a chain decrease, due to a larger number of polymer chains. On the other hand, the solid inhomogeneity Ξ was found to decrease from 450 Å for CS 0.25 wt% to about 300 Å for CS 1.5 wt%, suggesting that smaller inhomogeneities are formed at larger CS concentrations (**Figure I - 39c**).

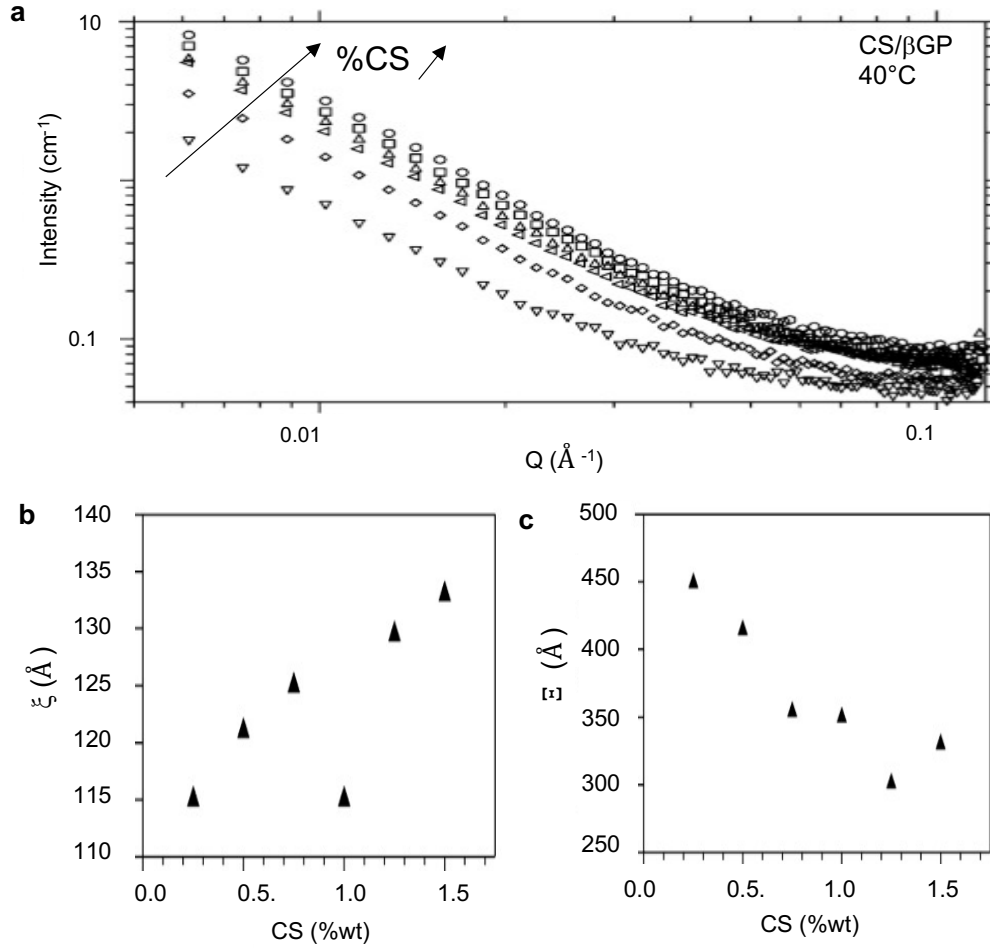


Figure I - 39. **a)** SANS profile; **b)** Correlation length ξ , and **c)** Characteristic length Ξ for CS/βGP hydrogels prepared with CS concentration ranging from 0.25 to 1.5 wt%. Adapted from Crompton *et al.*²⁴⁵

USANS technique was also used as it provides access to the same length scales as LSCM. The scattering data (**Figure I - 40a**) were fitted with the unified fit model giving the $I(Q)$ profile for an arbitrary number (n) of interrelated structure levels, as follows:

$$I(Q) = \sum_{i=1}^n \left(G_i \exp\left(\frac{-Q^2 R_{gi}^2}{3}\right) + B_i \exp\left[\operatorname{erf}\left(\frac{QR_{gi}}{3}\right)\right] \left[\frac{\operatorname{erf}(QkR_{gi}/\sqrt{6})}{Q}\right]^{P_i} \right) \quad (I-3)$$

where for each structural element i , G_i , is the exponential Guinier prefactor which is proportional to the scattering length density difference (contrast); B_i is a constant prefactor to the power-law function that is specific to the region where the exponent P_i decreases; erf is the error function and R_{gi} the radius of

gyration. From the fit, the average structural size was found to be of the order of 1-2 μm which was in agreement with the particle size observed by confocal microscopy (**Figure I - 40b**). Interestingly, this particle size decreases from $2.4 \pm 0.3 \mu\text{m}$ for CS 0.5 wt% to $1.39 \pm 0.03 \mu\text{m}$ for CS 1.5 wt%. This trend can be explained by the decrease of the characteristic length of hydrophobic junction Ξ as measured by SANS (**Figure I - 39c**). A similar trend was earlier observed by Shibayama *et al.* for *N*-isopropylacrylamide hydrogels.²⁴⁶

From this combination of confocal microscopy and scattering observations, Crompton *et al.* proposed a picture for the multiscale microstructure of individual CS hydrogel particles, as shown in **Figure I - 40c**. In this picture, the individual particle, which size is about 1-2 μm , is a highly heterogeneous object composed of hydrophobic domains and hydrophilic domains. These two studies reported by Crompton *et al.* bring valuable elements for the understanding of the gelation mechanisms in CS/ β GP mixtures.

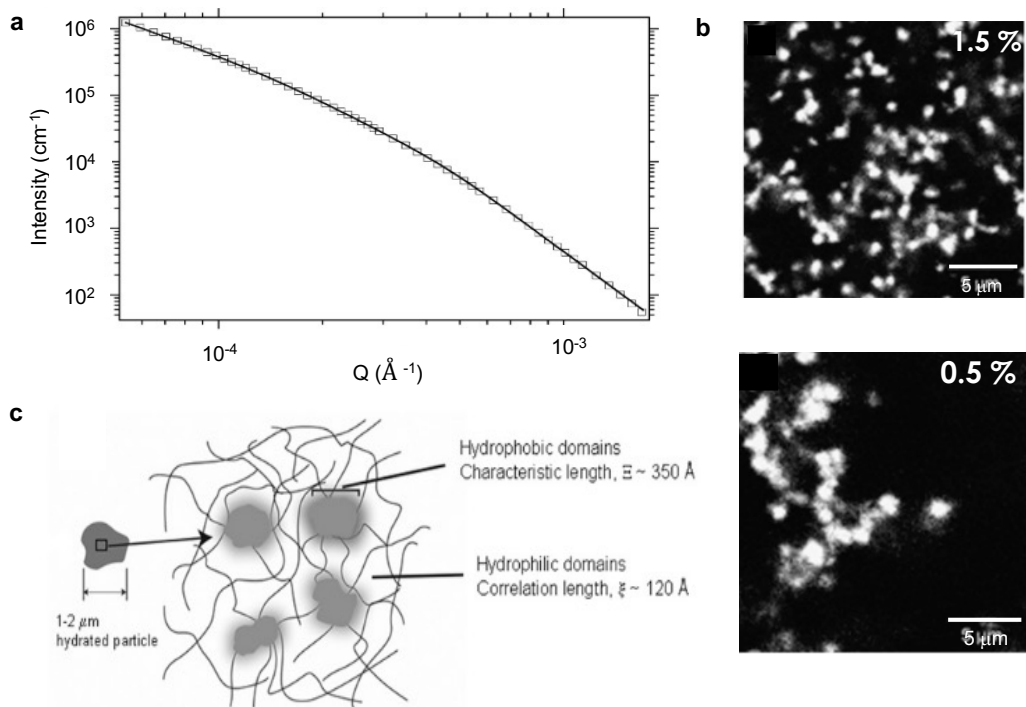


Figure I - 40. **a)** USANS profile of CS/ β GP hydrogel at 40°C (symbols) with calculated scattering from equation (I - 3) (line); **b)** Confocal microscopy images of CS/ β GP hydrogels prepared with CS concentration at 0.5 or 1.5 wt%; **c)** Schematic representation of the structure of a hydrated CS particle.

In this PhD project, the question of how the macroporosity emerges in the thermosensitive CS/phosphate salts system will be investigated. From our point of view, this question is crucial in the context of the targeted application, in which the gelation process occurs *in situ* and in the presence of cells. In chapter III, the thermo-responsive emergence of the microstructure in CS/salt mixture will be monitored in real-time, by combining confocal microscopy observations, light scattering and rheological measurements.

3.2.c. Biological properties and application of CS/ β GP gels as *in situ* forming carriers

Chenite *et al.* stated that CS/ β GP gels could be an ideal delivery carrier for sensitive biological materials, like proteins and living cells.¹²⁹ They performed *in vitro* encapsulation of several cell lines (cos-7, L929 and Rat-1) and found 80% of cell viability over an extended period (data not shown). They also carried out *in vivo* transplantation of chondrocytes in mice. After 3 weeks, they observed several areas of tissue remodeling with chondrocytes secreting a matrix having characteristic features of normal cartilage. However, in a later study, Ahmadi & Bruijn (2007) showed that the biocompatibility of CS/ β GP gels decreased with increasing β GP content.²⁴⁷ Mesenchymal stem cells (MSCs) were cultured in extraction medium from CS/ β GP at various CS and β GP concentrations. The cell death began to increase significantly when β GP concentration exceeded 10 w/v% as the cells shrank due to the high salt concentration which is needed to achieve quick gelation at 37°C (**Figure I - 41**). In order to solve this issue concerning the high osmolarity induced by β GP, different strategies have been explored, which mostly consisted in replacing β GP by other salts.^{158,248} For example, Nair *et al.* developed thermosensitive mixtures composed of CS and ammonium hydrogen phosphate (AHP) in which the quantity of needed salt did not induce a hyperosmolarity.²⁴⁸

Despite this limitation, CS/ β GP systems still present considerable potential as *in situ* forming hydrogels. Thermosensitive systems based on CS and salts were widely explored for various delivery applications using therapeutic molecules^{249–258} or cells^{259–267}. Crompton *et al.* studied cell survival and behavior of fetal mouse cortical cells in 2D and 3D culture in poly-D-lysine-grafted-CS/ β GP gels. They observed an improvement in cell survival and neurite outgrowth as compared to native CS.²⁶² Derived systems containing a third component which can be a protein (*e.g.* collagen^{263,265,268–270}) or a polysaccharide (*e.g.* starch²⁶⁵, dextran²⁷¹) were explored for cell encapsulation and delivery. Yang *et al.* combined CS/ β GP mixtures with collagen to encapsulate 3D MSC spheroids for wound healing and showed that the hydrogel provides a favorable environment for cell attachment and proliferation.²⁶⁹ When combined with dextran, CS/ β GP systems remain injectable and were shown to support the viability and proliferation of mouse embryonic fibroblasts cells and human umbilical vein endothelial cells *in vitro*, as reported by Ke *et al.*²⁷¹

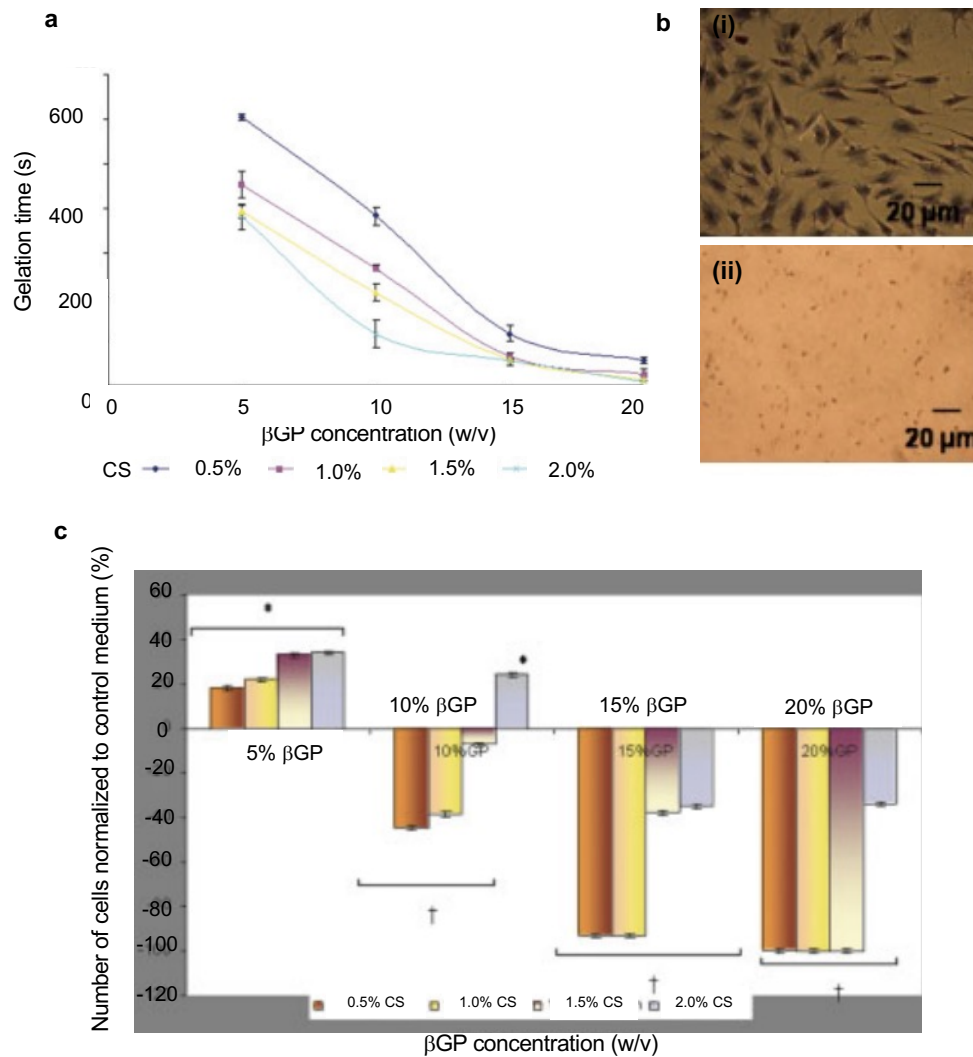


Figure I - 41. a) Gelation time at 37°C of CS/ β GP mixtures at various concentrations of CS and β GP, **b)** Microscopic images of MSCs incubated in control medium (i) versus extraction medium from 1.5 w/v% CS – 20 w/v% β GP hydrogel (ii), **c)** Normalized proliferation rate for MSCs incubated with different CS/ β GP extracts. Reproduced from Ahmadi & De Bruijn.²⁴⁷

As β GP itself is a component of the osteogenic medium, CS/ β GP and derived systems enriched with bioactive components (hydroxyapatite, bioglass, tricalcium phosphate, gallic acid, phloroglucinol), offer particularly promising strategies for bone tissue regeneration.^{209,272} For example, Dhiyva *et al.* developed a system containing zinc-doped CS, nanohydroxyapatite and β GP (Zn-CS/nHAp/ β GP).²⁷³ The presence of zinc improves the osteoconductive and antibacterial properties. *In vitro* experiments showed the addition of nHAp to the hydrogel enhanced osteoblast differentiation under osteogenic conditions. They also showed acceleration in bone formation *in vivo* in rat tibia as seen from the deposition of apatite and collagen (**Figure I - 42**).

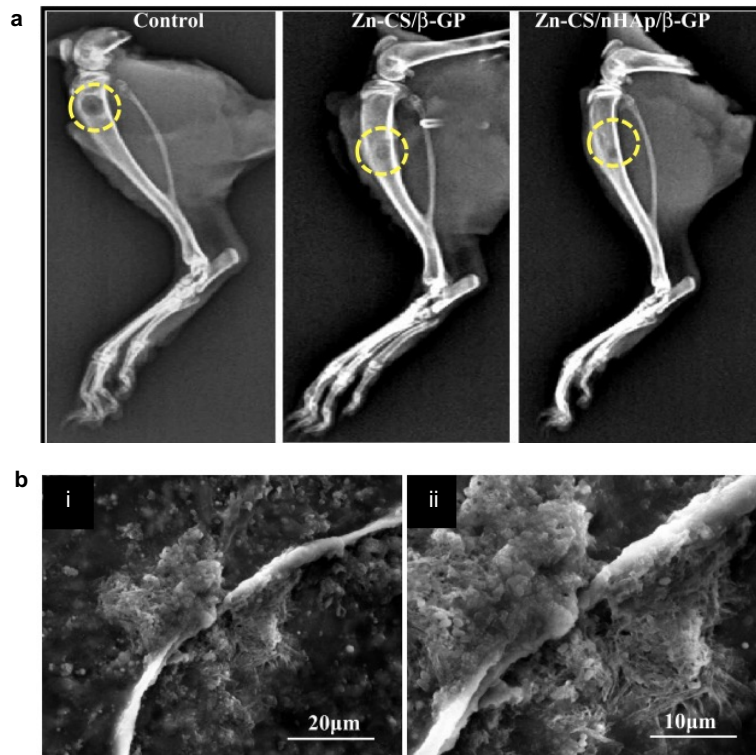


Figure I - 42. a) Radiographic images of the rat tibial defects obtained 2 weeks after they were filled with Zn-CS /βGP or Zn-CS/nHAp/βGP, the defect in control group was left unfilled; **b)** SEM images of Zn-CS/βGP (i) and Zn-CS/nHAp/βGP (ii) hydrogels in simulated body fluid after 21 days showing a more intense pattern of apatite formation on the surface of the Zn-CS/nHAp/βGP hydrogel. Reproduced from Dhivya et al.²⁷³

References

- (1) Campbell, N. G.; Kaneko, M.; Shintani, Y.; Narita, T.; Sawhney, V. Cell Size Critically Determines Initial Retention of Bone Marrow Mononuclear Cells in the Heart after Intracoronary Injection : Evidence from a Rat Model. **2016**, 1–19. <https://doi.org/10.1371/journal.pone.0158232>.
- (2) Li, J.; Hu, S.; Zhu, D.; Huang, K. Retention and Outcomes From Various Delivery Routes of Cell Therapy Products to the Heart. **2021**, 1–17. <https://doi.org/10.1161/JAHA.120.020402>.
- (3) Liang, Y.; Walczak, P.; Bulte, J. W. M. Biomaterials The Survival of Engrafted Neural Stem Cells within Hyaluronic Acid Hydrogels. *Biomaterials* **2013**, *34* (22), 5521–5529. <https://doi.org/10.1016/j.biomaterials.2013.03.095>.
- (4) Marquardt, L. M.; Doulames, V. M.; Wang, A. T.; Dubbin, K.; Suhar, R. A.; Kratochvil, M. J.; Medress, Z. A.; Plant, G. W.; Heilshorn, S. C. Designer, Injectable Gels to Prevent Transplanted Schwann Cell Loss during Spinal Cord Injury Therapy. *Sci. Adv.* **2020**, *6* (14), eaaz1039. <https://doi.org/10.1126/sciadv.aaz1039>.
- (5) Guyot, C.; Lerouge, S. Can We Achieve the Perfect Injectable Scaffold for Cell Therapy? *Futur. Sci. OA* **2018**, *4* (4), FSO284. <https://doi.org/10.4155/fsoa-2017-0153>.
- (6) Correia, C. R.; Reis, R. L.; Mano, J. F. Design Principles and Multifunctionality in Cell Encapsulation Systems for Tissue Regeneration. *Adv. Healthc. Mater.* **2018**, *7* (19), 1–20. <https://doi.org/10.1002/adhm.201701444>.
- (7) Correia, C. R.; Bjørge, I. M.; Nadine, S.; Mano, J. F. Minimalist Tissue Engineering Approaches Using Low Material-Based Bioengineered Systems. *Adv. Healthc. Mater.* **2021**, *10* (9), 1–18. <https://doi.org/10.1002/adhm.202002110>.
- (8) Marquardt, L. M.; Heilshorn, S. C. Design of Injectable Materials to Improve Stem Cell Transplantation. *Curr. Stem Cell Reports* **2016**, *2* (3), 207–220. <https://doi.org/10.1007/s40778-016-0058-0>.
- (9) Tong, X.; Yang, F. Recent Progress in Developing Injectable Matrices for Enhancing Cell Delivery and Tissue Regeneration. *Adv. Healthc. Mater.* **2018**, *7* (7), 1–16. <https://doi.org/10.1002/adhm.201701065>.
- (10) Kondziolka, D.; Gobbel, G. T.; Fellows-Mayle, W.; Chang, Y. F.; Uram, M. Injection Parameters Affect Cell Viability and Implant Volumes in Automated Cell Delivery for the Brain. *Cell Transplant.* **2011**, *20* (11–12), 1901–1906. <https://doi.org/10.3727/096368911X566190>.
- (11) Matta, R.; Lee, S.; Genet, N.; Hirschi, K. K.; Thomas, J. L.; Gonzalez, A. L. Minimally Invasive Delivery of Microbeads with Encapsulated, Viable and Quiescent Neural Stem Cells to the Adult Subventricular Zone. *Sci. Rep.* **2019**, *9* (1), 1–13. <https://doi.org/10.1038/s41598-019-54167-1>.
- (12) Wang, Y.; Adokoh, C. K.; Narain, R. Recent Development and Biomedical Applications of Self-Healing Hydrogels. *Expert Opin. Drug Deliv.* **2018**, *15* (1), 77–91. <https://doi.org/10.1080/17425247.2017.1360865>.
- (13) Rogers, Z. J.; Bencherif, S. A. Cryogelation and Cryogels. *Gels* **2019**, *5* (4), 7–8. <https://doi.org/10.3390/gels5040046>.
- (14) Li, Z.; Fan, Z.; Xu, Y.; Lo, W.; Wang, X.; Niu, H.; Li, X.; Xie, X.; Khan, M.; Guan, J. PH-Sensitive and Thermosensitive Hydrogels as Stem-Cell Carriers for Cardiac Therapy. *ACS Appl. Mater. Interfaces* **2016**, *8* (17), 10752–10760. <https://doi.org/10.1021/acsami.6b01374>.
- (15) Yap, L. S.; Yang, M. C. Thermo-Reversible Injectable Hydrogel Composing of Pluronic F127 and Carboxymethyl Hexanoyl Chitosan for Cell-Encapsulation. *Colloids Surfaces B Biointerfaces* **2020**, *185* (September 2019), 110606. <https://doi.org/10.1016/j.colsurfb.2019.110606>.
- (16) Jeon, O.; Bouhadir, K. H.; Mansour, J. M.; Alsberg, E. Photocrosslinked Alginate Hydrogels with Tunable Biodegradation Rates and Mechanical Properties. *Biomaterials* **2009**, *30* (14), 2724–2734. <https://doi.org/10.1016/j.biomaterials.2009.01.034>.
- (17) Bidarra, S. J.; Barrias, C. C.; Fonseca, K. B.; Barbosa, M. A.; Soares, R. A.; Granja, P. L. Injectable in Situ Crosslinkable RGD-Modified Alginate Matrix for Endothelial Cells Delivery. *Biomaterials* **2011**, *32* (31), 7897–7904. <https://doi.org/10.1016/j.biomaterials.2011.07.013>.
- (18) Janowski, M.; Lyczek, A.; Engels, C.; Xu, J.; Lukomska, B.; Bulte, J. W. M.; Walczak, P. Cell Size and Velocity of Injection Are Major Determinants of the Safety of Intracarotid Stem Cell Transplantation. *J. Cereb. Blood Flow Metab.* **2013**, *33* (6), 921–927. <https://doi.org/10.1038/jcbfm.2013.32>.

- (19) Janowski, M.; Lyczek, A.; Engels, C.; Xu, J.; Lukomska, B.; Bulte, J. W. M.; Walczak, P. Cell Size and Velocity of Injection Are Major Determinants of the Safety of Intracarotid Stem Cell Transplantation. *J. Cereb. Blood Flow & Metab.* **2013**, *33* (6), 921–927. <https://doi.org/10.1038/jcbfm.2013.32>.
- (20) Merten, O. W. Advances in Cell Culture: Anchorage Dependence. *Philos. Trans. R. Soc. B Biol. Sci.* **2015**, *370* (1661). <https://doi.org/10.1098/rstb.2014.0040>.
- (21) Chan, B. P.; Hui, T. Y.; Yeung, C. W.; Li, J.; Mo, I.; Chan, G. C. F. Self-Assembled Collagen-Human Mesenchymal Stem Cell Microspheres for Regenerative Medicine. *Biomaterials* **2007**, *28* (31), 4652–4666. <https://doi.org/10.1016/j.biomaterials.2007.07.041>.
- (22) Asghari Sana, F.; Çapkin Yurtsever, M.; Kaynak Bayrak, G.; Tunçay, E. Ö.; Kiremitçi, A. S.; Gümüşderelioğlu, M. Spreading, Proliferation and Differentiation of Human Dental Pulp Stem Cells on Chitosan Scaffolds Immobilized with RGD or Fibronectin. *Cytotechnology* **2017**, *69* (4), 617–630. <https://doi.org/10.1007/s10616-017-0072-9>.
- (23) Matsuda, A.; Kobayashi, H.; Itoh, S.; Kataoka, K.; Tanaka, J. Immobilization of Laminin Peptide in Molecularly Aligned Chitosan by Covalent Bonding. *Biomaterials* **2005**, *26* (15), 2273–2279. <https://doi.org/10.1016/j.biomaterials.2004.07.032>.
- (24) Bellis, S. L. Advantages of RGD Peptides for Directing Cell Association with Biomaterials. *Biomaterials* **2011**, *32* (18), 4205–4210. <https://doi.org/10.1016/j.biomaterials.2011.02.029>.
- (25) Chung, T.; Lu, Y.; Wang, S.; Lin, Y.; Chu, S. Growth of Human Endothelial Cells on Photochemically Grafted Gly – Arg – Gly – Asp (GRGD) Chitosans. *Biomaterials* **2002**, *23*, 4803–4809.
- (26) Comisar, W. A.; Kazmers, N. H.; Mooney, D. J.; Linderman, J. J. Engineering RGD Nanopatterned Hydrogels to Control Preosteoblast Behavior: A Combined Computational and Experimental Approach. *Biomaterials* **2007**, *28* (30), 4409–4417. <https://doi.org/10.1016/j.biomaterials.2007.06.018>.
- (27) Hansson, A.; Hashom, N.; Falson, F.; Rousselle, P.; Jordan, O.; Borchard, G. In Vitro Evaluation of an RGD-Functionalized Chitosan Derivative for Enhanced Cell Adhesion. *Carbohydr. Polym.* **2012**, *90* (4), 1494–1500. <https://doi.org/10.1016/j.carbpol.2012.07.020>.
- (28) Alipour, M.; Baneshi, M.; Hosseinkhani, S.; Mahmoudi, R.; Jabari Arabzadeh, A.; Akrami, M.; Mehrzad, J.; Bardania, H. Recent Progress in Biomedical Applications of RGD-Based Ligand: From Precise Cancer Theranostics to Biomaterial Engineering: A Systematic Review. *J. Biomed. Mater. Res. - Part A* **2020**, *108* (4), 839–850. <https://doi.org/10.1002/jbm.a.36862>.
- (29) Akiyama, S. K.; Aota, S. I.; Yamada, K. M. Function and Receptor Specificity of a Minimal 20 Kilodalton Cell Adhesive Fragment of Fibronectin. *Cell Commun. Adhes.* **1995**, *3* (1), 13–25. <https://doi.org/10.3109/15419069509081275>.
- (30) Custodio, C.; Alves, C.; Reis, R.; Mano, J. Immobilization of Fibronectin in Chitosan Substrates Improves Cell Adhesion and Proliferation. *J. Tissue Eng. Regen. Med.* **2010**, *4* (7), 524–531. <https://doi.org/10.1002/term>.
- (31) Tsai, W. B.; Chen, Y. R.; Liu, H. L. RGD-Conjugated Crosslinked Chitosan Scaffolds for Culture and Osteogenic Differentiation of Mesenchymal Stem Cells. *J. Taiwan Inst. Chem. Eng.* **2013**, *44* (1), 1–7. <https://doi.org/10.1016/j.jtice.2012.09.003>.
- (32) Tıgli, R. S.; Gümüşderelioğlu, M. Evaluation of RGD- or EGF-Immobilized Chitosan Scaffolds for Chondrogenic Activity. *Int. J. Biol. Macromol.* **2008**, *43* (2), 121–128. <https://doi.org/10.1016/j.ijbiomac.2008.04.003>.
- (33) Chang, H.-I.; Wang, Y. Cell Responses to Surface and Architecture of Tissue Engineering Scaffolds. *Regen. Med. Tissue Eng. - Cells Biomater.* **2011**. <https://doi.org/10.5772/21983>.
- (34) Guimarães, C. F.; Gasperini, L.; Marques, A. P.; Reis, R. L. The Stiffness of Living Tissues and Its Implications for Tissue Engineering. *Nat. Rev. Mater.* **2020**, *5* (5), 351–370. <https://doi.org/10.1038/s41578-019-0169-1>.
- (35) Kamimura, M.; Sugawara, M.; Yamamoto, S.; Yamaguchi, K.; Nakanishi, J. Dynamic Control of Cell Adhesion on a Stiffness-Tunable Substrate for Analyzing the Mechanobiology of Collective Cell Migration. *Biomater. Sci.* **2016**, *4* (6), 933–937. <https://doi.org/10.1039/C6BM00100A>.
- (36) Guvendiren, M.; Burdick, J. A. Stiffening Hydrogels to Probe Short- and Long-Term Cellular Responses to Dynamic Mechanics. *Nat. Commun.* **2012**, *3*, 792–799. <https://doi.org/10.1038/ncomms1792>.

- (37) Mrksich, M. Dynamic Substrates for Cell Biology. *MRS Bull.* **2005**, *30* (March), 180–184.
- (38) Pek, Y. S.; Wan, A. C. A.; Ying, J. Y. The Effect of Matrix Stiffness on Mesenchymal Stem Cell Differentiation in a 3D Thixotropic Gel. *Biomaterials* **2010**, *31* (3), 385–391. <https://doi.org/10.1016/j.biomaterials.2009.09.057>.
- (39) Mao, A. S.; Shin, J. W.; Mooney, D. J. Effects of Substrate Stiffness and Cell-Cell Contact on Mesenchymal Stem Cell Differentiation. *Biomaterials* **2016**, *98*, 184–191. <https://doi.org/10.1016/j.biomaterials.2016.05.004>.
- (40) Wang, X.; Young, D. J. Thermogelling 3D Systems towards Stem Cell-Based Tissue Regeneration Therapies. **2018**, 1–14. <https://doi.org/10.3390/molecules23030553>.
- (41) Reilly, G. C.; Engler, A. J. Intrinsic Extracellular Matrix Properties Regulate Stem Cell Differentiation. *J. Biomech.* **2010**, *43* (1), 55–62. <https://doi.org/10.1016/j.jbiomech.2009.09.009>.
- (42) Huebsch, N.; Arany, P. R.; Mao, A. S.; Shvartsman, D.; Ali, O. A.; Bencherif, S. A.; Rivera-Feliciano, J.; Mooney, D. J. Harnessing Traction-Mediated Manipulation of the Cell/Matrix Interface to Control Stem-Cell Fate. *Nat. Mater.* **2010**, *9* (6), 518–526. <https://doi.org/10.1038/nmat2732>.
- (43) Chaudhuri, O.; Cooper-White, J.; Janmey, P. A.; Mooney, D. J.; Shenoy, V. B. Effects of Extracellular Matrix Viscoelasticity on Cellular Behaviour. *Nature* **2020**, *584* (7822), 535–546. <https://doi.org/10.1038/s41586-020-2612-2>.
- (44) Nam, S.; Gupta, V. K.; Lee, H. pyo; Lee, J. Y.; Wisdom, K. M.; Varma, S.; Flaum, E. M.; Davis, C.; West, R. B.; Chaudhuri, O. Cell Cycle Progression in Confining Microenvironments Is Regulated by a Growth-Responsive TRPV4-PI3K/Akt-P27Kip1 Signaling Axis. *Sci. Adv.* **2019**, *5* (8). <https://doi.org/10.1126/sciadv.aaw6171>.
- (45) M. Madl, C.; LeSavage, B. L.; Dewi, R. E.; Dinh, C. B.; Stowers, R. S.; Khariton, M.; J. Lampe, K.; Nguyen, D.; Chaudhuri, O.; Annika, E.; Heilshorn, S. C. Maintenance of Neural Progenitor Cell Stemness in Remodeling, Hydrogels Requires Matrix. *Nat Mater* **2017**, *16* (12), 1233–1242. <https://doi.org/10.1038/nmat5020.Maintenance>.
- (46) Lee, H.; Gu, L.; Mooney, D. J.; Levenston, M. E.; Chaudhuri, O. Mechanical Confinement Regulates Cartilage Matrix Formation by Chondrocytes. *Nat Mater* **2017**, *16* (12), 1243–1251. <https://doi.org/10.1038/nmat4993.Mechanical>.
- (47) Chaudhuri, O.; Gu, L.; Klumpers, D.; Darnell, M.; Sidi, A.; Weaver, J. C.; Huebsch, N.; Lee, H.; Lippens, E.; Duda, G. N.; Mooney, D. J. Hydrogels with Tunable Stress Relaxation Regulate Stem Cell Fate and Activity. **2016**, *15* (3), 326–334. <https://doi.org/10.1038/nmat4489.Hydrogels>.
- (48) Vogel, V.; Sheetz, M. Local Force and Geometry Sensing Regulate Cell Functions. *Nat. Rev. Mol. Cell Biol.* **2006**, *7* (4), 265–275. <https://doi.org/10.1038/nrm1890>.
- (49) Cameron, A. R.; Frith, J. E.; Cooper-White, J. J. The Influence of Substrate Creep on Mesenchymal Stem Cell Behaviour and Phenotype. *Biomaterials* **2011**, *32* (26), 5979–5993. <https://doi.org/10.1016/j.biomaterials.2011.04.003>.
- (50) Mooney, D. J.; Langer, R.; Ingber, D. E. Cytoskeletal Filament Assembly and the Control of Cell Spreading and Function by Extracellular Matrix. *J. Cell Sci.* **1995**, *108* (6), 2311–2320. <https://doi.org/10.1242/jcs.108.6.2311>.
- (51) Chaudhuri, O.; Gu, L.; Klumpers, D.; Darnell, M.; Bencherif, S. A.; Weaver, J. C.; Huebsch, N.; Lee, H. P.; Lippens, E.; Duda, G. N.; Mooney, D. J. Hydrogels with Tunable Stress Relaxation Regulate Stem Cell Fate and Activity. *Nat. Mater.* **2016**, *15* (3), 326–334. <https://doi.org/10.1038/nmat4489>.
- (52) Fu, F.; Zhu, X.; Qin, Z.; Wang, J.-J.; Xu, C.; Wang, L.-N.; Tu, Y.; Zhang, S.; Li, R.-X.; Li, X.-H.; Zhao, M.-L. Differential Degradation Rate and Underlying Mechanism of a Collagen/Chitosan Complex in Subcutis, Spinal Cord and Brain Tissues of Rat. *J. Mater. Sci. Mater. Med.* **2018**, *29* (4). <https://doi.org/10.1007/s10856-018-6033-9>.
- (53) Sivashanmugam, A.; Arun Kumar, R.; Vishnu Priya, M.; Nair, S. V.; Jayakumar, R. An Overview of Injectable Polymeric Hydrogels for Tissue Engineering. *Eur. Polym. J.* **2015**, *72*, 543–565. <https://doi.org/10.1016/j.eurpolymj.2015.05.014>.
- (54) Croisier, F.; Jérôme, C. Chitosan-Based Biomaterials for Tissue Engineering. *Eur. Polym. J.* **2013**, *49* (4), 780–792. <https://doi.org/10.1016/j.eurpolymj.2012.12.009>.

- (55) Kretlow, J. D.; Klouda, L.; Mikos, A. G. Injectable Matrices and Scaffolds for Drug Delivery in Tissue Engineering. *Adv. Drug Deliv. Rev.* **2007**, *59* (4–5), 263–273. <https://doi.org/10.1016/j.addr.2007.03.013>.
- (56) Loh, Q. L.; Choong, C. Three-Dimensional Scaffolds for Tissue Engineering Applications: Role of Porosity and Pore Size. *Tissue Eng. Part B Rev.* **2013**, *19* (6), 485–502. <https://doi.org/10.1089/ten.teb.2012.0437>.
- (57) Yannas, I. V.; Lee, E.; Orgill, D. P.; Skrabut, E. M.; Murphy, G. F. Synthesis and Characterization of a Model Extracellular Matrix That Induces Partial Regeneration of Adult Mammalian Skin. *Proc. Natl. Acad. Sci.* **1989**, *86* (3), 933–937. <https://doi.org/10.1073/pnas.86.3.933>.
- (58) O'Brien, F. J.; Harley, B. A.; Yannas, I. V.; Gibson, L. J. The Effect of Pore Size on Cell Adhesion in Collagen-GAG Scaffolds. *Biomaterials* **2005**, *26* (4), 433–441. <https://doi.org/10.1016/j.biomaterials.2004.02.052>.
- (59) O'Brien, F. F. J.; Harley, B. B. A.; Waller, M. A.; Yannas, I. V.; Gibson, L. J.; Prendergast, P. J. The Effect of Pore Size on Permeability and Cell Attachment in Collagen Scaffolds for Tissue Engineering. *Technol. Heal. care* **2007**, *15* (1), 3–17. <https://doi.org/10.1016/j.biomaterials.2009.09.063>.
- (60) Zeltinger, J.; Ph, D.; Sherwood, J. K.; Ph, D.; Graham, D. a; Müller, R.; Ph, D.; Griffith, L. G.; Ph, D. Effect of Pore Size and Void Fraction on Cellular Adhesion, Proliferation, and Matrix Deposition. *Tissue Eng.* **2001**, *7* (5), 557–572.
- (61) Salem, A. K.; Stevens, R.; Pearson, R. G.; Davies, M. C.; Tendler, S. J. B.; Roberts, C. J.; Williams, P. M.; Shakesheff, K. M. Interactions of 3T3 Fibroblasts and Endothelial Cells with Defined Pore Features. *J. Biomed. Mater. Res.* **2002**, *61* (2), 212–217. <https://doi.org/10.1002/jbm.10195>.
- (62) Akay, G.; Birch, M. A.; Bokhari, M. A. Microcellular PolyHIPE Polymer Supports Osteoblast Growth and Bone Formation in Vitro. *Biomaterials* **2004**, *25* (18), 3991–4000. <https://doi.org/10.1016/j.biomaterials.2003.10.086>.
- (63) Senuma, Y.; Franceschin, S.; Hilborn, J. G.; Tissières, P.; Bisson, I.; Frey, P. Bioresorbable Microspheres by Spinning Disk Atomization as Injectable Cell Carrier: From Preparation to in Vitro Evaluation. *Biomaterials* **2000**, *21* (11), 1135–1144. [https://doi.org/10.1016/S0142-9612\(99\)00276-8](https://doi.org/10.1016/S0142-9612(99)00276-8).
- (64) McGlohorn, J. B.; Grimes, L. W.; Webster, S. S.; Burg, K. J. L. Characterization of Cellular Carriers for Use in Injectable Tissue-Engineering Composites. *J. Biomed. Mater. Res. - Part A* **2003**, *66* (3), 441–449. <https://doi.org/10.1002/jbm.a.10546>.
- (65) Taek, K. K.; Jun, J. Y.; Doo, S. L.; Park, T. G. Gas Foamed Open Porous Biodegradable Polymeric Microspheres. *Biomaterials* **2006**, *27* (2), 152–159. <https://doi.org/10.1016/j.biomaterials.2005.05.081>.
- (66) Cheng, D.; Gao, H.; Hao, L.; Cao, X.; Wang, Y. Facile Development of a Hollow Composite Microsphere with Porous Surface for Cell Delivery. *Mater. Lett.* **2013**, *111*, 238–241. <https://doi.org/10.1016/j.matlet.2013.08.111>.
- (67) Rong, K.; Zhang, Z.; Jin, X.; Hu, J.; Gupte, M. J.; Ni, L.; Ma, P. X. Nanofibrous Spongy Microspheres Enhance Odontogenic Differentiation of Human Dental Pulp Stem Cells. *Adv. Healthc. Mater.* **2015**, *4* (13), 1993–2000. <https://doi.org/doi:10.1002/adhm.201500308>.
- (68) Gong, Y.; Wang, Y.; Qu, Q.; Hou, Z.; Guo, T.; Xu, Y.; Qing, R.; Deng, J.; Wang, B.; Hao, S. Nanoparticle Encapsulated Core-Shell Hydrogel for on-Site BMSCs Delivery Protects from Iron Overload and Enhances Functional Recovery. *J. Control. Release* **2020**, *320* (January), 381–391. <https://doi.org/10.1016/j.jconrel.2020.01.029>.
- (69) Lim, S. M.; Lee, H. J.; Oh, S. H.; Kim, J. M.; Lee, J. H. Novel Fabrication of PCL Porous Beads for Use as an Injectable Cell Carrier System. *J. Biomed. Mater. Res. - Part B Appl. Biomater.* **2009**, *90 B* (2), 521–530. <https://doi.org/10.1002/jbm.b.31313>.
- (70) Shin, U. S.; Park, J. H.; Hong, S. J.; Won, J. E.; Yu, H. S.; Kim, H. W. Porous Biomedical Composite Microspheres Developed for Cell Delivering Scaffold in Bone Regeneration. *Mater. Lett.* **2010**, *64* (20), 2261–2264. <https://doi.org/10.1016/j.matlet.2010.06.069>.
- (71) Jin, G. Z.; Park, J. H.; Seo, S. J.; Kim, H. W. Dynamic Cell Culture on Porous Biopolymer Microcarriers in a Spinner Flask for Bone Tissue Engineering: A Feasibility Study. *Biotechnol. Lett.* **2014**, *36* (7), 1539–1548. <https://doi.org/10.1007/s10529-014-1513-6>.
- (72) Zhang, Q.; Tan, K.; Ye, Z.; Zhang, Y.; Tan, W.; Lang, M. Preparation of Open Porous Polycaprolactone Microspheres and Their Applications as Effective Cell Carriers in Hydrogel System. *Mater. Sci. Eng. C*

- 2012, 32 (8), 2589–2595. <https://doi.org/10.1016/j.msec.2012.07.045>.
- (73) Liao, J.; Wang, B.; Huang, Y.; Qu, Y.; Peng, J.; Qian, Z. Injectable Alginate Hydrogel Cross-Linked by Calcium Gluconate-Loaded Porous Microspheres for Cartilage Tissue Engineering. *ACS Omega* **2017**, 2 (2), 443–454. <https://doi.org/10.1021/acsomega.6b00495>.
- (74) Headen, D. M.; Aubry, G.; Lu, H.; García, A. J. Microfluidic-Based Generation of Size-Controlled, Biofunctionalized Synthetic Polymer Microgels for Cell Encapsulation. *Adv. Mater.* **2014**, 26 (19), 3003–3008. <https://doi.org/10.1002/adma.201304880>.
- (75) Yao, R.; Zhang, R.; Lin, F.; Luan, J. Injectable Cell/Hydrogel Microspheres Induce the Formation of Fat Lobule-like Microtissues and Vascularized Adipose Tissue Regeneration. *Biofabrication* **2012**, 4 (4). <https://doi.org/10.1088/1758-5082/4/4/045003>.
- (76) Natesan, S.; Baer, D. G.; Walters, T. J.; Babu, M.; Christy, R. J. Adipose-Derived Stem Cell Delivery into Collagen Gels Using Chitosan Microspheres. *Tissue Eng. - Part A* **2010**, 16 (4), 1369–1384. <https://doi.org/10.1089/ten.tea.2009.0404>.
- (77) Luetchford, K. A.; Chaudhuri, J. B.; De Bank, P. A. Silk Fibroin/Gelatin Microcarriers as Scaffolds for Bone Tissue Engineering. *Mater. Sci. Eng. C* **2020**, 106 (August 2019). <https://doi.org/10.1016/j.msec.2019.110116>.
- (78) Matamoros-Veloz, A.; Hossain, K. M. Z.; Scammell, B. E.; Ahmed, I.; Hall, R.; Kapur, N. Formulating Injectable Pastes of Porous Calcium Phosphate Glass Microspheres for Bone Regeneration Applications. *J. Mech. Behav. Biomed. Mater.* **2020**, 102 (July 2019), 103489. <https://doi.org/10.1016/j.jmbbm.2019.103489>.
- (79) Hossain, K. M. Z.; Patel, U.; Kennedy, A. R.; Macri-Pellizzeri, L.; Sottile, V.; Grant, D. M.; Scammell, B. E.; Ahmed, I. Porous Calcium Phosphate Glass Microspheres for Orthobiologic Applications. *Acta Biomater.* **2018**, 72, 396–406. <https://doi.org/10.1016/j.actbio.2018.03.040>.
- (80) Leong, W.; Wang, D. A. Cell-Laden Polymeric Microspheres for Biomedical Applications. *Trends Biotechnol.* **2015**, 33 (11), 653–666. <https://doi.org/10.1016/j.tibtech.2015.09.003>.
- (81) Nejati, S.; Karimi Soflou, R.; Khorshidi, S.; Karkhaneh, A. Development of an Oxygen-Releasing Electroconductive in-Situ Crosslinkable Hydrogel Based on Oxidized Pectin and Grafted Gelatin for Tissue Engineering Applications. *Colloids Surfaces B Biointerfaces* **2020**, 196 (August), 111347. <https://doi.org/10.1016/j.colsurfb.2020.111347>.
- (82) Memic, A.; Colombani, T.; Eggermont, L. J.; Rezaeeyazdi, M.; Steingold, J.; Rogers, Z. J.; Navare, K. J.; Mohammed, H. S.; Bencherif, S. A. Latest Advances in Cryogel Technology for Biomedical Applications. *Adv. Ther.* **2019**, 2 (4), 1800114. <https://doi.org/10.1002/adtp.201800114>.
- (83) Dainiak, M. B.; Allan, I. U.; Savina, I. N.; Cornelio, L.; James, E. S.; James, S. L.; Mikhalovsky, S. V.; Jungvid, H.; Galaev, I. Y. Gelatin-Fibrinogen Cryogel Dermal Matrices for Wound Repair: Preparation, Optimisation and in Vitro Study. *Biomaterials* **2010**, 31 (1), 67–76. <https://doi.org/10.1016/j.biomaterials.2009.09.029>.
- (84) Liu, W.; Li, Y.; Zeng, Y.; Zhang, X.; Wang, J.; Xie, L.; Li, X.; Du, Y. Microcryogels as Injectable 3-D Cellular Microniches for Site-Directed and Augmented Cell Delivery. *Acta Biomater.* **2014**, 10 (5), 1864–1875. <https://doi.org/10.1016/j.actbio.2013.12.008>.
- (85) Li, Y.; Liu, W.; Liu, F.; Zeng, Y.; Zuo, S.; Feng, S.; Qi, C.; Wang, B.; Yan, X.; Khademhosseini, A.; Bai, J.; Du, Y. Primed 3D Injectable Microniches Enabling Low-Dosage Cell Therapy for Critical Limb Ischemia. *Proc. Natl. Acad. Sci. U. S. A.* **2014**, 111 (37), 13511–13516. <https://doi.org/10.1073/pnas.1411295111>.
- (86) Qi, C.; Li, Y.; Badger, P.; Yu, H.; You, Z.; Yan, X.; Liu, W.; Shi, Y.; Xia, T.; Dong, J.; Huang, C.; Du, Y. Pathology-Targeted Cell Delivery via Injectable Micro-Scaffold Capsule Mediated by Endogenous TGase. *Biomaterials* **2017**, 126, 1–9. <https://doi.org/10.1016/j.biomaterials.2017.02.021>.
- (87) Bencherif, S. A.; Sands, R. W.; Bhatta, D.; Arany, P.; Verbeke, C. S.; Edwards, D. A.; Mooney, D. J. Injectable Preformed Scaffolds with Shape-Memory Properties. *Proc. Natl. Acad. Sci.* **2012**, 109 (48), 19590–19595. <https://doi.org/10.1073/pnas.1211516109>.
- (88) Baudron, V.; Gurikov, P.; Smirnova, I.; Whitehouse, S. Porous Starch Materials via Supercritical-and Freeze-Drying. *Gels* **2019**, 5 (1). <https://doi.org/10.3390/gels5010012>.
- (89) Newland, B.; Welzel, P. B.; Newland, H.; Renneberg, C.; Kolar, P.; Tsurkan, M.; Rosser, A.; Freudenberg,

- U.; Werner, C. Tackling Cell Transplantation Anoikis: An Injectable, Shape Memory Cryogel Microcarrier Platform Material for Stem Cell and Neuronal Cell Growth. *Small* **2015**, *11* (38), 5047–5053. <https://doi.org/10.1002/smll.201500898>.
- (90) Hwang, Y.; Zhang, C.; Varghese, S. Poly(Ethylene Glycol) Cryogels as Potential Cell Scaffolds: Effect of Polymerization Conditions on Cryogel Microstructure and Properties. *J. Mater. Chem.* **2010**, *20* (2), 345–351. <https://doi.org/10.1039/b917142h>.
- (91) Van Rie, J.; Declercq, H.; Van Hoorick, J.; Dierick, M.; Van Hoorebeke, L.; Cornelissen, R.; Thienpont, H.; Dubruel, P.; Van Vlierberghe, S. Cryogel-PCL Combination Scaffolds for Bone Tissue Repair. *J. Mater. Sci. Mater. Med.* **2015**, *26* (3). <https://doi.org/10.1007/s10856-015-5465-8>.
- (92) Kim, I.; Lee, S. S.; Bae, S.; Lee, H.; Hwang, N. S. Heparin Functionalized Injectable Cryogel with Rapid Shape-Recovery Property for Neovascularization. *Biomacromolecules* **2018**, *19* (6), 2257–2269. <https://doi.org/10.1021/acs.biomac.8b00331>.
- (93) Bédurier, A.; Piacentini, N.; Aeberli, L.; Da Silva, A.; Verheyen, C. A.; Bonini, F.; Rochat, A.; Filippova, A.; Serex, L.; Renaud, P.; Braschler, T. Additive Manufacturing of Hierarchical Injectable Scaffolds for Tissue Engineering. *Acta Biomater.* **2018**, *76*, 71–79. <https://doi.org/10.1016/j.actbio.2018.05.056>.
- (94) Serex, L.; Braschler, T.; Filippova, A.; Rochat, A.; Bédurier, A.; Bertsch, A.; Renaud, P. Pore Size Manipulation in 3D Printed Cryogels Enables Selective Cell Seeding. *Adv. Mater. Technol.* **2018**, *3* (4), 1–8. <https://doi.org/10.1002/admt.201700340>.
- (95) Bédurier, A.; Braschler, T.; Peric, O.; Fantner, G. E.; Mosser, S.; Fraering, P. C.; Benchérif, S.; Mooney, D. J.; Renaud, P. A Compressible Scaffold for Minimally Invasive Delivery of Large Intact Neuronal Networks. *Adv. Healthc. Mater.* **2015**, *4* (2), 301–312. <https://doi.org/10.1002/adhm.201400250>.
- (96) Aldemir Dikici, B.; Claeysens, F. Basic Principles of Emulsion Templating and Its Use as an Emerging Manufacturing Method of Tissue Engineering Scaffolds. *Front. Bioeng. Biotechnol.* **2020**, *8* (August). <https://doi.org/10.3389/fbioe.2020.00875>.
- (97) Kramer, S.; Cameron, N. R.; Krajnc, P. Porous Polymers from High Internal Phase Emulsions as Scaffolds for Biological Applications. *Polymers (Basel)*. **2021**, *13* (11), 1–24. <https://doi.org/10.3390/polym13111786>.
- (98) Oh, B. H. L.; Bismarck, A.; Chan-Park, M. B. Injectable, Interconnected, High-Porosity Macroporous Biocompatible Gelatin Scaffolds Made by Surfactant-Free Emulsion Templating. *Macromol. Rapid Commun.* **2015**, *36* (4), 364–372. <https://doi.org/10.1002/marc.201400524>.
- (99) Zhou, S.; Bismarck, A.; Steinke, J. H. G. Ion-Responsive Alginate Based Macroporous Injectable Hydrogel Scaffolds Prepared by Emulsion Templating. *J. Mater. Chem. B* **2013**, *1* (37), 4736–4745. <https://doi.org/10.1039/c3tb20888e>.
- (100) Young, S. A.; Riahinezhad, H.; Amsden, B. G. In Situ -Forming, Mechanically Resilient Hydrogels for Cell Delivery. *J. Mater. Chem. B* **2019**, *7* (38), 5742–5761. <https://doi.org/10.1039/c9tb01398a>.
- (101) Yun, E. J.; Yon, B.; Joo, M. K.; Jeong, B. Cell Therapy for Skin Wound Using Fibroblast Encapsulated Poly(Ethylene Glycol)-Poly(L-Alanine) Thermogel. *Biomacromolecules* **2012**, *13* (4), 1106–1111. <https://doi.org/10.1021/bm2018596>.
- (102) Tong, X.; Yang, F. Recent Progress in Developing Injectable Matrices for Enhancing Cell Delivery and Tissue Regeneration. *Adv. Healthc. Mater.* **2017**, *1701065*, 1–16. <https://doi.org/10.1002/adhm.201701065>.
- (103) Yan, S.; Zhang, X.; Zhang, K.; Di, H.; Feng, L.; Li, G.; Fang, J.; Cui, L.; Chen, X.; Yin, J. Injectable in Situ Forming Poly(L-Glutamic Acid) Hydrogels for Cartilage Tissue Engineering. *J. Mater. Chem. B* **2016**, *4* (5), 947–961. <https://doi.org/10.1039/c5tb01488c>.
- (104) Li, T.; Song, X.; Weng, C.; Wang, X.; Sun, L.; Gong, X.; Yang, L.; Chen, C. Self-Crosslinking and Injectable Chondroitin Sulfate/Pullulan Hydrogel for Cartilage Tissue Engineering. *Appl. Mater. Today* **2018**, *10*, 173–183. <https://doi.org/10.1016/j.apmt.2017.12.002>.
- (105) Lü, S.; Li, B.; Ni, B.; Sun, Z.; Liu, M.; Wang, Q. Thermoresponsive Injectable Hydrogel for Three-Dimensional Cell Culture: Chondroitin Sulfate Bioconjugated with Poly(N-Isopropylacrylamide) Synthesized by RAFT Polymerization. *Soft Matter* **2011**, *7* (22), 10763–10772. <https://doi.org/10.1039/c1sm06053h>.
- (106) Yeon, B.; Park, M. H.; Moon, H. J.; Kim, S. J.; Cheon, Y. W.; Jeong, B. 3D Culture of Adipose-Tissue-

- Derived Stem Cells Mainly Leads to Chondrogenesis in Poly(Ethylene Glycol)-Poly(L-Alanine) Diblock Copolymer Thermogel. *Biomacromolecules* **2013**, *14* (9), 3256–3266. <https://doi.org/10.1021/bm400868j>.
- (107) Dong, R.; Zhao, X.; Guo, B.; Ma, P. X. Self-Healing Conductive Injectable Hydrogels with Antibacterial Activity as Cell Delivery Carrier for Cardiac Cell Therapy. *ACS Appl. Mater. Interfaces* **2016**, *8* (27), 17138–17150. <https://doi.org/10.1021/acsami.6b04911>.
- (108) Han, S. S.; Yoon, H. Y.; Yhee, J. Y.; Cho, M. O.; Shim, H. E.; Jeong, J. E.; Lee, D. E.; Kim, K.; Guim, H.; Lee, J. H.; Huh, K. M.; Kang, S. W. In Situ Cross-Linkable Hyaluronic Acid Hydrogels Using Copper Free Click Chemistry for Cartilage Tissue Engineering. *Polym. Chem.* **2018**, *9* (1), 20–27. <https://doi.org/10.1039/c7py01654a>.
- (109) Pupkaite, J.; Rosenquist, J.; Hilborn, J.; Samanta, A. Injectable Shape-Holding Collagen Hydrogel for Cell Encapsulation and Delivery Cross-Linked Using Thiol-Michael Addition Click Reaction. *Biomacromolecules* **2019**, *20* (9), 3475–3484. <https://doi.org/10.1021/acs.biomac.9b00769>.
- (110) Zou, Y.; Zhang, L.; Yang, L.; Zhu, F.; Ding, M.; Lin, F.; Wang, Z.; Li, Y. “Click” Chemistry in Polymeric Scaffolds: Bioactive Materials for Tissue Engineering. *J. Control. Release* **2018**, *273* (January), 160–179. <https://doi.org/10.1016/j.jconrel.2018.01.023>.
- (111) Wang, J.; He, H.; Cooper, R.; Yang, H.; Engineering, L. S.; States, U.; States, U.; States, U. In Situ-Forming Polyamidoamine Dendrimer Hydrogels with Tunable Properties Prepared via Aza-Michael Addition Reaction. *ACS Appl Mater Interfaces* **2017**, *9* (12), 10494–10503. <https://doi.org/10.1021/acsami.7b00221>.
- (112) Li, X.; Tian, T. Phytochemical Characterization of *Mentha Spicata* L. Under Differential Dried-Conditions and Associated Nephrotoxicity Screening of Main Compound With Organ-on-a-Chip. *Front. Pharmacol.* **2018**, *9* (September), 1–10. <https://doi.org/10.3389/fphar.2018.01067>.
- (113) Neves, L. S.; Babo, P. S.; Gonçalves, A. I.; Costa-Almeida, R.; Caridade, S. G.; Mano, J. F.; Domingues, R. M. A.; Rodrigues, M. T.; Reis, R. L.; Gomes, M. E. Injectable Hyaluronic Acid Hydrogels Enriched with Platelet Lysate as a Cryostable Off-the-Shelf System for Cell-Based Therapies. *Regen. Eng. Transl. Med.* **2017**, *3* (2), 53–69. <https://doi.org/10.1007/s40883-017-0029-8>.
- (114) Jeon, O.; Powell, C.; Ahmed, S. M.; Alsberg, E. Biodegradable, Photocrosslinked Alginate Hydrogels with Independently Tailorable Physical Properties and Cell Adhesivity. *Tissue Eng. Part A* **2010**, *16* (9), 2915–2925. <https://doi.org/10.1089/ten.tea.2010.0096>.
- (115) Kumar, D.; Lyness, A.; Gerges, I.; Lenardi, C.; Forsyth, N. R.; Liu, Y. Stem Cell Delivery with Polymer Hydrogel for Treatment of Intervertebral Disc Degeneration: From 3D Culture to Design of the Delivery Device for Minimally Invasive Therapy. *Cell Transplant.* **2016**, *25* (12), 2213–2220. <https://doi.org/10.3727/096368916X692618>.
- (116) Barati, D.; Kader, S.; Pajoum Shariati, S. R.; Moeinzadeh, S.; Sawyer, R. H.; Jabbari, E. Synthesis and Characterization of Photo-Cross-Linkable Keratin Hydrogels for Stem Cell Encapsulation. *Biomacromolecules* **2017**, *18* (2), 398–412. <https://doi.org/10.1021/acs.biomac.6b01493>.
- (117) Schoof, H.; Apel, J.; Heschel, I.; Rau, G. Control of Pore Structure and Size in Freeze-Dried Collagen Sponges. *J. Biomed. Mater. Res.* **2001**, *58* (4), 352–357. <https://doi.org/10.1002/jbm.1028>.
- (118) Xia, P.; Zhang, K.; Gong, Y.; Li, G.; Yan, S.; Yin, J. Injectable Stem Cell Laden Open Porous Microgels That Favor Adipogenesis: In Vitro and in Vivo Evaluation. *ACS Appl. Mater. Interfaces* **2017**, *9* (40), 34751–34761. <https://doi.org/10.1021/acsami.7b13065>.
- (119) Fraylich, M. R.; Liu, R.; Richardson, S. M.; Baird, P.; Hoyland, J.; Freemont, A. J.; Alexander, C.; Shakesheff, K.; Cellesi, F.; Saunders, B. R. Thermally-Triggered Gelation of PLGA Dispersions: Towards an Injectable Colloidal Cell Delivery System. *J. Colloid Interface Sci.* **2010**, *344* (1), 61–69. <https://doi.org/10.1016/j.jcis.2009.12.030>.
- (120) Oyama, N.; Minami, H.; Kawano, D.; Miyazaki, M.; Maeda, T.; Toma, K.; Hotta, A.; Nagahama, K. A Nanocomposite Approach to Develop Biodegradable Thermogels Exhibiting Excellent Cell-Compatibility for Injectable Cell Delivery. *Biomater. Sci.* **2014**, *2* (8), 1057–1062. <https://doi.org/10.1039/c4bm00074a>.
- (121) Park, K. H.; Na, K.; Sung, W. K.; Sung, Y. J.; Kyu, H. P.; Chung, H. M. Phenotype of Hepatocyte Spheroids Behavior within Thermo-Sensitive Poly(NiPAAm-Co-PEG-g-GRGDS) Hydrogel as a Cell Delivery Vehicle. *Biotechnol. Lett.* **2005**, *27* (15), 1081–1086. <https://doi.org/10.1007/s10529-005-8453-0>.

- (122) Thorpe, A. A.; Dougill, G.; Vickers, L.; Reeves, N. D.; Sammon, C.; Cooper, G.; Le Maitre, C. L. Thermally Triggered Hydrogel Injection into Bovine Intervertebral Disc Tissue Explants Induces Differentiation of Mesenchymal Stem Cells and Restores Mechanical Function. *Acta Biomater.* **2017**, *54*, 212–226. <https://doi.org/10.1016/j.actbio.2017.03.010>.
- (123) Frith, J. E.; Cameron, A. R.; Menzies, D. J.; Ghosh, P.; Whitehead, D. L.; Gronthos, S.; Zannettino, A. C. W.; Cooper-White, J. J. An Injectable Hydrogel Incorporating Mesenchymal Precursor Cells and Pentosan Polysulphate for Intervertebral Disc Regeneration. *Biomaterials* **2013**, *34* (37), 9430–9440. <https://doi.org/10.1016/j.biomaterials.2013.08.072>.
- (124) Yin, H.; Yan, Z.; Bauer, R. J.; Peng, J.; Schieker, M.; Nerlich, M. Functionalized Thermosensitive Hydrogel Combined with Tendon Stem / Progenitor Cells as Injectable Cell Delivery Carrier for Tendon Tissue Engineering Functionalized Thermosensitive Hydrogel Combined with Tendon Stem / Progenitor Cells as Injectable Cell. *Biomed. Mater.* **2018**, *13* (3), 034107. <https://doi.org/10.1088/1748-605X/aaadd1>.
- (125) Liu, H.; Cheng, Y.; Chen, J.; Chang, F.; Wang, J.; Ding, J.; Chen, X. Component Effect of Stem Cell-Loaded Thermosensitive Polypeptide Hydrogels on Cartilage Repair. *Acta Biomater.* **2018**, *73*, 103–111. <https://doi.org/10.1016/j.actbio.2018.04.035>.
- (126) Fitzpatrick, S.; Sheardown, H.; Liu, L. PNIPAAm-Grafted-Collagen as an Injectable, in Situ Gelling Cell Delivery Scaffold. *8th World Biomater. Congr. 2008* **2008**, *3*, 1314.
- (127) Liu, H.; Liu, J.; Qi, C.; Fang, Y.; Zhang, L.; Zhuo, R.; Jiang, X. Thermosensitive Injectable In-Situ Forming Carboxymethyl Chitin Hydrogel for Three-Dimensional Cell Culture. *Acta Biomater.* **2016**, *35*, 228–237. <https://doi.org/10.1016/j.actbio.2016.02.028>.
- (128) Dang, L. H.; Doan, P.; Nhi, T. T. Y.; Nguyen, D. T.; Nguyen, B. T.; Nguyen, T. P.; Tran, N. Q. Multifunctional Injectable Pluronic-Cystamine-Alginate-Based Hydrogel as a Novel Cellular Delivery System towards Tissue Regeneration. *Int. J. Biol. Macromol.* **2021**, *185* (June), 592–603. <https://doi.org/10.1016/j.ijbiomac.2021.06.183>.
- (129) Chenite, A.; Chaput, C.; Wang, D.; Combes, C.; Buschmann, M. D.; Hoemann, C. D.; Leroux, J. C.; Atkinson, B. L.; Binette, F.; Selmani, A. Novel Injectable Neutral Solutions of Chitosan Form Biodegradable Gels in Situ. *Biomaterials* **2000**, *21* (21), 2155–2161. [https://doi.org/10.1016/S0142-9612\(00\)00116-2](https://doi.org/10.1016/S0142-9612(00)00116-2).
- (130) Riley, L.; Schirmer, L.; Segura, T. Granular Hydrogels: Emergent Properties of Jammed Hydrogel Microparticles and Their Applications in Tissue Repair and Regeneration. *Curr. Opin. Biotechnol.* **2019**, *60*, 1–8. <https://doi.org/10.1016/j.copbio.2018.11.001>.
- (131) Cai, B.; Zou, Q.; Zuo, Y.; Mei, Q.; Ma, J.; Lin, L.; Chen, L.; Li, Y. Injectable Gel Constructs with Regenerative and Anti-Infective Dual Effects Based on Assembled Chitosan Microspheres. *ACS Appl. Mater. Interfaces* **2018**, *10* (30), 25099–25112. <https://doi.org/10.1021/acsami.8b06648>.
- (132) Qutachi, O.; Vetsch, J. R.; Gill, D.; Cox, H.; Scurr, D. J.; Hofmann, S.; Müller, R.; Quirk, R. A.; Shakesheff, K. M.; Rahman, C. V. Injectable and Porous PLGA Microspheres That Form Highly Porous Scaffolds at Body Temperature. *Acta Biomater.* **2014**, *10* (12), 5090–5098. <https://doi.org/10.1016/j.actbio.2014.08.015>.
- (133) Griffin, D. R.; Weaver, W. M.; Scumpia, P.; Carlo, D. Di. Accelerated Wound Healing by Injectable Microporous Gel Scaffolds Assembled from Annealed Building Blocks. *Nat Mater* **2016**, *14* (7), 737–744. <https://doi.org/10.1038/nmat4294>. Accelerated.
- (134) Koh, J.; Griffin, D. R.; Archang, M. M.; Feng, A. C.; Horn, T.; Margolis, M.; Zalazar, D.; Segura, T.; Scumpia, P. O.; Di Carlo, D. Enhanced In Vivo Delivery of Stem Cells Using Microporous Annealed Particle Scaffolds. *Small* **2019**, *15* (39), 1–10. <https://doi.org/10.1002/sml.201903147>.
- (135) Darling, N. J.; Sideris, E.; Hamada, N.; Carmichael, S. T.; Segura, T. Injectable and Spatially Patterned Microporous Annealed Particle (MAP) Hydrogels for Tissue Repair Applications. *Adv. Sci.* **2018**, *5* (11), 1–8. <https://doi.org/10.1002/adv.201801046>.
- (136) Nih, L. R.; Sideris, E.; Carmichael, S. T.; Segura, T. Injection of Microporous Annealing Particle (MAP) Hydrogels in the Stroke Cavity Reduces Gliosis and Inflammation and Promotes NPC Migration to the Lesion. *Adv. Mater.* **2017**, *29* (32), 1–8. <https://doi.org/10.1002/adma.201606471>.
- (137) Griffin, D. R.; Weaver, W. M.; Scumpia, P. O.; Di Carlo, D.; Segura, T. Accelerated Wound Healing by Injectable Microporous Gel Scaffolds Assembled from Annealed Building Blocks. *Nat. Mater.* **2015**, *14* (7), 737–744. <https://doi.org/10.1038/nmat4294>.

- (138) Sideris, E.; Griffin, D. R.; Ding, Y.; Li, S.; Weaver, W. M.; Di Carlo, D.; Hsiai, T.; Segura, T. Particle Hydrogels Based on Hyaluronic Acid Building Blocks. *ACS Biomater. Sci. Eng.* **2016**, *2* (11), 2034–2041. <https://doi.org/10.1021/acsbiomaterials.6b00444>.
- (139) Caldwell, A. S.; Campbell, G. T.; Shekiri, K. M. T.; Anseth, K. S. Clickable Microgel Scaffolds as Platforms for 3D Cell Encapsulation. *Adv. Healthc. Mater.* **2017**, *6* (15), 1–8. <https://doi.org/10.1002/adhm.201700254>.
- (140) Cruz, D. I.; J, G.; M, R.; Sanchez, M.; Reis, R. L.; Mano, J. F. Chitosan Microparticles as Injectable Scaffolds for Tissue Engineering. *J. Tissue Eng. Regen. Med.* **2008**, *2*, 378–38°. <https://doi.org/10.1002/term>.
- (141) Custódio, C. A.; Santo, V. E.; Oliveira, M. B.; Gomes, M. E.; Reis, R. L.; Mano, J. F. Functionalized Microparticles Producing Scaffolds in Combination with Cells. *Adv. Funct. Mater.* **2014**, *24* (10), 1391–1400. <https://doi.org/10.1002/adfm.201301516>.
- (142) Leferink, A.; Schipper, D.; Arts, E.; Vrij, E.; Rivron, N.; Karperien, M.; Mittmann, K.; Van Blitterswijk, C.; Moroni, L.; Truckenmüller, R. Engineered Micro-Objects as Scaffolding Elements in Cellular Building Blocks for Bottom-up Tissue Engineering Approaches. *Adv. Mater.* **2014**, *26* (16), 2592–2599. <https://doi.org/10.1002/adma.201304539>.
- (143) Han, L. H.; Yu, S.; Wang, T.; Behn, A. W.; Yang, F. Microribbon-like Elastomers for Fabricating Macroporous and Highly Flexible Scaffolds That Support Cell Proliferation in 3D. *Adv. Funct. Mater.* **2013**, *23* (3), 346–358. <https://doi.org/10.1002/adfm.201201212>.
- (144) Conrad, B.; Han, L. H.; Yang, F. Gelatin-Based Microribbon Hydrogels Accelerate Cartilage Formation by Mesenchymal Stem Cells in Three Dimensions. *Tissue Eng. - Part A* **2018**, *24* (21–22), 1631–1640. <https://doi.org/10.1089/ten.tea.2018.0011>.
- (145) Gegg, C.; Yang, F. Spatially Patterned Microribbon-Based Hydrogels Induce Zonally-Organized Cartilage Regeneration by Stem Cells in 3D. *Acta Biomater.* **2020**, *101*, 196–205. <https://doi.org/10.1016/j.actbio.2019.10.025>.
- (146) Rogan, H.; Ilagan, F.; Tong, X.; Chu, C. R.; Yang, F. Microribbon-Hydrogel Composite Scaffold Accelerates Cartilage Regeneration in Vivo with Enhanced Mechanical Properties Using Mixed Stem Cells and Chondrocytes. *Biomaterials* **2020**, *228* (May 2019), 119579. <https://doi.org/10.1016/j.biomaterials.2019.119579>.
- (147) Conrad, B.; Hayashi, C.; Yang, F. Gelatin-Based Microribbon Hydrogels Support Robust MSC Osteogenesis across a Broad Range of Stiffness. *ACS Biomater. Sci. Eng.* **2020**, *6* (6), 3454–3463. <https://doi.org/10.1021/acsbiomaterials.9b01792>.
- (148) Han, L. H.; Tong, X.; Yang, F. Photo-Crosslinkable PEG-Based Microribbons for Forming 3D Macroporous Scaffolds with Decoupled Niche Properties. *Adv. Mater.* **2014**, *26* (11), 1757–1762. <https://doi.org/10.1002/adma.201304805>.
- (149) Barati, D.; Watkins, K.; Wang, Z.; Yang, F. Injectable and Crosslinkable PLGA-Based Microribbons as 3D Macroporous Stem Cell Niche. **2020**, *1905820*, 1–8. <https://doi.org/10.1002/smll.201905820>.
- (150) Salehi, S.; Ostrovidov, S.; Ebrahimi, M.; Sadeghian, R. B.; Liang, X.; Nakajima, K.; Bae, H.; Fujie, T.; Khademhosseini, A. Development of Flexible Cell-Loaded Ultrathin Ribbons for Minimally Invasive Delivery of Skeletal Muscle Cells. *ACS Biomater. Sci. Eng.* **2017**, *3* (4), 579–589. <https://doi.org/10.1021/acsbiomaterials.6b00696>.
- (151) Huebsch, N.; Lippens, E.; Lee, K.; Mehta, M.; Sandeep, T.; Jak-gu, D. Matrix Elasticity of Void-Forming Hydrogels Controls Transplanted Stem Cell-Mediated Bone Formation. *Nat. Mater.* **2016**, *14* (12), 1269–1277. <https://doi.org/10.1038/nmat4407>.Matrix.
- (152) Sokic, S.; Christenson, M.; Larson, J.; Papavasiliou, G. In Situ Generation of Cell-Laden Porous MMP-Sensitive PEGDA Hydrogels by Gelatin Leaching. *Macromol. Biosci.* **2014**, *14* (5), 731–739. <https://doi.org/10.1002/mabi.201300406>.
- (153) Hammer, J.; Han, L. H.; Tong, X.; Yang, F. A Facile Method to Fabricate Hydrogels with Microchannel-like Porosity for Tissue Engineering. *Tissue Eng. - Part C Methods* **2014**, *20* (2), 169–176. <https://doi.org/10.1089/ten.tec.2013.0176>.
- (154) Liu, J.; Xu, H. H. K.; Zhou, H.; Weir, M. D.; Chen, Q.; Trotman, C. A. Human Umbilical Cord Stem Cell Encapsulation in Novel Macroporous and Injectable Fibrin for Muscle Tissue Engineering. *Acta Biomater.*

- 2013, 9 (1), 4688–4697. <https://doi.org/10.1016/j.actbio.2012.08.009>.
- (155) Han, L. H.; Lai, J. H.; Yu, S.; Yang, F. Dynamic Tissue Engineering Scaffolds with Stimuli-Responsive Macroporosity Formation. *Biomaterials* **2013**, *34* (17), 4251–4258. <https://doi.org/10.1016/j.biomaterials.2013.02.051>.
- (156) Hwang, C. M.; Sant, S.; Masaali, M.; Kachouie, N. N.; Zamanian, B.; Lee, S. H.; Khademhosseini, A. Fabrication of Three-Dimensional Porous Cell-Laden Hydrogel for Tissue Engineering. *Biofabrication* **2010**, *2* (3). <https://doi.org/10.1088/1758-5082/2/3/035003>.
- (157) Wang, K.; Nune, K. C.; Misra, R. D. K. The Functional Response of Alginate-Gelatin-Nanocrystalline Cellulose Injectable Hydrogels toward Delivery of Cells and Bioactive Molecules. *Acta Biomater.* **2016**, *36*, 143–151. <https://doi.org/10.1016/j.actbio.2016.03.016>.
- (158) Monette, A.; Ceccaldi, C.; Assaad, E.; Lerouge, S.; Lapointe, R. Chitosan Thermogels for Local Expansion and Delivery of Tumor-Specific T Lymphocytes towards Enhanced Cancer Immunotherapies. *Biomaterials* **2016**, *75*, 237–249. <https://doi.org/10.1016/j.biomaterials.2015.10.021>.
- (159) Tang, Y.; Lin, S.; Yin, S.; Jiang, F.; Zhou, M.; Yang, G.; Sun, N.; Zhang, W.; Jiang, X. In Situ Gas Foaming Based on Magnesium Particle Degradation: A Novel Approach to Fabricate Injectable Macroporous Hydrogels. *Biomaterials* **2020**, *232* (August 2019), 119727. <https://doi.org/10.1016/j.biomaterials.2019.119727>.
- (160) Wang, L.; Deng, F.; Wang, W.; Li, A.; Lu, C.; Chen, H.; Wu, G.; Nan, K.; Li, L. Construction of Injectable Self-Healing Macroporous Hydrogels via a Template-Free Method for Tissue Engineering and Drug Delivery. *ACS Appl. Mater. Interfaces* **2018**, *10* (43), 36721–36732. <https://doi.org/10.1021/acsami.8b13077>.
- (161) Zhang, H.; Yun, S.; Song, L.; Zhang, Y.; Zhao, Y. The Preparation and Characterization of Chitin and Chitosan under Large-Scale Submerged Fermentation Level Using Shrimp by-Products as Substrate. *Int. J. Biol. Macromol.* **2017**, *96*, 334–339. <https://doi.org/10.1016/j.ijbiomac.2016.12.017>.
- (162) Sivashankari, P. R.; Prabakaran, M. Deacetylation Modification Techniques of Chitin and Chitosan. *Chitosan Based Biomater.* **2017**, *1* (October 2020), 117–133. <https://doi.org/10.1016/B978-0-08-100230-8.00005-4>.
- (163) Kasaai, M. R. Various Methods for Determination of the Degree of N-Acetylation of Chitin and Chitosan: A Review. *J. Agric. Food Chem.* **2009**, *57* (5), 1667–1676. <https://doi.org/10.1021/jf803001m>.
- (164) Lavertu, M.; Xia, Z.; Serreqi, A. N.; Berrada, M.; Rodrigues, A.; Wang, D.; Buschmann, M. D.; Gupta, A. A Validated ¹H NMR Method for the Determination of the Degree of Deacetylation of Chitosan. *J. Pharm. Biomed. Anal.* **2003**, *32* (6), 1149–1158. [https://doi.org/10.1016/S0731-7085\(03\)00155-9](https://doi.org/10.1016/S0731-7085(03)00155-9).
- (165) Yun Yang, B.; Montgomery, R. Degree of Acetylation of Heteropolysaccharides. *Carbohydr. Res.* **1999**, *323* (1–4), 156–162. [https://doi.org/10.1016/S0008-6215\(99\)00242-6](https://doi.org/10.1016/S0008-6215(99)00242-6).
- (166) Kasaai, M. R. Determination of the Degree of N-Acetylation for Chitin and Chitosan by Various NMR Spectroscopy Techniques: A Review. *Carbohydr. Polym.* **2010**, *79* (4), 801–810. <https://doi.org/10.1016/j.carbpol.2009.10.051>.
- (167) Dahmane, E. M.; Taourirte, M.; Eladlani, N.; Rhazi, M. Extraction and Characterization of Chitin and Chitosan from *Parapenaeus Longirostris* from Moroccan Local Sources. *Int. J. Polym. Anal. Charact.* **2014**, *19* (4), 342–351. <https://doi.org/10.1080/1023666X.2014.902577>.
- (168) Brugnerotto, J.; Lizardi, J.; Goycoolea, F. M.; Argüelles-Monal, W.; Desbrières, J.; Rinaudo, M. An Infrared Investigation in Relation with Chitin and Chitosan Characterization. *Polymer (Guildf).* **2001**, *42* (8), 3569–3580. [https://doi.org/10.1016/S0032-3861\(00\)00713-8](https://doi.org/10.1016/S0032-3861(00)00713-8).
- (169) Duarte, M. L.; Ferreira, M. C.; Marvão, M. R.; Rocha, J. An Optimised Method to Determine the Degree of Acetylation of Chitin and Chitosan by FTIR Spectroscopy. *Int. J. Biol. Macromol.* **2002**, *31* (1–3), 1–8. [https://doi.org/10.1016/S0141-8130\(02\)00039-9](https://doi.org/10.1016/S0141-8130(02)00039-9).
- (170) Kasaai, M. R. A Review of Several Reported Procedures to Determine the Degree of N-Acetylation for Chitin and Chitosan Using Infrared Spectroscopy. *Carbohydr. Polym.* **2008**, *71* (4), 497–508. <https://doi.org/10.1016/j.carbpol.2007.07.009>.
- (171) Cartier, N.; Domard, A.; Chanzy, H. Single Crystals of Chitosan. *Int. J. Biol. Macromol.* **1990**, *12* (5), 289–294. [https://doi.org/10.1016/0141-8130\(90\)90015-3](https://doi.org/10.1016/0141-8130(90)90015-3).

- (172) Ogawa, K.; Yui, T. Crystallinity of Partially N-Acetylated Chitosans. *Biosci. Biotechnol. Biochem.* **1993**, *57* (9), 1466–1469. <https://doi.org/10.1271/bbb.57.1466>.
- (173) Ioelovich, M. Research and Reviews : Journal of Chemistry Crystallinity and Hydrophilicity of Chitin and Chitosan. **2014**, *3* (3), 7–14.
- (174) Facchinatto, W. M.; Santos, D. M. dos; Fiamingo, A.; Bernardes-Filho, R.; Campana-Filho, S. P.; Azevedo, E. R. de; Colnago, L. A. Evaluation of Chitosan Crystallinity: A High-Resolution Solid-State NMR Spectroscopy Approach. *Carbohydr. Polym.* **2020**, *250* (June). <https://doi.org/10.1016/j.carbpol.2020.116891>.
- (175) Ogawa, K. Effect of Heating an Aqueous Suspension of Chitosan on the Crystallinity and Polymorphs. *Agric. Biol. Chem.* **1991**, *55* (9), 2375–2379. <https://doi.org/10.1080/00021369.1991.10870939>.
- (176) Baklagina, Y. G.; Klechkovskaya, V. V.; Kononova, S. V.; Petrova, V. A.; Poshina, D. N.; Orekhov, A. S.; Skorik, Y. A. Polymorphic Modifications of Chitosan. *Crystallogr. Reports* **2018**, *63* (3), 303–313. <https://doi.org/10.1134/S1063774518030033>.
- (177) Roy, J. C.; Salaün, F.; Giraud, S.; Ferri, A.; Guoqiang, C.; Guan, J. Solubility of Chitin: Solvents, Solution Behaviors and Their Related Mechanisms. In *Intech*; 2016; Vol. 7, pp 110–127.
- (178) Rinaudo, M. Chitin and Chitosan: Properties and Applications. *Prog. Polym. Sci.* **2006**, *31* (7), 603–632. <https://doi.org/10.1016/j.progpolymsci.2006.06.001>.
- (179) Gardner, K. H.; Blackwell, J. Refinement of the Structure of B-Chitin. **1975**, *14*, 1581–1595.
- (180) Minke, R.; Blackwell, J. The Structure of α -Chitin. *J. Mol. Biol.* **1978**, *120* (2), 167–181. [https://doi.org/10.1016/0022-2836\(78\)90063-3](https://doi.org/10.1016/0022-2836(78)90063-3).
- (181) Okuyama, K.; Noguchi, K.; Miyazawa, T.; Yui, T.; Ogawa, K. *Molecular and Crystal Structure of Hydrated Chitosan*; 1997.
- (182) Jaworska, M.; Sakurai, K.; Gaudon, P.; Guibal, E. Influence of Chitosan Characteristics on Polymer Properties. I: Crystallographic Properties. *Polym. Int.* **2003**, *52* (2), 198–205. <https://doi.org/10.1002/pi.1159>.
- (183) Aranaz, I.; Mengibar, M.; Harris, R.; Panos, I.; Miralles, B.; Acosta, N.; Galed, G.; Heras, A. Functional Characterization of Chitin and Chitosan. *Curr. Chem. Biol.* **2009**, *3* (2), 203–230. <https://doi.org/10.2174/187231309788166415>.
- (184) Croisier, F.; Jérôme, C. Chitosan-Based Biomaterials for Tissue Engineering. *Eur. Polym. J.* **2013**, *49* (4), 780–792. <https://doi.org/10.1016/j.eurpolymj.2012.12.009>.
- (185) Rinaudo, M.; Pavlov, G.; Desbrières, J. Solubilization of Chitosan in Strong Acid Medium. *Int. J. Polym. Anal. Charact.* **1999**, *5* (3), 267–276. [https://doi.org/10.1016/0022-1759\(85\)90285-6](https://doi.org/10.1016/0022-1759(85)90285-6).
- (186) Rinaudo, M.; Pavlov, G.; Desbrie, J. Influence of Acetic Acid Concentration on the Solubilization of Chitosan. **1999**, *40*, 7029–7032.
- (187) Rinaudo, M.; Milas, M.; Dung, P. Le. Characterization of Chitosan. Influence of Ionic Strength and Degree of Acetylation on Chain Expansion. *Int. J. Biol. Macromol.* **1993**, *15* (5), 281–285. [https://doi.org/10.1016/0141-8130\(93\)90027-J](https://doi.org/10.1016/0141-8130(93)90027-J).
- (188) Kubota, N.; Eguchi, Y. Facile Preparation of Water-Soluble N-Acetylated Chitosan and Molecular Weight Dependence of Its Water-Solubility. *Polym. J.* **1997**, *29* (2), 123–127. <https://doi.org/10.1295/polymj.29.123>.
- (189) Philippova, O. E.; Korchagina, E. V.; Volkov, E. V.; Smirnov, V. A.; Khokhlov, A. R.; Rinaudo, M. Aggregation of Some Water-Soluble Derivatives of Chitin in Aqueous Solutions: Role of the Degree of Acetylation and Effect of Hydrogen Bond Breaker. *Carbohydr. Polym.* **2012**, *87* (1), 687–694. <https://doi.org/10.1016/j.carbpol.2011.08.043>.
- (190) Varum, K.; Ottøy, M.; Olav, S. Water-Solubility of Partially N-Acetylated Chitosans as a Function of PH: Effect of Chemical Water-Solubility of Partially N-Acetylated Chitosans as a Function of PH: Effect of Chemical Composition and Depolymerisation Chitosans as a Function of PH: Effec. *Carbohydr. Polym.* **1994**, *25*, 65–70. <https://doi.org/10.1109/ICEICE.2011.5778303>.
- (191) Ottøy, M. H.; Vårum, K. M.; Christensen, B. E.; Anthonsen, M. W.; Smidsrød, O. Preparative and Analytical Size-Exclusion Chromatography of Chitosans. *Carbohydr. Polym.* **1996**, *31* (4), 253–261.

[https://doi.org/10.1016/S0144-8617\(96\)00096-3](https://doi.org/10.1016/S0144-8617(96)00096-3).

- (192) Dash, M.; Chiellini, F.; Ottenbrite, R. M.; Chiellini, E. Chitosan - A Versatile Semi-Synthetic Polymer in Biomedical Applications. *Prog. Polym. Sci.* **2011**, *36* (8), 981–1014. <https://doi.org/10.1016/j.progpolymsci.2011.02.001>.
- (193) Janes, K. A.; Calvo, P.; Alonso, M. J. Polysaccharide Colloidal Particles as Delivery Systems for Macromolecules. *Adv. Drug Deliv. Rev.* **2001**, *47* (1), 83–97. [https://doi.org/10.1016/S0169-409X\(00\)00123-X](https://doi.org/10.1016/S0169-409X(00)00123-X).
- (194) Li, Y.; Chi, Y. Q.; Yu, C. H.; Xie, Y.; Xia, M. Y.; Zhang, C. L.; Han, X.; Peng, Q. Drug-Free and Non-Crosslinked Chitosan Scaffolds with Efficient Antibacterial Activity against Both Gram-Negative and Gram-Positive Bacteria. *Carbohydr. Polym.* **2020**, *241* (May), 116386. <https://doi.org/10.1016/j.carbpol.2020.116386>.
- (195) Yang, J.; Tian, F.; Wang, Z.; Wang, Q.; Zeng, Y.-J.; Chen, S.-Q. Effect of Chitosan Molecular Weight and Deacetylation Degree on Hemostasis. *J. Biomed. Res. Part B Appl. Biomater.* **2007**, 131–137. <https://doi.org/10.1002/jbmb>.
- (196) Di Martino, A.; Sittering, M.; Risbud, M. V. Chitosan: A Versatile Biopolymer for Orthopaedic Tissue-Engineering. *Biomaterials* **2005**, *26* (30), 5983–5990. <https://doi.org/10.1016/j.biomaterials.2005.03.016>.
- (197) Lončarević, A.; Ivanković, M.; Rogina, A. Lysozyme-Induced Degradation of Chitosan: The Characterisation of Degraded Chitosan Scaffolds. *J. Tissue Repair Regen.* **2017**, *1* (1), 12–22. <https://doi.org/10.14302/issn.2640-6403.jtrr-17-1840>.
- (198) Vårum, K. M.; Myhr, M. M.; Hjerde, R. J. N.; Smidsrød, O. In Vitro Degradation Rates of Partially N-Acetylated Chitosans in Human Serum. *Carbohydr. Res.* **1997**, *299* (1–2), 99–101. [https://doi.org/10.1016/S0008-6215\(96\)00332-1](https://doi.org/10.1016/S0008-6215(96)00332-1).
- (199) Vårum, K. M.; Myhr, M. M.; Hjerde, R. J. N.; Smidsrød, O. In Vitro Degradation Rates of Partially N-Acetylated Chitosans in Human Serum. *Carbohydr. Res.* **1997**, *299* (1–2), 99–101. [https://doi.org/10.1016/S0008-6215\(96\)00332-1](https://doi.org/10.1016/S0008-6215(96)00332-1).
- (200) Yang, Y. M.; Hu, W.; Wang, X. D.; Gu, X. S. The Controlling Biodegradation of Chitosan Fibers by N-Acetylation in Vitro and in Vivo. *J. Mater. Sci. Mater. Med.* **2007**, *18* (11), 2117–2121. <https://doi.org/10.1007/s10856-007-3013-x>.
- (201) Hirano, S.; Tsuchida, H.; Nagao, N. N-Acetylation in Chitosan and the Rate of Its Enzymic Hydrolysis. *Biomaterials* **1989**, *10* (8), 574–576. [https://doi.org/10.1016/0142-9612\(89\)90066-5](https://doi.org/10.1016/0142-9612(89)90066-5).
- (202) Kean, T.; Thanou, M. Biodegradation, Biodistribution and Toxicity of Chitosan. *Adv. Drug Deliv. Rev.* **2010**, *62* (1), 3–11. <https://doi.org/10.1016/j.addr.2009.09.004>.
- (203) Varum, K. M.; Ottoy, M. H.; Smidsrod, O. Acid Hydrolysis of Chitosans. *Carbohydr. Polym.* **2001**, *46* (1), 89–98. [https://doi.org/10.1016/S0144-8617\(00\)00288-5](https://doi.org/10.1016/S0144-8617(00)00288-5).
- (204) Sikorski, D.; Gzyra-Jagiela, K.; Draczyński, Z. The Kinetics of Chitosan Degradation in Organic Acid Solutions. *Mar. Drugs* **2021**, *19* (5), 1–17. <https://doi.org/10.3390/md19050236>.
- (205) Varum, K. M.; Ottoy, M. H.; Smidsrod, O. Acid Hydrolysis of Chitosans. *Carbohydr. Polym.* **2001**, *46* (1), 89–98. [https://doi.org/10.1016/S0144-8617\(00\)00288-5](https://doi.org/10.1016/S0144-8617(00)00288-5).
- (206) Rodríguez-Vázquez, M.; Vega-Ruiz, B.; Ramos-Zúñiga, R.; Saldaña-Koppel, D. A.; Quiñones-Olvera, L. F. Chitosan and Its Potential Use as a Scaffold for Tissue Engineering in Regenerative Medicine. *Biomed Res. Int.* **2015**, *2015*. <https://doi.org/10.1155/2015/821279>.
- (207) Chatelet, C.; Damour, O.; Domard, a. Influence of the Degree of Acetylation on Some Biological Properties of Chitosan Films. *Biomaterials* **2001**, *22* (3), 261–268. [https://doi.org/10.1016/S0142-9612\(00\)00183-6](https://doi.org/10.1016/S0142-9612(00)00183-6).
- (208) Riva, R.; Ragelle, H.; Des Rieux, A.; Duhem, N.; Jérôme, C.; Prétat, V. Chitosan and Chitosan Derivatives in Drug Delivery and Tissue Engineering. *Adv. Polym. Sci.* **2011**, *244* (1), 19–44. https://doi.org/10.1007/12_2011_137.
- (209) Saravanan, S.; Vimalraj, S.; Thanikaivelan, P.; Banudevi, S.; Manivasagam, G. A Review on Injectable Chitosan/Beta Glycerophosphate Hydrogels for Bone Tissue Regeneration. *Int. J. Biol. Macromol.* **2019**, *121*, 38–54. <https://doi.org/10.1016/j.ijbiomac.2018.10.014>.

- (210) Jiang, T.; James, R.; Kumbar, S. G.; Laurencin, C. T. *Chitosan as a Biomaterial: Structure, Properties, and Applications in Tissue Engineering and Drug Delivery*, 1st ed.; Elsevier Inc., 2014. <https://doi.org/10.1016/B978-0-12-396983-5.00005-3>.
- (211) Mekhail, M.; Tabrizian, M. Injectable Chitosan-Based Scaffolds in Regenerative Medicine and Their Clinical Translatability. *Adv. Healthc. Mater.* **2014**, *3* (10), 1529–1545. <https://doi.org/10.1002/adhm.201300586>.
- (212) Chenite, A.; Buschmann, M.; Wang, D.; Chaput, C.; Kandani, N. Rheological Characterisation of Thermogelling Chitosan/Glycerol-Phosphate Solutions. *Carbohydr. Polym.* **2001**, *46*, 39–47.
- (213) Zhou, H. Y.; Jiang, L. J.; Cao, P. P.; Li, J. B.; Chen, X. G. Glycerophosphate-Based Chitosan Thermosensitive Hydrogels and Their Biomedical Applications. *Carbohydr. Polym.* **2015**, *117*, 524–536. <https://doi.org/10.1016/j.carbpol.2014.09.094>.
- (214) Zhou, H. Y.; Jiang, L. J.; Cao, P. P.; Li, J. B.; Chen, X. G. Glycerophosphate-Based Chitosan Thermosensitive Hydrogels and Their Biomedical Applications. *Carbohydr. Polym.* **2015**, *117*, 524–536. <https://doi.org/10.1016/j.carbpol.2014.09.094>.
- (215) Dang, Q.; Liu, K.; Zhang, Z.; Liu, C.; Liu, X.; Xin, Y.; Cheng, X.; Xu, T.; Cha, D.; Fan, B. Fabrication and Evaluation of Thermosensitive Chitosan/Collagen/ α , β -Glycerophosphate Hydrogels for Tissue Regeneration. *Carbohydr. Polym.* **2017**, *167*, 145–157. <https://doi.org/10.1016/j.carbpol.2017.03.053>.
- (216) Bodmeier, R.; Oh, K. H.; Pramar, Y. Preparation and Evaluation of Drug-Containing Chitosan Beads. *Drug Dev. Ind. Pharm.* **1989**, *15* (9), 1475–1494. <https://doi.org/10.3109/03639048909062758>.
- (217) Wu, Y.; Yang, W.; Wang, C.; Hu, J.; Fu, S. Chitosan Nanoparticles as a Novel Delivery System for Ammonium Glycyrrhizinate. *Int. J. Pharm.* **2005**, *295* (1–2), 235–245. <https://doi.org/10.1016/j.ijpharm.2005.01.042>.
- (218) Bhumkar, R. D.; Pokharkar, V. B. Studies on Effect of PH on Cross-Linking of Chitosan with Sodium Tripolyphosphate: A Technical Note. *AAPS PharmSciTech* **2006**, *7* (2), 2–7. <https://doi.org/10.1208/pt070250>.
- (219) Tsai, M. L.; Chen, R. H.; Bai, S. W.; Chen, W. Y. The Storage Stability of Chitosan/Tripolyphosphate Nanoparticles in a Phosphate Buffer. *Carbohydr. Polym.* **2011**, *84* (2), 756–761. <https://doi.org/10.1016/j.carbpol.2010.04.040>.
- (220) de Paz, L. E. C.; Resin, A.; Howard, K. A.; Sutherland, D. S.; Wejse, P. L. Antimicrobial Effect of Chitosan Nanoparticles on Streptococcus Mutans Biofilms. *Appl. Environ. Microbiol.* **2011**, *77* (11), 3892–3895. <https://doi.org/10.1128/AEM.02941-10>.
- (221) Berger, J.; Reist, M.; Mayer, J. M.; Felt, O.; Peppas, N. A.; Gurny, R. Structure and Interactions in Covalently and Ionically Crosslinked Chitosan Hydrogels for Biomedical Applications. *Eur. J. Pharm. Biopharm.* **2004**, *57* (1), 19–34. [https://doi.org/10.1016/S0939-6411\(03\)00161-9](https://doi.org/10.1016/S0939-6411(03)00161-9).
- (222) Fan, W.; Yan, W.; Xu, Z.; Ni, H. Formation Mechanism of Monodisperse, Low Molecular Weight Chitosan Nanoparticles by Ionic Gelation Technique. *Colloids Surfaces B Biointerfaces* **2012**, *90* (1), 21–27. <https://doi.org/10.1016/j.colsurfb.2011.09.042>.
- (223) Yuan, Y.; Huang, Y. Ionically Crosslinked Polyelectrolyte Nanoparticle Formation Mechanisms: The Significance of Mixing. *Soft Matter* **2019**, *15* (48), 9871–9880. <https://doi.org/10.1039/c9sm01441a>.
- (224) López-León, T.; Carvalho, E. L. S.; Seijo, B.; Ortega-Vinuesa, J. L.; Bastos-González, D. Physicochemical Characterization of Chitosan Nanoparticles: Electrokinetic and Stability Behavior. *J. Colloid Interface Sci.* **2005**, *283* (2), 344–351. <https://doi.org/10.1016/j.jcis.2004.08.186>.
- (225) Mazancová, P.; Némethová, V.; Treľová, D.; Kleščíková, L.; Lacík, I.; Rázga, F. Dissociation of Chitosan/Tripolyphosphate Complexes into Separate Components upon PH Elevation. *Carbohydr. Polym.* **2018**, *192* (January), 104–110. <https://doi.org/10.1016/j.carbpol.2018.03.030>.
- (226) Morris, G. A.; Castile, J.; Smith, A.; Adams, G. G.; Harding, S. E. The Effect of Prolonged Storage at Different Temperatures on the Particle Size Distribution of Tripolyphosphate (TPP)-Chitosan Nanoparticles. *Carbohydr. Polym.* **2011**, *84* (4), 1430–1434. <https://doi.org/10.1016/j.carbpol.2011.01.044>.
- (227) Li, X. Y.; Kong, X. Y.; Wang, X. H.; Shi, S.; Guo, G.; Luo, F.; Zhao, X.; Wei, Y. Q.; Qian, Z. Y. Gel-Sol-Gel Thermo-Gelation Behavior Study of Chitosan-Inorganic Phosphate Solutions. *Eur. J. Pharm. Biopharm.* **2010**, *75* (3), 388–392. <https://doi.org/10.1016/j.ejpb.2010.04.015>.

- (228) Filion, D.; Lavertu, M.; Buschmann, M. D. Ionization and Solubility of Chitosan Solutions Related to Thermosensitive Chitosan/Glycerol-Phosphate Systems. *Biomacromolecules* **2007**, *8* (10), 3224–3234. <https://doi.org/10.1021/bm700520m>.
- (229) Filion, D.; Buschmann, M. D. Chitosan-Glycerol-Phosphate (GP) Gels Release Freely Diffusible GP and Possess Titratable Fixed Charge. *Carbohydr. Polym.* **2013**, *98* (1), 813–819. <https://doi.org/10.1016/j.carbpol.2013.06.055>.
- (230) Gekko, K. Hydration—Structure—Function Relationships of Polysaccharides and Proteins. *Top. Catal.* **1989**, *3* (4), 289–299. [https://doi.org/10.1016/S0268-005X\(89\)80040-2](https://doi.org/10.1016/S0268-005X(89)80040-2).
- (231) Hakan, B. Israelachvili1996Nature_review_Role of Hydration and Water Structure in Biological_colloidal Interactions_marked.Pdf. 219–225.
- (232) Despond, S.; Espuche, E.; Cartier, N.; Domard, A. Hydration Mechanism of Polysaccharides: A Comparative Study. *J. Polym. Sci. Part B Polym. Phys.* **2005**, *43* (1), 48–58. <https://doi.org/10.1002/polb.20277>.
- (233) Bellissent-Funel, M. C.; Hassanali, A.; Havenith, M.; Henschman, R.; Pohl, P.; Sterpone, F.; Van Der Spoel, D.; Xu, Y.; Garcia, A. E. Water Determines the Structure and Dynamics of Proteins. *Chem. Rev.* **2016**, *116* (13), 7673–7697. <https://doi.org/10.1021/acs.chemrev.5b00664>.
- (234) Politi, R.; Sapir, L.; Harries, D. The Impact of Polyols on Water Structure in Solution: A Computational Study. *J. Phys. Chem. A* **2009**, *113* (26), 7548–7555. <https://doi.org/10.1021/jp9010026>.
- (235) Liu, F. F.; Ji, L.; Zhang, L.; Dong, X. Y.; Sun, Y. Molecular Basis for Polyol-Induced Protein Stability Revealed by Molecular Dynamics Simulations. *J. Chem. Phys.* **2010**, *132* (22). <https://doi.org/10.1063/1.3453713>.
- (236) Na, G. C.; Butz, L. J.; Bailey, D. G.; Carroll, R. J. In Vitro Collagen Fibril Assembly in Glycerol Solution: Evidence for a Helical Cooperative Mechanism Involving Microfibrils. *Biochemistry* **1986**, *25* (5), 958–966. <https://doi.org/10.1021/bi00353a003>.
- (237) Supper, S.; Anton, N.; Seidel, N.; Riemenschnitter, M.; Schoch, C.; Vandamme, T. Rheological Study of Chitosan/Polyol-Phosphate Systems: Influence of the Polyol Part on the Thermo-Induced Gelation Mechanism. *Langmuir* **2013**, *29* (32), 10229–10237. <https://doi.org/10.1021/la401993q>.
- (238) Grinberg, V. Y.; Burova, T. V.; Grinberg, N. V.; Tikhonov, V. E.; Dubovik, A. S.; Moskalets, A. P.; Khokhlov, A. R. Thermodynamic Insight into the Thermoresponsive Behavior of Chitosan in Aqueous Solutions: A Differential Scanning Calorimetry Study. *Carbohydr. Polym.* **2019**, *229* (September 2019), 115558. <https://doi.org/10.1016/j.carbpol.2019.115558>.
- (239) Lavertu, M.; Filion, D.; Buschmann, M. D. Heat-Induced Transfer of Protons from Chitosan to Glycerol Phosphate Produces Chitosan Precipitation and Gelation. *Biomacromolecules* **2008**, *9* (2), 640–650. <https://doi.org/10.1021/bm700745d>.
- (240) Cho, J.; Heuzy, M. C.; Bégin, A.; Carreau, P. J. Effect of Urea on Solution Behavior and Heat-Induced Gelation of Chitosan- β -Glycerophosphate. *Carbohydr. Polym.* **2006**, *63* (4), 507–518. <https://doi.org/10.1016/j.carbpol.2005.10.013>.
- (241) Cho, J.; Heuzy, M. C.; Bégin, A.; Carreau, P. J. Physical Gelation of Chitosan in the Presence of β -Glycerophosphate: The Effect of Temperature. *Biomacromolecules* **2005**, *6* (6), 3267–3275. <https://doi.org/10.1021/bm050313s>.
- (242) Aliaghaie, M.; Mirzadeh, H.; Dashtimoghadam, E.; Taranejoo, S. Investigation of Gelation Mechanism of an Injectable Hydrogel Based on Chitosan by Rheological Measurements for a Drug Delivery Application. *Soft Matter* **2012**, *8* (27), 7128. <https://doi.org/10.1039/c2sm25254f>.
- (243) Philippova, O. E.; Volkov, E. V.; Sitnikova, N. L.; Khokhlov, A. R.; Desbrieres, J.; Rinaudo, M. Two Types of Hydrophobic Aggregates in Aqueous Solutions of Chitosan and Its Hydrophobic Derivative. *Biomacromolecules* **2001**, *2* (2), 483–490. <https://doi.org/10.1021/bm005649a>.
- (244) Crompton, K. E.; Prankerd, R. J.; Paganin, D. M.; Scott, T. F.; Horne, M. K.; Finkelstein, D. I.; Gross, K. A.; Forsythe, J. S. Morphology and Gelation of Thermosensitive Chitosan Hydrogels. *Biophys. Chem.* **2006**, *121* (1), 14–20. <https://doi.org/10.1016/j.bpc.2005.12.005>.
- (245) Crompton, K. E.; Forsythe, J. S.; Horne, M. K.; Finkelstein, D. I.; Knott, R. B. Molecular Level and Microstructural Characterisation of Thermally Sensitive Chitosan Hydrogels. *Soft Matter* **2009**, *5* (23), 4704–4711. <https://doi.org/10.1039/b907593c>.

- (246) Shibayama, M.; Tanaka, T.; Han, C. C. Small Angle Neutron Scattering Study on Poly(N-Isopropyl Acrylamide) Gels near Their Volume-Phase Transition Temperature. *J. Chem. Phys.* **1992**, *97* (9), 6829–6841. <https://doi.org/10.1063/1.463636>.
- (247) Ahmadi, R.; De Bruijn, J. D. Biocompatibility and Gelation of Chitosan-Glycerol Phosphate Hydrogels. *J. Biomed. Mater. Res. - Part A* **2008**, *86* (3), 824–832. <https://doi.org/10.1002/jbm.a.31676>.
- (248) Nair, L. S.; Starnes, T.; Ko, J. W. K.; Laurencin, C. T. Development of Injectable Thermogelling Chitosan-Inorganic Phosphate Solutions for Biomedical Applications. *Biomacromolecules* **2007**, *8* (12), 3779–3785. <https://doi.org/10.1021/bm7006967>.
- (249) Boles, L.; Alexander, C.; Pace, L.; Haggard, W.; Bumgardner, J.; Jennings, J. Development and Evaluation of an Injectable Chitosan/ β -Glycerophosphate Paste as a Local Antibiotic Delivery System for Trauma Care. *J. Funct. Biomater.* **2018**, *9* (4), 56. <https://doi.org/10.3390/jfb9040056>.
- (250) Zhao, Q. S.; Ji, Q. X.; Xing, K.; Li, X. Y.; Liu, C. S.; Chen, X. G. Preparation and Characteristics of Novel Porous Hydrogel Films Based on Chitosan and Glycerophosphate. *Carbohydr. Polym.* **2009**, *76* (3), 410–416. <https://doi.org/10.1016/j.carbpol.2008.11.020>.
- (251) Kolawole, O. M.; Lau, W. M.; Khutoryanskiy, V. V. Chitosan/ β -Glycerophosphate in Situ Gelling Mucoadhesive Systems for Intravesical Delivery of Mitomycin-C. *Int. J. Pharm. X* **2019**, *1* (November 2018), 100007. <https://doi.org/10.1016/j.ijpx.2019.100007>.
- (252) Zang, S.; Mu, R.; Chen, F.; Wei, X.; Zhu, L.; Han, B.; Yu, H.; Bi, B.; Chen, B.; Wang, Q.; Jin, L. Injectable Chitosan/ β -Glycerophosphate Hydrogels with Sustained Release of BMP-7 and Ornidazole in Periodontal Wound Healing of Class III Furcation Defects. *Mater. Sci. Eng. C* **2019**, *99* (January), 919–928. <https://doi.org/10.1016/j.msec.2019.02.024>.
- (253) Fookes, F. A.; Mengatto, L. N.; Rigalli, A.; Luna, J. A. Controlled Fluoride Release for Osteoporosis Treatment Using Orally Administered Chitosan Hydrogels. *J. Drug Deliv. Sci. Technol.* **2019**, *51* (February), 268–275. <https://doi.org/10.1016/j.jddst.2019.03.004>.
- (254) Ruel-Gariépy, E.; Shive, M.; Bichara, A.; Berrada, M.; Le Garrec, D.; Chenite, A.; Leroux, J. C. A Thermosensitive Chitosan-Based Hydrogel for the Local Delivery of Paclitaxel. *Eur. J. Pharm. Biopharm.* **2004**, *57* (1), 53–63. [https://doi.org/10.1016/S0939-6411\(03\)00095-X](https://doi.org/10.1016/S0939-6411(03)00095-X).
- (255) Qing Min 1,†, Jiaoyan Liu 2,†, Xiaofeng Yu 2, Yuchen Zhang 1, Jiliang Wu 1, and Y. W. Sequential Delivery of Dual Growth Factors from Injectable Chitosan-Based Composite Hydrogels. *Mar. Drugs* **2003**, *2*, 54–65.
- (256) Wu, S.; Zhou, Y.; Yu, Y.; Zhou, X.; Du, W.; Wan, M.; Fan, Y.; Zhou, X.; Xu, X.; Zheng, L. Evaluation of Chitosan Hydrogel for Sustained Delivery of VEGF for Odontogenic Differentiation of Dental Pulp Stem Cells. *Stem Cells Int.* **2019**, *2019*. <https://doi.org/10.1155/2019/1515040>.
- (257) Liu, L.; Gao, Q.; Lu, X.; Zhou, H. In Situ Forming Hydrogels Based on Chitosan for Drug Delivery and Tissue Regeneration. *Asian J. Pharm. Sci.* **2016**, *11* (6), 673–683. <https://doi.org/10.1016/j.ajps.2016.07.001>.
- (258) Kolawole, O. M.; Lau, W. M.; Khutoryanskiy, V. V. Chitosan/ β -Glycerophosphate in Situ Gelling Mucoadhesive Systems for Intravesical Delivery of Mitomycin-C. *Int. J. Pharm. X* **2019**, *1* (November 2018), 100007. <https://doi.org/10.1016/j.ijpx.2019.100007>.
- (259) Richardson, S. M.; Hughes, N.; Hunt, J. A.; Freemont, A. J.; Hoyland, J. A. Human Mesenchymal Stem Cell Differentiation to NP-like Cells in Chitosan-Glycerophosphate Hydrogels. *Biomaterials* **2008**, *29* (1), 85–93. <https://doi.org/10.1016/j.biomaterials.2007.09.018>.
- (260) Dang, Q. F.; Yan, J. Q.; Lin, H.; Chen, X. G.; Liu, C. S.; Ji, Q. X.; Li, J. J. Design and Evaluation of a Highly Porous Thermosensitive Hydrogel with Low Gelation Temperature as a 3D Culture System for *Penaeus Chinensis* Lymphoid Cells. *Carbohydr. Polym.* **2012**, *88* (1), 361–368. <https://doi.org/10.1016/j.carbpol.2011.12.014>.
- (261) Kim, K. S.; Lee, J. H.; Ahn, H. H.; Lee, J. Y.; Khang, G.; Lee, B.; Lee, H. B.; Kim, M. S. The Osteogenic Differentiation of Rat Muscle-Derived Stem Cells in Vivo within in Situ-Forming Chitosan Scaffolds. *Biomaterials* **2008**, *29* (33), 4420–4428. <https://doi.org/10.1016/j.biomaterials.2008.08.005>.
- (262) Crompton, K. E.; Goud, J. D.; Bellamkonda, R. V.; Gengenbach, T. R.; Finkelstein, D. I.; Horne, M. K.; Forsythe, J. S. Polylysine-Functionalised Thermoresponsive Chitosan Hydrogel for Neural Tissue Engineering. *Biomaterials* **2007**, *28* (3), 441–449. <https://doi.org/10.1016/j.biomaterials.2006.08.044>.

- (263) Hoemann, C. D.; Sun, J.; Légaré, A.; McKee, M. D.; Buschmann, M. D. Tissue Engineering of Cartilage Using an Injectable and Adhesive Chitosan-Based Cell-Delivery Vehicle. *Osteoarthr. Cartil.* **2005**, *13* (4), 318–329. <https://doi.org/10.1016/j.joca.2004.12.001>.
- (264) Lu, S.; Wang, H.; Lu, W.; Liu, S.; Lin, Q.; Li, D.; Duan, C.; Hao, T.; Zhou, J.; Wang, Y.; Gao, S.; Wang, C. Both the Transplantation of Somatic Cell Nuclear Stem Cells with Temperature-Responsive Chitosan Hydrogel. *Tissue Eng.* **2010**, *16* (4), 1–14. <https://doi.org/10.1089>.
- (265) Ngoenkam, J.; Faikrua, A.; Yasothornsrikul, S.; Viyoch, J. Potential of an Injectable Chitosan/Starch/ β -Glycerol Phosphate Hydrogel for Sustaining Normal Chondrocyte Function. *Int. J. Pharm.* **2010**, *391* (1–2), 115–124. <https://doi.org/10.1016/j.ijpharm.2010.02.028>.
- (266) Gao, J.; Liu, R.; Wu, J.; Liu, Z.; Li, J.; Zhou, J.; Hao, T.; Wang, Y.; Du, Z.; Duan, C.; Wang, C. The Use of Chitosan Based Hydrogel for Enhancing the Therapeutic Benefits of Adipose-Derived MSCs for Acute Kidney Injury. *Biomaterials* **2012**, *33* (14), 3673–3681. <https://doi.org/10.1016/j.biomaterials.2012.01.061>.
- (267) Santi, S.; Corridori, I.; Pugno, N. M.; Motta, A.; Migliaresi, C. Injectable Scaffold-Systems for the Regeneration of Spinal Cord: Advances of the Past Decade. *ACS Biomater. Sci. Eng.* **2021**, *7* (3), 983–999. <https://doi.org/10.1021/acsbomaterials.0c01779>.
- (268) Annamalai, R. T.; Hong, X.; Schott, N. G.; Tiruchinapally, G.; Levi, B.; Stegemann, J. P. Injectable Osteogenic Microtissues Containing Mesenchymal Stromal Cells Conformally Fill and Repair Critical-Size Defects. *Biomaterials* **2019**, *208* (November 2018), 32–44. <https://doi.org/10.1016/j.biomaterials.2019.04.001>.
- (269) Yang, M.; He, S.; Su, Z.; Yang, Z.; Liang, X.; Wu, Y. Thermosensitive Injectable Chitosan/Collagen/ β -Glycerophosphate Composite Hydrogels for Enhancing Wound Healing by Encapsulating Mesenchymal Stem Cell Spheroids. *ACS Omega* **2020**. <https://doi.org/10.1021/acsomega.0c02580>.
- (270) Zhou, P.; Li, X.; Zhang, B.; Shi, Q.; Li, D.; Ju, X. A Human Umbilical Cord Mesenchymal Stem Cell-Conditioned Medium/Chitosan/Collagen/ β -Glycerophosphate Thermosensitive Hydrogel Promotes Burn Injury Healing in Mice. *Biomed Res. Int.* **2019**, *2019*. <https://doi.org/10.1155/2019/5768285>.
- (271) Ke, X.; Li, M.; Wang, X.; Liang, J.; Wang, X.; Wu, S.; Long, M.; Hu, C. An Injectable Chitosan/Dextran/ β -Glycerophosphate Hydrogel as Cell Delivery Carrier for Therapy of Myocardial Infarction. *Carbohydr. Polym.* **2020**, *229* (October 2019), 115516. <https://doi.org/10.1016/j.carbpol.2019.115516>.
- (272) Langenbach, F.; Handschel, J. Effects of Dexamethasone, Ascorbic Acid and β -Glycerophosphate on the Osteogenic Differentiation of Stem Cells in Vitro. *Stem Cell Res. Ther.* **2013**, *4* (117). <https://doi.org/10.1089/ten.teb.2011.0199>.
- (273) Dhivya, S.; Saravanan, S.; Sastry, T. P.; Selvamurugan, N. Nanohydroxyapatite-Reinforced Chitosan Composite Hydrogel for Bone Tissue Repair in Vitro and in Vivo. *J. Nanobiotechnology* **2015**, *13* (1), 1–13. <https://doi.org/10.1186/s12951-015-0099-z>.

CHAPTER II

RATIONAL FORMULATION DESIGN OF INJECTABLE THERMOSENSITIVE CHITOSAN-BASED HYDROGELS FOR CELL ENCAPSULATION AND DELIVERY

TABLE OF CONTENTS

Résumé en français	99
II.1. Introduction.....	100
II.2. Materials & Methods.....	101
II.2.1. Materials & Cells	101
II.2.2. Experimental methods	102
2.2.a Preparation and sterilization.....	102
2.2.b pH titration of CS/ β GP solution with AHP solution	102
2.2.c Osmolarity measurement.....	102
2.2.d Gelation time measurement.....	102
2.2.e Rheological characterization	103
2.2.f Injectability evaluation.....	103
2.2.g Cell encapsulation in thermosensitive chitosan hydrogels.....	103
2.2.h Statistical analysis.....	104
II.3. Results & discussion	105
II.3.1. Controlling the pH using CS/ β GP/AHP formulations	105
II.3.2. CS/ β GP/AHP formulations with adjustable pH and osmolarity	110
II.3.3. Gelation kinetics of CS/ β GP/AHP formulations	113
II.3.4. Cell encapsulation in CS/ β GP/AHP hydrogels.....	117
II.3.5. Mechanical property of CS/ β GP/AHP hydrogels	119
II.4. Conclusion.....	120
References.....	121

Résumé en français

Cette étude fait partie d'un article plus général publié dans *Carbohydrate Polymers* sous le titre *Rational formulation design of injectable thermosensitive chitosan-based hydrogels for cell encapsulation and delivery* (<https://doi.org/10.1016/j.carbpol.2021.118836>). Le manuscrit correspondant à cet article est reporté en grande partie dans la suite de ce chapitre.

Comme vu dans l'étude bibliographique, le mélange thermosensible CS/ β GP est clairement un système potentiel pour la délivrance de cellules. Cependant, augmenter les concentrations de β GP pour atteindre des valeurs de pH appropriées augmente également l'osmolarité du mélange jusqu'à des valeurs cytotoxiques. Par conséquent, des stratégies ont été mises en œuvre dans la littérature pour améliorer le système standard, principalement en remplaçant partiellement ou totalement le β GP par d'autres sels. Néanmoins, les nombreuses variables, pH, osmolarité, concentrations en sel et en CS sont toutes interdépendantes. Il manquait une plateforme générale et rationnelle permettant de contrôler indépendamment le pH et l'osmolarité, et donc la cinétique de gélification et la cytocompatibilité, quelle que soit la concentration en CS.

Dans ce chapitre, nous présentons un guide rationnel pour préparer des solutions de CS thermosensibles, en remplaçant partiellement β GP par le phosphate de diammonium, AHP. Grâce à ce troisième composant, l'AHP, on peut découpler le contrôle du pH et de l'osmolarité, quelle que soit la concentration en CS. Nous montrons que ces deux paramètres peuvent être ajustés indépendamment en jouant sur les ratios $[\text{sel}]/[\text{NH}_2]$, où $[\text{NH}_2]$ désigne la concentration en monomère D-glucosamine. Les solutions obtenues sont capables de former un gel en quelques minutes à 37°C. Nous avons étudié en profondeur la cinétique de gélification pour les formulations physiologiques et déterminé une température critique de gélification, en dessous de laquelle le système reste liquide au fil du temps, pour différentes concentrations de CS.

Nous avons vérifié la cytocompatibilité de nos formulations et exploré l'effet de l'osmolarité sur l'activité cellulaire en encapsulant des cellules de souris préostéoblastiques (MC3T3-E1) et des fibroblastes gingivaux humains (HGF) dans des gels hypertoniques (CS/ β GP) et isotoniques (CS/ β GP/AHP). Les deux types de cellules montrent une viabilité d'au moins 80% à 24 h post-encapsulation dans des formulations isotoniques tandis que la viabilité des cellules MC3T3-E1 diminue de manière significative dans des formulations hypertoniques.

La méthodologie proposée peut être appliquée à des solutions de CS présentant divers M_w et DD , fournissant ainsi une plateforme générale pour préparer des hydrogels thermosensibles pour l'encapsulation et l'administration de cellules.

II.1. Introduction

This study is part of a more general article published in Carbohydrate Polymers under the title *Rational formulation design of injectable thermosensitive chitosan-based hydrogels for cell encapsulation and delivery* (<https://doi.org/10.1016/j.carbpol.2021.118836>). The manuscript corresponding to this article is substantially reported in this chapter.

As detailed in the literature review, CS- β GP mixtures appeared clearly as a promising thermo-gelling system for cell injection, remaining liquid at physiological pH and turning rapidly into a gel at body temperature. However, increasing salt concentrations to reach appropriate values of pH also increases the osmolarity of the mixture up to cytotoxic values.¹ Hence, strategies were implemented to improve the standard system, mostly by replacing partially or totally β GP by other salts. Using ammonium hydrogen phosphate (AHP, **Figure II - 1**), a lower salt concentration was required to reach neutral pHs (7.0 – 7.2) resulting in physiological osmolarity ($300 \pm 30 \text{ mOsm.L}^{-1}$).² Other inorganic phosphate salts without polyol moieties, like dipotassium hydrogen phosphate K_2HPO_4 ³, basic sodium phosphates as NaH_2PO_4 , Na_2HPO_4 , or even Na_3PO_4 ,^{4,5} have also been studied to produce thermo-sensitive CS formulations. Sodium hydrogen carbonate (SHC) has been studied as a gelling agent, alone^{6,7} or in combination with β GP⁸⁻¹¹. Mixtures of CS/AHP² or CS/ β GP/SHC^{9,11} have been evaluated *in vitro* as 3D scaffolds for cells. Encapsulation of mouse preosteoblastic cells and fibroblasts as well as human mesenchymal stem cells confirmed the cytocompatibility for days for some formulations. The feasibility of using these chitosan-based hydrogels as a cell carrier vehicle has therefore been demonstrated. Nevertheless, the numerous variables, pH, osmolarity, salt and chitosan concentrations leading to injectable cytocompatible solutions are all interdependent. A general platform is still lacking, enabling to control independently pH and osmolarity, and therefore gelation kinetics and cytocompatibility, whatever the chitosan concentration. Yet, controlling chitosan concentration is a key to adjust the viscoelastic and microstructural properties of the injected hydrogels, which are of the utmost importance to favor cell anchorage and growth.

In this study we present a rational formulation design to make thermosensitive CS solutions, by partially replacing β GP by AHP in the mixture. With this third component, AHP, we can decouple the control on pH and osmolarity, whatever the CS concentration. We show that these two parameters can be adjusted independently by the simple ratios $[\text{salt}]/[\text{NH}_2]$, where $[\text{NH}_2]$ denotes the concentration in D-glucosamine monomer in the solution, *i.e.* the concentration in deacetylated chitin monomers bearing NH_2 functions. This approach gives rise to a robust platform, to easily formulate physiological solutions able to form a gel within a couple of minutes at body temperature. We investigated in depth the gelation kinetics for physiological formulations and determined a critical temperature of gelation, under which the system

remains liquid overtime, for different CS concentrations. We checked the cytocompatibility of our controlled CS/ β GP/AHP formulations and explored the effect of osmolarity on cell activity by encapsulating preosteoblastic mouse cells (MC3T3-E1) and human gingival fibroblasts (HGF). By means of confocal microscopy and rheology, we showed that hydrogel microstructure and mechanical properties can be varied by changing CS concentration while maintaining fixed pH and osmolarity.

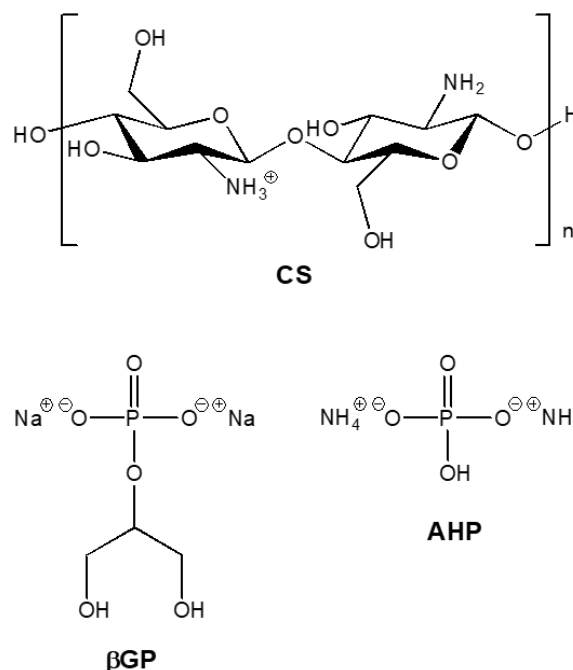


Figure II - 1. Structures of chitosan CS, β -glycerophosphate β GP and ammonium hydrogen phosphate AHP.

II.2. Materials & Methods

II.2.1. Materials & Cells

Three grades of chitosan (CS) having high purity (impurity level $< 1.0\%$) were purchased from Glentham Life Sciences Limited. All the study was performed with chitosan low molar mass (viscosity 30-100 cps) having the following characteristics given by the supplier: deacetylation degree $DD = 91\%$, as measured by potentiometric titration, average molar mass $M_w = 250 \text{ kg}\cdot\text{mol}^{-1}$, as measured by viscometry. For pH titration experiments, two other grades with DD of 95% were also used: chitosan very low molar mass (10 cps) with $M_w = 30 \text{ kg}\cdot\text{mol}^{-1}$, and chitosan (100-300 cps) with $M_w = 890 \text{ kg}\cdot\text{mol}^{-1}$.

β -glycerophosphate disodium salt hydrate BioUltra (β GP) and ammonium hydrogen phosphate BioUltra (AHP) were purchased from Sigma-Aldrich. Glacial acetic acid (AcOH, 99%) was purchased from Alfa

Aesar. Alexa Fluor 488 was purchased from Abcam. The Live/Dead™ kit and AlamarBlue™ reagent were purchased from Invitrogen. MC3T3-E1 pre-osteoblastic cells were procured from ATCC®, and human gingival fibroblasts were isolated from healthy donors and kindly donated by Laboratory BioS, Reims University. α -MEM, DMEM, phosphate buffer saline without calcium and magnesium (PBS) were purchased from Gibco. Deionized distilled water from a Milli-Q system was used to prepare all aqueous solutions.

II.2.2. Experimental methods

2.2.a. Preparation and sterilization of reactants

Aqueous suspensions of CS were sterilized in autoclave at 121°C for 10 min using standard liquid cycle according to San Juan *et al.*¹² After autoclaving, acetic acid (AcOH) was added to the suspension with molar ratio $[\text{AcOH}]/[\text{NH}_2] = 1$, which was stirred at room temperature ($21 \pm 1^\circ\text{C}$) for 24 h. The concentration of the CS stock solution was 1.33 wt%. CS stock solutions were stored at 5°C until further use. β GP, AHP and AcOH solutions at 1 mol.L⁻¹ were prepared in deionized water and sterilized by filtration using syringe filters having pore size of 0.2 μm .

2.2.b. pH titration of CS/ β GP solution with AHP solution

Stock solutions of β GP and AHP as well as CS solution at 0.8 wt% were chilled in an ice bath prior to mixture. All pH titrations were performed at $4 \pm 1^\circ\text{C}$. The β GP solution was added dropwise to the CS solution under vigorous stirring. Solutions with molar ratio $[\beta\text{GP}]/[\text{NH}_2]$ ranging from 0 to 4 were prepared. For each $[\beta\text{GP}]/[\text{NH}_2]$ ratio, titration was carried out with AHP solution until the pH reached 7.4.

2.2.c. Osmolarity measurement

Osmolality of different solutions was measured with a cryoscopic osmometer (Osmomat 30, Gonotec). The apparatus measures the osmolality (mOsm.kg⁻¹), which is proportional through the density to the osmolarity (mOsm.L⁻¹). In this study, since all solutions are diluted, the difference between osmolarity and osmolality is insignificant.

2.2.d. Gelation time measurement

The gelation times were determined by the test tube inversion method. The sol phase was defined as the flowing phase and the gel phase as the non-flowing phase when the test tube was inverted. 1 mL of CS/ β GP solutions was introduced into 1.5 mL tubes that were incubated in a thermostat at fixed temperature (15-37°C). Time between inversions was as follows: 30 s from 0 to 10 min, 1 min from 10 to 30 min, 5 min

from 30 to 60 min, 10 min from 60 to 120 min, 15 min from 2 h to 5 h, 30 min from 5 h to 10 h and 3 h after 10 h. The time at which the gel did not flow anymore was recorded as the gelation time and the time interval between two inversions gave the experimental uncertainty. Each measure was duplicated. The shortest measurable gelation time is given by the duration of thermal equilibration, which in these tubes was measured to be 1 min for a solution at 4°C immersed in a thermostat at 37°C.

2.2.e. Rheological characterization

Rheological properties of physiological formulations prepared with 0.5 wt% or 0.8 wt% of CS were studied using rheometer MCR502 (Anton Paar) with a cone-and-plate geometry (CP50-2TG). The temperature was managed by a Peltier controller and the geometry was previously stabilized at 18°C. Formulations were loaded immediately after preparation and silicone oil was added to the interface between the sample and the air to prevent evaporation. The temperature was rapidly increased 37°C at a rate of 20°C.min⁻¹. The values of storage and loss moduli (G' , G'') were measured during 6 h, at a constant oscillatory strain of 0.1% and an angular frequency of 1 rad.s⁻¹.

2.2.f. Injectability evaluation

Injectability test was performed using the protocol reported by Kondziolka *et al.*¹³ For visualization, a small amount of rose Bengal dye was added to CS/βGP/AHP mixture. Immediately following the preparation, the mixture was loaded into a 5 mL syringe equipped with a 21G needle and placed on a pump syringe. A volume of 1.5 mL was then injected at a rate of 250 μL.min⁻¹ into a PBS solution at pH 7.4 and 37°C.

2.2.g. Cell encapsulation in thermosensitive chitosan hydrogels

We compared two formulations of hydrogels for cell encapsulation: CS/βGP (600 mOsm.L¹) and CS/βGP/AHP (300 mOsm.L⁻¹) at fixed CS concentration (0.8 wt%) and at pH 7.4 on two cell models: primary human gingival fibroblast (HGF) and pre-osteoblast immortalized murine cell line (MC3T3-E1). HGF were cultured in DMEM and MC3T3-E1 cells were cultured in α-MEM, both cell culture medium supplemented with 10%v/v fetal calf serum and 1%v/v penicillin-streptomycin. For both cell types, the encapsulation protocol was as follows: (1) cells were trypsinized, resuspended in serum-free media and mixed gently with CS/βGP or CS/βGP/AHP solutions at a final concentration of 10⁶ cells.mL⁻¹; (2) 300 μL of the mixture containing cells were dispensed into a 24-well culture plate (Nunc™ F96 MicroWell™) and incubated for 1 h at 37°C and 5% CO₂ to induce gelation; (3) 1 mL of culture medium supplemented with 10%v/v fetal calf serum and 1%v/v penicillin-streptomycin was added into each well. Hydrogels without cells were also prepared by replacing the cell suspension by culture medium.

Live/Dead assay

After 1 h or 24 h, the encapsulated cells were stained using calcein AM/ethidium homodimer (CalAM/EthD-1) mixture at optimized concentrations ([CalAM]/[EthD-1]: 2 μM /2 μM and 1 μM /0.5 μM for MC3T3-E1 cells and HGF, respectively). For positive control, cells were seeded directly into the well at a density of $10^4 \text{ cells.cm}^{-2}$. For negative control, cells were killed using methanol solution at 70 wt%. 1 mL of the staining mixture was added into each well and the plates were incubated at 37°C and 5% CO_2 for 45 min then the mixture was removed and the hydrogels or cells were rinsed with PBS. 500 μL of PBS solution were added into each well to prevent drying. The distribution and the state of the cells were visualized using a laser scanning confocal microscope (LSM 710, Zeiss) using lasers at 488 nm and 561 nm. Each hydrogel sample was scanned from bottom to 300 μm depth at 8 random positions. Stacks were taken at $\times 20$ magnification and a 512×512 pixel resolution with the pinhole at 1 Airy unit and interval of 4 μm . Recorded images were then analyzed with ImageJ using 3D Object counter plugin.¹⁴ The cell viability (%) was determined as the number of living cells over the total number of cells. Experiments were carried out with $n = 2$ for MC3T3 and $n = 1$ for HGF and all samples were prepared in triplicate.

AlamarBlue assay

The cell metabolism was evaluated using the AlamarBlue assay at 1 h and 24 h following encapsulation. After incubation, a solution of 10 %v/v AlamarBlue in culture medium (1 mL/well) was added directly on each hydrogel and incubated for 3 h at 37°C and 5% of CO_2 . Then, the supernatant was homogenized by pipetting and 150 μL were transferred into a 96-well plate (Nunc™ F96 MicroWell™). The intensity of fluorescence was determined by using Xenius XM spectrofluorometer (SAFAS Monaco) at 560 nm excitation and 590 nm emission. A value of the metabolic activity per cell was estimated by normalizing the measured intensity by the number of living cells obtained from the Live/Dead assay.

2.2.h. Statistical analysis

Statistical analysis was performed using a t-test with normality assumption. Statistical significance was accepted at the level of $p < 0.05$.

II.3. Results & discussion

In all the following, $[\text{NH}_2]$ denotes the concentration in D-glucosamine monomer in the solution.

II.3.1. Controlling the pH using CS/ β GP/AHP formulations

Control of the pH of thermogelling CS/ β GP solutions is determinant for the viability and the injectability of encapsulated cells. Cell viability requires that the pH be maintained close to 7.4 during cell suspension and storage until injection and immersion in other buffering media. The gelation time of CS/ β GP solutions was also shown to depend greatly on pH.¹⁵ Accordingly, we measured that the gelation time of CS/ β GP solutions increases from 1 min to 10 h when pH decreases from 7.5 to 7.1 (**Figure II - 2**). In the present study, CS was dissolved in acidic aqueous solutions with a fixed molar ratio $[\text{AcOH}]/[\text{NH}_2] = 1$. This ratio was chosen as the minimum amount of acid required to ensure the solubilization of chitosan chains.¹⁶ In CS/ β GP/AHP formulations, β GP and AHP are both weak bases that raise the pH of the solution. As demonstrated thereafter, the pH can be finely controlled by the molar ratios between each phosphate salt and D-glucosamine monomer, $[\beta\text{GP}]/[\text{NH}_2]$ and $[\text{AHP}]/[\text{NH}_2]$.

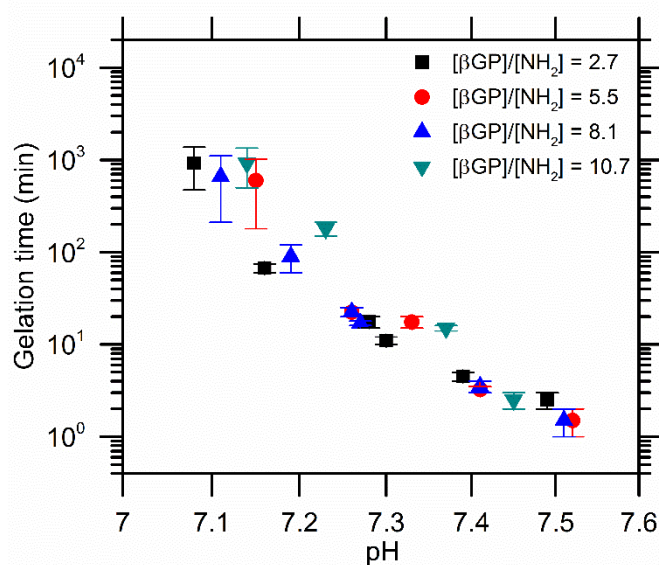


Figure II - 2. Gelation time as a function of pH for formulations CS/ β GP having various ratios of $[\beta\text{GP}]/[\text{NH}_2]$ ranging from 2.7 to 10.7. CS concentration was fixed to 1 wt% and pH was adjusted by changing $[\text{AcOH}]/[\text{NH}_2]$ from 0.6 to 1.5. The gelation times were determined by the test tube inversion method.

We carried out pH titration at 4°C by adding AHP (1 mol.L⁻¹) to solutions having an initial CS concentration of 0.8 wt% and different ratios of $[\beta\text{GP}]/[\text{NH}_2]$. The evolution of pH as a function of $[\text{AHP}]/[\text{NH}_2]$ is reported in **Figure II - 3a**. For a given $[\beta\text{GP}]/[\text{NH}_2]$, all titration curves show an increase in pH with increasing $[\text{AHP}]/[\text{NH}_2]$. Similarly, for a given $[\text{AHP}]/[\text{NH}_2]$, pH increases with increasing $[\beta\text{GP}]/[\text{NH}_2]$. From those curves, we extracted the pairs of ratios $[\beta\text{GP}]/[\text{NH}_2]$ and $[\text{AHP}]/[\text{NH}_2]$

producing a given pH and built the iso-pH curves represented in **Figure II - 3b**. Those iso-pH curves are linear in the studied range of pH from 7.0 to 7.4. Formulations using the ratios of the iso-pH curve at 7.4 but different initial CS concentrations (0.5 and 0.6 wt%) exhibit a pH 7.4 as well, which confirms that the pH is fully determined by the ratios $[\beta\text{GP}]/[\text{NH}_2]$ and $[\text{AHP}]/[\text{NH}_2]$, irrespectively of the CS concentrations.

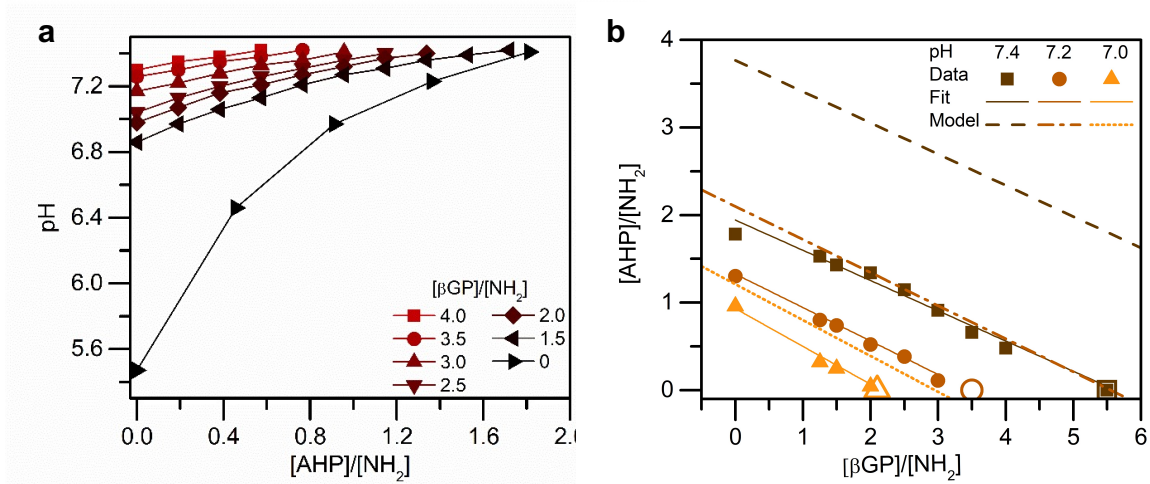


Figure II - 3. (a) Evolution of the pH as a function of $[\text{AHP}]/[\text{NH}_2]$ for formulations with initial CS concentration of 0.8 wt% and $[\beta\text{GP}]/[\text{NH}_2]$ ranging from 0 to 4. **(b)** Iso-pH curves at 7.0, 7.2 and 7.4 as a function of $[\text{AHP}]/[\text{NH}_2]$ and $[\beta\text{GP}]/[\text{NH}_2]$. Experimental data are shown as filled symbols. Linear fitting curves are shown as continuous lines and model predictions as interrupted lines. Predictions accounting for the polyelectrolyte effect based on Filion et al¹⁷ are shown as open symbols for CS/βGP mixtures ($[\text{AHP}]/[\text{NH}_2] = 0$).

The pH of CS and CS/βGP solutions is known to decrease substantially with increasing temperature.^{18,19} A similar effect was observed in the CS/βGP/AHP formulations. For instance, the pH of a solution at CS 0.8 wt% decreases from 7.40 ± 0.05 at 4°C to 6.95 ± 0.05 at 37°C (**Figure II - 4**). Therefore, it seems more appropriate to target formulations having a pH 7.4 at 4°C to ensure that the pH of cell-laden solutions remains within a physiological range (typically 7.0–7.4) during cell dispersion and encapsulation.

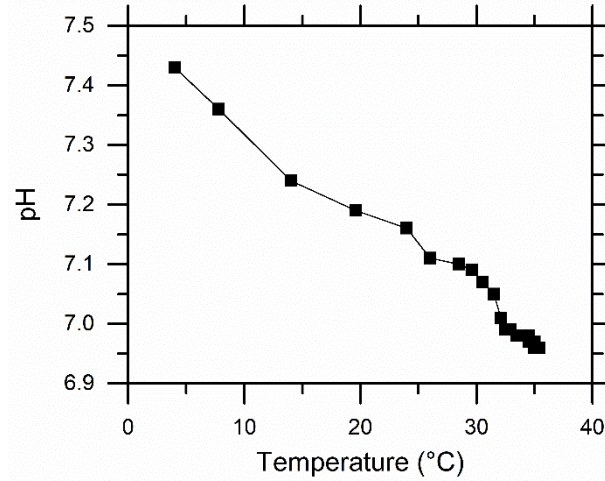
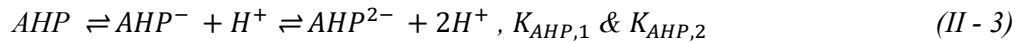


Figure II - 4. Evolution of the pH as function of temperature for formulation prepared with 0.8 wt% of CS, $[\beta GP]/[NH_2] = 1.5$ and $[AHP]/[NH_2] = 1.4$.

The linear relationship observed in **Figure II - 3b** can be rationalized by considering the dissociation of the different species present in the solution, as follows:



The values of the dissociation constants of AHP and βGP were measured by pH titration at 4°C and 25°C (**Appendix A**). Only the second equilibrium is observed for pH ranging from 2 to 8: $K_{AHP,2} = 10^{-6.7}$ and $K_{\beta GP,2} = 10^{-6.2}$. For CS and AcOH, values are chosen from the literature: $K_{CS} = 10^{-7.1}$ (4°C) and $K_{Ac} = 10^{-4.8}$ (25°C).^{20,21}

To a first approximation, we assume here that CS behaves like a small molecule and we do not take into account its polyelectrolyte nature. Electroneutrality implies:

$$[AcO^-] + [AHP^-] + [\beta GP^-] + 2[AHP^{2-}] + 2[\beta GP^{2-}] + [OH^-] = [NH_3^+] + [H^+] + [NH_4^+] + [Na^+] \quad (II - 6)$$

As the working pH is near neutral, the first equilibrium whose pKa is around 2 for both salts may be neglected. Thus, according to the conservation of matter:

$$2([AHP^-] + [AHP^{2-}]) = [NH_4^+] \quad (II - 7)$$

$$2([\beta GP^-] + [\beta GP^{2-}]) = [Na^+] \quad (II - 8)$$

By substituting (II - 7) and (II - 8) into (II - 6), we obtain:

$$[AcO^-] - [AHP^-] - [\beta GP^-] + [OH^-] = [NH_3^+] + [H^+] \quad (II - 9)$$

By using the acid-base equilibria (II - 1) - (II - 5), equation (II - 9) becomes:

$$\frac{[AcOH]}{1 + \frac{h}{K_{Ac}}} - \frac{[\beta GP]}{1 + \frac{K_{\beta GP,2}}{h}} - \frac{[AHP]}{1 + \frac{K_{AHP,2}}{h}} - \frac{[NH_2]}{DD(1 + \frac{K_{CS}}{h})} + \frac{K_e}{h} - h = 0 \quad (II - 10)$$

with h is the concentration of proton H^+ ; $[AcOH]$, $[\beta GP]$, $[AHP]$, $[NH_2]$ are respectively the initial concentrations of AcOH, βGP , AHP and D-glucosamine monomer; DD is the degree of deacetylation of the chitosan.

Defining denominators as: $C_{Ac} = \frac{1}{1 + \frac{h}{K_{Ac}}}$, $C_{\beta GP} = \frac{1}{1 + \frac{K_{\beta GP,2}}{h}}$, $C_{AHP} = \frac{1}{1 + \frac{K_{AHP,2}}{h}}$ and $C_{CS} = \frac{1}{1 + \frac{K_{CS}}{h}}$ and

normalizing by $[NH_2]$ equation (II - 10) can be re-written as:

$$\frac{[AHP]}{[NH_2]} = -\frac{C_{\beta GP}}{C_{AHP}} \cdot \frac{[\beta GP]}{[NH_2]} + \frac{C_{Ac}}{C_{AHP}} \cdot \frac{[AcOH]}{[NH_2]} - \frac{C_{CS}}{C_{AHP} \cdot DD} + \frac{(\frac{K_e}{h} - h)}{C_{AHP}} \cdot \frac{1}{[NH_2]} \quad (II - 11)$$

Near neutral pH, the term $\frac{(\frac{K_e}{h} - h)}{C_{AHP}} \cdot \frac{1}{[NH_2]}$ is negligible with respect to other terms. Indeed, the pre-factor

$\frac{(\frac{K_e}{h} - h)}{C_{AHP}}$ ranges from 0 to 10^{-8} for pH ranging from 7.0 to 7.4. Hence, for a given pH and a given ratio

$[AcOH]/[NH_2]$ (here is fixed to 1), the relationship between $[AHP]/[NH_2]$ and $[\beta GP]/[NH_2]$ is linear.

The negative slope $-\frac{C_{\beta GP}}{C_{AHP}}$ depends on the pH of the mixture and the dissociation constants of the two salts βGP and AHP. For a fixed ratio $[AcOH]/[NH_2]$, these iso-pH curves remain constant when CS concentration $[NH_2]$ is varied.

$$\frac{[AHP]}{[NH_2]} = -\frac{C_{\beta GP}}{C_{AHP}} \cdot \frac{[\beta GP]}{[NH_2]} + \frac{C_{Ac}}{C_{AHP}} \cdot \frac{[AcOH]}{[NH_2]} - \frac{C_{CS}}{C_{AHP} \cdot DD} \quad (II - 12)$$

where $[AcOH]$, $[\beta GP]$, $[AHP]$, $[NH_2]$ are respectively the initial concentrations in AcOH, βGP , AHP and D-glucosamine monomer, DD is the degree of deacetylation of CS. Factors C_{Ac} , $C_{\beta GP}$, C_{AHP} and C_{CS} are all functions of the concentration in protons h as follows: $C_{Ac} = \left(1 + \frac{h}{K_{Ac}}\right)^{-1}$, $C_{\beta GP} = \left(1 + \frac{K_{\beta GP,2}}{h}\right)^{-1}$, $C_{AHP} = \left(1 + \frac{K_{AHP,2}}{h}\right)^{-1}$ and $C_{CS} = \left(1 + \frac{K_{CS}}{h}\right)^{-1}$.

For a fixed ratio $[\text{AcOH}]/[\text{NH}_2]$, here equal to 1, equation (II-12) captures that for a given pH, the relationship between $[\text{AHP}]/[\text{NH}_2]$ and $[\beta\text{GP}]/[\text{NH}_2]$ is linear. The negative slope $-\frac{C_{\beta\text{GP}}}{C_{\text{AHP}}}$ depends weakly on the pH of the mixture and the dissociation constants of the two salts βGP and AHP . The model predicts the experimental values of the slopes with a good precision including the slight increase when the pH decreases from 7.4 to 7.0, as shown in **Figure II - 3b** and **Table II - 1**. However, it fails to predict the intercept. We attribute this discrepancy to the polyelectrolyte nature of CS. In particular, the protonation of NH_2 along the CS chains is very sensitive to entropic effects and pK_{CS} increases with increasing salt concentration.¹⁷ Accordingly, predictions of pH for CS/ βGP accounting for these polyelectrolyte effects using a model by Filion *et al.* (**Figure II - 5**) are in perfect agreement with our experimental measurements, as indicated by the open symbols in **Figure II - 3b**. The simple small molecule model also confirms that the linear relationship between $[\text{AHP}]/[\text{NH}_2]$ and $[\beta\text{GP}]/[\text{NH}_2]$ is independent on the CS concentration as long as the ratio $[\text{AcOH}]/[\text{NH}_2]$ is fixed. Therefore, such iso-pH curves may serve as an efficient platform to prepare CS/ βGP / AHP formulations having a controlled pH.

Table II - 1. Values of slope and intercept for iso-pH curves from 7.0 to 7.4 determined from experiments or calculations.

pH	7.0		7.2		7.4	
	Slope	Intercept	Slope	Intercept	Slope	Intercept
Calculation	-0.410	1.122	-0.378	2.098	-0.357	3.767
Experiment	-0.432	0.932	-0.382	1.326	-0.345	1.943

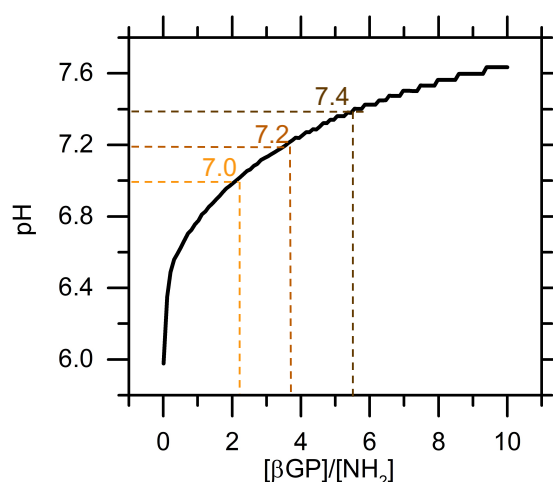


Figure II - 5. Predicted evolution of the pH of CS/ βGP mixture based on the model developed by Filion *et al.*,¹⁷ with following parameters: CS 0.8 wt%; $T = 4^\circ\text{C}$; $[\text{AcOH}]/[\text{NH}_2] = 1$; $DD = 90\%$ and following dissociation constants $pK_{\beta\text{GP},2} = 6.2$; $pK_{\text{CS}} = 7.1$; $pK_{\text{Ac}} = 4.8$. The calculation parameters (using the same notations as in¹⁷) are: the monomer length $l = 0.52$ nm, the radius of the inner cylinder $a = 1.3$ nm.

II.3.2. CS/ β GP/AHP formulations with adjustable pH and osmolarity

The contribution of β GP, AHP and AcOH to the osmolarity of the formulations was determined by measuring independently their osmolarity at different concentrations. We verified that osmolarity was proportional to the molar concentration for all three components (**Figure II - 6**). As expected from the dissociation constants, the osmolarity induced by β GP is higher than the one induced by AHP. The osmolarity of a CS solution at 0.8 wt% is negligible. The total osmolarity (expressed in $\text{Osm}\cdot\text{L}^{-1}$) was calculated as the linear combination of the three contributions:

$$\text{Osmolarity} = 1.03 \cdot [\text{AcOH}] + 2.35 \cdot [\beta\text{GP}] + 1.82 \cdot [\text{AHP}] \quad (\text{II} - 13)$$

Normalizing Equation (7) by $[\text{NH}_2]$ gives a relationship between $[\text{AHP}]/[\text{NH}_2]$ and $[\beta\text{GP}]/[\text{NH}_2]$:

$$\frac{[\text{AHP}]}{[\text{NH}_2]} = -A_1 \cdot \frac{[\beta\text{GP}]}{[\text{NH}_2]} - A_2 \cdot \frac{[\text{AcOH}]}{[\text{NH}_2]} + A_3 \cdot \frac{\text{Osmolarity}}{[\text{NH}_2]} \quad (\text{II} - 14)$$

where $A_1 = 1.29$, $A_2 = 0.57$ and $A_3 = 0.55$ are dimensionless constants.

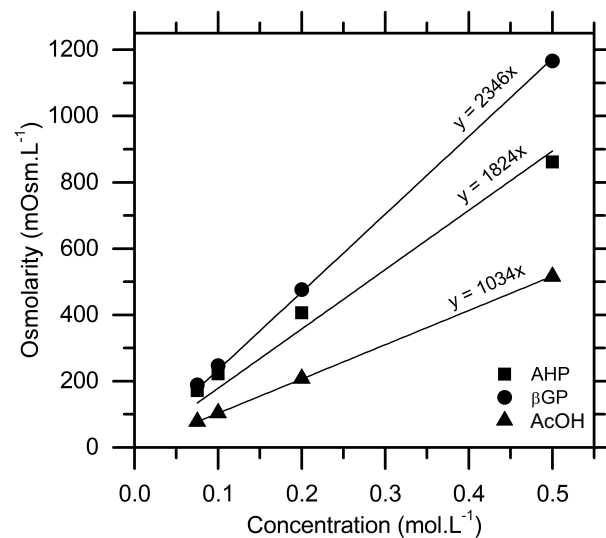


Figure II - 6. Osmolarity values of aqueous solutions of AcOH, AHP and β GP at concentrations ranging from 0.075 to 0.5 $\text{mol}\cdot\text{L}^{-1}$.

For a fixed ratio $[\text{AcOH}]/[\text{NH}_2]$, we obtain linear iso-osmolarity lines between $[\text{AHP}]/[\text{NH}_2]$ and $[\beta\text{GP}]/[\text{NH}_2]$. Unlike the iso-pH curves above, the intercept of these curves depends on the CS concentration. The curves obtained for a physiological osmolarity of $300 \text{ mOsm}\cdot\text{L}^{-1}$ are presented in **Figure II - 7a** for CS concentrations ranging from 0.4 to 1.2 wt%. For a given CS concentration, the intersection between the iso-pH ($\text{pH} = 7.4$) and iso-osmolarity lines give the unique formulation satisfying both conditions on targeted pH and osmolarity.

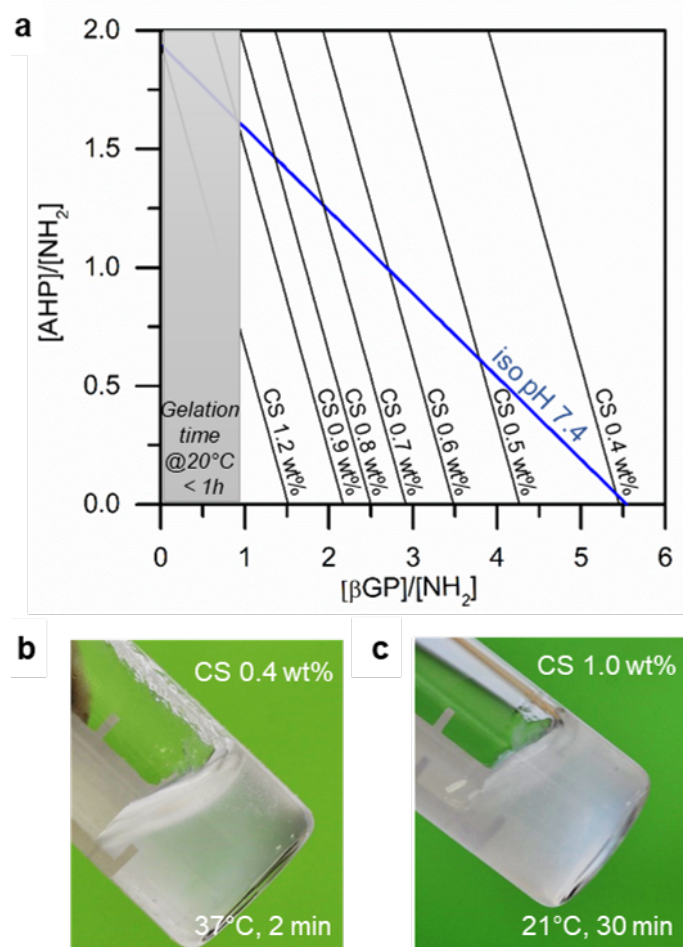


Figure II - 7. (a) Iso-osmolarity curves at 300 mOsm.L^{-1} (black) and iso-pH curve at 7.4 (blue) as a function of $[AHP]/[NH_2]$ and $[\beta GP]/[NH_2]$ ratios for CS concentration ranging from 0.4 to 1.2 wt%. Shaded area indicates formulations for which gelation time at 21°C is less than 1 h. (b) Hydrogel (300 mOsm.L^{-1} ; $\text{pH} = 7.4$) obtained with 0.4 wt% of CS after 2 min of incubation at 37°C , (c) Hydrogel (300 mOsm.L^{-1} ; $\text{pH} = 7.4$) obtained with 1.0 wt% of CS after 30 min at $21 \pm 1^\circ\text{C}$.

The representation in **Figure II - 7a** provides a way to determine the formulations of interest for thermosensitive cell-laden hydrogels. In particular, it shows that the double constraint on pH and osmolarity restricts the range of pertinent CS concentrations. As shown in **Figure II - 7a**, CS concentration of 0.4 wt% is the lowest concentration allowing to achieve physiological pH (7.4) and osmolarity (300 mOsm.L^{-1}). CS concentrations lower than 0.4 wt% would require either a hypotonic mixture to satisfy $\text{pH} = 7.4$ or a basic pH (>7.4) to satisfy an osmolarity of 300 mOsm.L^{-1} . We verified that the physiological formulation at 0.4 wt% corresponding to $[\beta GP]/[NH_2] = 5.5$ and $[AHP]/[NH_2] = 0$ forms a macroscopically homogeneous gel after 2 min at 37°C (**Figure II - 7b**). In **Figure II - 7a**, the highest CS concentration allowing to achieve physiological pH and osmolarity is 1.2 wt%. However, this concentration (corresponding to $[\beta GP]/[NH_2] = 0$) is not pertinent for practical applications, because the gelation time at room temperature (*i.e.* before injection) decreases when decreasing $[\beta GP]/[NH_2]$, as

will be presented in section 3. We found that a minimum ratio $[\beta\text{GP}]/[\text{NH}_2] = 1.0$, corresponding to a CS concentration of 0.9 wt%, is required to maintain the thermosensitive solution in a liquid state for more than 1 h at $21 \pm 1^\circ\text{C}$. A duration of 1 h corresponds to the time needed to comfortably carry out cell trypsination, dispersion in CS/salt solution and injection. Accordingly, solutions prepared at a higher concentration than 0.9 wt% form a gel in less than 1 h at room temperature, as shown for example for a 1 wt% solution ($[\beta\text{GP}]/[\text{NH}_2] = 0.7$, $[\text{AHP}]/[\text{NH}_2] = 1.7$) which formed a gel within 30 min (**Figure II - 7c**).

These results and methodology show how the pH and osmolarity of CS/ β GP/AHP mixtures can be independently adjusted for different CS concentrations. It is worth to note that the concentration range for cytocompatible values of pH and osmolarity has been measured here for one type of CS having a given degree of deacetylation ($DD = 91\%$) and a given molar mass distribution (viscosity 30-100 cps, $M_w = 250 \text{ kg}\cdot\text{mol}^{-1}$). It has been reported that the gelation rate of CS/ β GP solutions at given pH increases with CS of higher DD .²² Therefore, the upper bound of the accessible concentration range is expected to decrease with increasing DD . As regards the molar mass, we verified that the pH can be adjusted by the $[\text{salts}]/[\text{NH}_2]$ ratios whatever the chitosan chain length is as long as the deacetylation degree is known, as shown for CS with $DD = 95\%$ for two different molar masses (**Figure II - 8**). Hence, this rationalized formulation is applicable to other types of CS.

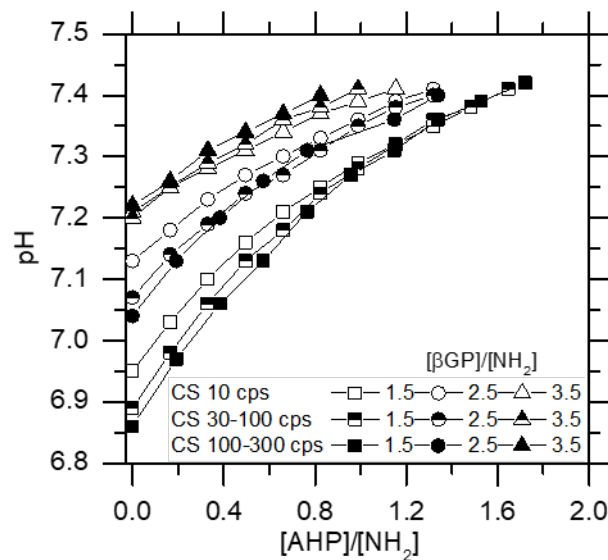


Figure II - 8. Evolution of the pH as a function of $[\text{AHP}]/[\text{NH}_2]$ in formulations with initial CS concentration of 0.8 wt% and fixed $[\beta\text{GP}]/[\text{NH}_2] = 1.5, 2.5$ and 3.5 for three different chitosan grades (10 cps, 30-100 cps and 100-300 cps) having $DD = 95\%, 91\%$ and 95% , respectively.

II.3.3. Gelation kinetics of CS/ β GP/AHP formulations

It is important to notice that the gelation time of CS/ β GP systems depends greatly on the pH.¹⁵ As a result, we focus here on the gelation kinetics at a fixed pH = 7.4.

A systematic characterization of the thermosensitivity of CS/ β GP/AHP mixtures was performed using the test tube inversion method (**Figure II - 9a**). We verified that the time measured by this method is consistent with the time to reach the gel point as determined by rheology (**Figure II - 9b-c**). In a first series of experiments, we studied the effect of the relative salt ratio [AHP]/[β GP] on the gelation time. For that, a fixed CS concentration of 0.8 wt% was chosen. Four ratios [β GP]/[NH₂] were studied (0, 1.5, 3 and 5.5) and the corresponding [AHP]/[NH₂] ratios were adjusted to maintain pH = 7.4 (1.9, 1.4, 0.8 and 0, respectively). In those solutions, the osmolarity varied from 300 to 600 mOsm.L⁻¹. **Figure II - 10a** shows that the gelation time decreases by at least four orders of magnitude when temperature increases from 15°C to 37°C for all four formulations. At a given temperature, the gelation time decreases with decreasing [β GP]/[NH₂] ratio or increasing [AHP]/[NH₂] ratio. This sensitivity to [AHP]/[β GP] becomes increasingly pronounced with decreasing temperature. At 20°C, the formulation with only β GP become a gel more than 100 times slower than the one with AHP only.

The temperature dependence of the gelation time of CS/ β GP formulations was presented in an earlier study by Chenite *et al.* who concluded that the gelation time displayed an exponential decay with temperature.¹⁵ Our data which cover a larger range of times and temperatures do not fit with a simple exponential decay, but rather with a model of critical transition, as already observed in thermosensitive gelatin gels.²³ Our experimental data were successfully fitted with the critical-like model $t_{\text{gel}} = k(T-T_c)^\gamma$ where T_c is a critical temperature above which the sol-gel transition occurs and γ is a critical exponent (**Figure II - 10b**). The exponent γ and the prefactor k decrease with increasing [β GP]/[NH₂] (**Figure II - 11a-b**). Conversely, T_c increases from 4 to 18°C when going from CS/AHP to CS/ β GP as shown in **Figure II - 10c**. Overall these results show that the thermal stability of CS/ β GP/AHP solutions at a fixed pH increases with [β GP]/[NH₂]. This observation supports the hypothesis that the polyol part of β GP hinders the interactions between CS chains as suggested by Supper *et al.*¹⁹

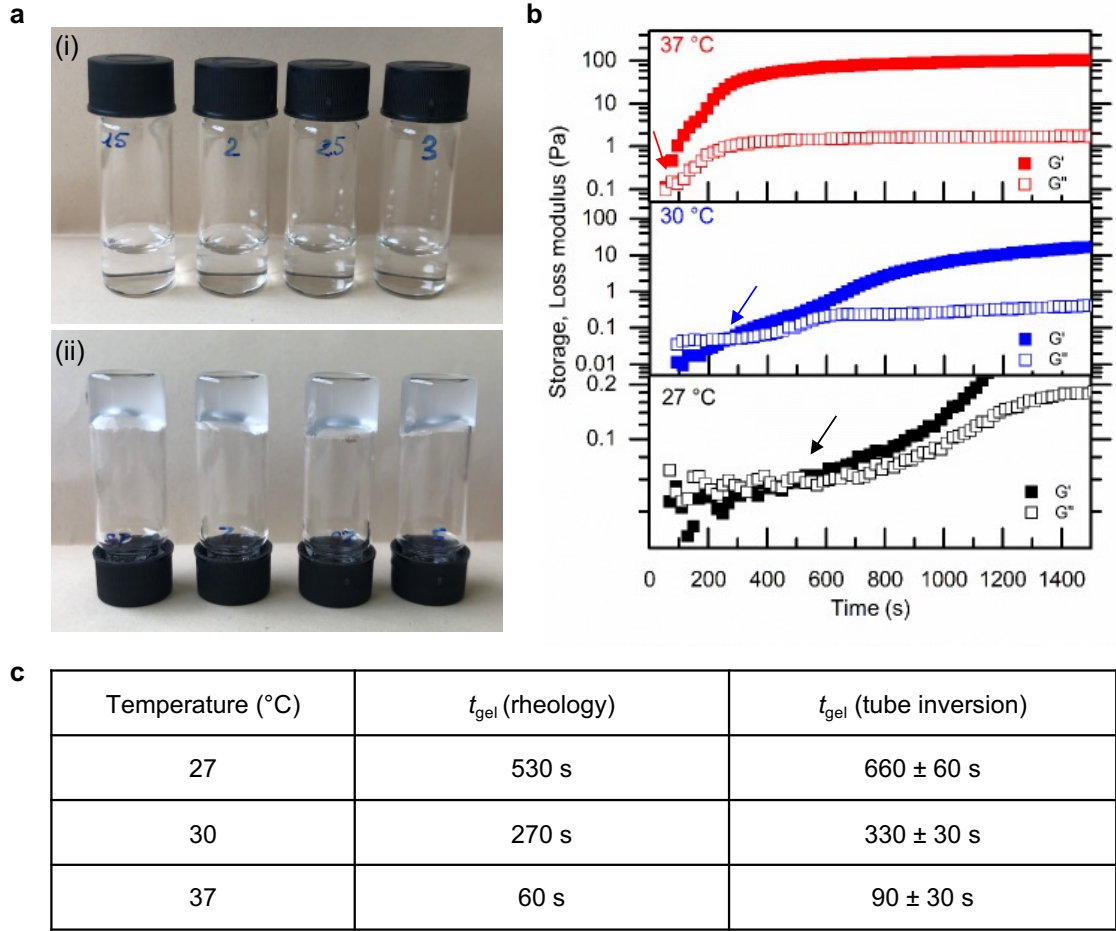


Figure II - 9. (a) Photographs showing the thermosensitive gelation of CS/ β GP/AHP formulations as characterized by the inverted tube method: (i) liquid and transparent state at 21°C; (ii) gel state after 2 min at 37°C. (b) Isothermal rheological experiments ($\omega = 1 \text{ rad}\cdot\text{s}^{-1}$, $\gamma = 1\%$) at various $T = 27, 30$ and 37°C for formulation prepared with CS 0.8 wt%, $[\beta\text{GP}]/[\text{NH}_2] = 1.5$ and $[\text{AHP}]/[\text{NH}_2] = 1.4$, arrows indicate the gel point. (c) Table comparing gelation time obtained with rheological experiment and tube inversion method.

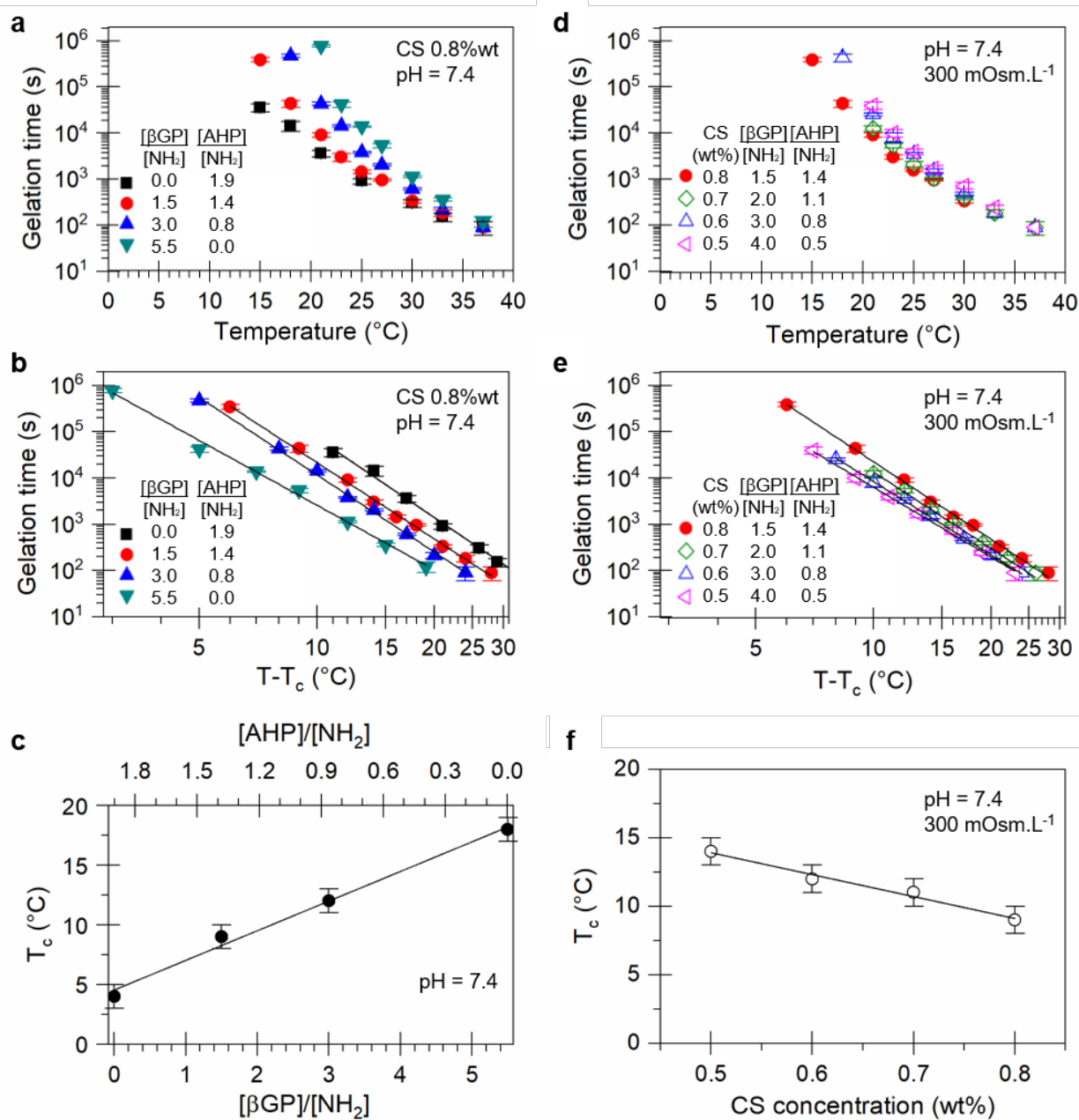


Figure II - 10. (a-c) Gelation kinetics of formulations having fixed CS 0.8 wt% and pH 7.4 and various $[\beta\text{GPI}]/[\text{NH}_2]$ and $[\text{AHP}]/[\text{NH}_2]$ ratios. Gelation time as a function of temperature (a) and $(T-T_c)$ (b). Full lines show fits by a power law. (c) Critical temperature as a function of $[\beta\text{GPI}]/[\text{NH}_2]$ and $[\text{AHP}]/[\text{NH}_2]$. (d-f) Gelation kinetics of physiological formulations ($\text{pH} = 7.4$ and 300 mOsm.L^{-1}) for CS concentration ranging from 0.5 to 0.8 wt%. Gelation time as a function of temperature (d) and $(T-T_c)$ (e). Full lines show fits by a power law. (f) Critical temperature as a function of CS concentration.

Similar experiments were performed in a second series with formulations defined by the iso-pH (7.4) and iso-osmolarity (300 mOsm.L^{-1}) curves for different CS concentrations ranging from 0.5 to 0.8 wt%. The gelation time decayed strongly with increasing temperature in a similar way to the first series, as shown in **Figure II - 10d**. For a given temperature, gelation occurred faster with increasing CS

concentration (together with decreasing $[\beta\text{GP}]/[\text{NH}_2]$ and increasing $[\text{AHP}]/[\text{NH}_2]$ to maintain physiological conditions). Again, a critical power law behavior was observed as shown in **Figure II - 10e** and **Figure II - 11c-d**). The critical temperature, and therefore the thermal stability of the solution, decreased with increasing CS concentration.

From a practical point of view, these results show that all the formulations having physiological pH and osmolarity present an adequate gelation kinetics for use as cell delivery vehicles. At 21°C, they remain liquid for more than 2 h, which is appropriate for cell dispersion and manipulation. At body temperature, they form a gel within less than 1 min, therefore preventing cells from being dispersed away. The injectability of the formulation having a CS concentration of 0.8 wt% was verified using standard injection parameters into a PBS solution at 37°C. A continuous injection could be performed with the quasi-instantaneous formation of a macroscopic hydrogel. The video of the *in vitro* injection experiment can be visualized in this following link, section Supplementary Data:

<https://www.sciencedirect.com/science/article/abs/pii/S0144861721012236?dgcid=coauthor>

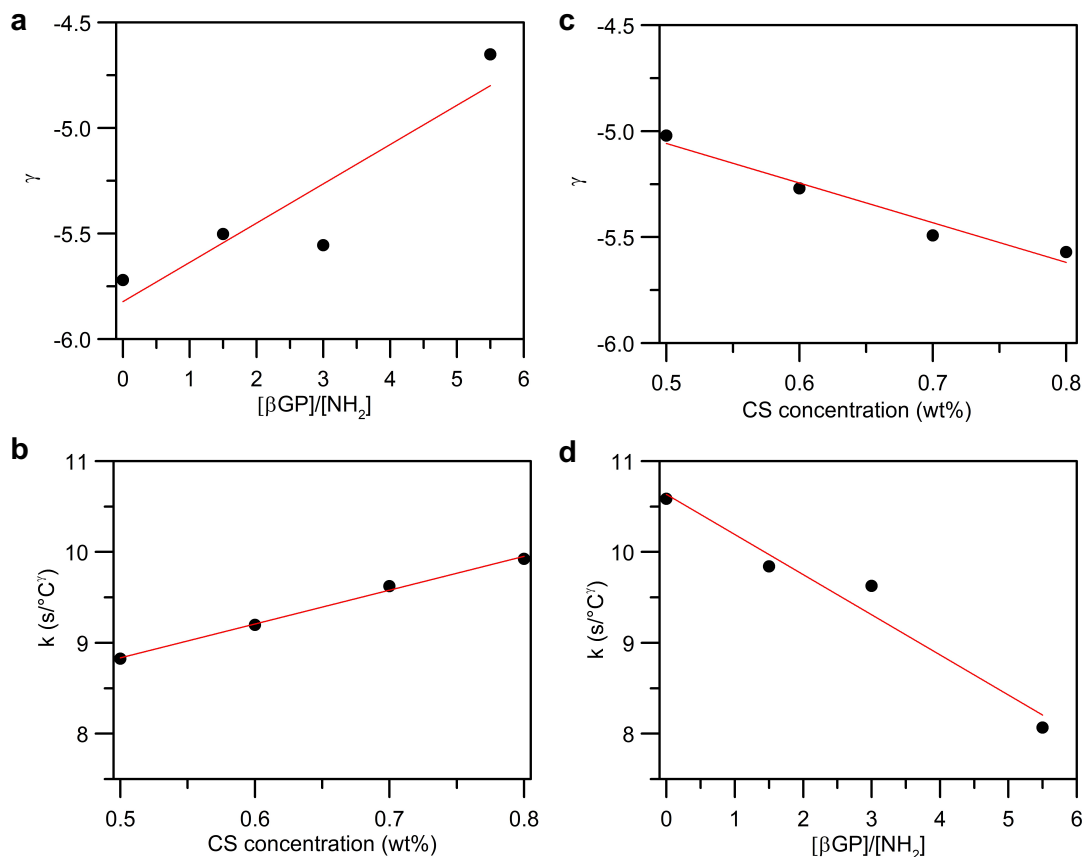


Figure II - 11. Evolution of the exponent γ and the prefactor k : (**a-b**) as a function of $[\beta\text{GP}]/[\text{NH}_2]$ for formulations having a fixed $\text{pH} = 7.4$ and fixed CS concentration at 0.8 wt%; (**c-d**) as a function of CS concentration for physiological formulations ($300 \text{ mOsm}\cdot\text{L}^{-1}$ and $\text{pH} = 7.4$) where $[\beta\text{GP}]/[\text{NH}_2]$ ranges from 1.5 to 4 and $[\text{AHP}]/[\text{NH}_2]$ from 1.4 to 0.5.

II.3.4. Cell encapsulation in CS/ β GP/AHP hydrogels

The viability and the metabolism of encapsulated cells was studied using Live/Dead and AlamarBlue assays with formulations having a CS concentration of 0.8 wt% and pH 7.4. Two formulations were compared to assess the effect of osmolarity: an isotonic formulation denoted CS/ β GP/AHP (300 mOsm.L⁻¹) produced with ratios $[\beta\text{GP}]/[\text{NH}_2] = 1.5$ and $[\text{AHP}]/[\text{NH}_2] = 1.4$, and a hypertonic formulation denoted CS/ β GP (600 mOsm.L⁻¹) obtained with ratios $[\beta\text{GP}]/[\text{NH}_2] = 5.5$ and $[\text{AHP}]/[\text{NH}_2] = 0$. Two cell types were studied: pre-osteoblast immortalized murine cell line (MC3T3-E1) and primary human gingival fibroblasts (HGF). Cells were dispersed in the liquid formulations at 20°C at a concentration of 10⁶ cells.mL⁻¹. Encapsulation was achieved by gelation at 37°C for 1 h in an incubator prior to the addition of culture medium. Cells were stained and observed at 1 h and 24 h after encapsulation. The staining efficiency was verified on positive and negative controls (**Figure II - 12**). The homogeneity of the cell dispersion was verified by cell counting in multiple areas of the gels (**Figure II - 13**) and a local cell concentration of $1.2 \times 10^6 \pm 0.2$ cells per cm³ was found, which is in agreement with the density of seeded cells.

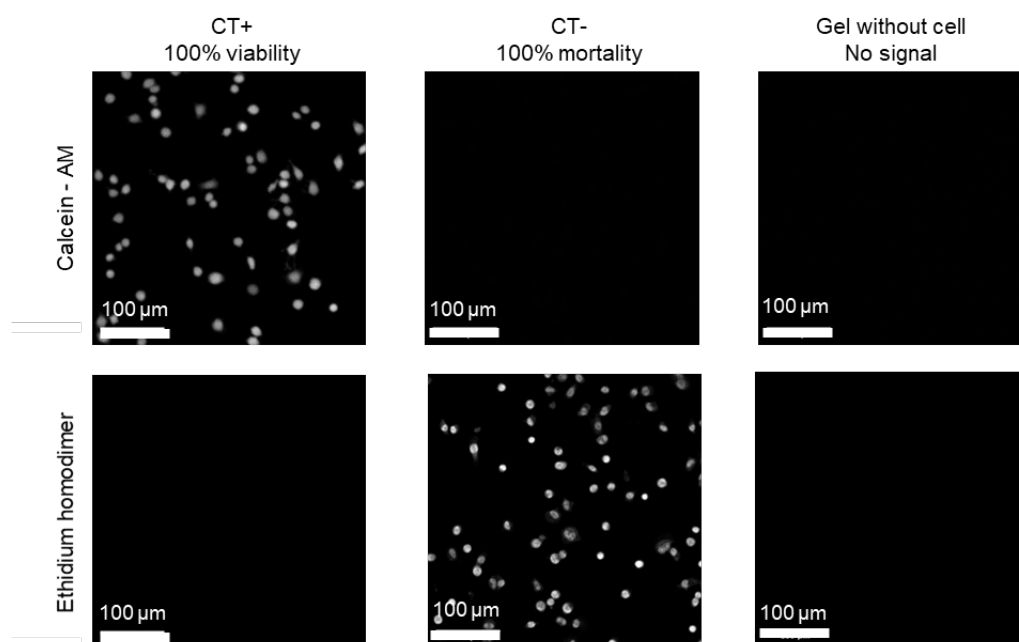


Figure II - 12. Confocal microscopy images for positive control (CT+), negative control (CT-) and CS/ β GP/AHP hydrogel without cells after Live/Dead staining on MC3T3-E1 cells after 1 h of incubation at 37°C.

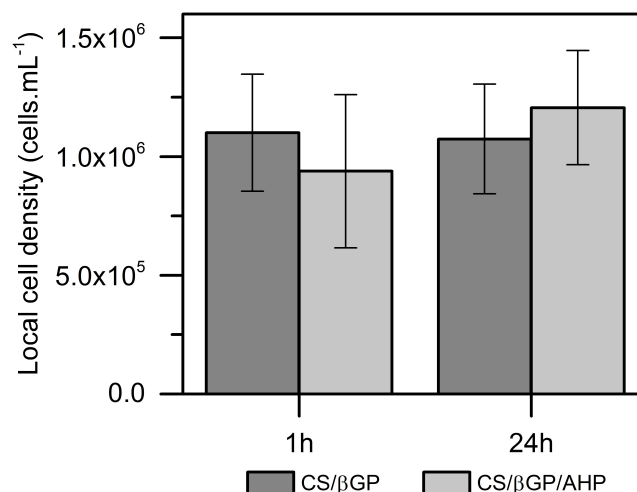


Figure II - 13. Local cell density determined by image analysis for encapsulated MC3T3-E1 at 1 h and 24 h of incubation ($n = 2$, triplicate).

Typical images obtained with Live/Dead staining are shown in **Figure II - 14** for MC3T3-E1 and HGF, respectively. At 1 h, the viability for both cell types is high (90%) for the two studied formulations (**Figure II - 14c**). At 24 h, differences are observed: for MC3T3-E1 cells, a significantly better cell viability is observed in CS/βGP/AHP hydrogel ($78 \pm 6\%$) than in CS/βGP hydrogel ($52 \pm 5\%$); for HGF, cell viability remains high in both hydrogels. The metabolic activity of the encapsulated cells was assessed with an AlamarBlue assay (**Figure II - 14d**). A value of the metabolic activity per cell was estimated by normalizing the measured intensity by the number of living cells. At 1 h, a clear difference can be seen between the two cell types: MC3T3 have a much higher metabolic activity in the isotonic formulation CS/βGP/AHP than in CS/βGP while HGF have a similar metabolic activity in both formulations. At 24 h, the same trend is observed but the metabolic activity drops significantly for both cell types.

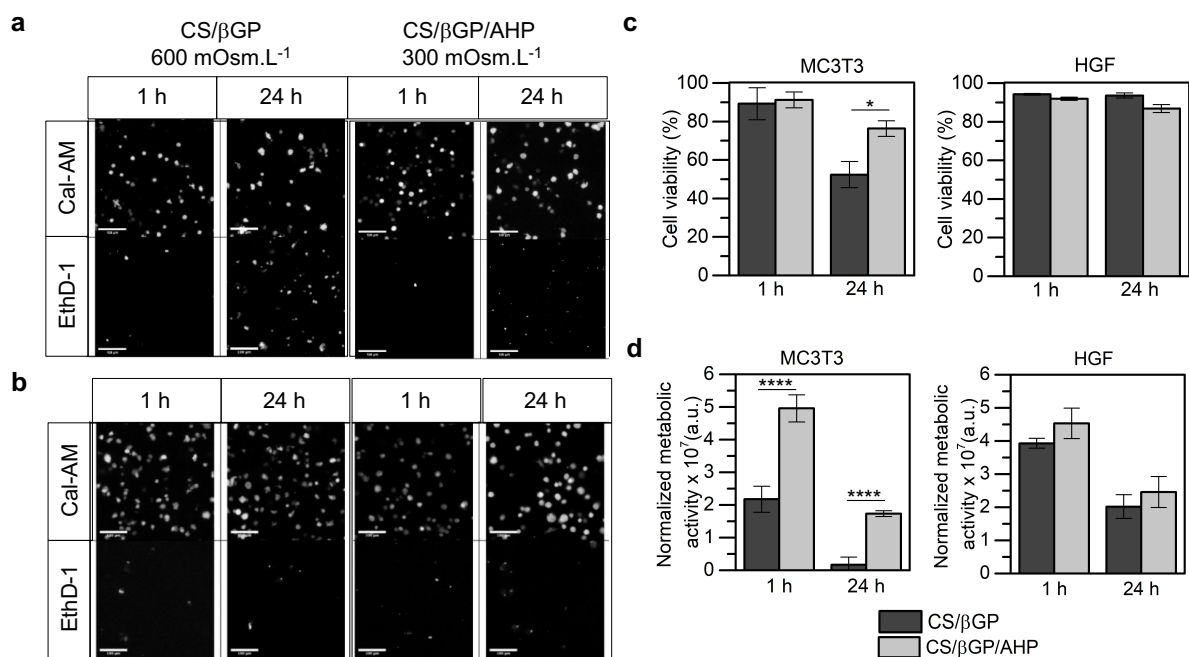


Figure II - 14. Cell encapsulation in CS/βGP/AHP and CS/βGP hydrogels for 1 h and 24 h. (a-b) Confocal microscopy images of Live/Dead assays for MC3T3 (a) and HGF (b) cells. Images are obtained from the projection of 76 slices taken at a random position in the hydrogel with a field of $425 \times 425 \times 300 \mu\text{m}$. (c) Cell viability. (d) Normalized metabolic activity. Statistically significant at $p < 0.05$ (*) or $p < 0.0001$ (****).

These differences in viability and activity may be explained by the different ability of the cell types to adapt to hypertonic conditions.²⁴ To our knowledge, no study has been reported on MC3T3-E1 whereas it has been shown that HGF are resistant to osmotic shocks.²⁵ In our study, the encapsulated cells exhibit rounded phenotypes after 24 h, which reflects a poor adhesion to the chitosan matrix. This observation is in agreement with a previous study on encapsulated MC3T3-E1 in CS/AHP hydrogels.² Therefore, the proposed approach could be advantageously combined with bio-functionalization strategies providing adhesion sites to the encapsulated cells. For example, covalent grafting of peptides or proteins responsible for cell adhesion on chitosan chains have shown promising results.^{26,27}

II.3.5. Mechanical property of CS/βGP/AHP hydrogels

The possibility to vary the CS concentration while maintaining physiological conditions, provides a way to tune the hydrogel properties, such as the mechanical properties. The mechanical properties of hydrogels prepared with 0.5 and 0.8 wt% at 4°C were characterized by oscillatory rheology during an isotherm at 37°C as shown in **Figure II - 15**. Gelation occurs within one minute for both formulations with a rapid increase in the storage modulus (G') reaching approximately 30 Pa for 0.5 wt% and 180 Pa for 0.8 wt% at 1 h of incubation. After 6 h, G' reaches 60 Pa for 0.5 wt% and 300 Pa for 0.8 wt%. These

values of G' are low as compared to the ones of most biological tissues. For this reason, these hydrogels might be more particularly appropriate for very soft tissues, such as brain tissue which G' is in the range 100-300 Pa.²⁸ Accordingly, CS gels were shown to be suitable matrices for cells of the nervous system.

29

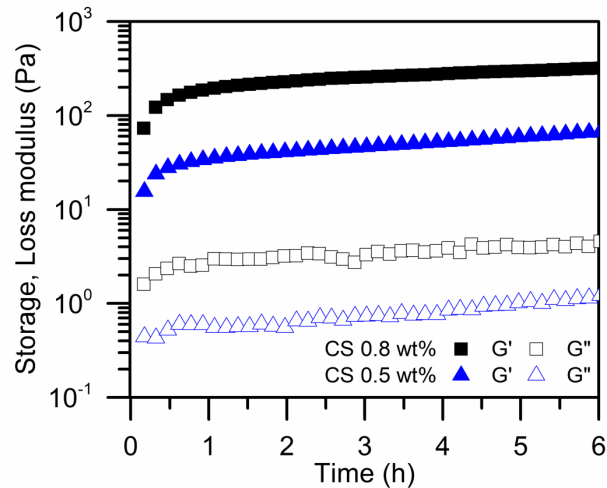


Figure II - 15. Storage modulus (G') and loss modulus (G'') as function of time at 37°C for physiological formulations prepared with a CS concentration of 0.5 wt% ($[\beta\text{GP}]/[\text{NH}_2] = 4.0$ and $[\text{AHP}]/[\text{NH}_2] = 0.5$) and 0.8 wt% ($[\beta\text{GP}]/[\text{NH}_2] = 1.5$ and $[\text{AHP}]/[\text{NH}_2] = 1.4$).

II.4. Conclusion

In this study, we report a rational formulation design to prepare thermo-gelling systems composed of chitosan CS and two phosphate salts, βGP and AHP. We show how the pH and the osmolarity can be adjusted independently by the ratios $[\text{salts}]/[\text{NH}_2]$, arising possibility to obtain physiological formulations having tunable CS concentration. Moreover, a systematic study of the gelation kinetics revealed that the gelation time follows a power law that diverges at a critical temperature. With this approach, injectable solutions having a pH of 7.4 and a physiological osmolarity of 300 mOsm.L⁻¹ can be produced for CS concentrations ranging from 0.4 to 0.9 wt%. The cytocompatibility of the subsequent gels was demonstrated by *in vitro* encapsulation of MC3T3-E1 and HGF cells. Elastic moduli of the gels can reach up to 300 Pa, a value found in brain tissues. The proposed methodology could be applied to solutions of chitosan or functionalized chitosan having various molar mass and deacetylation degrees, therefore providing a general platform to prepare valuable thermosensitive hydrogels for cell encapsulation and delivery.

References

- (1) Ahmadi, R.; De Bruijn, J. D. Biocompatibility and Gelation of Chitosan-Glycerol Phosphate Hydrogels. *J. Biomed. Mater. Res. - Part A* **2008**, *86* (3), 824–832. <https://doi.org/10.1002/jbm.a.31676>.
- (2) Nair, L. S.; Starnes, T.; Ko, J. W. K.; Laurencin, C. T. Development of Injectable Thermogelling Chitosan-Inorganic Phosphate Solutions for Biomedical Applications. *Biomacromolecules* **2007**, *8* (12), 3779–3785. <https://doi.org/10.1021/bm7006967>.
- (3) Ta, H. T.; Han, H.; Larson, I.; Dass, C. R.; Dunstan, D. E. Chitosan-Dibasic Orthophosphate Hydrogel: A Potential Drug Delivery System. *Int. J. Pharm.* **2009**, *371* (1–2), 134–141. <https://doi.org/10.1016/j.ijpharm.2009.01.018>.
- (4) Li, X. Y.; Kong, X. Y.; Wang, X. H.; Shi, S.; Guo, G.; Luo, F.; Zhao, X.; Wei, Y. Q.; Qian, Z. Y. Gel-Sol-Gel Thermo-Gelation Behavior Study of Chitosan-Inorganic Phosphate Solutions. *Eur. J. Pharm. Biopharm.* **2010**, *75* (3), 388–392. <https://doi.org/10.1016/j.ejpb.2010.04.015>.
- (5) Casettari, L.; Cespi, M.; Palmieri, G. F.; Bonacucina, G. Characterization of the Interaction between Chitosan and Inorganic Sodium Phosphates by Means of Rheological and Optical Microscopy Studies. *Carbohydr. Polym.* **2013**, *91* (2), 597–602. <https://doi.org/10.1016/j.carbpol.2012.08.037>.
- (6) Huang, Z.; Yu, B.; Feng, Q.; Li, S. Modification of an Injectable Chitosan Scaffold by Blending with NaHCO₃ to Improve Cytocompatibility. *Polym. Polym. Compos.* **2011**, *19* (9), 781–787. <https://doi.org/10.1177/096739111101900908>.
- (7) Liu, L.; Tang, X.; Wang, Y.; Guo, S. Smart Gelation of Chitosan Solution in the Presence of NaHCO₃ for Injectable Drug Delivery System. *Int. J. Pharm.* **2011**, *414* (1–2), 6–15. <https://doi.org/10.1016/j.ijpharm.2011.04.052>.
- (8) Assaad, E.; Maire, M.; Lerouge, S. Injectable Thermosensitive Chitosan Hydrogels with Controlled Gelation Kinetics and Enhanced Mechanical Resistance. *Carbohydr. Polym.* **2015**, *130*, 87–96. <https://doi.org/10.1016/j.carbpol.2015.04.063>.
- (9) Ceccaldi, C.; Assaad, E.; Hui, E.; Buccionyte, M.; Adoungotchodo, A.; Lerouge, S. Optimization of Injectable Thermosensitive Scaffolds with Enhanced Mechanical Properties for Cell Therapy. *Macromol. Biosci.* **2017**, *17* (6), 1–10. <https://doi.org/10.1002/mabi.201600435>.
- (10) Deng, A.; Kang, X.; Zhang, J.; Yang, Y.; Yang, S. Enhanced Gelation of Chitosan/ β -Sodium Glycerophosphate Thermosensitive Hydrogel with Sodium Bicarbonate and Biocompatibility Evaluated. *Mater. Sci. Eng. C* **2017**, *78*, 1147–1154. <https://doi.org/10.1016/j.msec.2017.04.109>.
- (11) Alinejad, Y.; Adoungotchodo, A.; Grant, M. P.; Epure, L. M.; Antoniou, J.; Mwale, F.; Lerouge, S. Injectable Chitosan Hydrogels with Enhanced Mechanical Properties for Nucleus Pulposus Regeneration. *Tissue Eng. - Part A* **2019**, *25* (5–6), 303–313. <https://doi.org/10.1089/ten.tea.2018.0170>.
- (12) San Juan, A.; Montembault, A.; Gillet, D.; Say, J. P.; Rouif, S.; Bouet, T.; Royaud, I.; David, L. Degradation of Chitosan-Based Materials after Different Sterilization Treatments. *IOP Conf. Ser. Mater. Sci. Eng.* **2012**, *31*, 6–11. <https://doi.org/10.1088/1757-899X/31/1/012007>.
- (13) Kondziolka, D.; Gobbel, G. T.; Fellows-Mayle, W.; Chang, Y. F.; Uram, M. Injection Parameters Affect Cell Viability and Implant Volumes in Automated Cell Delivery for the Brain. *Cell Transplant.* **2011**, *20* (11–12), 1901–1906. <https://doi.org/10.3727/096368911X566190>.
- (14) Bolte, S.; Cordelières, F. P. A Guided Tour into Subcellular Colocalization Analysis in Light Microscopy. *J. Microsc.* **2006**, *224* (3), 213–232. <https://doi.org/10.1111/j.1365-2818.2006.01706.x>.
- (15) Chenite, A.; Buschmann, M.; Wang, D.; Chaput, C.; Kandani, N. Rheological Characterisation of Thermogelling Chitosan/Glycerol-Phosphate Solutions. *Carbohydr. Polym.* **2001**, *46*, 39–47.
- (16) Rinaudo, M. Chitin and Chitosan: Properties and Applications. *Prog. Polym. Sci.* **2006**, *31* (7), 603–632. <https://doi.org/10.1016/j.procpolymsci.2006.06.001>.
- (17) Filion, D.; Lavertu, M.; Buschmann, M. D. Ionization and Solubility of Chitosan Solutions Related to Thermosensitive Chitosan/Glycerol-Phosphate Systems. *Biomacromolecules* **2007**, *8* (10), 3224–3234. <https://doi.org/10.1021/bm700520m>.
- (18) Lavertu, M.; Filion, D.; Buschmann, M. D. Heat-Induced Transfer of Protons from Chitosan to Glycerol Phosphate Produces Chitosan Precipitation and Gelation. *Biomacromolecules* **2008**, *9* (2), 640–650. <https://doi.org/10.1021/bm700745d>.

- (19) Supper, S.; Anton, N.; Seidel, N.; Riemenschnitter, M.; Schoch, C.; Vandamme, T. Rheological Study of Chitosan/Polyol-Phosphate Systems: Influence of the Polyol Part on the Thermo-Induced Gelation Mechanism. *Langmuir* **2013**, *29* (32), 10229–10237. <https://doi.org/10.1021/la401993q>.
- (20) Fillion, D.; Buschmann, M. D. Chitosan-Glycerol-Phosphate (GP) Gels Release Freely Diffusible GP and Possess Titratable Fixed Charge. *Carbohydr. Polym.* **2013**, *98* (1), 813–819. <https://doi.org/10.1016/j.carbpol.2013.06.055>.
- (21) Kortum, G.; Vogel, W.; Andrussov, K. Dissociation Constants of Organic Acids in Aqueous Solution. In *Intern. union of pure and applied chemistry*; London : Butterworths, 1961., Ed.; 1960; p 241.
- (22) Ruel-Gariépy, E.; Chenite, A.; Chaput, C.; Guirguis, S.; Leroux, J. C. Characterization of Thermosensitive Chitosan Gels for the Sustained Delivery of Drugs. *Int. J. Pharm.* **2000**, *203* (1–2), 89–98. [https://doi.org/10.1016/S0378-5173\(00\)00428-2](https://doi.org/10.1016/S0378-5173(00)00428-2).
- (23) Te Nijenhuis, K. Dynamic Mechanical Studies on Thermo-Reversible Ageing Processes in Gels of Polyvinyl Chloride and of Gelatin, Delf University, 1979.
- (24) Dmitrieva, N. I.; Burg, M. B. Hypertonic Stress Response. *Mutat. Res. - Fundam. Mol. Mech. Mutagen.* **2005**, *569* (1–2), 65–74. <https://doi.org/10.1016/j.mrfmmm.2004.06.053>.
- (25) Huynh, N. C. N.; Everts, V.; Leethanakul, C.; Pavasant, P.; Ampornaramveth, R. S. Rinsing with Saline Promotes Human Gingival Fibroblast Wound Healing in Vitro. *PLoS One* **2016**, *11* (7), 1–13. <https://doi.org/10.1371/journal.pone.0159843>.
- (26) Custodio, C.; Alves, C.; Reis, R.; Mano, J. Immobilization of Fibronectin in Chitosan Substrates Improves Cell Adhesion and Proliferation. *J. Tissue Eng. Regen. Med.* **2010**, No. 4, 316–323. <https://doi.org/10.1002/term>.
- (27) Tsai, W. B.; Chen, Y. R.; Liu, H. L. RGD-Conjugated Crosslinked Chitosan Scaffolds for Culture and Osteogenic Differentiation of Mesenchymal Stem Cells. *J. Taiwan Inst. Chem. Eng.* **2013**, *44* (1), 1–7. <https://doi.org/10.1016/j.jtice.2012.09.003>.
- (28) Tabet, A.; Mommer, S.; Vigil, J. A.; Hallou, C.; Bulstrode, H.; Scherman, O. A. Mechanical Characterization of Human Brain Tissue and Soft Dynamic Gels Exhibiting Electromechanical Neuro-Mimicry. *Adv. Healthc. Mater.* **2019**, *8* (10), 1–5. <https://doi.org/10.1002/adhm.201900068>.
- (29) Kornev, V. A.; Grebenik, E. A.; Solovieva, A. B.; Dmitriev, R. I.; Timashev, P. S. Hydrogel-Assisted Neuroregeneration Approaches towards Brain Injury Therapy: A State-of-the-Art Review. *Comput. Struct. Biotechnol. J.* **2018**, *16*, 488–502. <https://doi.org/10.1016/j.csbj.2018.10.011>.

CHAPTER III

MOLECULAR AND MICROSCOPIC MECHANISMS OF
THE SOL/GEL TRANSITION IN CHITOSAN/SALT
MIXTURES

TABLE OF CONTENTS

Résumé en français	127
III.1. Introduction.....	128
III.2. Materials.....	128
III.3. Molecular mechanisms of the sol/gel transition in CS/ β GP/AHP mixtures.....	129
III.3.1. Experimental methods	129
3.1.a. Preparation of stock solutions	129
3.1.b. pH titration.....	129
3.1.c. Rheological measurement	130
3.1.d. Confocal microscopy observation	130
3.1.e. Dynamic light scattering	131
III.3.2. Results	132
3.2.a. Behavior of CS/salt mixtures at 4°C.....	132
3.2.b. Thermally-induced gelation	136
3.2.c. Reversibility of the thermally induced gelation in CS/salt mixtures	138
III.3.3. Discussion.....	138
3.3.a. Ionotropic crosslinking in the presence of divalent salts	139
3.3.b. Hydration layer governs the thermal stability in CS/salt mixtures	140
3.3.c. Mechanism of the thermogelling process in CS solutions	141
3.3.d. Molecular picture of the thermally-induced gelation in CS/ β GP or CS/AHP mixtures.....	143
III.4. Microscopic mechanisms of macropore formation in CS/ β GP/AHP mixtures	145
III.4.1. Experimental methods	146
4.1.a. Preparation of the cytocompatible CS/ β GP/AHP mixture at 0.8 wt%	146
4.1.b. Time-resolved confocal microscopy.....	146
4.1.c. Rheological measurement	146
4.1.d. Small angle dynamic light scattering.....	147
III.4.2. Results	148
4.2.a. Time-resolved confocal observations	148
4.2.b. Rheological characterization of the sol/gel transition	150
4.2.c. Microscopic dynamics during the sol/gel transition	152
III.4.3. Microscopic picture for the emergence of macroporosity in thermosensitive CS/salt mixtures	154
4.3.a. Formation of CS colloidal-like particles	156
4.3.b. Clustering of CS colloidal-like particles	157
4.3.c. Percolation into a network.....	157
4.3.d. Ageing of the hydrogel	157
III.5. Conclusions.....	158
References	159

Résumé en français

Les mécanismes impliqués dans la transition sol/gel du système thermosensible composé de CS et de sels de phosphate, tant au niveau moléculaire que microscopique, sont complexes. Une meilleure compréhension pourrait fournir des idées pour le contrôle du processus de gélification et des propriétés finales du gel. Dans ce chapitre, nous allons nous concentrer sur deux questions principales : 1) Quels sont les mécanismes moléculaires régissant la thermosensibilité des systèmes CS/sels. En particulier, quels sont les effets de la nature et de la structure chimique des sels ? 2) Quels sont les mécanismes impliqués dans l'émergence de la structure macroporeuse de ces hydrogels ?

Dans la première partie de ce chapitre, nos résultats montrent que la formation d'une couche d'hydratation autour des macromolécules de CS est cruciale pour maintenir la solubilité du CS à pH neutre et à basse température. La formation de cette couche d'hydratation ne nécessite pas exclusivement l'utilisation de sels ayant des fonctions polyols mais est plus généralement possible avec des sels établissant des interactions à la fois avec les chaînes CS et les molécules d'eau. En particulier, nous avons identifié un autre sel capable de remplir cette fonction : le sel de sodium de l'acide 2-[N-morpholino]-éthane-sulfonique (MES). Nous avons également démontré l'existence d'un hydrogel à basse température en présence d'un sel divalent tel que l'AHP, et élucidé son mécanisme de formation par réticulation ionotrope. Ce gel est complètement différent du gel induit par la séparation de phases lors du chauffage. Nos résultats combinés avec ceux d'études précédentes de la littérature suggèrent que le processus de thermogélification dans les mélanges CS/sels est dû à la forte dépendance intrinsèque à la température du pKa des monomères D-glucosamine. Quand la température augmente, ce pKa diminue fortement rendant les chaînes CS moins chargées. La couche d'hydratation est donc déstabilisée et se dissocie. L'agrégation ou la gélification se produisent alors quand les forces répulsives sont dépassées par les forces attractives inter-chaînes telles que les liaisons H, les interactions hydrophobes ou la cristallisation. Ces résultats ouvrent des perspectives pour le contrôle de la cinétique de gélification en jouant sur les interactions entre CS-sel et sel-eau, qui sont des paramètres cruciaux dans la conception de matrices cellulaires injectables.

Dans la seconde partie de ce chapitre, la formation de la microstructure d'une formulation CS/βGP/AHP cytotocompatible (CS 0.8 wt%, pH = 7.4, 300 mOsm.L⁻¹) a été étudiée en temps réel. En couplant des observations directes au microscope confocal et des mesures indirectes de rhéologie et de diffusion de la lumière, l'émergence de la macroporosité par l'agrégation et la percolation de particules de CS a été démontrée. Nous découvrons que la formation et l'évolution de la microstructure dans le système CS/sel présentent des caractéristiques très similaires à celles des gels colloïdaux. De plus, nos observations suggèrent qu'il existe un régime où les particules de type colloïdal et les chaînes CS enchevêtrées en solution coexistent, induisant ainsi une dynamique particulière. Ces observations et résultats soulèvent de nouvelles questions, comme la compréhension des effets de la concentration et des caractéristiques du CS sur la macroporosité, ainsi que sur le possible effet de cellules vivantes sur la microstructure de l'hydrogel lors de l'encapsulation. Ces questions seront étudiées dans le chapitre IV.

III.1. Introduction

In the previous chapter, we demonstrated how to prepare CS/βGP/AHP formulations compatible with cell encapsulation and injection. By combining AHP and βGP, we showed how to finely adjust the pH, the osmolarity and the gelation kinetics for various CS concentrations. The mechanisms involved in the peculiar sol/gel transition of this system, both at the molecular and microstructural levels, are complex and still poorly understood. In this chapter, we will focus on two main questions:

Firstly, what are the molecular mechanisms governing the thermosensitive behavior of CS/βGP/AHP mixtures? In particular, what are the roles of the nature and of the chemical structure of the salts in the sol/gel transition?

Secondly, what are the mechanisms involved in the emergence of the macroporous structure in CS/βGP/AHP mixtures?

III.2. Materials

Glacial acetic acid (AcOH, 99%) was purchased from Alfa Aesar. Alexa Fluor 488 was purchased from Abcam. β-glycerophosphate disodium salt hydrate BioUltra (βGP), ammonium hydrogen phosphate BioUltra (AHP), 2-(*N*-morpholino) ethanesulfonic sodium salt (MES) and sodium hydroxide (NaOH) were purchased from Sigma-Aldrich.

In this chapter, we use one grade of chitosan (CS), which is the same CS low molar mass (viscosity 30–100 cps) as the one studied in Chapter II. The overlap concentration, c^* , was determined by viscometry and was found to be around 0.18 ± 0.03 wt% (see Appendix B).

III.3. Molecular mechanisms of the sol/gel transition in CS/ β GP/AHP mixtures

As shown in the literature review (Chapter I, section I.3.2), several studies have investigated the gelation mechanism of CS/salt mixtures at the molecular level. On the one hand, Supper *et al.* showed that the gelation is more strongly hindered when the size of the polyol moiety of the salt increases and proposed that this polyol moiety is responsible for the thermosensitivity by favoring the formation of a hydrated shell of ions and water molecules around them, thus preventing interactions between CS chains.¹ This hypothesis is also supported by a recent calorimetric study by Grinberg *et al.*² On the other hand, Lavertu *et al.* suggested that the thermogelling process is induced by the neutralization of the CS positive charges due to the temperature dependence of the pK_a of the D-glucosamine monomers, whatever the salt is.³ Other inorganic phosphate salts without polyol moieties, like ammonium hydrogen phosphate $(NH_4)_2HPO_4$,⁴ dipotassium hydrogen phosphate K_2HPO_4 ,⁵ basic sodium phosphates as NaH_2PO_4 , Na_2HPO_4 , or even Na_3PO_4 ,⁶ have also been used to produce thermo-sensitive CS solutions. However, in most of these studies, the pH of the CS/salt mixtures was not controlled, whereas it had been shown that the gelation time of CS/ β GP systems depends exponentially on the pH.⁷ Therefore, the precise role of salts in the thermo-gelling process of CS solutions still remains unclear.

In this section, we propose to gain a deeper understanding of this role. For that, we investigated the sol-gel transition in CS/salt mixtures which pH is precisely adjusted. Salts having various characteristic features (monovalent without polyol: MES and NaOH, divalent without polyol: AHP, and divalent with polyol: β GP) were compared combining rheological studies and direct observations by laser confocal scanning microscopy.

III.3.1. Experimental methods

3.1.a. Preparation of stock solutions

Aqueous suspensions of CS were prepared using milliQ water and AcOH at fixed molar ratio $[AcOH]/[NH_2] = 1$ and final concentration of CS at 1.33 wt%. The suspensions were stirred at room temperature ($21 \pm 1^\circ C$) and were stored at $5^\circ C$ until further use. The pH of CS stock solutions is about 5.3 ± 0.1 at $4^\circ C$.

Solutions of β GP, AHP, MES, AcOH at 1 mol.L^{-1} and NaOH at 0.5 mol.L^{-1} were prepared in milliQ water.

3.1.b. pH titration

Stock solutions of titrant as well as CS solution at 0.8 wt% were chilled in an ice bath prior to titration. All pH titrations were performed at $4 \pm 1^\circ C$. The titrant solution was added dropwise to the CS solution under vigorous stirring. Titration was carried out until pH reached the 7.4 value.

3.1.c. Rheological measurement

Physiological formulations prepared with 0.8 wt% of CS and various compositions of salt were studied using a strain-controlled rheometer (MCR502, Anton Paar) with a cone-plate geometry (CP50-2TG). The temperature was managed by a Peltier controller. Formulations were loaded immediately after preparation and silicone oil was added to the interface between the sample and the air to prevent evaporation. The values of storage and loss moduli (G' , G'') were measured at a constant oscillatory strain of 0.1% and an angular frequency of 1 rad.s⁻¹.

For isothermal measurements at 4°C, the geometry was previously stabilized at 4°C. The values of storage and loss moduli (G' , G'') were measured during a period of 10 min.

For temperature sweep measurements, two protocols were used. In the first protocol, we reproduced the same heating profile as the one created on the laser confocal scanning microscope: the temperature was increased by steps from 12°C to 37°C at a rate of 20°C.min⁻¹ with 10 min plateaus at 12°C, 25°C and 37°C. In the second protocol, the temperature was increased continuously from 4°C to 60°C then decreased from 60°C to 4°C, at a rate of 5°C.min⁻¹.

3.1.d. Confocal microscopy observation

CS was labelled with Alexa Fluor 488 (Alexa Fluor monomer units:NH₂ = 1:150) following a protocol adapted from Zhang *et al.*⁸ The fluorescently labelled CS was then added to regular CS suspensions before the autoclave process. Labelled CS chains represented only 0.5 wt% of the total amount of CS in each formulation. The amount of grafted fluorophore was three orders of magnitude smaller than in Zhang *et al.* (AlexaFluor/NH₂ units 1:30000). Hence, the perturbation caused by the labelling was considered to be negligible. Accordingly, there was no difference in gelation time at 37°C between regular CS and fluorescently labelled CS.

A customized sample holder was filled with a few hundreds of microliters of CS/salt solution immediately after mixing. The sample holder was sealed using two glass coverslips and silicon oil was added at areas where evaporation might occur. A thermocouple sensor was inserted via a small aperture on the side of the sample holder which was then sealed using commercial adhesive paste. The setup is illustrated in **Figure III - 1**. The temperature was monitored using a Peltier controller. The temperature was stabilized to 12°C prior to observation. Images of 56 μm × 56 μm were recorded at 12°C, 25°C and 37°C after 10 min of stabilization using confocal microscopy (Zeiss Axiovert 200M) equipped with a laser at 488 nm and objective ×40/0.6 Korr.

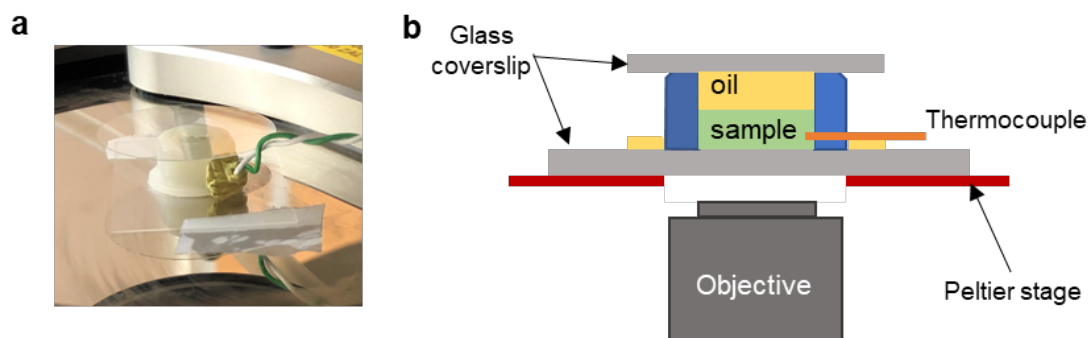


Figure III - 1. Photograph (a) and scheme (b) illustrating the sample holder and the setup for time-resolved confocal observation at controlled temperature.

3.1.e. Dynamic light scattering

Dynamic light scattering (DLS) on CS/ β GP and CS/AHP mixtures at fixed pH = 7.4, 4°C and various CS concentration ranging from 0.1 to 0.5 wt% were performed using a conventional apparatus (ALV/CGS-3 compact Goniometer system). The light source was a He-Ne laser ($\lambda = 632$ nm). The angle ranged from 40° to 90° and q^{-1} ranged from 40 nm to 100 nm. The temperature was controlled by a thermal bath and was stabilized for 10 min before measurements.

III.3.2. Results

3.2.a. Behavior of CS/salt mixtures at 4°C

The pH titration of CS solutions at an initial concentration of 0.8 wt% and $\text{pH} = 5.3 \pm 0.1$ was carried out at $4 \pm 1^\circ\text{C}$ for various bases or salts: NaOH, MES, βGP and AHP (**Table III - 1**). NaOH is a strong base while MES is a monovalent weak base and βGP , AHP are divalent weak bases. βGP is the only base bearing a polyol moiety.

Table III - 1. Molecular structures and pK_a values of the studied bases.

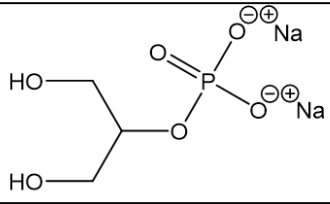
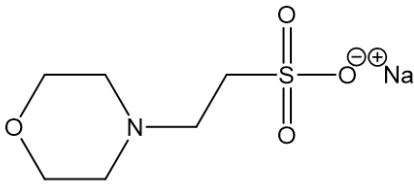
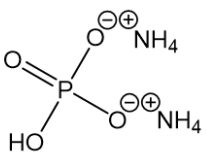
Name	Chemical structure	pK_a , 25°C
β -glycerophosphate, βGP		6.2
2-(N-morpholino)ethanesulfonic sodium salt, MES		6.2
Ammonium hydrogen phosphate, AHP		6.7
Sodium hydroxide, NaOH	$\text{Na}^+ \text{OH}^-$	strong base

Figure III - 2 shows the evolution of the pH as a function of the molar ratio between the concentration in titrant and the concentration in D-glucosamine monomer, $[\text{NH}_2]$. Both solutions of CS with MES and βGP at $\text{pH} 7.4$ and 4°C are transparent and homogeneous to the naked eye. For these two salts, the titration curves at 4°C are very similar and the same ratio $[\text{titrant}]/[\text{NH}_2]$ (~ 5.5) is required to reach $\text{pH} 7.4$. For titration with AHP at 4°C , white macroscopic precipitates appear when the pH reaches the vicinity of 7.0 and they continue to grow with increasing $[\text{AHP}]/[\text{NH}_2]$ and pH . A pH of 7.4 is reached with $[\text{AHP}]/[\text{NH}_2] = 1.8$. For titration with NaOH, precipitates are formed instantaneously when NaOH is added into the CS solution but they re-dissolve after a few minutes of mixing. We suggest that these precipitates are simply due to the very high pH created locally when droplets of NaOH fall into the solution. A transparent solution at $\text{pH} 7.0$ can be obtained at $[\text{NaOH}]/[\text{NH}_2] = 0.54$. Contrarily to the

precipitates formed in the presence of NaOH, the precipitates formed with AHP do not redissolve under stirring, and a macroscopic hydrogel is formed in the absence of stirring.

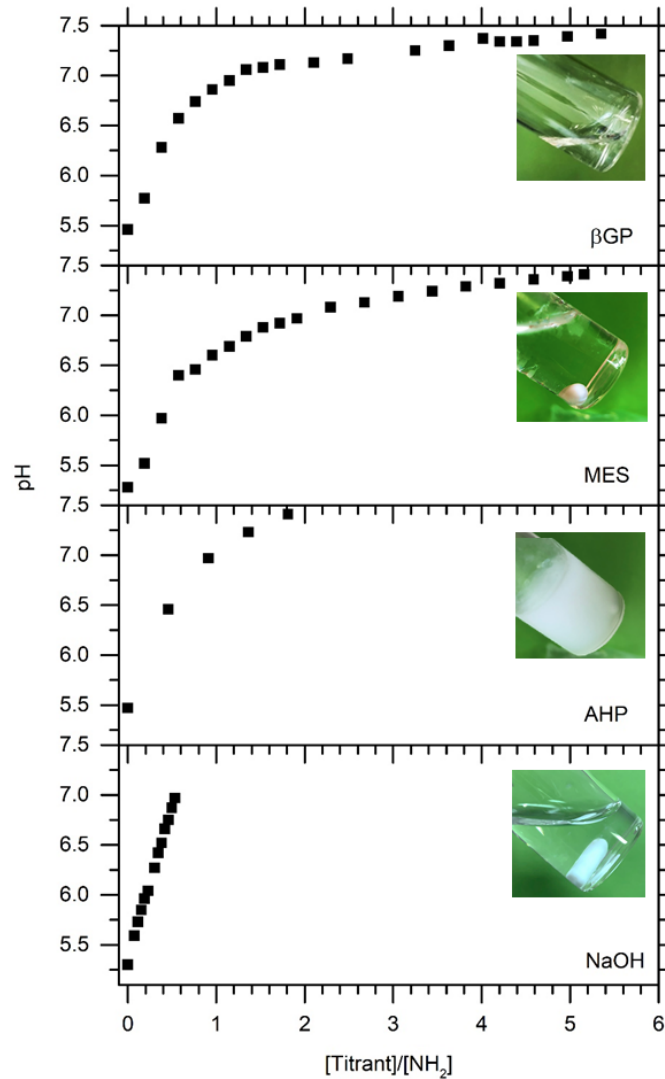


Figure III - 2. Titration at 4°C of CS solutions prepared with an initial concentration of 0.8 wt% with various bases or salts. The inset shows photographs taken at the end of the titration experiments.

The rheological behavior of CS solutions with βGP, with AHP and with a mixture of both salts were studied at a fixed pH 7.4 and at 4°C. We focused on these two salts as they are used for preparing our system of interest. For the CS/βGP mixture, the ratio [βGP/NH₂] was fixed at 5.5. For the CS/AHP mixture, the ratio [AHP]/[NH₂] was fixed at 1.8. The CS/βGP/AHP mixture was prepared with [βGP/NH₂] = 1.5 and [AHP/NH₂] = 1.4, which corresponds to the physiological formulation, as determined in Chapter II. The CS concentration was fixed at 0.8 wt%. The storage, G' , and loss, G'' , moduli of the three mixtures at 4°C were measured during 10 min immediately after mixing, as shown in **Figure III - 3**. The CS/AHP mixture was already a gel when the measurement started and remained stable during the whole measurement. The CS/βGP mixture exhibited macroscopically a liquid behavior

after mixing. In rheological measurement, a continuous increase of both moduli was observed. However, at 10 min, both moduli remained very weak (< 1 Pa). The CS/ β GP/AHP mixture did not exhibit an intermediate behavior and stayed completely liquid during the whole 10 min of the measurement.

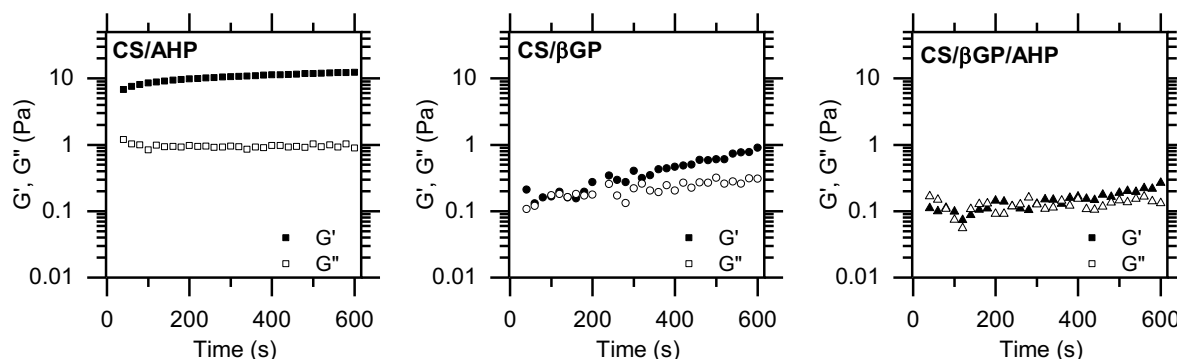


Figure III - 3. Evolution of the storage, G' , and loss, G'' , moduli of CS/AHP, CS/ β GP and CS/ β GP/AHP as a function of time. CS 0.8 wt%, $pH = 7.4$ and $T = 4^{\circ}C$.

To further investigate the effect of the chemical structure of the phosphate salt on CS solutions, dynamic light scattering measurements were performed using a conventional apparatus which angle ranges from 40° to 90° and q^{-1} ranges from 40 nm to 100 nm. Measurements were carried out at $4^{\circ}C$ and $pH = 7.4$ directly after mixing, for CS/ β GP and CS/AHP solutions prepared at different concentrations of CS ranging from 0.1 to 0.5 wt%, corresponding to different regimes from diluted to semi-diluted. **Figure III - 4a** shows the normalized intensity correlation function, $g_2(\tau) - 1$, measured at 90° . The raw data are shown in the Appendix C.

For both CS/ β GP and CS/AHP mixtures, $g_2(\tau) - 1$ is very similar when the concentration of CS is lower than the overlap concentration, $c^* = 0.18$ wt%. Above c^* , for a CS concentration of 0.5 wt%, there is a clear difference in the dynamics between CS/ β GP and CS/AHP. While the $g_2(\tau) - 1$ function of the CS/ β GP mixture remains similar for the three studied CS concentrations, a significant change is observed for the CS/AHP mixture at a CS concentration of 0.5 wt%. This difference was also noticeable to the naked eye: at 0.5 wt%, the CS/AHP mixture formed a turbid liquid while the CS/ β GP mixture was a transparent liquid (**Figure III - 4b**).

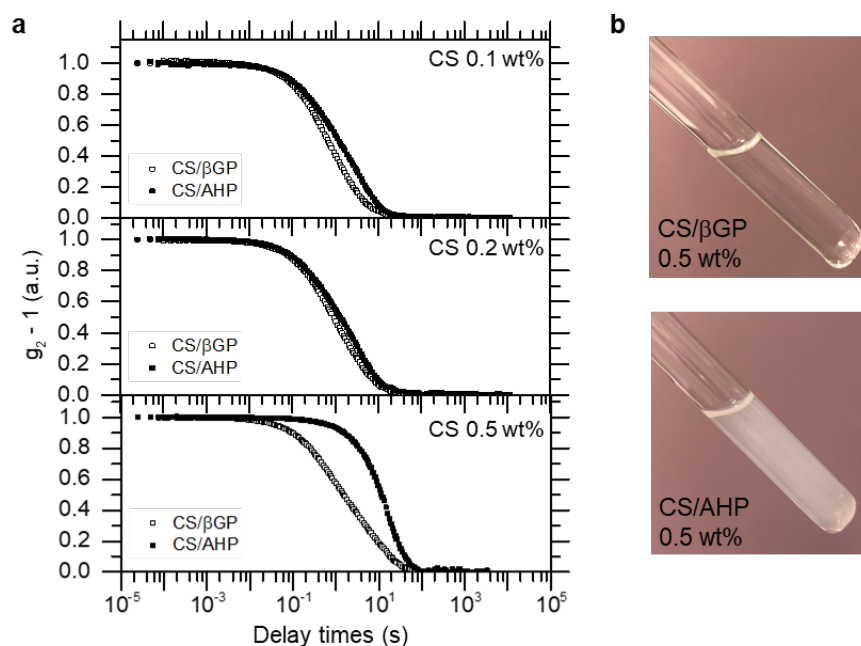


Figure III - 4. a) Normalized intensity correlation function, $g_2 - 1$, measured at 90° ($q^{-1} = 53$ nm) after 15 min at 4°C for CS/βGP and CS/AHP mixtures having $\text{pH} = 7.4$ at various CS concentrations. **b)** Photographs showing CS/βGP and CS/AHP mixtures immediately after mixing.

A characteristic time, τ^* , was extracted from these normalized intensity correlation functions using a fit by a simple exponential decay, $\exp(-2t/\tau^*)$. The evolution of τ^* as a function of the CS concentration for both CS/βGP and CS/AHP mixtures is shown in **Figure III - 5**. For CS/βGP, τ^* increases very slightly from 2 ms for CS 0.1 wt% to 5 ms for CS 0.5 wt%. On the contrary, for CS/AHP, τ^* rises sharply from 3 ms for CS 0.1 wt% to 33 ms for CS 0.5 wt%.

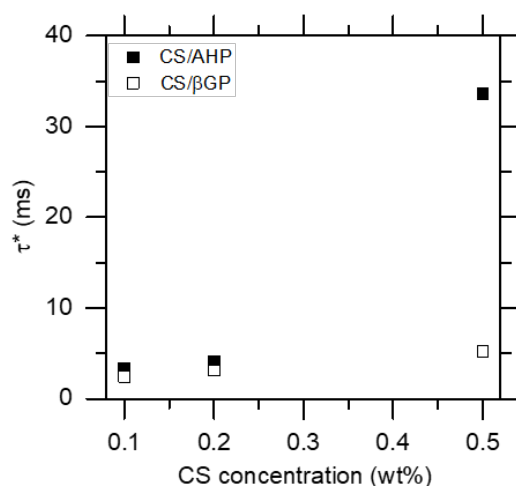


Figure III - 5. Characteristic decay time extracted from the normalized intensity correlation function, τ^* , as a function of CS concentration for CS/AHP and CS/βGP mixtures. $\text{pH} = 7.4$, $T = 4^\circ\text{C}$.

3.2.b. Thermally-induced gelation

The microstructures of fluorescently-labelled CS/AHP, CS/ β GP and CS/ β GP/AHP mixtures were observed by confocal microscopy using a customized setup at controlled temperature. For that, the pH of all three mixtures was adjusted to 7.4 at 4°C. After mixing, the mixtures were poured into a customized sample holder and placed onto the temperature-controlled stage. The temperature was then stabilized at 12°C, then was increased by steps from 12°C to 37°C at a rate of 10°C.min⁻¹ with 10 min plateaus at 12°C, 25°C and 37°C. Images were recorded at the end of the 10 min plateau for each mixture. In a separate experiment, the evolution of the storage and the loss moduli of these three formulations was assessed using oscillatory rheological measurement with the exact same thermal history. The results of both experiments are combined and shown in **Figure III - 6**.

At 12°C, for the CS/AHP mixture, confocal microscopy observations show a dense network, which solid nature is confirmed by rheological measurements (**Figure III - 6a-i, ii**). The storage modulus increases continuously from 0.1 to 0.8 Pa during this period. For CS/ β GP, confocal observations show a homogeneous aspect and no visible objects are detected at the observation scale during 10 min (**Figure III - 6b-i, ii**). Accordingly, rheology indicates a liquid behavior. The results are similar for the CS/ β GP/AHP mixture (**Figure III - 6c-i, ii**).

Upon heating to 25°C, for CS/AHP, a little decrease of G' is observed which corresponds to the partial disappearance of the previously observed network at 12°C (**Figure III - 6a-i, iii**). For CS/ β GP, the homogeneous aspect observed by confocal microscopy and the liquid behavior measured by rheology are maintained (**Figure III - 6b-i, iii**). Similarly, CS/ β GP/AHP remains homogeneous and liquid (**Figure III - 6c-i, iii**).

While heating up to 37°C, for the CS/AHP mixture, a decrease in G' is observed around $t = 1300$ s, followed by a sharp increase, indicating the formation of a stronger gel than the one formed at 12°C (**Figure III - 6a-i**). Confocal observations indicate the formation of a network looking different from the first network observed at 12°C (**Figure III - 6a-iv**). For CS/ β GP, G' increases rapidly and the gel point, determined as the cross-over of G' and G'' , is observed around $t = 1500$ s (**Figure III - 6b-i**). Correspondingly, the formation of a network is observed by confocal microscopy (**Figure III - 6b-iv**). Similarly, for CS/ β GP/AHP, the gel point is detected around $t = 1300$ s, along with the formation of a network (**Figure III - 6c-i,iv**). Interestingly, all three formulations show a similar structure consisting of a heterogeneous and porous network. Moreover, the gel strength depends on the composition of the formulation. After 10 min at 37°C the three gels can be ranked as follows: $G'(\text{CS/AHP}) = 41 \text{ Pa} > G'(\text{CS}/\beta\text{GP/AHP}) = 25 \text{ Pa} > G'(\text{CS}/\beta\text{GP}) = 8 \text{ Pa}$.

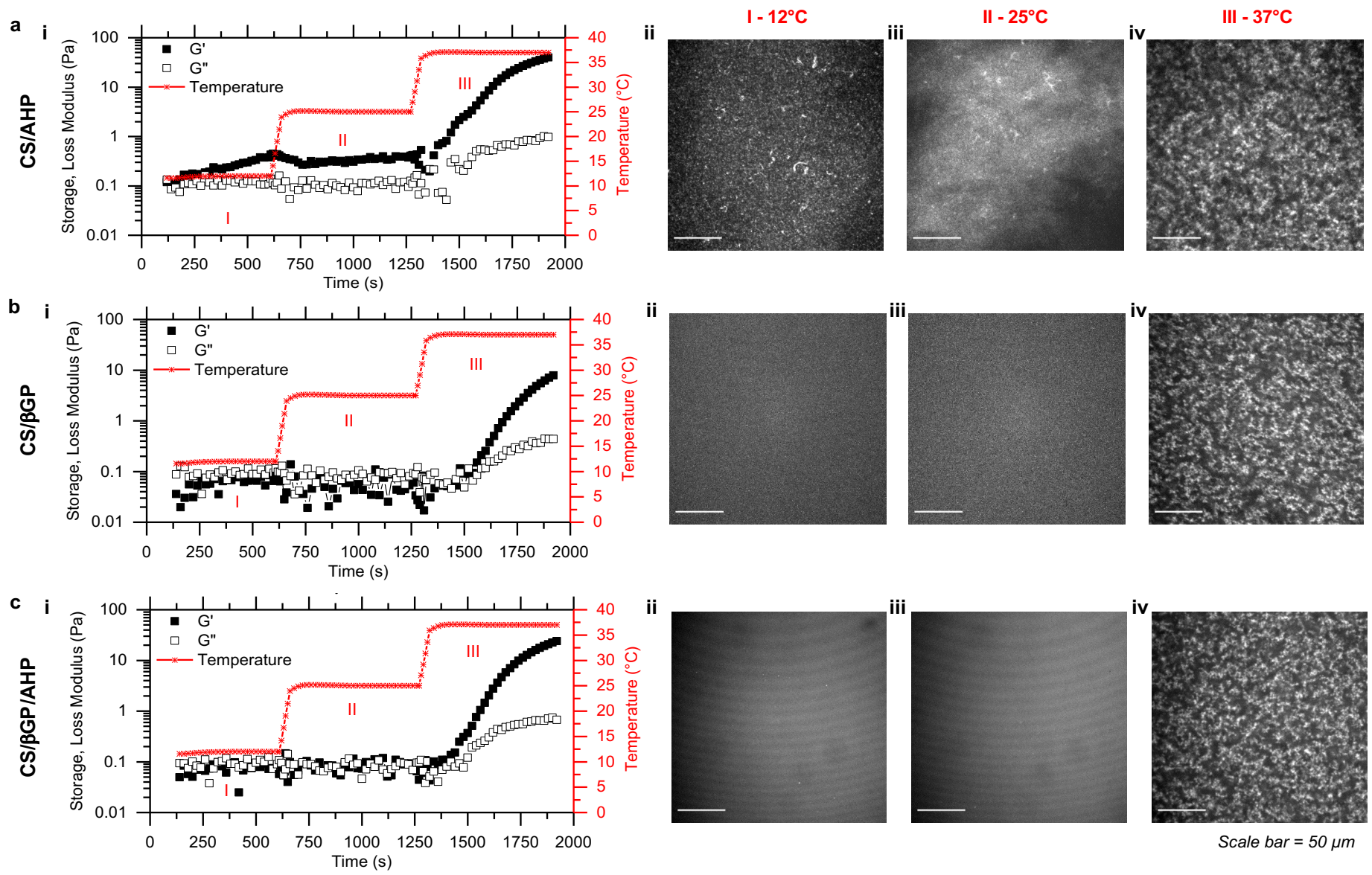


Figure III - 6. Evolution of the storage and loss moduli, and confocal micrographs during a step heating ramp at 12°C, 25°C and 37°C for CS/AHP (a), CS/βGP (b) and CS/βGP/AHP (c). CS 0.8 wt%, pH = 7.4 at 4°C.

3.2.c. Reversibility of the thermally induced gelation in CS/salt mixtures

Within the previous rheological experiment, after 10 min of incubation at 37°C, the reversibility of the thermally induced gelation process in CS/AHP, CS/ β GP and CS/ β GP/AHP mixtures was studied by monitoring G' and G'' upon cooling from 37°C to 12°C (**Figure III - 7a**). The storage modulus remained constant for CS/AHP and CS/ β GP/AHP hydrogels but decreased significantly for CS/ β GP.

In a second experiment, we explored a larger range of temperature, from 60°C to 4°C. All three formulations exhibited a partial reversibility of the gelation indicated by a substantial decrease in G' (**Figure III - 7b**). In particular, the value of G' at 4°C follows the same trend as for the hydrogels formed at 37°C: $G'(\text{CS/AHP}) = 125 \text{ Pa} > G'(\text{CS}/\beta\text{GP/AHP}) = 32 \text{ Pa} > G'(\text{CS}/\beta\text{GP}) = 10 \text{ Pa}$.

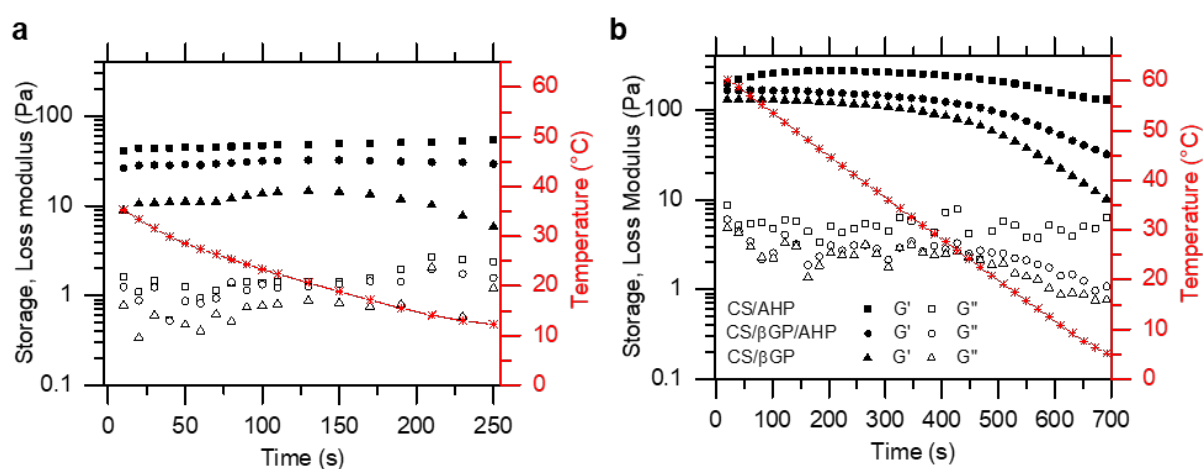


Figure III - 7. Evolution of the storage and the loss moduli for CS/AHP (squares), CS/ β GP/AHP (circles) and CS/ β GP (triangles) upon cooling from 37°C to 12°C (**a**) or from 60°C to 4°C (**b**). Cooling rate = 5°C.min⁻¹, $\gamma = 0.1\%$, $\omega = 1 \text{ rad.s}^{-1}$.

III.3.3. Discussion

In this study, we investigated the temperature-dependence of CS solutions in presence of various salts, all prepared at a same fixed initial pH 7.4 at 4°C. Exploring the effect of the nature and the chemical structure of the salts provides valuable elements in the understanding of the molecular mechanisms governing the behavior of CS/salt mixtures. In the following discussion, we firstly investigate the effect of the valence of the salt and the formation of a gel at low temperature via ionotropic crosslinking. Secondly, by comparing polyol-free salts (MES, AHP) with β GP, we discuss the role of the polyol moiety and the role of the interactions between the salt ions, the CS chains and the water molecules in thermosensitivity. Finally, explanations on the molecular mechanisms involved in the thermally-induced gelation of CS/salt mixtures are proposed.

3.3.a. Ionotropic crosslinking in the presence of divalent salts

We found that CS/AHP mixtures (CS 0.8 wt%, pH = 7.4 at 4°C) form a weak gel at low temperatures, 4°C or 12°C, as shown by confocal microscopy and rheology (**Figure III - 3, Figure III - 6a-i, ii**). This phenomenon is very similar to what has been reported for polyvalent salts like TPP (see Chapter I, section I.3.2.b) and for divalent salts like dibasic sodium phosphate.⁹ Li *et al.* reported the formation of a CS gel at 4°C in the presence of dibasic sodium phosphate and speculated that hydrogen bonds are responsible for this gelation.⁹ However, this might not be the unique explanation. We attribute this gelation to ionotropic crosslinking due to the electrostatic interactions between the positively charged amino groups of CS and the negatively charged phosphate groups of AHP. This hypothesis is confirmed when comparing with a monovalent salt (MES) and with a base (NaOH) for which no gelation was observed at 4°C. Interestingly, for β GP, which is also a divalent salt, G' increased only very slightly and reached 1 Pa after 10 min at 4°C while the mixture stayed completely liquid after 10 min at 12°C (**Figure III - 3, Figure III - 6b-i, ii**). These observations are in agreement with the previous results reported by Supper *et al.*¹ These authors suggested that the polyol moiety on β GP promotes the formation of a hydration protective layer around CS chains, thus contributing to maintain CS in solution even at neutral pHs. Thus, we propose that the ionotropic crosslinking is hindered by such a hydration layer.

The idea of ionotropic crosslinking of CS solutions with polyvalent salts is also supported by the observed dependence of this process on CS concentration and on the molar ratio [salt]/[NH₂]. When the CS concentration in CS/AHP mixtures was increased from 0.2 to 0.5 wt%, we observed a clear transition from transparent to turbid solutions (**Figure III - 4b**) and a strong slowing down of the dynamics, as shown by dynamic light scattering (**Figure III - 5**). These changes coincide with the transition from dilute to semi-dilute regimes which occurs at the overlap concentration $c^* = 0.18 \pm 0.03$ wt%. This is consistent with the idea that CS chains need to overlap in order to create a network cross-linked by ionic complexes. Additionally, titration experiments at 4°C showed that the CS/AHP solution became turbid when the pH reached the vicinity of 7.0 which corresponds to [AHP]/[NH₂] = 1 (**Figure III - 2**). On the contrary, no turbidity was observed with the monovalent salts, NaOH and MES, at the same pH 7.0. This result strongly suggests that there a critical molar ratio is required to reach the gel point by ionotropic crosslinking between AHP and CS. Similar results have been previously reported for the well-known CS/TPP ionogels.¹⁰

Rheological measurements in CS/AHP mixtures at 4°C and 12°C also show that ionogel formation strongly depends on temperature. The gel formed at 4°C is much stronger ($G' = 10$ Pa) than the one formed at 12°C ($G' = 0.8$ Pa) (**Figure III - 3, Figure III - 6a-i, ii**). This can be explained by the temperature-dependence of the pK_a of the D-glucosamine monomers. According to previous studies by Filion, Lavertu and coworkers, the apparent pK_a of CS decreases strongly when the temperature

increases.^{3,11} Therefore, the ionization degree of CS at 12°C is lower than at 4°C, thus the complexation by electrostatic interactions with AHP is less favorable. This effect would also explain the decrease in G' observed in CS/AHP mixtures during the heating ramp from 12°C to 25°C (**Figure III - 6a-i**).

The ionogels formed at low temperatures, 4°C or 12°C, differ from the gels formed when the mixtures are heated. Confocal observations in CS/AHP demonstrate that the microstructure of these two gels is very different, as shown in **Figure III - 6a-ii, iv**. The gel formed at 12°C has a dense structure having no pores at the microscopic scale, while the gel formed at 37°C possesses macropores having sizes up to few tens of microns. This can be explained by the very different physical nature of these two gels. The gel at low temperature is a polymer gel formed by ionotropic crosslinking of CS chains while the gel obtained during heating emerges from a phase separation process. Interestingly, all phase-separated gels formed at 37°C have very similar microstructure whatever the composition of the salts (**Figure III - 6a-c, iv**). This suggests that the formation of a ionogel at low temperature, even if this gel is not completely dissolved while heating, does not significantly alter the formation of the phase separated gel.

3.3.b. Hydration layer governs the thermal stability in CS/salt mixtures

In Chapter II, we compared CS/ β GP and CS/AHP mixtures and showed that the gelation kinetics greatly depends on the chemical structure of the salts (**Figure II-14**). In particular the critical temperature, T_c , defined as the temperature above which the sol/gel transition occurs, was found to increase with increasing β GP content. T_c is significantly lower for CS/AHP mixtures ($4 \pm 1^\circ\text{C}$) than for CS/ β GP mixtures ($18 \pm 1^\circ\text{C}$). This difference in thermal stability is well explained by the presence of polyol moieties in β GP, which induce the formation of a hydration layer, as discussed in the previous sections.

Interestingly, our results show that a polyol-free salt, MES, can be used to neutralize CS solutions without inducing immediate precipitation or gelation. In a previous study, Lavertu *et al.* reported the thermally-induced CS precipitation in the presence of MES and concluded that the polyol moiety is not essential.³ However, in their study, the pH of the mixture was not given. No clear explanation was proposed to clarify why CS chains can remain in solution at neutral pH at room temperature with MES. We propose that MES is able to form ionic interactions with the amine groups of CS and to form H-bonds with water molecules via electronegative atoms, as illustrated in **Figure III - 8a**. Despite the absence of polyol moieties in MES, these interactions should lead to the creation of a hydration shell in a similar manner as with β GP, as illustrated in **Figure III - 8b**. Thus, we suggest that the solubility of CS can be maintained at neutral pHs and low temperatures using other salts than β GP as long as the conditions required for the formation of the hydration layer are fulfilled.

Our results show that the liquid state obtained with CS/MES mixtures is more stable than with the CS/ β GP mixtures: $t_{\text{gel}}(\text{CS/MES}) = 5 \pm 0.5 \text{ min} > t_{\text{gel}}(\text{CS}/\beta\text{GP}) = 2 \pm 0.5 \text{ min}$ at 37°C. We propose to explain this result by the difference in the strength of the hydration layer formed by these two salts

around CS chains. In particular, MES can form a stronger H-bond with the nitrogen atom, $\text{OH}\cdots\text{N}$ ($\Delta H = -7.65 \text{ kcal.mol}^{-1}$), than βGP with the oxygen atom, $\text{OH}\cdots\text{O}$ ($\Delta H = -5.02 \text{ kcal.mol}^{-1}$).¹² Moreover, the distance between the ionizable group and the farthest group forming H-bond is larger in MES than in βGP . As reported by Supper *et al.*, larger distances between the ionizable group and the group forming H-bond improve the protection of CS chains from self-interaction.¹ Therefore, it is reasonable to assume that the hydration layer formed in the presence of MES is more stable than the one formed by βGP .

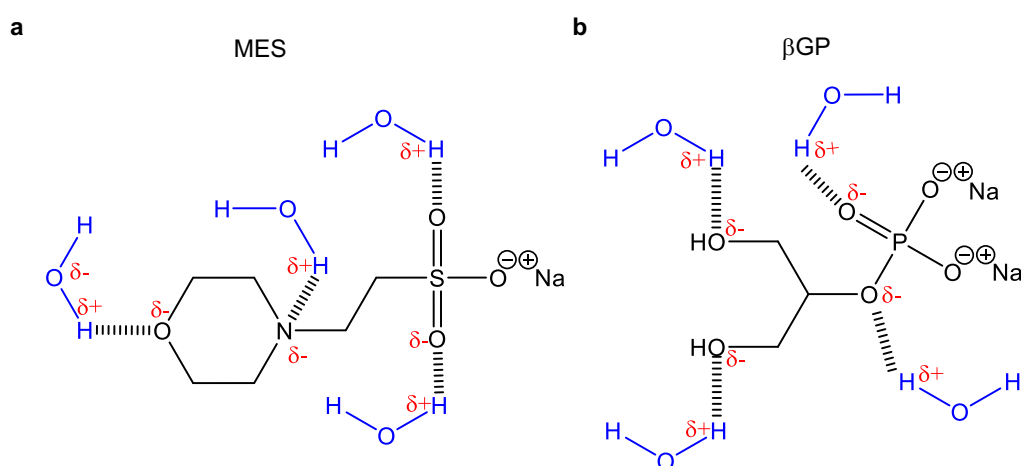


Figure III - 8. Possible H-bonds formed by MES (a) and βGP (b) in aqueous solution.

3.3.c. Mechanism of the thermogelling process in CS solutions

The three CS/AHP, CS/ βGP and CS/ βGP /AHP mixtures form a very similar gel after heating. In chapter II, we demonstrated that the gelation kinetics obeys to the same power law for all of these systems. Moreover, the microstructure of the gel formed at 37°C exhibits the same features whatever the composition of the mixture (Figure III - 6a-c, iv). These results strongly suggest that the same mechanisms are governing this thermally induced gelation, independently of the interactions between the salts and CS chains. This observation is consistent with the explanation by Lavertu and coworkers^{3,11} who proposed that the thermosensitivity of CS solutions would be due to the intrinsic temperature-dependence of the $\text{p}K_a$ of the D-glucosamine monomers. They found that this $\text{p}K_a$ decreases strongly when the temperature increases. As a result, an increase in temperature leads to a strong decrease in the ionization degree of CS chains until a critical value where repulsive CS-CS electrostatic forces are overcome by attractive interchain forces, inducing CS aggregation. However, this might not be the only explanation.

Our results showed that in the presence of some specific salts, a hydration layer can be formed and plays an important role, which is consistent with the suggestion of Supper *et al.*¹ about the role of the polyol moiety. However, we would like to stress that the thermally-induced gelation does not originate from

these specific CS-salt and salt-water interactions, as suggested by our observations on the CS/AHP mixture. The gelation of CS/salt mixtures should occur when the CS-CS electrostatic repulsion and the energy barrier created by the hydration layer can no longer prevent the aggregation driven by attractive interchain forces, which can be H-bonds, hydrophobic interactions or crystallization. In other words, CS aqueous solutions can intrinsically exhibit a thermosensitive sol/gel transition and the addition of some specific salts inducing the formation of a protective hydration layer provides a way to shift this sol/gel transition to higher temperatures.

These molecular mechanisms can also explain the reversibility of thermogelling upon cooling. At pH 7.4, a partial reversibility with a large hysteresis was observed for all three studied mixtures (**Figure III - 7**), similarly to previous observations in CS/ β GP.¹³ Upon cooling, the pK_a of CS increases, leading to the re-ionization of D-glucosamine monomers. On the one hand, this leads to an increase of the repulsive electrostatic forces. On the other hand, this restores the interactions between the salt and the CS chains, thus inducing the reformation of a hydration layer and a weakening of the gel. For these reasons, the reversibility is emphasized when the content in β GP increases. The important hysteresis observed in all the systems can be explained by the energy barrier that must be overcome to disrupt the previously formed aggregates. This energy barrier is expected to depend strongly on the pH of the mixture. For instance, Chenite *et al.* reported a complete reversibility to liquid state for CS/ β GP having pH = 6.85 at 4°C.¹³ While no clear explanation was given by these authors, we propose that for mixtures having lower pH, the ionization degree of CS is higher, thus hindering the aggregation of CS chains and making the reversibility easier.

We remark that the thermogelling process and its reversibility in CS/salt mixtures is very similar to the thermosensitive coil-to-globule transition in aqueous solutions of poly(N-isopropylacrylamide), PNIPAM. PNIPAM possesses a low critical solution temperature (LCST) in the vicinity of 32°C, below which the polymer is in random coil conformation (soluble) and above which the polymer undergoes a transition to globule conformation (insoluble).¹⁴⁻¹⁸ At temperatures below the LCST, hydrogen bonds between the polymer and water molecules are formed along the polymer chain due to the cooperative interaction between nearest-neighboring bound water, making PNIPAM soluble.¹⁵ When temperatures exceeds the LCST, these hydrogen bonds are broken, leading to collapse of PNIPAM chains via hydrophobic interactions between nonpolar groups.¹⁶

3.3.d. Molecular picture of the thermally-induced gelation in CS/ β GP or CS/AHP mixtures

To summarize, we investigated in this study the behavior of CS solutions in the presence of different bases/salts for which the pH was precisely adjusted to 7.4 at 4°C prior to experiments. From these results, we propose a picture explaining the molecular mechanisms governing the temperature-dependent behavior of CS solutions in the presence of β GP or AHP salts. This molecular picture is shown in **Figure III - 9** and is described below.

a. At $\text{pHs} < \text{p}K_{\text{app}}$ and at 4°C or room temperature, CS behaves like a cationic polyelectrolyte, thus is soluble thanks to electrostatic repulsion.

b. At $\text{pHs} > \text{p}K_{\text{app}}$ and at 4°C, two situations depending on the characteristics of the two studied salts are presented below.

i) For **CS/ β GP**, the solubility of CS is maintained thanks to a hydration layer. This hydration layer relies on the electrostatic interactions between the anionic phosphate groups and the cationic amino groups, and the H-bonding between the polyol and water molecules. Such hydration layer can be induced by other polyol-free salts, such as MES, as long as they can interact with both CS and water. Due to the divalent nature of β GP, some interchain ionically crosslinked points can be formed; however, this process is strongly hindered by the presence of the hydration layer.

ii) For **CS/AHP**, a weak ionogel is formed by ionotropic crosslinking due to the electrostatic interactions between the positively charged amino groups of CS and the negatively charged phosphate groups of AHP. No hydration layer can be formed in the presence of AHP, therefore the formation of the ionogel is more favorable in presence of AHP than β GP.

c. At $\text{pHs} > \text{p}K_{\text{app}}$ and $T > T_c$, CS aqueous solutions intrinsically exhibit a thermosensitive sol/gel transition whatever the interactions between CS chains and the salts. The addition of some specific salts, like β GP or MES, inducing the formation of a protective hydration layer provides a way to shift this sol/gel transition to higher temperatures.

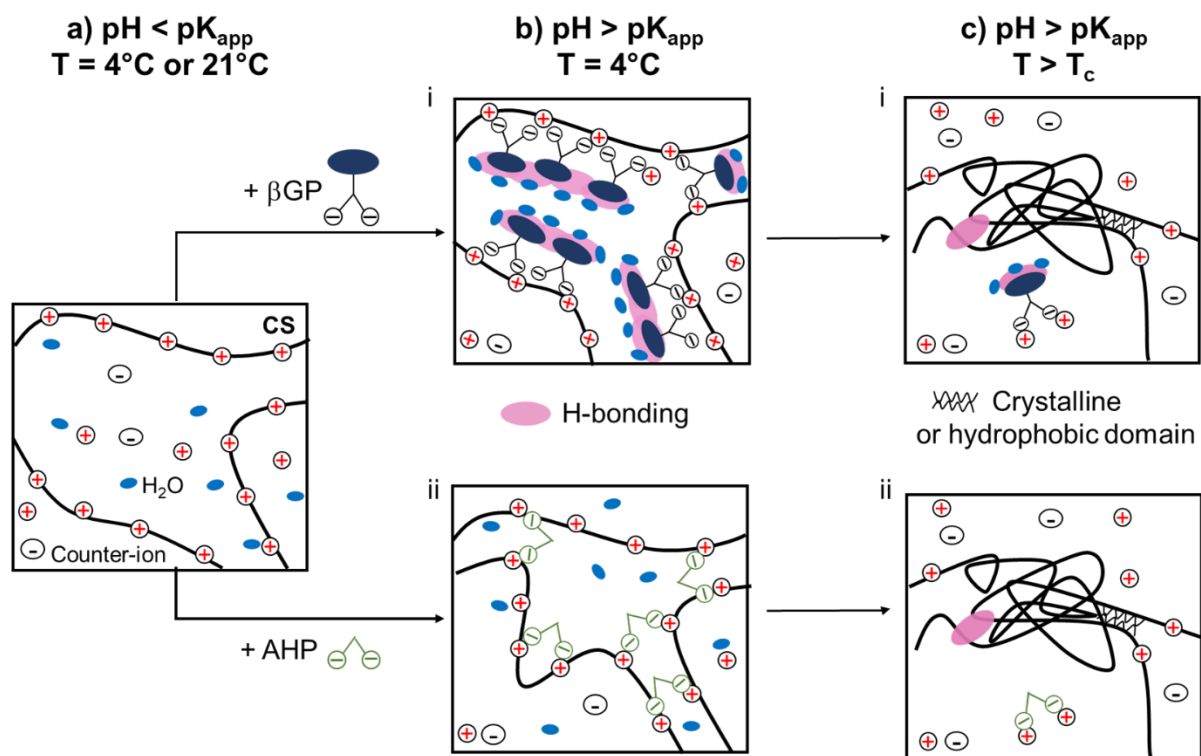


Figure III - 9. Schematic illustration of the molecular mechanisms taking place during the thermally-induced gelation in CS/ βGP and CS/AHP mixtures at CS concentrations higher than c^* .

III.4. Microscopic mechanisms of macropore formation in CS/ β GP/AHP mixtures

In section III.3 above, we have shown that the thermally-induced gelation in CS/salt mixtures can be well explained by the strong temperature dependence of the pK_a of the D-glucosamine monomers and the supramolecular interactions occurring between the salts and the CS chains. The molecular mechanisms induced by increasing the temperature lead to the phase separation of the CS chains in a similar way to what occurs in LCST polymer solutions like PNIPAM in water.

The gelation by phase-separation in CS/salt mixtures results in the formation of a macroporous structure with pore sizes up to tens of microns, as shown previously in the literature.¹⁹ The possible interactions involved in this process, such as salt-CS complexation, H-bonding, crystallization and hydrophobic interactions, do not provide sufficient elements to understand fully the formation and the final properties of the hydrogels. In particular, their macroporous structure cannot be described in terms of the molecular scale interactions above. A microscopic characterization is thus needed to capture the mechanisms involved in the formation of the hydrogel microstructure and in particular the emergence of the macroporosity.

Control and tuning of macroporosity are essential in the context of injectable cell-laden systems for which the microstructure is formed *in situ* in the presence of cells. In this study, we investigated the microscopic mechanisms leading to the formation of macropores in one cytocompatible formulation of CS/ β GP/AHP (CS concentration = 0.8 wt%, pH 7.4, 300 mOsm.L⁻¹) by combining direct microscopic observations and indirect rheological and scattering measurements. More precisely, using a customized temperature-controlled setup, we observed in real time by confocal microscopy the formation of CS/ β GP/AHP hydrogels at a microscopic scale. In addition, we measured using shear rheology the mechanical properties of the hydrogels forming under the same thermal history. Finally, the microscopic dynamics during the sol/gel transition in these mixtures was quantitatively measured by small angle dynamic light scattering.

This work was carried out in collaboration with Dr. Stefano Aime and Dr. Michel Cloître (C3M, ESPCI Paris – PSL).

III.4.1. Experimental methods

4.1.a. Preparation of the cytocompatible CS/ β GP/AHP mixture at 0.8 wt%

A CS/ β GP/AHP mixture satisfying physiological conditions ($\text{pH} = 7.4 \pm 0.05$ at 4°C , osmolarity = $300 \pm 30 \text{ mOsm.L}^{-1}$) was prepared according to the protocol reported in previous study.²⁰ The concentration of CS was 0.8 wt%, $[\beta\text{GP}]/[\text{NH}_2] = 1.5$ and $[\text{AHP}]/[\text{NH}_2] = 1.4$ in the final mixture.

4.1.b. Time-resolved confocal microscopy

A temperature-controlled stage was used with the same sample holder as described in section III.3. The temperature was stabilized to 18°C prior to observation. Once the sample was in place, the temperature was raised to 27°C at a rate of $10^\circ\text{C.min}^{-1}$. However, the thermal transfer was limited by the setup and 27°C was reached after about 20 min (**Figure III - 10**). Images of $56 \mu\text{m} \times 56 \mu\text{m}$ were recorded every 2 min using a confocal microscope (Zeiss Axiovert 200M) equipped with a laser at 488 nm and oil immersion objective $\times 40/1.3$ oil DIC.

4.1.c. Rheological measurement

The evolution in time of the storage and loss moduli (G' , G'') was monitored using a MCR502 apparatus (Anton Paar) with a cone-and-plate geometry (CP50-2TG). The temperature was managed by a Peltier controller and the geometry was initially stabilized at 18°C . Formulations were loaded immediately after preparation and the interface between the sample and the air was sealed with silicone oil to prevent evaporation. The temperature was increased to 27°C using a heating profile that reproduces the one applied in confocal microscopy (see **Figure III - 10**). The values of G' and G'' were measured during 24 h, at constant oscillatory strain of 0.1% and angular frequency of 1 rad.s^{-1} .

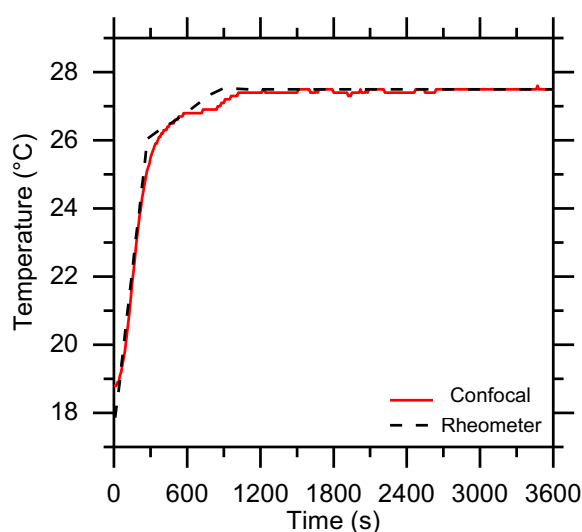


Figure III - 10. Heating ramp from 18°C to 27°C used in confocal microscopy observation (continuous

line) and in rheological experiment (dotted line).

4.1.d. Small angle dynamic light scattering

The light scattering setup was inspired by the one reported by Tamborini & Cipelletti.²¹ The light source is a He Ne laser (wavelength $\lambda = 632$ nm). 8-bit images of 2040×1088 pixels were recorded using a CMOS camera (Basler acA2000-340km, pixel size = $5.5 \mu\text{m}$). To capture a wide range of delay times, we adapted from Philippe *et al.*²² a specific acquisition time scheme that enables probing fast dynamics at a low average acquisition rate. The exposure time was fixed at 2 ms.

For a sample having a finite thickness, the scattering angle associated to a pixel located at a distance r from the optical axis was calculated according to equation (III - 1).

$$\theta = \arcsin\left(\frac{1}{n} \cdot a \cdot r\right) \quad (\text{III} - 1)$$

where $a^{-1} = 17.27 \text{ mm}^{-1}$ is the effective focal length of the optical system; $n = 1.33$ is the refractive index of the solvent. The scattering vector, q , corresponding to an annular set of pixels at the same distance r to the optical axis, was calculated according to equation (III - 2).

$$q = \frac{4\pi n}{\lambda} \sin \frac{\theta}{2} \quad (\text{III} - 2)$$

Our setup probes simultaneously scattering angles, θ , in the range of $[0.014; 0.21]$ rad corresponding to scattering vectors q in the range of $[0.19; 2.77] \mu\text{m}^{-1}$ (**Figure III - 11**).

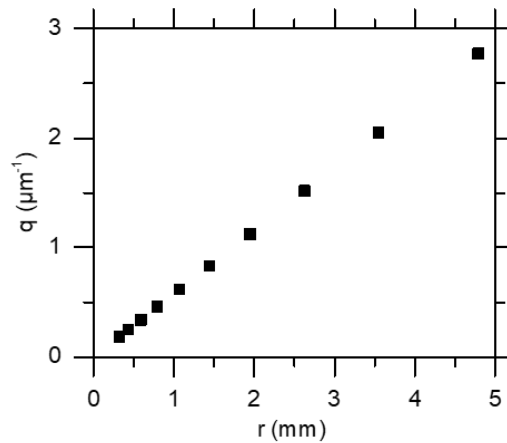


Figure III - 11. Conversion from the distance to the optical axis, r , to the scattering vector, q .

From recorded CMOS images, ten annular set of pixels were obtained and were associated to ten regions having an average q . For pixels in the same annulus, intensity correlation function was calculated from two images taken at t and $(t + \tau)$ using the following equation:

$$g_2 - 1 = \beta \left(\frac{\langle I(t)_p I(t+\tau)_p \rangle_{p \in \text{annulus}}}{\langle I(t) \rangle_{p \in \text{annulus}} \langle I(t+\tau) \rangle_{p \in \text{annulus}}} - 1 \right) \quad (\text{III} - 3)$$

where $I(t)_p$ is the intensity of the pixel p at time t and $\langle I(t) \rangle_p$ is the average intensity of all pixels belonging to the same annulus.

A customized sample holder was prepared using a microscope slide and a glass coverslip with a spacer composed of two layers of Parafilm[®] which thickness is about 200 μm . Immediately after the preparation, CS/ β GP/AHP mixture was placed in the sample holder and grease was used to seal the sample holder interfaces to minimize evaporation. The dynamics of the gelation was monitored for 6 h at room temperature ($23 \pm 1^\circ\text{C}$).

III.4.2. Results

4.2.a. Time-resolved confocal observations

The evolution of the microstructure of a CS/ β GP/AHP mixture was monitored overtime during a heating ramp from 18°C to 27°C during the first 20 min followed by an isotherm at 27°C during 24 h. This temperature was chosen in order to facilitate observation as the sol/gel transition is slowed down compared to 37°C (Chapter II, section II.3). These observations were performed on an area of $56 \mu\text{m} \times 56 \mu\text{m}$ at a $100 \mu\text{m}$ depth from the sample-glass interface. Images at different times during this experiment are reported hereafter in **Figure III - 12** (0 -1 h), **Figure III - 13** (1 h - 5 h) and **Figure III - 14** (22 h - 24 h). Movies showing the evolution of the microstructure can be downloaded in this link <https://dl.espci.fr/ticket/6c6a5598c24869d9e0a1b9b9b5051edc>.

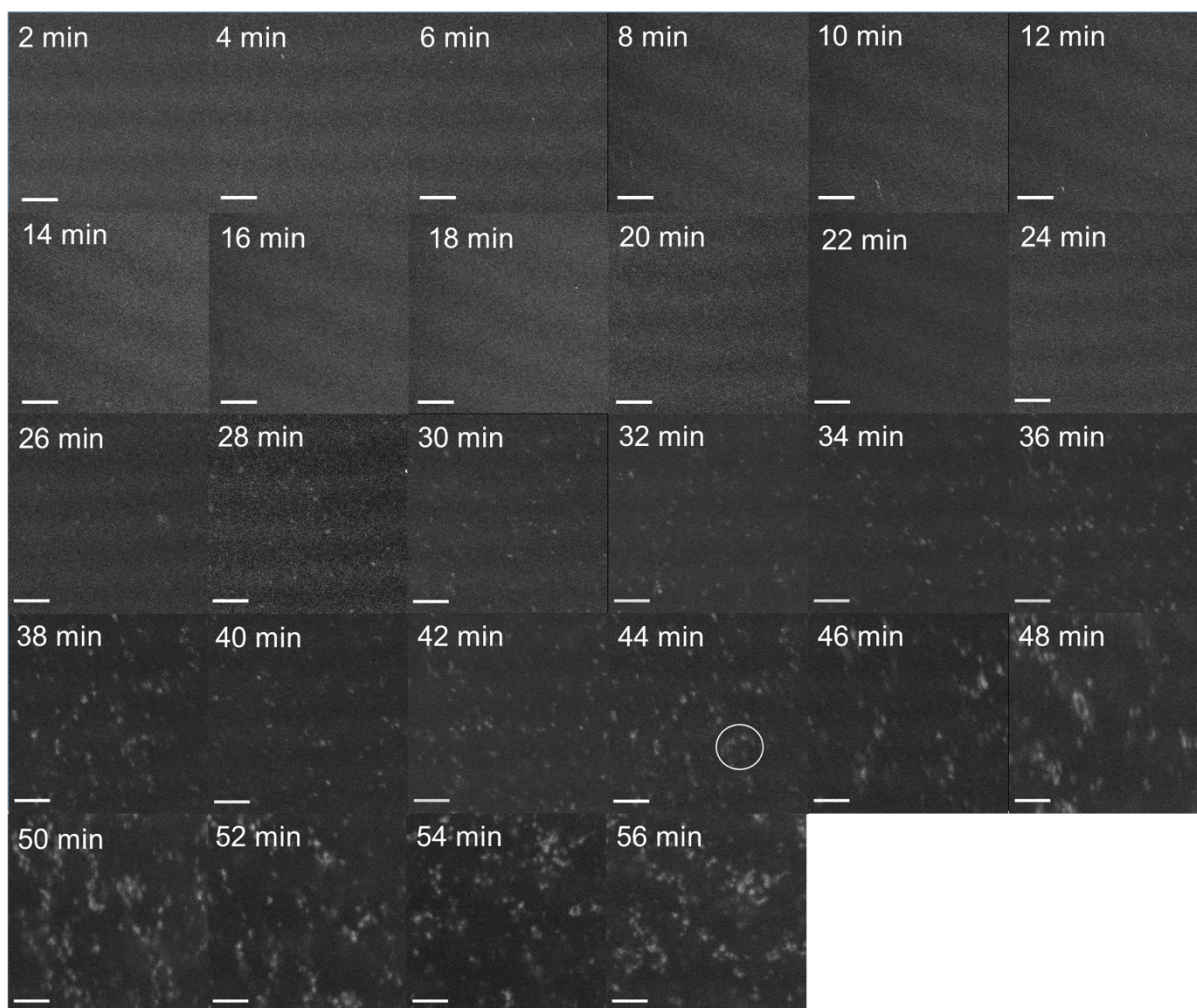


Figure III - 12. Time-resolved confocal micrographs showing the aggregation of fluorescently-labelled CS chains in a physiological CS/ β GP/AHP mixture (CS 0.8 wt%) during the heating ramp from 18 to 27°C (0 to 20 min) then at isothermal condition at 27°C (after 20 min). Scale bar = 10 μ m.

During the first 22 min, the mixture appeared homogeneous at the observed length scale. Bright points about 1-2 μ m in size, corresponding to aggregates of fluorescently-labelled CS could be distinguished starting from 24 min. The number of these aggregates increased continuously up to 42 min. From 44 min, clusters of several aggregates were observed (white circle in **Figure III - 12**) and the number of these aggregates increased overtime. At this stage (44 min - 54 min), the clusters were very mobile and seemed to exhibit thermal random motion. From 60 min to 120 min, the clusters percolated the field of view. The motion and the number of individual clusters decreased (**Figure III - 13**). The network that was formed drifted slightly in the vertical direction from 120 min to 180 min, then remained relatively unchanged up to 290 min. At very long times, from 22 h to 24 h, the hydrogel microstructure stayed completely static during an observation period of 2 h, as shown in **Figure III - 14**.

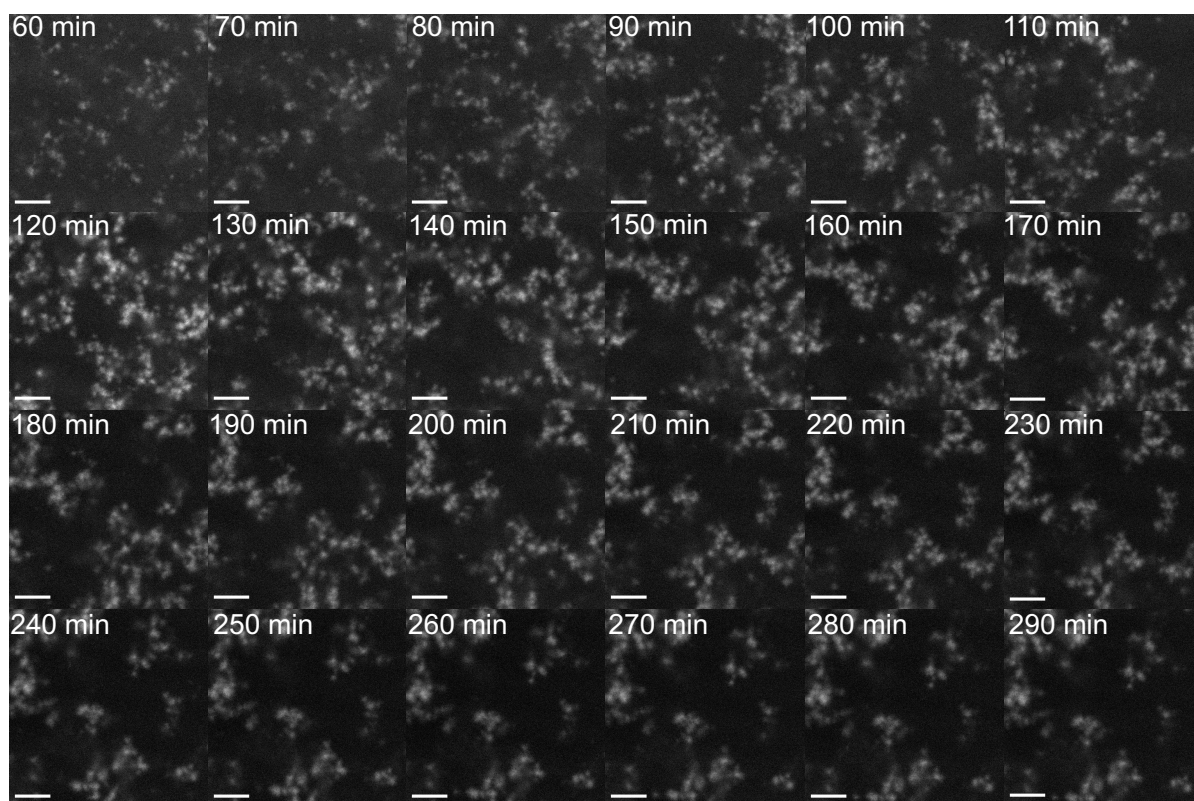


Figure III - 13. Time-resolved confocal micrographs showing the percolation of CS clusters at 27°C for the incubation period from 60 min to 290 min. Scale bar = 10 μm .

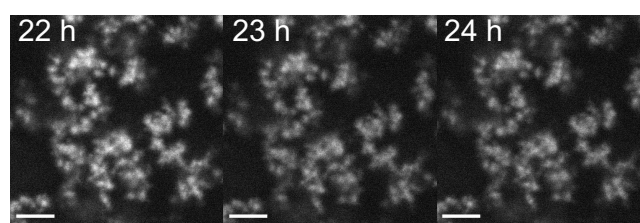


Figure III - 14. Confocal micrographs showing the structure of CS/βGP/AHP hydrogel after a long incubation period (22 - 24 h) at 27°C. Scale bar = 10 μm .

4.2.b. Rheological characterization of the sol/gel transition

Figure III - 15 shows the evolution of the storage, G' , and the loss, G'' , moduli of the studied CS/βGP/AHP mixture. The heating ramp reproduces the same thermal history with a final temperature of 27°C as for the confocal microscopy observation (**Figure III - 10**). The gel point, defined as the cross-over of G' and G'' , is detected around 18 min. From this point, G' increased sharply while G'' increased at a lower rate during the first hour (**Figure III - 15a**). From 1 h to 2 h, G' continued to increase rapidly while G'' increased at a lower rate (**Figure III - 15b**). From 2 h to 5 h of incubation at

27°C, G' continued to increase at a lower rate while G'' barely changed. Finally, from 5 h to 24 h, both G' and G'' reached a regime where they slowly increased with time. In particular, the value of G' increased from 40 Pa at 5 h to 120 Pa at 24 h.

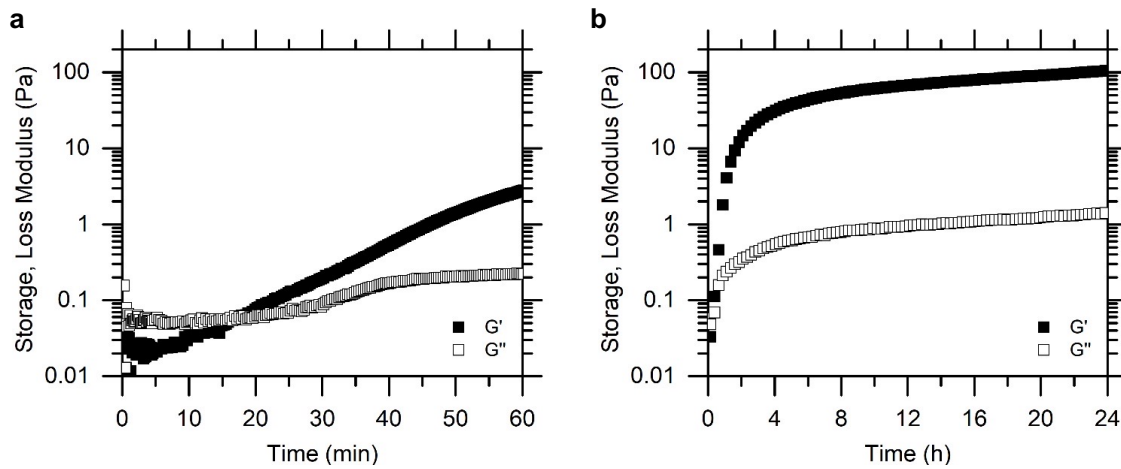


Figure III - 15. Evolution of G' and G'' of a physiological CS/ β GP/AHP mixture (CS 0.8 wt%) during the customized heating ramp from 18°C to 27°C for the first hour (a) and up to 24 h (b). $\gamma = 0.1\%$, $T = 27^\circ\text{C}$.

The rheological behavior of the CS/ β GP/AHP mixture was further assessed at 23°C, the same temperature at which light scattering measurements were carried out, using a series of dynamic frequency sweeps, as shown in **Figure III - 16**. At 1 h, the mixture exhibited a fluid-like behavior for all probed frequencies. At 2 h, G' was greater than G'' on the whole frequency range, indicating a solid-like behavior even though the value of G' is relatively low (~ 1 Pa). Like for the previous isotherm measurements at 27°C, both moduli continuously increased overtime after the gel point with G' increasing much faster than G'' .

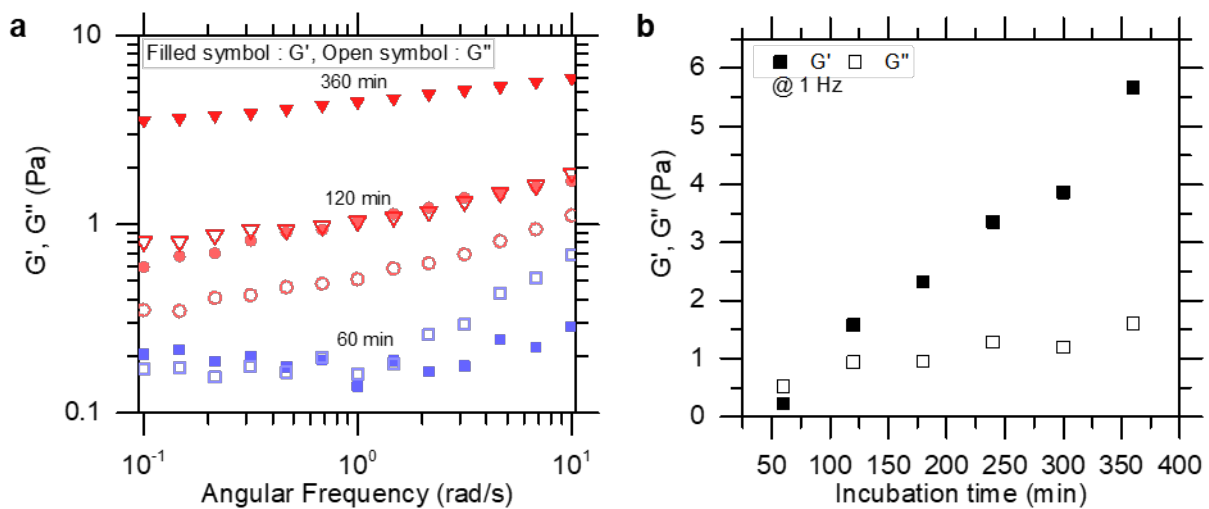


Figure III - 16. a) Frequency sweep measurements for the physiological CS/ β GP/AHP mixture (CS 0.8 wt%) at different incubation times; b) Evolution of G' and G'' overtime at 1 Hz. $\gamma = 0.1\%$, $T = 23^\circ\text{C}$.

4.2.c. Microscopic dynamics during the sol/gel transition

The dynamics at the microscopic scale in CS/ β GP/AHP mixtures was monitored during the sol/gel transition at room temperature ($23 \pm 2^\circ\text{C}$) using small angle dynamic light scattering. **Figure III - 17** shows the intensity correlation functions, $g_2(\tau) - 1$, calculated after different incubation times for a given scattering angle corresponding to a characteristic length $q^{-1} = 0.89 \mu\text{m}$. The intensity correlation functions were fitted to simple exponential decays, $\exp(-2\tau/\tau^*)$, with τ^* the characteristic decay time. **Figure III - 18** shows the evolution of τ^* as a function of the incubation time for different q^{-1} values ranging from 0.36 to $2.19 \mu\text{m}$.

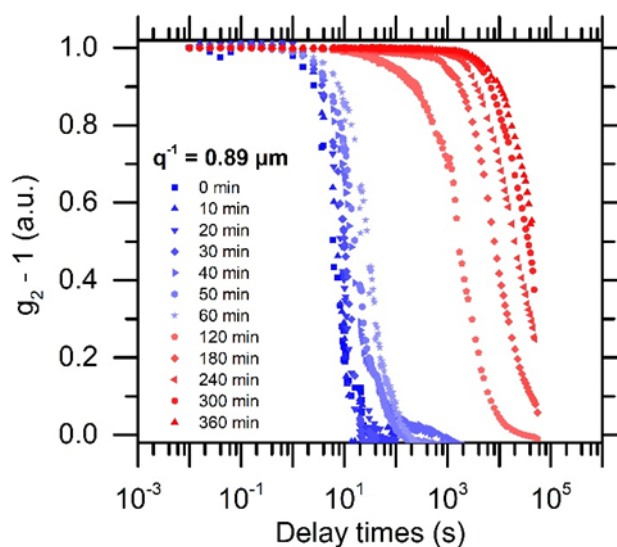


Figure III - 17. The intensity correlation function, $g_2(\tau) - 1$, for physiological CS/ β GP/AHP mixture (CS 0.8 wt%) at $23 \pm 2^\circ\text{C}$ measured at different incubation times.

During the first hour of incubation, $g_2(\tau) - 1$ exhibits very little evolution, as shown in **Figure III - 17**. For each q value, τ^* shows very slight increase, as shown in **Figure III - 18a**. For example, for $q^{-1} = 0.89 \mu\text{m}$, τ^* only increases from 8 s at 0 min to 24 s at 60 min. From 1 h to 2 h, $g_2(\tau) - 1$ showed an abrupt transition and significantly evolved towards longer delay times. In particular, for $q^{-1} = 0.89 \mu\text{m}$, τ^* increases about 60 times from 40 s at 1 h to 2500 s at 2 h (**Figure III - 18b**). This transition indicates a substantial slowing down of the microscopic dynamics. For incubation times longer than 2 h, $g_2(\tau) - 1$ shows a continuous albeit slower evolution towards larger delay times. Moreover, in these last curves, the correlation function did not decay completely to zero, corresponding to some very slow dynamics, which can be observed in a gel network.

These results shown in **Figure III - 17** and **Figure III - 18** suggest the existence of a least two distinct regimes: 1) τ^* remains fairly constant at a given q during the first hour; and 2) τ^* increases abruptly between 1 h and 2 h and continues to increase overtime. Using linear interpolation, we determined that

the abrupt increase in τ^* occurs at an incubation time of about 90 min, as shown in **Figure III - 18c** for $q^{-1} = 1.62 \mu\text{m}$.

Figure III - 18d shows the evolution of the characteristic decay time, τ^* , as a function of q^{-1} for different incubation times. During the first 2 h of incubation, τ^* scales with $q^{-\alpha}$ with $\alpha = 1.2$. This exponent indicates that the motion at the probed length scales does not purely correspond to a simple Brownian motion. Beyond 2 h, no clear dependency is found between τ^* and q . Similar observations were previously reported for colloidal gels by Cho *et al.*²³ This was interpreted as the signature of the domination of the motion at the length scale of clusters over the gel dynamics, once the network is formed. In our case, we thus propose that once the gelation occurs, the motion of CS colloidal-like particles is confined by the other neighboring particles.

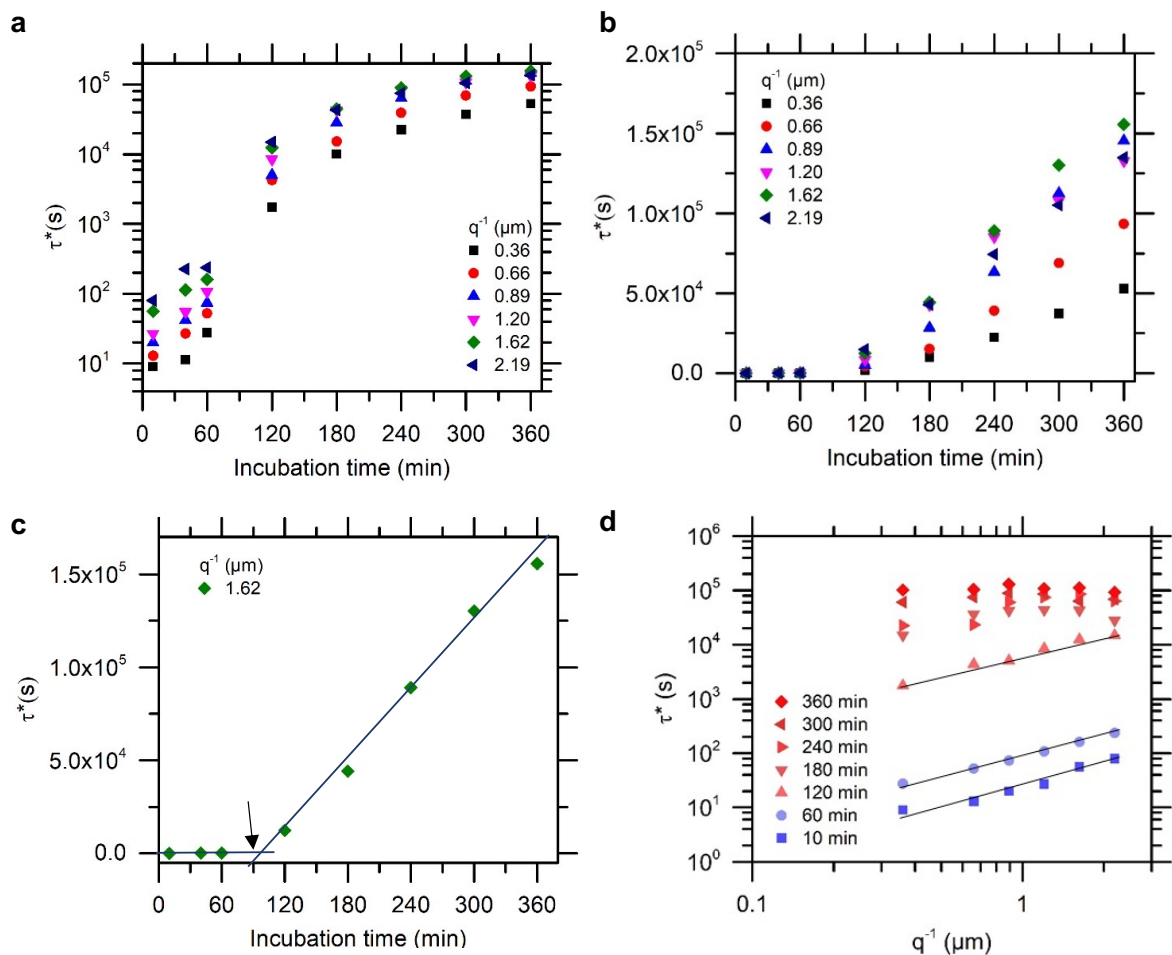


Figure III - 18. Characteristic decay time, τ^* as a function of the incubation time for various q^{-1} in semi-log plot (a) and in linear plot (b). Linear fitting to determine the transition time, as indicated by the black arrow (c). τ^* as a function of q^{-1} at different incubation times (d). $T = 23 \pm 2^\circ\text{C}$.

III.4.3. Microscopic picture for the emergence of macroporosity in thermosensitive CS/salt mixtures

We characterized the formation of the hydrogel microstructure by a combination of direct and indirect observations during the sol/gel transition at 23 or 27°C of a CS/βGP/AHP mixture. In particular, rheological measurements and time-resolved confocal microscopy were carried out using a very similar heating ramp followed by an isotherm at 27°C (**Figure III - 10**). Despite our careful attention, we expect that the temperature was not as homogeneous in the confocal set-up than in the rheometer. Some heat exchange most likely occurred near the contact between the sample holder heated by the Peltier stage and the microscope lens thermalized at room temperature. As a result, the temperature of the sample in the observed area (100 μm away from the glass slide) might have been different from the one measured by the thermocouple, which was closer to the Peltier stage (**Figure III - 1**). Because of the strong thermosensitivity of CS/βGP/AHP mixtures, such a temperature difference between the two protocols would be enough to create a substantial discrepancy in the gelation kinetics. For example, the gelation time increases from 10 ± 2 min at 27°C to 40 ± 5 min at 25°C (Chapter II, section II.3). Consequently, it is difficult to relate with a good precision the confocal observations and the mechanical properties, especially at the beginning of the measurement, where the temperature is not stabilized yet, and close to the gel point. However, these observations along with light scattering measurements still provide valuable information to better understand the mechanisms involved in the formation of the hydrogel microstructure and in particular the emergence of the macroporosity. We propose here a microscopic picture explaining the different steps of this thermally-induced gelation. These steps are illustrated in **Figure III - 19** and are discussed in more detail below.

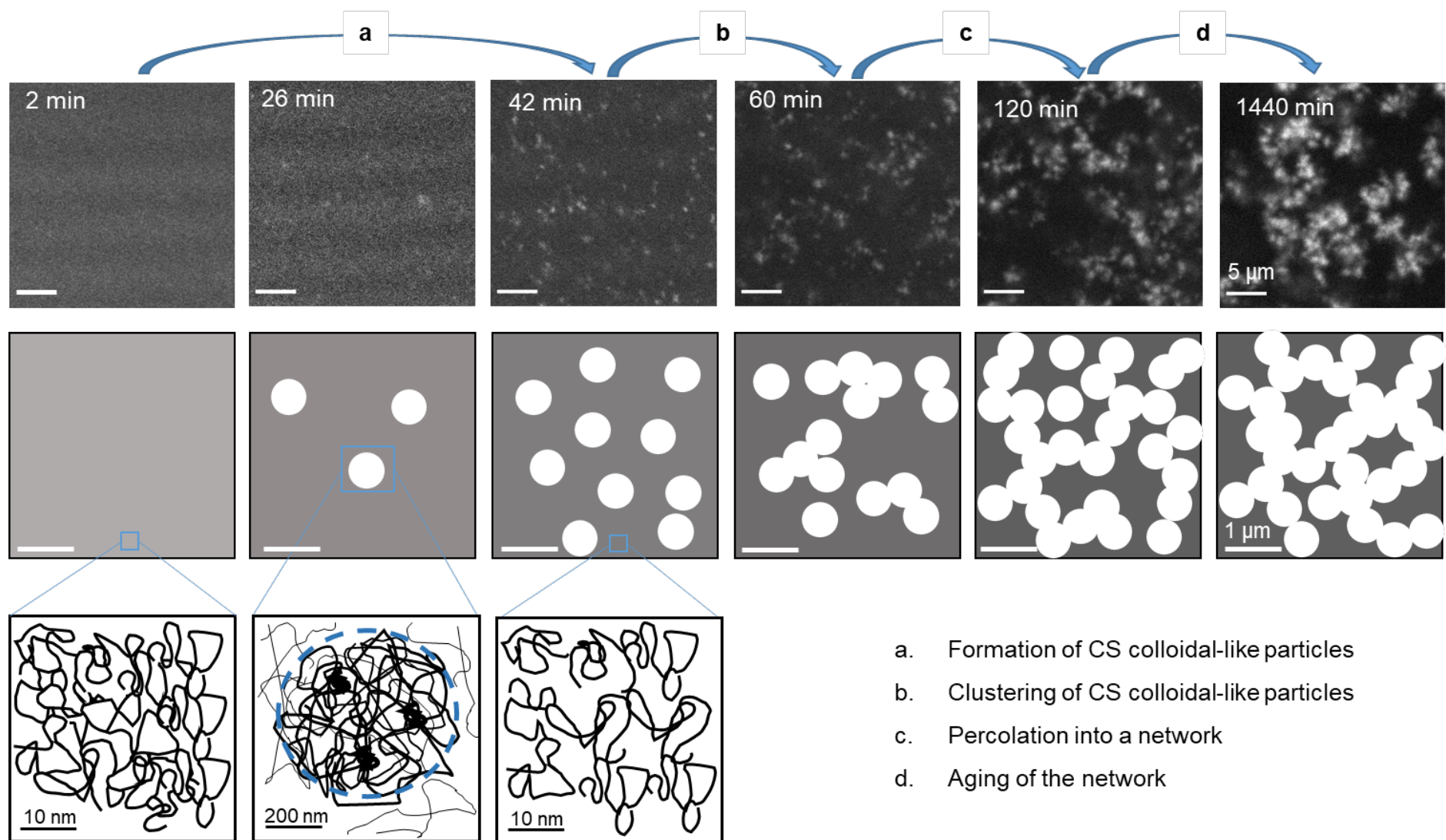


Figure III - 19. Schematic representation of the proposed microscopic mechanisms leading to the formation of macroporous gels in thermosensitive CS/salt mixtures. $c > c^*$, $T > T_c$.

4.3.a. Formation of CS colloidal-like particles

The characterization techniques used in this study do not allow us to access the events that occur below the microscopic scale. In particular, the small-scale events occurring during the first 10 – 20 min of the gelation process at 23-27°C could not be observed. However, interpretations can be proposed based on previous studies. Using SANS observations, Crompton *et al.* demonstrated the formation of CS particles having two characteristic length scales in CS/βGP hydrogels.²⁴ They proposed that these CS individual particles are highly heterogeneous objects composed of hydrophobic domains (~ 350 Å) and hydrophilic domains (~ 120 Å) (see Chapter I, section I.3.2.b for more details).

We suggest that the formation of CS colloidal-like particles in our liquid homogeneous CS/βGP/AHP mixtures upon heating would be preceded by the formation of small hydrophobic domains involving several CS chains. This chain aggregation should lead to the growth of microscopic objects in the form of CS colloidal-like particles. In our CS/βGP/AHP formulation at 27°C, the appearance of such CS colloidal-like particles was the first detected microscopic event and occurred at 24 - 26 min, as shown in **Figure III - 12**. These particles have sizes about 1 μm. Individual particles of about the same size were previously observed by Crompton *et al.* for CS/βGP hydrogels prepared with CS concentrations ranging from 0.5 to 0.8 wt%.²⁴

As time goes by, the number of CS colloidal-like particles continuously increases, as observed from 24 to 44 min (**Figure III - 12**). At this stage, these particles are very mobile, and the sample rheology is liquid-like, as demonstrated in frequency sweep experiments at 23°C (**Figure III - 16**). Light scattering measurements indicate that the dynamics of these colloidal-like particles is not purely Brownian. First, the characteristic decay times, τ^* , scales with $q^{-1.2}$ indicating hyperdiffusive dynamics (**Figure III - 18d**). Second, τ^* is larger than expected for sub-micrometer particles: effective diffusion coefficient extracted from measurements at $q^{-1} = 0.89 \mu\text{m}$ would decrease from $4.4 \times 10^{-14} \text{m}^2.\text{s}^{-1}$ at 0 min to $2.3 \times 10^{-14} \text{m}^2.\text{s}^{-1}$ at 40 min, which corresponds to hydrodynamic diameters of about 4 μm and 10 μm, respectively. Our direct confocal observations show much smaller particles (**Figure III - 12**).

A possible explanation can be proposed for this hyperdiffusive dynamics if we assume that there are no artefacts from the setup, such as evaporation or convection, that can induce a collective displacement. An analogy could be made with colloid-polymer dispersions for which a hyperdiffusive dynamics was previously reported.²⁵ For instance, Srivastava *et al.* studied the dynamics of colloidal dispersions of laponite nanoparticles in the presence of poly(ethylene oxide) (PEO) in a semi-diluted regime and reported an exponent of 1.5.²⁵ They suggested that in this regime, the polymers behave like an uniform polymer matrix that might exert some elastic forces on the laponite nanoparticles. In our study, CS/βGP/AHP mixtures were prepared in the semi-dilute regime ($c = 0.8 \text{ wt}\% > c^* = 0.18 \text{ wt}\%$). Hence, we propose that there is a hybrid regime where the CS particles are surrounded by an entangled network

of CS chains and the observed hyperdiffusive motion of these particles would be a response to the local forces created by the polymer matrix.

4.3.b. Clustering of CS colloidal-like particles

As the density in CS particles increases, a second step occurs, consisting in the aggregation of these particles into clusters. These clusters are formed by the attachment of several colloidal-like particles, as shown by confocal microscopy from 44 min to 60 min (**Figure III - 12**). We observed that the number of clusters increases overtime and fewer individual colloidal-like particles are observed. Previous studies on CS/ β GP reported a fractal-like structure with a fractal dimension of 2.3-2.5,^{19,26} which is in accordance with a reaction-limited aggregation. As previously demonstrated and discussed in section III.3, a similar regime was found in CS/salt mixtures regardless of the salt. Therefore, we propose that the clustering in CS/ β GP/AHP mixtures is also described by a reaction-limited aggregation process.

4.3.c. Percolation into a network

At some point, clusters percolate into a network spanning the whole probed volume, as directly shown by confocal microscopy images from 60 to 120 min (**Figure III - 13**). This process is accompanied by a significant slowing-down of the dynamics and an increase in the storage modulus. The slowing-down of the dynamics was directly observed by confocal (**Figure III - 13**) and quantitatively measured by light scattering (**Figure III - 17**) with τ^* increasing from 40 s at 1 h to 2500 s at 2 h (**Figure III - 18**). Using linear fitting, we determined the transition time around 90 min at 23°C. This time is consistent with the gelation time determined by the tube inversion method and by frequency-sweep rheological measurements (**Figure III - 16**).

4.3.d. Ageing of the hydrogel

After gelation by the percolation of clusters, the hydrogel keeps evolving through an ageing process. Direct observations by confocal microscopy indicate that the microstructure still evolves after 2 h, even if the motion is much slower compared to the previous steps (**Figure III - 13**). The storage modulus increases continuously from 10 Pa at 2 h to 120 Pa at 24 h, as shown in **Figure III - 15b**. The dynamics continues to slow down beyond 2 h: τ^* increases from $2.5 \cdot 10^3$ s at 2 h to 1.5×10^5 s at 6 h (**Figure III - 17**, **Figure III - 18**). Similar slowing down of the dynamics and strengthening of the storage modulus have been observed and interpreted for colloidal gels in several previous studies.²⁷⁻³⁰ As a matter of fact, a shrinking process is usually reported for hydrogels, which is opposed by the adhesion of the gel to the sample holder walls. The competition of these two phenomena induces internal stress that produce intermittent micro-collapses or local re-organization events.²⁹ For our CS/ β GP/AHP hydrogels, we indeed observed syneresis when the hydrogel was not confined in all three dimensions (data not shown).

In addition, this tendency for the gel to shrink is also supported by the continuous increase of the absolute value of the normal force after the gel point, as measured by rheology (**Figure III - 20**).

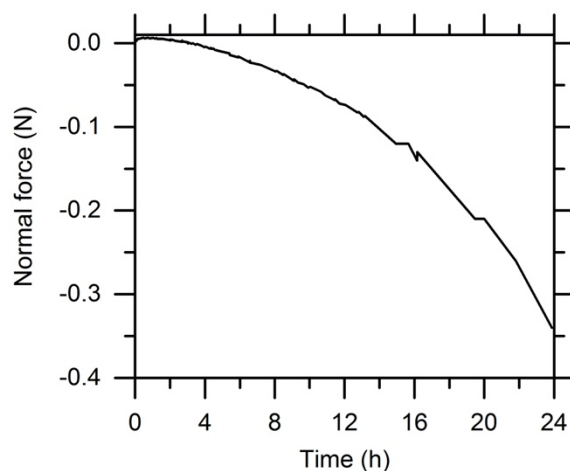


Figure III - 20. Evolution of the normal force measured for CS/ β GP/AHP mixture at 27°C during 24 h.

III.5. Conclusions

Our results bring several new insights into the molecular and microscopic mechanisms involved in the thermosensitivity of CS/salt mixtures.

By comparing mixtures with different salts, we highlighted that the formation of a hydration layer is crucial for maintaining the solubility of CS at neutral pHs and low temperatures. We showed that the formation of this hydration layer does not require exclusively the presence of polyol moieties and could be achieved with salts that are able to associate with both CS chains and water molecules. In particular, we identified another cytocompatible salt able to fulfill this function: MES. We demonstrated the existence of a hydrogel at low temperature in the presence of divalent salts such as AHP and explain its formation by ionotropic crosslinking. This gel is completely different from the phase separated gel induced by heating. These results give rise to promising perspectives for the control of thermal stability and gelation kinetics, which are crucial features in the design of injectable cell-laden matrices.

To the best of our knowledge, our study presented in section III.4 is the first one that reported time-resolved characterization of the formation of the microstructure in thermosensitive CS/salt mixtures. By coupling direct observations and indirect rheological and light scattering measurements, we demonstrated the emergence of the microstructure by the clustering and percolation of CS particles in a similar manner to the formation of other colloidal gels. Interestingly, our observations suggest that there is a regime where the colloidal-like particles and entangled CS chains in solution co-exist, thus inducing some peculiar dynamics. Further investigations using adequate techniques for monitoring submicronic length scales, such as SAXS, would be interesting to gain more insights into this peculiar combination of colloidal and polymer behavior.

References

- (1) Supper, S.; Anton, N.; Seidel, N.; Riemenschmitter, M.; Schoch, C.; Vandamme, T. Rheological Study of Chitosan/Polyol-Phosphate Systems: Influence of the Polyol Part on the Thermo-Induced Gelation Mechanism. *Langmuir* **2013**, *29* (32), 10229–10237. <https://doi.org/10.1021/la401993q>.
- (2) Grinberg, V. Y.; Burova, T. V.; Grinberg, N. V.; Tikhonov, V. E.; Dubovik, A. S.; Moskalets, A. P.; Khokhlov, A. R. Thermodynamic Insight into the Thermoresponsive Behavior of Chitosan in Aqueous Solutions: A Differential Scanning Calorimetry Study. *Carbohydr. Polym.* **2019**, *229* (September 2019), 115558. <https://doi.org/10.1016/j.carbpol.2019.115558>.
- (3) Lavertu, M.; Filion, D.; Buschmann, M. D. Heat-Induced Transfer of Protons from Chitosan to Glycerol Phosphate Produces Chitosan Precipitation and Gelation. *Biomacromolecules* **2008**, *9* (2), 640–650. <https://doi.org/10.1021/bm700745d>.
- (4) Nair, L. S.; Starnes, T.; Ko, J. W. K.; Laurencin, C. T. Development of Injectable Thermogelling Chitosan-Inorganic Phosphate Solutions for Biomedical Applications. *Biomacromolecules* **2007**, *8* (12), 3779–3785. <https://doi.org/10.1021/bm7006967>.
- (5) Ta, H. T.; Han, H.; Larson, I.; Dass, C. R.; Dunstan, D. E. Chitosan-Dibasic Orthophosphate Hydrogel: A Potential Drug Delivery System. *Int. J. Pharm.* **2009**, *371* (1–2), 134–141. <https://doi.org/10.1016/j.ijpharm.2009.01.018>.
- (6) Casettari, L.; Cespi, M.; Palmieri, G. F.; Bonacucina, G. Characterization of the Interaction between Chitosan and Inorganic Sodium Phosphates by Means of Rheological and Optical Microscopy Studies. *Carbohydr. Polym.* **2013**, *91* (2), 597–602. <https://doi.org/10.1016/j.carbpol.2012.08.037>.
- (7) Chenite, A.; Buschmann, M.; Wang, D.; Chaput, C.; Kandani, N. Rheological Characterisation of Thermogelling Chitosan/Glycerol-Phosphate Solutions. *Carbohydr. Polym.* **2001**, *46*, 39–47.
- (8) Zhang, H.; Zhu, D.; Song, L.; Liu, L.; Dong, X.; Liu, Z.; Leng, X. Arginine Conjugation Affects the Endocytic Pathways of Chitosan/DNA Nanoparticles. *J. Biomed. Mater. Res. - Part A* **2011**, *98 A* (2), 296–302. <https://doi.org/10.1002/jbm.a.33115>.
- (9) Li, X. Y.; Kong, X. Y.; Wang, X. H.; Shi, S.; Guo, G.; Luo, F.; Zhao, X.; Wei, Y. Q.; Qian, Z. Y. Gel-Sol-Gel Thermo-Gelation Behavior Study of Chitosan-Inorganic Phosphate Solutions. *Eur. J. Pharm. Biopharm.* **2010**, *75* (3), 388–392. <https://doi.org/10.1016/j.ejpb.2010.04.015>.
- (10) Yuan, Y.; Huang, Y. Ionically Crosslinked Polyelectrolyte Nanoparticle Formation Mechanisms: The Significance of Mixing. *Soft Matter* **2019**, *15* (48), 9871–9880. <https://doi.org/10.1039/c9sm01441a>.
- (11) Filion, D.; Lavertu, M.; Buschmann, M. D. Ionization and Solubility of Chitosan Solutions Related to Thermosensitive Chitosan/Glycerol-Phosphate Systems. *Biomacromolecules* **2007**, *8* (10), 3224–3234. <https://doi.org/10.1021/bm700520m>.
- (12) Lewis, D. F. V. Hydrogen Bonding in Human P450-Substrate Interactions: A Major Contribution to Binding Affinity. *Scientific World Journal*. **2004**, *4*, 1074–1082. <https://doi.org/10.1100/tsw.2004.210>.
- (13) Chenite, A.; Chaput, C.; Wang, D.; Combes, C.; Buschmann, M. D.; Hoemann, C. D.; Leroux, J. C.; Atkinson, B. L.; Binette, F.; Selmani, A. Novel Injectable Neutral Solutions of Chitosan Form Biodegradable Gels in Situ. *Biomaterials* **2000**, *21* (21), 2155–2161. [https://doi.org/10.1016/S0142-9612\(00\)00116-2](https://doi.org/10.1016/S0142-9612(00)00116-2).
- (14) Kojima, H. Studies on the Phase Transition of Hydrogels and Aqueous Solutions of Thermosensitive Polymers. *Polym. J.* **2018**, *50* (6), 411–418. <https://doi.org/10.1038/s41428-018-0035-9>.
- (15) Okada, Y.; Tanaka, F. Cooperative Hydration, Chain Collapse, and Flat LCST Behavior in Aqueous Poly(N-Isopropylacrylamide) Solutions. *Macromolecules* **2005**, *38* (10), 4465–4471. <https://doi.org/10.1021/ma0502497>.
- (16) Vatalis, A. S.; Kehayoglou, A. H. Solution Properties of Poly(N-Isopropylacrylamide). *J. Macromol. Sci. - Pure Appl. Chem.* **1968**, *A2* (8), 1441–1455. <https://doi.org/10.1081/MA-100103872>.
- (17) Tavagnacco, L.; Zaccarelli, E.; Chiessi, E. On the Molecular Origin of the Cooperative Coil-to-Globule Transition of Poly(N-Isopropylacrylamide) in Water. *Phys. Chem. Chem. Phys.* **2018**, *20* (15), 9997–10010. <https://doi.org/10.1039/c8cp00537k>.

- (18) Bischofberger, I.; Calzolari, D. C. E.; De Los Rios, P.; Jelezarov, I.; Trappe, V. Hydrophobic Hydration of Poly-N-Isopropyl Acrylamide: A Matter of the Mean Energetic State of Water. *Sci. Rep.* **2014**, *4*, 1–7. <https://doi.org/10.1038/srep04377>.
- (19) Crompton, K. E.; Prankerd, R. J.; Paganin, D. M.; Scott, T. F.; Horne, M. K.; Finkelstein, D. I.; Gross, K. A.; Forsythe, J. S. Morphology and Gelation of Thermosensitive Chitosan Hydrogels. *Biophys. Chem.* **2006**, *121* (1), 14–20. <https://doi.org/10.1016/j.bpc.2005.12.005>.
- (20) Dang, P. A.; Palomino-Durand, C.; Elsafi Mabrouk, M.; Marquaille, P.; Odier, C.; Norvez, S.; Pauthe, E.; Corté, L. Rational Formulation Design of Injectable Thermosensitive Chitosan-Based Hydrogels for Cell Encapsulation and Delivery. *Carbohydr. Polym.* **2022**, *277*, 118836. <https://doi.org/10.1016/j.carbpol.2021.118836>.
- (21) Tamborini, E.; Cipelletti, L. Multiangle Static and Dynamic Light Scattering in the Intermediate Scattering Angle Range. *Rev. Sci. Instrum.* **2012**, *83* (9). <https://doi.org/10.1063/1.4751864>.
- (22) Philippe, A.; Aime, S.; Roger, V.; Jelinek, R.; Prévot, G.; Berthier, L.; Cipelletti, L. An Efficient Scheme for Sampling Fast Dynamics at a Low Average Data Acquisition Rate. *J. Phys. Condens. Matter* **2016**, *28* (7). <https://doi.org/10.1088/0953-8984/28/7/075201>.
- (23) Cho, J. H.; Cerbino, R.; Bischofberger, I. Emergence of Multiscale Dynamics in Colloidal Gels. *Phys. Rev. Lett.* **2020**, *124* (8), 88005. <https://doi.org/10.1103/PhysRevLett.124.088005>.
- (24) Crompton, K. E.; Forsythe, J. S.; Horne, M. K.; Finkelstein, D. I.; Knott, R. B. Molecular Level and Microstructural Characterisation of Thermally Sensitive Chitosan Hydrogels. *Soft Matter* **2009**, *5* (23), 4704–4711. <https://doi.org/10.1039/b907593c>.
- (25) Srivastava, S.; Kishore, S.; Narayanan, S.; Sandy, A. R.; Bhatia, S. R. Multiple Dynamic Regimes in Colloid-Polymer Dispersions: New Insight Using X-Ray Photon Correlation Spectroscopy. *J. Polym. Sci. Part B Polym. Phys.* **2016**, *54* (7), 752–760. <https://doi.org/10.1002/polb.23973>.
- (26) Aliaghaie, M.; Mirzadeh, H.; Dashtimoghadam, E.; Taranejoo, S. Investigation of Gelation Mechanism of an Injectable Hydrogel Based on Chitosan by Rheological Measurements for a Drug Delivery Application. *Soft Matter* **2012**, *8* (27), 7128. <https://doi.org/10.1039/c2sm25254f>.
- (27) Bouchaud, J. P.; Pitard, E. Anomalous Dynamical Light Scattering in Soft Glassy Gels. *Eur. Phys. J. E* **2002**, *9* (3), 287–291. <https://doi.org/10.1140/epje/i2002-10075-3>.
- (28) Cipelletti, L.; Ramos, L. Slow Dynamics in Glassy Soft Matter. *J. Phys. Condens. Matter* **2005**, *17* (6), 1–41. <https://doi.org/10.1088/0953-8984/17/6/R01>.
- (29) Cipelletti, L.; Manley, S.; Ball, R. C.; Weitz, D. A. Universal Aging Features in the Restructuring of Fractal Colloidal Gels. *Phys. Rev. Lett.* **2000**, *84* (10), 2275–2278. <https://doi.org/10.1103/PhysRevLett.84.2275>.
- (30) Jain, A.; Schulz, F.; Lokteva, I.; Frenzel, L.; Grübel, G.; Lehmkuhler, F. Anisotropic and Heterogeneous Dynamics in an Aging Colloidal Gel. *Soft Matter* **2020**, *16* (11), 2864–2872. <https://doi.org/10.1039/c9sm02230a>.

CHAPTER IV

THE MICROSTRUCTURE IN CS/ β GP/AHP HYDROGELS

TABLE OF CONTENTS

Résumé en français	165
IV.1. Introduction.....	167
IV.2. Quantitative analysis of the microstructure of CS/ β GP/AHP hydrogels	168
IV.2.1. Theoretical background	168
2.1.a. Point spread function (PSF).....	168
2.1.b. Deconvolution	169
2.1.c. Binarization (thresholding)	169
2.1.d. Morphological sieve technique.....	170
IV.2.2. Experimental methods and image processing	170
2.2.a. Confocal microscopy observation	170
2.2.b. Deconvolution and binarization	171
2.2.c. Porosity	171
2.2.d. Pore size distribution.....	171
IV.2.3. Results & Discussion	171
2.3.a. Deconvolution and binarization of confocal images	171
2.3.b. Effect of the CS concentration on the hydrogel microstructure.....	173
IV.3. Effect of CS characteristics on the properties of CS/ β GP/AHP hydrogels	175
IV.3.1. Materials & experimental methods.....	175
3.1.a. Materials.....	175
3.1.b. Experimental methods	175
IV.3.2. Results & Discussion	176
3.2.a. Characterization of the molar mass distribution	176
3.2.b. Gelation kinetics.....	178
3.2.c. Microstructure and mechanical properties	181
IV.4. Effect of the presence of cells on the microstructure of CS/ β GP/AHP hydrogels	187
IV.4.1. Materials & Methods	187
4.1.a. Materials & Cells	187
4.1.b. Experimental methods	187
IV.4.2. Results and discussion	190
4.2.a. Cell distribution in hydrogels	190
4.2.b. Effect of cells on the porosity and the pore size distribution	191
IV.5. Conclusions.....	194
References.....	195

Résumé en français

La microstructure de la matrice est un paramètre crucial régissant la survie et l'activité des cellules qui y sont encapsulées. Par conséquent, il est essentiel de caractériser la porosité et la distribution de la taille des pores de nos hydrogels. Comme décrit dans le Chapitre III, les mélanges thermosensibles CS/ β GP/AHP forment des hydrogels macroporeux par un processus d'agrégation et de percolation, d'une manière très similaire aux gels colloïdaux. Ces macropores ont des formes allongées et sont interconnectés. Les images au microscope confocal semblent révéler une taille caractéristique atteignant des dizaines de microns, mais il est beaucoup plus difficile d'analyser quantitativement la distribution des tailles de pores dans des microstructures aussi complexes et tortueuses, que dans des structures ayant des pores sphériques bien définis. Dans ce chapitre, nous avons caractérisé quantitativement la microstructure de nos systèmes en développant des méthodes et des outils basés sur l'analyse d'images obtenues en microscopie confocale.

Dans une première partie (IV.2), nous avons développé un protocole d'analyse d'images permettant de quantifier la porosité, définie comme la fraction totale de pores, et la distribution de taille de pores pour les hydrogels CS/ β GP/AHP. La validation de ce protocole a été démontrée sur les hydrogels physiologiques préparés à différentes concentrations en CS. Nous avons trouvé une bonne corrélation entre la concentration en CS, et la porosité et la taille moyenne de pores. La porosité diminue linéairement avec l'augmentation de la concentration de CS, de $75 \pm 5\%$ pour CS 0.5 wt%, à $63 \pm 7\%$ pour CS 0.8 wt%. La taille moyenne des pores augmente avec la diminution de la concentration de CS, de $5.4 \pm 0.4 \mu\text{m}$ pour CS 0.8 wt%, à $7.5 \pm 0.9 \mu\text{m}$ pour CS 0.5 wt%.

Dans une seconde partie (IV.3), nous avons exploré les effets de différentes caractéristiques du CS (distribution de masse molaire, origine) sur les propriétés des hydrogels, en particulier la microstructure. Pour cela, des formulations CS/ β GP/AHP ayant un pH fixé à 7.4 à 4°C ont été préparées selon l'approche développée au Chapitre II. Utilisant notre protocole d'analyse d'images, nous montrons que la microstructure de ce système peut être ajustée en utilisant différents grades de CS. En particulier, pour une concentration fixe à 0.8 wt% de CS, nous avons pu obtenir une gamme de taille moyenne de pores allant de $4.9 \pm 0.3 \mu\text{m}$ à $14.3 \pm 1.8 \mu\text{m}$ et une gamme de porosité allant de $57 \pm 1\%$ à $83 \pm 1\%$ en variant les caractéristiques du CS. De plus, nous avons trouvé que le module élastique évolue avec la fraction volumique effective des hydrogels selon une loi de puissance, de manière similaire à des gels colloïdaux.

Dans une troisième et dernière partie (IV.4), nous avons exploré l'incidence de la présence de cellules sur la gélification et sur la microstructure des hydrogels CS/ β GP/AHP. Pour cela, nous avons comparé la microstructure d'un hydrogel ne contenant pas de cellules à des hydrogels contenant des cellules à une concentration de 10^6 ou 5.10^6 cellules.mL⁻¹. Considérant que le volume typique de la plupart des cellules de mammifères est de l'ordre de $4000 \mu\text{m}^3$, cette plage de concentrations correspond à une

fraction volumique allant de 0.05 à 0.25 %. Nous avons montré de manière quantitative que les cellules peuvent être dispersées de manière homogène dans des hydrogels CS/ β GP/AHP jusqu'à 5.10^6 cells.mL⁻¹. Un effet intéressant de la présence de cellules sur la microstructure de l'hydrogel a été mis en évidence : la sédimentation des cellules pendant la phase de gélification crée des pores allongés dont la taille va jusqu'à des dizaines de microns. La vitesse de sédimentation dépend de plusieurs paramètres dépendant des caractéristiques du type cellulaire, et de la formulation. En particulier, il est bien connu que la viscosité des solutions de polymère évolue de manière significative avec la concentration en polymère. Par conséquent, nous nous attendons à ce que la formation de ces pores allongés soit accentuée dans les formulations préparées avec une concentration de CS inférieure. Ce phénomène doit être considéré dans le contexte des systèmes thermosensibles où la microstructure se forme *in situ* et en présence des cellules.

IV.1. Introduction

In Chapter I, section 1.6, we reported on works showing that the microstructure is a crucial parameter governing the cell viability and mobility in cell-laden hydrogels for cell encapsulation and delivery.^{1,2} Hence, it is essential to properly characterize the porosity and the pore size distribution of our CS/βGP/AHP mixtures to assess their compatibility with cell encapsulation. As shown in Chapter III, CS/βGP/AHP mixtures undergo a thermally-induced phase separation, resulting in the formation of macroporous hydrogels. These macropores present elongated shapes and are interconnected. The confocal microscopy images seem to reveal some characteristic size reaching tens of microns, nevertheless it is much more challenging to analyze quantitatively the distribution in pore sizes in such complex and tortuous microstructures than in structures having well-defined spherical pores. In this chapter, we characterized quantitatively the microstructure of our systems by developing methods and tools based on the analysis of images acquired by confocal microscopy.

Several existing techniques allow to observe the microstructure of porous materials. However, most of them require a pre-treatment which can strongly alter the pore structure.³ Confocal microscopy is a powerful non-destructive technique allowing to explore porous materials without any pre-treatment provided that they are transparent enough, which is particularly interesting to observe hydrogels in their swollen-state.⁴ The image processing includes deconvolution and thresholding operations in order to improve the image quality, thus the identification of the structure of interest. In a first part, we propose an image analysis method to calculate the overall porosity and the pore size distribution of fluorescently labelled CS/βGP/AHP mixtures. The validation of this methodology was demonstrated on physiological formulations prepared at four different CS concentrations.

In the second and third parts of this chapter, these developed methods and tools were used to investigate two questions concerning the microstructure of this system. The first question (section 0) is about the possible effect of different CS characteristics on the hydrogel properties and more particularly on the microstructure. For that, we use the rational formulation approach presented in Chapter II to design thermosensitive CS/βGP/AHP mixtures from CS having various molar mass distributions, deacetylation degree (*DD*) and origins. The second question (section 0) is about the possible effect of the presence of cells on the gelation and on the microstructure of CS/βGP/AHP hydrogels. The typical cell concentrations in cell-laden systems range from 10^6 to 10^7 cells.mL⁻¹. Considering that the typical volume of most mammalian cells is of the order of $4000 \mu\text{m}^3$,⁵ this concentration range corresponds to a volume fraction ranging from 0.05 to 0.5 vol%. In systems where the structure is formed *in situ*, the presence of a third component at such a concentration has to be considered. To address this question, we characterized the hydrogel microstructures in the presence of fluorescently-labelled cells at two concentrations: 10^6 and 5.10^6 cells.mL⁻¹.

IV.2. Quantitative analysis of the microstructure of CS/βGP/AHP hydrogels

This section is devoted to the development of an image analysis protocol for characterizing quantitatively the microstructure of thermosensitive CS/salt hydrogels. The goal was to determine the overall porosity and the pore size distribution of these hydrogels using confocal microscopy images.

The following work was realized in collaboration with Dr. Etienne Decencière (Centre de Morphologie Mathématique, MINES ParisTech – PSL) and Pierre Marquaille in the context of his research project (C3M, ESPCI Paris – PSL).

IV.2.1. Theoretical background

2.1.a. Point spread function (PSF)

In fluorescence microscopy, the resolution is limited by the diffraction of light. Accordingly, the image of a point is a blurred point. This process can be mathematically described using the point spread function (PSF), which is defined as the 3D diffraction pattern of light emitted from an infinitely small source and transmitted to the image plane.⁶⁻⁸ Thus, the image of a single point is a 3D spread point which is the convolution of the point and the PSF and thus the image of an object is the sum of all points composing the object (**Figure IV - 1**).⁹

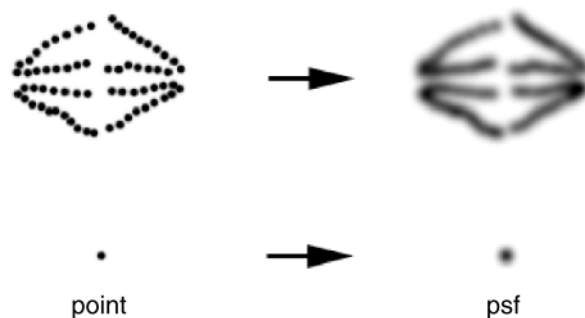


Figure IV - 1. Scheme illustrating how a single point and an extended object are transformed by the convolution with the PSF. Reproduced from Pawley et al.⁹

The PSF can be obtained either by experimental measurements or by theoretical calculations.^{10,11} The PSF of an ideal microscope, *i.e.* aberration free, is a circularly symmetric function and is given by equation (**IV - 1**).¹²

$$PSF(r) = \left(2 \frac{J_1(ar)}{r}\right)^2 \text{ with } a = \frac{2\pi NA}{\lambda} \quad (IV - 1)$$

Where J_1 is a Bessel function of the first kind, λ is the wavelength and NA is the numerical aperture of the lens.

2.1.b. Deconvolution

Assuming that the imaging process is linear and shift-invariant, the image of any object can be determined knowing the PSF.¹³ Therefore, the estimate of the real object structure can be improved by deconvoluting the observed image by the PSF.^{14,15} This procedure is illustrated in **Figure IV - 2**. Many algorithms have been developed for computational deconvolution of fluorescence microscopy images and detailed review can be found in reference ¹⁵.

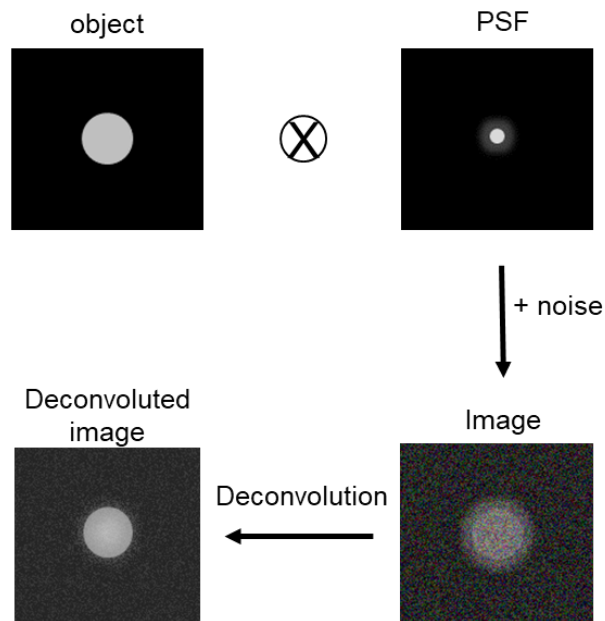


Figure IV - 2. Scheme illustrating the imaging process and the deconvolution procedure.

2.1.c. Binarization (thresholding)

Image segmentation is the process in which an image is partitioned into various groups of pixels, allowing to reduce the image complexity and facilitate the image analysis.¹⁶ Nowadays, image segmentation is one of the most exploited techniques in medical image analysis.¹⁷ When the segmentation results into two groups of pixels, one talks about binarization or thresholding. This method is based on a threshold value and transforms a gray-scale image (pixel values range 0–255) into a binary image (pixel value is 0 or 1). The key step of this method is the determination of the threshold value, and to transform pixels which value is below the threshold to black and the others to white. Numerous algorithms have been developed and can be classified as global or local thresholding.¹⁸ According to the characteristics and the properties of the image, one should choose the relevant approach. On the one hand, global thresholding algorithms are based on global statistics of the histogram of the image, allowing to choose a constant threshold value. On the other hand, local thresholding algorithms consist in analyzing local properties in the histogram, e.g., minima and maxima. In comparison with the global

approach, the local approach is more appropriate when the background of the image is not uniform. However, it is significantly more sensitive to noise. Two most well-known and widely used global thresholding techniques are reported by Otsu¹⁹ and Li *et al.*^{20,21} The Otsu's method selects the threshold which minimizes the intra-class intensity variance while the Li's method is based on the minimization of the cross entropy between segmented image and the original image.

2.1.d. Morphological sieve technique

The morphological sieve technique was first introduced in image analysis by Matheron.²² This method has been applied to calculate the size distribution of groups of objects.²³⁻²⁵ Its principle is very similar to sieving a powder.²⁴ In laboratory, the powder is passed through sieves with decreasing mesh size and a size distribution is obtained by measuring the quantity of power staying on each sieve. In image analysis, an analogous process is applied in an inverted order using morphological filters. Firstly, a structuring element having a given shape and size is defined and used as a probe. Secondly, this structuring element is used to scan the whole image. During this step, each time the structuring element passes above a smaller object, this object is removed, usually using a closing operation.²³ The corresponding area of removed objects is calculated. This step is repeated by increasing the size of the structuring element and scanning the image until complete removal of all objects. Therefore, a size distribution of the objects can be obtained. The process is illustrated in **Figure IV - 3**.

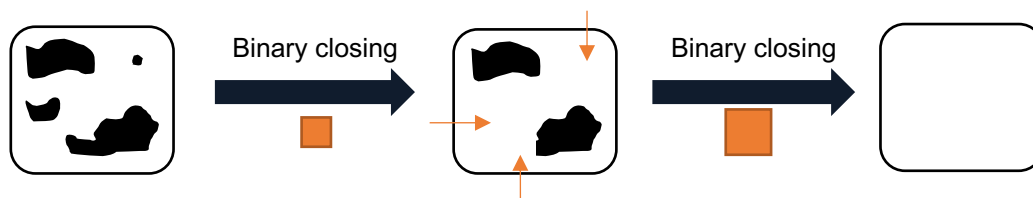


Figure IV - 3. Simplified scheme illustrating the principle of the morphological sieve technique to calculate size distribution of objects. Here, the structuring element is a square.

IV.2.2. Experimental methods and image processing

2.2.a. Confocal microscopy observation

A customized sample holder, as described in Chapter III, was filled with a few hundreds of microliters of fluorescently labelled CS/ β GP/AHP solution, sealed to prevent evaporation and incubated in a regular oven at 37°C for 30 min. The hydrogels prepared with 0.8 wt% or 0.5 wt% of CS were then observed at room temperature using Laser Confocal Scanning Microscopy (LCSM, Zeiss Axiovert 200M). For each sample, stacks of 10 images of (512 \times 512 pixels, 225 μ m \times 225 μ m) with an interval of 1 μ m were recorded in eight random positions at 100 μ m depth. Oil immersion objective \times 40/1.3 DIC was used.

2.2.b. Deconvolution and binarization

The image processing was realized using ImageJ.²⁶ The PSF was computed using the *Diffraction PSF* plugin in ImageJ (Robert Dougherty). This plugin takes for input experimental parameters (the index of refraction of the media, the numerical aperture of the objective, the emission wavelength, the image pixel spacing, the image size and the depth of the stack) and calculate a theoretical PSF based on analytical derivation using Fraunhofer diffraction. The calculated PSF was used for deconvoluted image stacks using the *Iterative Deconvolve 3D* plugin (Robert Dougherty) which is based on the DAMAS algorithm.²⁷ A despeckle filter was then applied to the deconvoluted image in order to reduce noise, following by binarization by either Li's or Otsu's method.

2.2.c. Porosity

The overall porosity of a hydrogel can be estimated as the fraction of the water-rich phase (pores). From binarized images, the porosity is calculated following equation (IV - 2). For each sample, the porosity value is averaged over 8 stacks of images.

$$Porosity (\%) = \frac{Black\ pixels}{Black+White\ pixels} \cdot 100\ \% \quad (IV - 2)$$

2.2.d. Pore size distribution

We developed a customized program in Python based on the morphological sieve technique. This program takes for input deconvoluted images, proceeds to binarization and calculates a distribution of pore fraction in which an increasing size structuring element can be fitted. The pore size distribution is averaged over 4 stacks of images for each sample.

IV.2.3. Results & Discussion

2.3.a. Deconvolution and binarization of confocal microscopy images

The performance of the image processing was evaluated on confocal microscopy images of CS/βGP/AHP hydrogels. The PSF was theoretically calculated for a stack of 10 slices of 215 × 215 μm spacing of 1 μm. The structure of a CS/βGP/AHP hydrogel prepared at 0.5 wt%, after 30 min at 37°C is shown in **Figure IV - 4a**. The hydrogel has heterogeneous structure composed of CS-rich phase (bright) and water-rich phase (dark). **Figure IV - 4b** shows the result of the deconvolution process on this image. **Figure IV - 4c** shows the intensity profile of pixels belonging to a line crossing the width of the image. The quality of the signal is clearly improved and the background is better defined after deconvolution. Hence, the deconvolution process is relevant for analyzing the microstructure of our system of interest. For the binarization, the global approach was chosen because the background of our

images is uniform. Thresholding was performed on deconvoluted images using either Otsu's or Li's method, the two most well-known global algorithms. For the image shown in **Figure IV - 4b**, the calculated threshold value is 22 for Otsu's method and 16 for Li's method. Comparing the images obtained with both methods (**Figure IV - 5**), it turned out that the threshold value given by Otsu's method was too high, inducing a partial loss of the information. Therefore, the Li's method was chosen for further analyses.

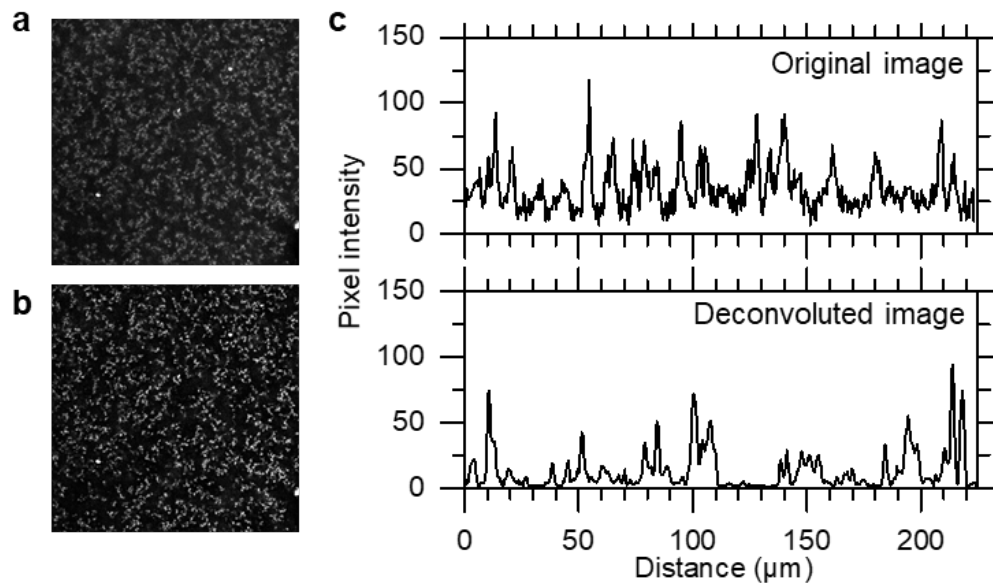


Figure IV - 4. Image processing for one micrograph of CS/βGP/AHP hydrogel at CS 0.5 wt%: **a)** original micrograph; **b)** deconvoluted image and **c)** comparison of the intensity profile of a horizontal line at $y = 100 \mu\text{m}$ between the original and the deconvoluted image.

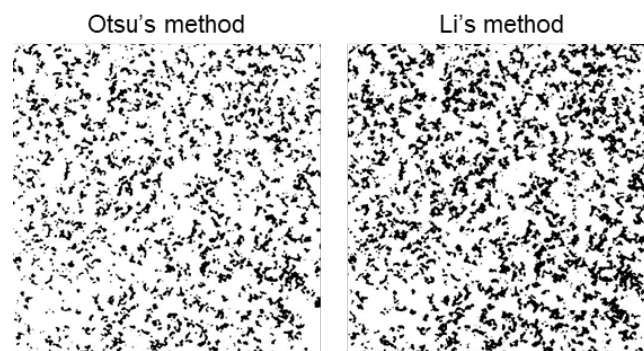


Figure IV - 5. Images obtained after thresholding process by Otsu's or Li's method on the deconvoluted image shown in **Figure IV - 4b**.

2.3.b. Effect of the CS concentration on the hydrogel microstructure

In Chapter II, we demonstrated the possibility to vary the CS concentration while maintaining physiological conditions of pH and osmolarity. This provides a way to adjust the properties of the hydrogels, in particular, their microstructure. Using the protocol for image processing presented above, the effect of the CS concentration on the microstructure was quantitatively investigated for four hydrogels ranging from 0.5 to 0.8 wt%. **Figure IV - 6a** shows the microstructure of physiological hydrogels prepared at CS concentration of 0.5 or 0.8 wt%.

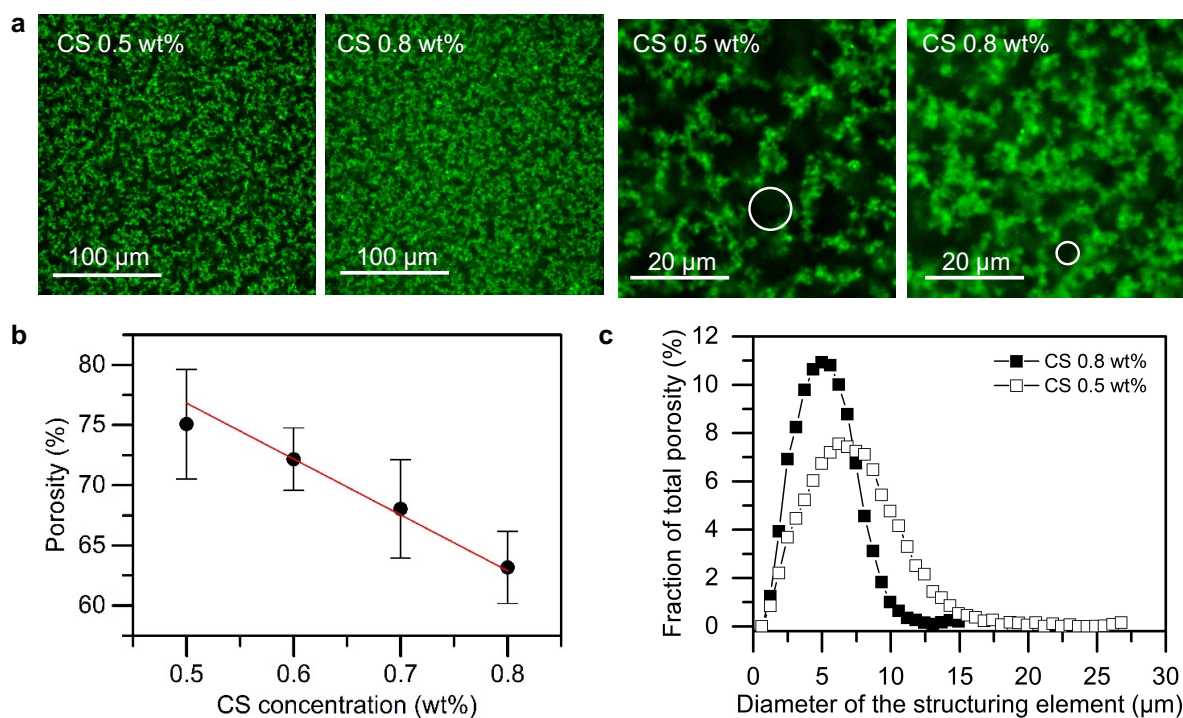


Figure IV - 6. (a) Original confocal microscopy images of fluorescently labelled CS/ β GP/AHP hydrogels prepared with 0.5 or 0.8 wt% after 30 min at 37°C, white circles show circular structuring elements having the mean diameter determined by a morphological sieve algorithm. (b) Hydrogel porosity as a function of CS concentration. (c) Pore size distributions determined by morphological sieve technique for CS/ β GP/AHP hydrogels prepared with 0.5 and 0.8 wt%.

Assuming that the structure of these hydrogels is isotropic, we measured the porosity from 8 binary stacks of 10 images. We found that the porosity decreases linearly with increasing CS concentration, as shown in **Figure IV - 6b**, from $75 \pm 5\%$ for CS 0.5 wt% to $63 \pm 7\%$ for CS 0.8 wt%. Such a linear relationship was reported earlier for CS/ β GP.²⁸ Our linear relationship extrapolates a porosity of 100% for CS concentration = 0 wt% and a porosity = 0 % for CS concentration = 2.2 wt%. On the one hand, this result indicates that there are very few free CS chains in the water-rich phase. On the other hand, this suggests that for all the studied formulations, the CS concentration in the CS-rich phase is about 2.2 wt% and the CS-rich phase is therefore still highly swollen by water. This is in agreement with previous

observations in CS/ β GP hydrogels reported by Crompton *et al.*²⁹ who carried out SANS measurements and proposed that the CS-rich phase is composed of two phases, small hydrophobic domains in a highly swollen phase.

Besides porosity, the pore size is another crucial parameter governing cell-cell interactions and vascularization.³⁰ Targeted pore sizes vary from tens to hundreds of micrometers depending on the cell type and on the application.^{30,31} With the present systems, we observed large interconnected elongated macropores. The longest dimension of the largest pores was found to reach 15 μm for CS 0.8 wt% and up to 30 μm for CS 0.5 wt%. The pore size distributions measured using a morphological sieve algorithm are shown in **Figure IV - 6c**. These distributions show the fraction of porosity able to fit a circular structuring element of a given diameter. This analysis clearly reveals that the characteristic size of the macropores increases with decreasing CS concentration. Indeed, 98% of the porosity can contain structuring elements having diameters ranging from 1 to 9 μm for CS 0.8 wt% and from 1 to 14 μm for CS 0.5 wt%. The mean diameter of the structuring element, which represents the mean pore size, increases with decreasing CS concentration, from $5.4 \pm 0.4 \mu\text{m}$ for CS 0.8 wt% to $7.5 \pm 0.9 \mu\text{m}$ for CS 0.5 wt%. For the sake of simplicity, in the following, the diameter of the structuring element will be considered as the pore size. However, we should be careful while interpreting these results because our system of interest possesses very elongated pores and the used image processing captures only the smallest dimension of the pores.

IV.3. Effect of CS characteristics on the properties of CS/ β GP/AHP hydrogels

Several studies have reported investigations on the effect of various CS characteristic (molar mass distribution and DD) on the mechanics and the microstructure of CS/ β GP mixtures.^{32–35} However, in these studies, no attention was paid to the control of pH of CS/ β GP mixtures. As previously shown in Chapter II, section II.3.3, the gelation kinetics evolves strongly with the pH for a given CS grade. In our study, the pH of CS/ β GP/AHP hydrogels is finely adjusted to 7.4 at 4°C according to the formulation approach reported in Chapter II to correctly evaluate the effect of CS characteristics on the hydrogel properties.

The following work was realized in collaboration with Andrey Kolosov in the context of his M1 internship at C3M laboratory, ESPCI Paris-PSL and Sonia Ortega, Dr. Raphaël Michel and Pr. Rachel Auzély-Velty from CERMAV, CNRS.

IV.3.1. Materials & experimental methods

3.1.a. Materials

Seven grades of chitosan (CS) having high purity (impurity level < 1.0%) and various characteristics (origin, molar mass, dispersity) were purchased from Glentham Life Sciences Limited. The characteristics are given in **Table IV - 1**. All CS grades originate from chitin extracted from shrimp, except for CS3, which is from squid.

3.1.b. Experimental methods

Preparation of physiological formulations with different CS grades

CS stock solutions were prepared by dissolving CS in acetic acid, AcOH, aqueous solution. The quantity of AcOH was adjusted in function of the DD in order to obtain the ratio $[\text{AcOH}]/[\text{NH}_2] = 1$.

Physiological CS/ β GP/AHP formulations at a fixed CS concentration of 0.8 wt% were prepared with various grades of CS according to the results of Chapter II. Briefly, the $[\beta\text{GP}]/[\text{NH}_2]$ ratio was fixed at 1.5 and the $[\text{AHP}]/[\text{NH}_2]$ ratio was adjusted using the equation of the iso-pH which is calculated for each DD .

Characterization of the molar mass distribution of CS

The molar mass distribution of the studied CS was obtained from gel permeation chromatography (GPC). Measurements were conducted on TSKgel GMPW XL (Tosoh Bioscience GmnH) column coupled to a refractive index detector (Optilab T-rEx) and multi-angle light scattering detector (Dawn Heleos II). The mobile phase was AcOH 0.2 M /AcONH₄ 0.15 M. Samples of CS were prepared at 0.2 – 2.0 mg.mL⁻¹ in function of the CS grades using the mobile phase as solvent. The concentration was 2

mg.mL⁻¹ for CS1 and CS2, 1 mg.mL⁻¹ for CS3, 0.6 mg.mL⁻¹ for CS4 and 0.2 mg.mL⁻¹ for CS5, CS6, CS7. All samples were filtered using syringe filters (MCE membrane, 0.45 μm) before experiment and a second filtration (0.1 μm) was realized before injection into the column. CS solutions were analyzed under the flow rate of 0.5 mL.min⁻¹ at 30°C. Each measure was duplicated. Pullulan having $M_w = 2.10^5$ g.mol⁻¹ was used as a standard for column verification. The value $dn/dc = 0.192$ was used for all samples.

Determination of gelation time

The gelation times were determined by the same test tube inversion method as in Chapter II, section II.2.2.

Rheological measurements

Rheological properties of CS/βGP/AHP formulations at 37°C prepared using various CS grades were studied using rheometer MCR502 (Anton Paar) with a cone-and-plate geometry (CP50-2TG) using the same protocol as in Chapter II. The values of storage and loss moduli (G' , G'') were measured during 6 h, at a constant oscillatory strain of 0.1% and an angular frequency of 1 rad.s⁻¹.

IV.3.2. Results & Discussion

3.2.a. Characterization of the molar mass distribution

The molar mass distribution of different CS grades was studied using GPC equipped with a special column adapted for CS. The differential weight distributions of the seven studied CS grades are shown in **Figure IV - 7**. The characteristics including the number-average molar mass, M_n , the mass-average molar mass, M_w , and the dispersity of the studied CS grades are shown in **Table IV - 1**. It is worth to notice that the viscosity-average molar mass, M_v , given by the supplier is noticeably different from the one obtained by our GPC measurements. This can be explained by the different methods and solvents used to characterize these CS grades. In general, for polymers having chains of various sizes, the relationship between these averaged molar masses is: $M_n < M_v < M_w$. However, the M_v given by the supplier is significantly higher than M_w determined by GPC. Therefore, the difference between the data given by the supplier and our analysis should arise from the used solvent. Indeed, the supplier used a solution of AcOH at 1 wt% while we used a buffer solution of 0.2 M AcOH/0.15 M AcONH₄, which was reported as a good solvent for CS thus minimizing the presence of aggregates.³⁶ Therefore, we suggest that the M_v value given by the supplier is overestimated due to the presence of aggregates. The overlap concentration, c^* , as we determined from viscometry, confirms that CS solutions used in GPC analysis was in the diluted regime (Appendix B).

The values of DD were given by the supplier and were determined by potentiometric titration. These values were used to calculate the quantities of AcOH for the solubilization and of phosphate salts for the preparation of physiological CS/ β GP/AHP formulations using different CS grades according to our previous study.³⁷ Accordingly, all CS CS/ β GP/AHP formulations had a $pH = 7.4 \pm 0.05$ at 4°C . The values of the dispersion, D , determined from GPC results, indicate that the dispersion is not uniform between the studied CS grades. Nonetheless, D ranges from 1.5 to 2.9, which can be considered as relatively low for a polymer of natural origin.

In the following discussion, whenever necessary, the notation CS grade- M_w - DD will be used, for example CS1-45kDa-95 for the CS1 grade.

Table IV - 1. Characteristics of the studied CS grades.

CS grade	M_v^* (kDa, viscometry)	DD^* (%, titration)	M_w^{**} (kDa, GPC)	M_n^{**} (kDa, GPC)	D^{**} M_w/M_n
CS1	30	95	45	22	2.1
CS2	250	91	188	84	2.1
CS3	590	94	205	62	3.3
CS4	890	95	225	77	2.9
CS5	1250	90	408	232	1.7
CS6	1500	90	540	260	2.1
CS7	1800	91	564	370	1.5

* from the supplier, solvent = AcOH 1 wt%

** from our GPC measurements, solvent = 0.2 M AcOH/0.15 M AcONH₄

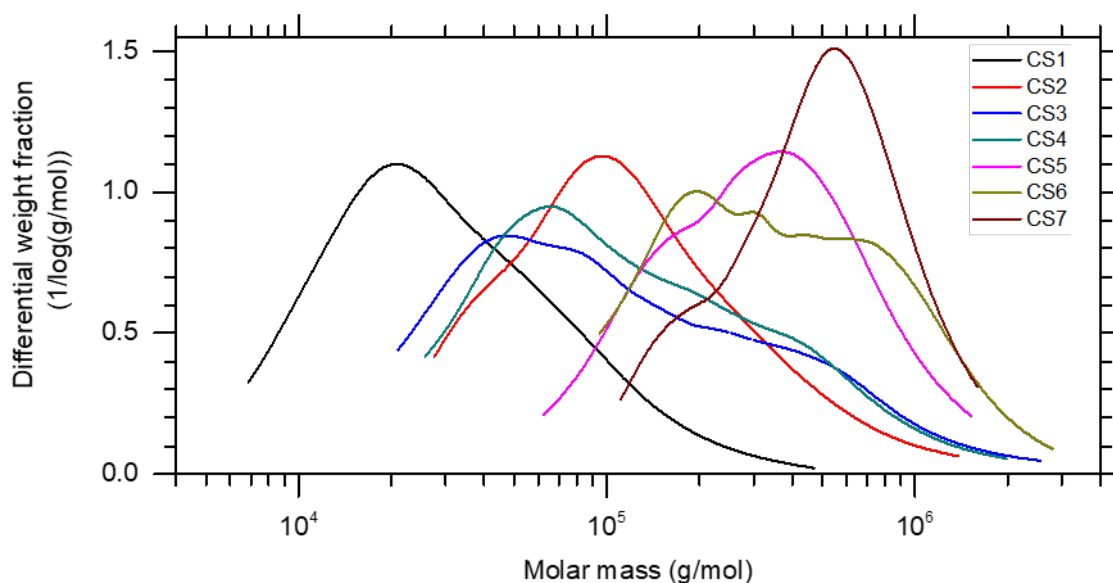


Figure IV - 7. Differential distributions of the molar mass of the studied CS grades. The area under each curve is normalized to 1.

3.2.b. Gelation kinetics

Physiological CS/ β GP/AHP formulations at a fixed CS concentration of 0.8 wt% were prepared with various grades of CS according to the formulation approach reported in our previous study.³⁷ The iso-pH equation at pH = 7.4 was determined for each CS grade knowing the DD . The $[\beta\text{GP}]/[\text{NH}_2]$ ratio was fixed at 1.5 and the $[\text{AHP}]/[\text{NH}_2]$ ratio was adjusted following the calculated iso-pH equation. We verified that all solutions had a pH = 7.4 ± 0.05 at 4°C . The difference in DD between the CS grades being relatively low ($\leq 5\%$), the calculated osmolarity for all CS grades was in the physiological range ($300 \pm 30 \text{ mOsm.L}^{-1}$). This confirms the robustness of our designed platform for preparing thermosensitive CS/ β GP/AHP formulations respecting the physiological conditions.³⁷

The gelation time at 37°C was determined both by the inversion tube method and by rheology. For the inversion tube method, the gelation time is defined as the time at which the mixture does not flow anymore. For rheological measurements, the gelation point is taken as the time at which G' crosses G'' . **Figure IV - 8** shows rheological measurement in oscillatory mode for a period of 12 min for all the studied formulations. CS2 to CS7 formulations showed a gelation time of 2 ± 0.5 min, as determined by both methods. For the formulation prepared with CS1, the gel point was determined at 2.5 min by rheological measurement but at 20 ± 5 min by the inverted tube method. We attribute this discrepancy to the weakness of this gel ($G' \sim 1 \text{ Pa}$), rendering the measurement by the inverted tube method very delicate.

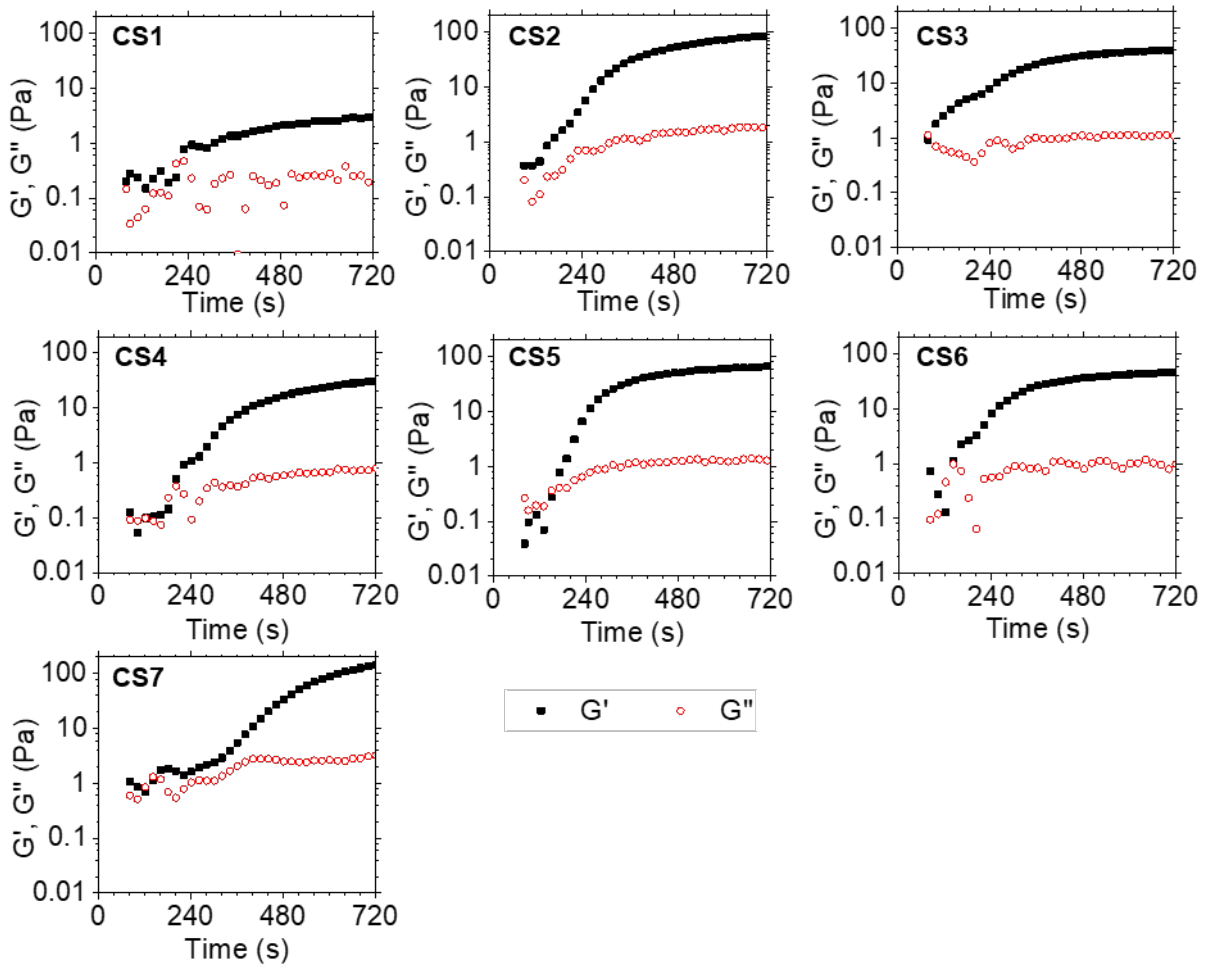


Figure IV - 8. Time-sweep measurement at 37°C of the storage modulus, G' , and the loss modulus, G'' , for CS/ β GP/AHP formulations prepared with various CS grades. CS concentration = 0.8 wt%, pH = 7.4 at 4°C, $\omega = 1 \text{ rad.s}^{-1}$, $\gamma = 1\%$.

The gelation kinetics of three formulations prepared with three different CS grades (CS2-188kDa-91, CS4-205kDa-95, CS5-408kDa-90) was investigated in more detail. The gelation time at various incubation temperatures was determined using the inverted tube technique. The results for CS2-188kDa-91 were already shown in Chapter II. For all the three CS grades, the gelation time decreased by at least four orders of magnitude when the temperature increases from 15°C to 37°C, as shown in **Figure IV - 9a**.

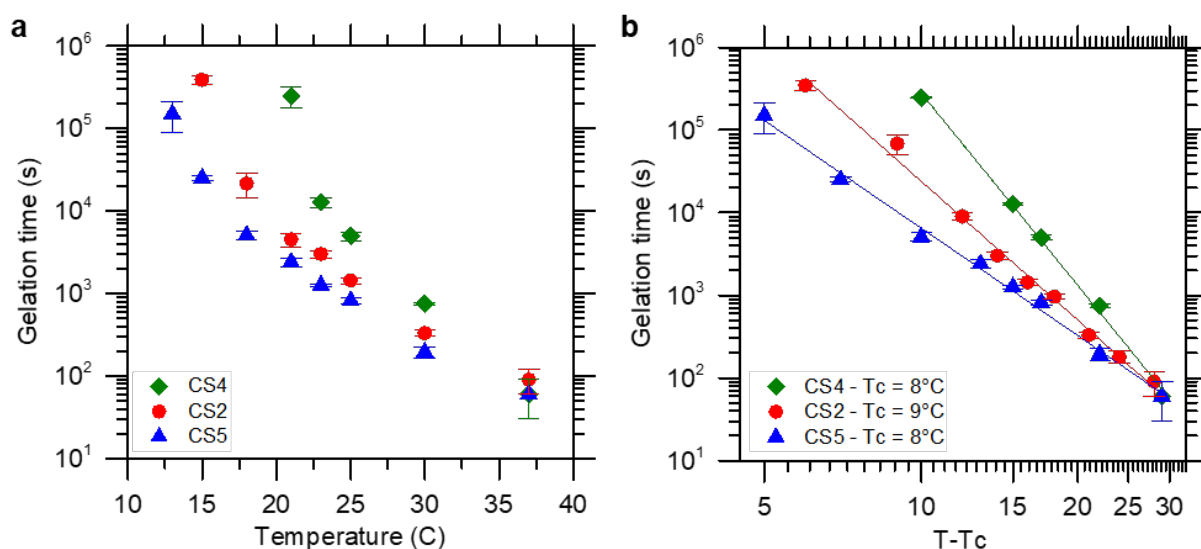


Figure IV - 9. Gelation kinetics of formulations having fixed CS 0.8 wt% and pH = 7.4 prepared with various CS grades: gelation time as a function of temperature **(a)** and of $(T-T_c)$ **(b)**, continuous lines show fits by a power law.

At a given temperature, the gelation time follows the order: CS5-408kDa-90 < CS2-188kDa-91 < CS4-205kDa-95. This trend is emphasized with decreasing temperature, especially between CS4-205kDa-95 and the two other grades. At 21°C, the gelation time is almost two orders of magnitude longer for CS4-205kDa-95 than for the two others. We propose to interpret this trend as follows.

For CS grades having similar DD , like CS5-232kDa-90 and CS2-84kDa-91, t_{gel} decreases with increasing chain length. This reduction of gelation time with higher M_w can be explained by the fact that interchain interactions are more favorable for long chains. Following the proposed molecular mechanisms (Chapter III), this effect would accelerate the aggregation of CS chains and the formation of CS particles.

For CS grades having similar molar mass distributions, like CS2-188kDa-91 and CS4-205kDa-95, t_{gel} increases strongly with increasing DD . Our results are inconsistent with the ones previously reported by Chenite *et al.* who measured the gelation temperature, T_{gel} , using temperature-ramp experiments and found that T_g decreases with increasing DD .³² In particular, they found that T_{gel} decreases from 66°C to 37°C with increasing DD from 70% to 91%. However, the same amount of β GP was used to prepare their mixtures whatever the CS characteristics. According to our calculations (Chapter II), the pH would be different for mixtures prepared with CS having different DD , therefore their conclusion regarding the DD might be arguable. Our results concerning the DD -dependency of t_{gel} can be explained by the fact that the difference in DD might induce changes in the molecular interactions involved in the sol/gel transition. First, when DD increases, the quantity of N -acetyl units contributing to hydrophobic interactions decreases, thus making the aggregation less favorable. Second, with increasing DD , the

quantity of D-glucosamine monomers increases, thus favoring the electrostatic repulsion and the creation of the hydration layer. However, the critical ionization degree at which aggregation occurs, only decreases slightly when *DD* increases, as shown in previous studies.^{38,39} Therefore, the energy barrier to overcome is higher for higher *DD*.

Like in Chapter II, the evolution of the gelation time as a function of the temperature is successfully fitted with a critical-like model $t_{\text{gel}} = k(T-T_c)^\gamma$ for the three CS grades, where T_c is a critical temperature above which the sol-gel transition occurs and γ is a constant exponent (**Figure IV - 9b**). Interestingly, the value of T_c was found to be the similar for the three CS grades, $8 \pm 1^\circ\text{C}$ for CS4-205kDa-95 and CS5-408kDa-90, and $9 \pm 1^\circ\text{C}$ for CS2-188kDa-91. These results suggest that at fixed pH and $[\beta\text{GP}]/[\text{NH}_2]$ ratio, the value of T_c does not depend on the characteristics of the CS (molar mass distribution and *DD*).

3.2.c. Microstructure and mechanical properties

The microstructure of the hydrogels prepared with different CS grades at a fixed CS concentration of 0.8 wt% (pH = 7.4 ± 0.05 at 4°C and $300 \pm 30 \text{ mOsm.L}^{-1}$) was characterized using confocal microscopy. **Figure IV - 10** shows deconvoluted images of hydrogels formed after 2 h of incubation at 37°C .

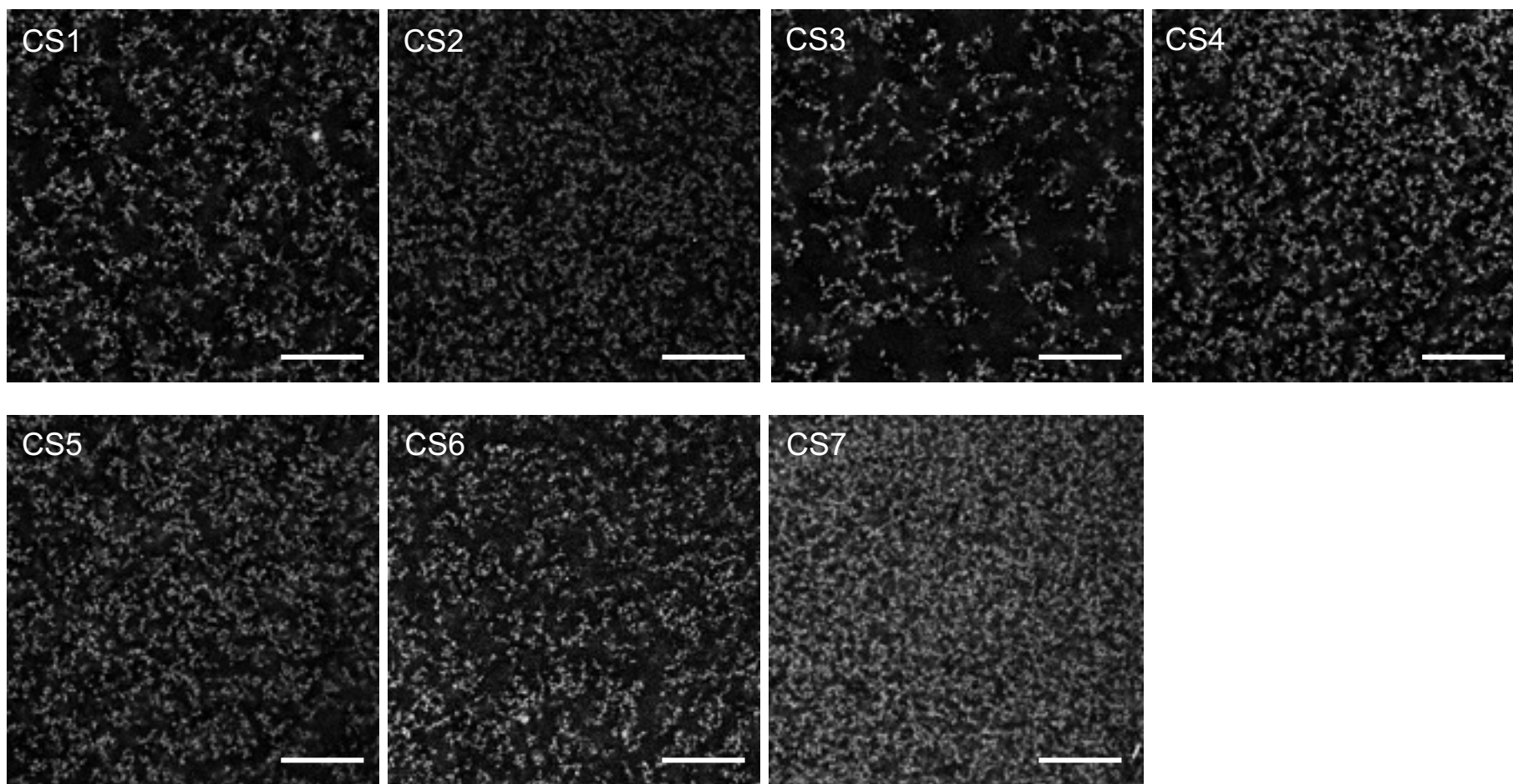


Figure IV - 10. Deconvoluted confocal microscopy images ($225 \times 225 \mu\text{m}$) for physiological CS/ β GP/AHP hydrogels prepared with different CS grades. Images were taken after 2 h of incubation at 37°C . CS 0.8 wt%, $\text{pH} = 7.4 \pm 0.05$ at 4°C and $300 \pm 30 \text{ mOsm}\cdot\text{L}^{-1}$. Scale bar = $50 \mu\text{m}$.

All hydrogels show a heterogeneous structure composed of a CS-rich phase (bright) and a water-rich phase (dark). The porosity and pore size defined as the area fraction and the characteristic size of the water-rich phase, respectively, vary remarkably with the different CS grades, even though the CS concentration is fixed. The porosity and the mean pore size were quantitatively determined based on the image analysis process described in the last section. The results are reported in **Table IV - 2**. The pore size measured with the molecular sieve method corresponds here to the mean diameter of a circular structuring element able to fit inside a pore, as described above in section IV.2.

Table IV - 2. Porosity, mean pore size and storage modulus, G' , of physiological CS/ β GP/AHP hydrogels prepared with different CS grades after 2 h at 37°C. CS 0.8 wt%, pH = 7.4 ± 0.05 at 4°C and 300 ± 30 mOsm.L⁻¹.

CS grade	M_w (kDa, GPC)	M_n (kDa)	\bar{D} , M_w/M_n	Porosity (%)	Mean pore size (μ m)	G' (Pa)
CS1	45	22	2.1	73 ± 2	9.4 ± 0.8	15
CS2	188	84	2.1	65 ± 1	6.1 ± 0.4	230
CS3	205	62	3.3	83 ± 1	14.3 ± 1.8	5
CS4	225	77	2.9	70 ± 2	8.1 ± 0.5	85
CS5	408	232	1.7	68 ± 4	6.8 ± 0.5	119
CS6	540	260	2.1	75 ± 2	7.4 ± 0.5	72
CS7	564	370	1.5	57 ± 1	4.9 ± 0.3	960

Due to the natural origin of CS, it is complicated to control and adjust CS characteristics such as the chain length and the dispersity. Hence, it is very difficult to study separately the effect of a unique characteristic for a large number of CS grades. No obvious trend was found between the porosity or the mean pore size, and the CS molar mass and dispersity (Appendix D.1).

For the chosen CS concentration of 0.8 wt%, the overall porosity and the pore size distribution can be nevertheless tuned using CS with various characteristics. For the seven studied CS grades, we found a good correlation between the mean pore size and the overall porosity, as shown in **Figure IV - 11**. We obtained a three-fold increase in the mean pore size going from 4.9 ± 0.3 μ m for the CS7 hydrogel having a porosity of $57 \pm 1\%$ to 14.3 ± 1.8 μ m for the CS3 hydrogel having a porosity of $83 \pm 1\%$.

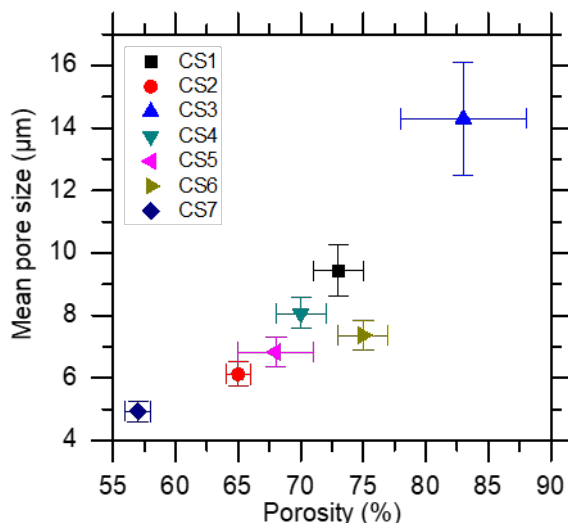


Figure IV - 11. Evolution of the mean pore size as a function of the overall porosity for hydrogels prepared with different CS grades at a fixed concentration of CS at 0.8 wt%.

The CS-rich phase is itself heterogeneous as it is highly-swollen, as demonstrated in the section IV.0 and in previous study.²⁸ For CS2, we found the concentration in the CS-rich phase around 2.2 wt%. In a similar manner, the concentration of CS in the CS-rich phase was determined for all studied CS grades and was found to range from 1.8 to 3.2 wt%. **Figure IV - 12** shows the evolution of porosity as a function of the concentration of CS in the CS-rich phase. Interestingly, a more porous hydrogel has a denser polymer-rich phase. Hence, the difference in porosity between hydrogels prepared with different CS grades can be explained by how concentrated is the CS-rich phase. The formation of the CS-rich phase is a result of the aggregation and phase separation process. We speculate that these processes might depend on the characteristics of the used CS including the molar mass distribution, the dispersity and the crystallinity.

The mechanical properties of the hydrogels prepared with different CS grades ($\text{pH} = 7.4 \pm 0.05$ at 4°C and $300 \pm 30 \text{ mOsm.L}^{-1}$) were characterized using oscillatory rheology at isothermal conditions at 37°C . Values of the storage modulus, G' , at 2 h are reported in the **Table IV - 2**. In a similar manner as the microstructure, no obvious trend was observed as function of the CS molar mass (Appendix D.2).

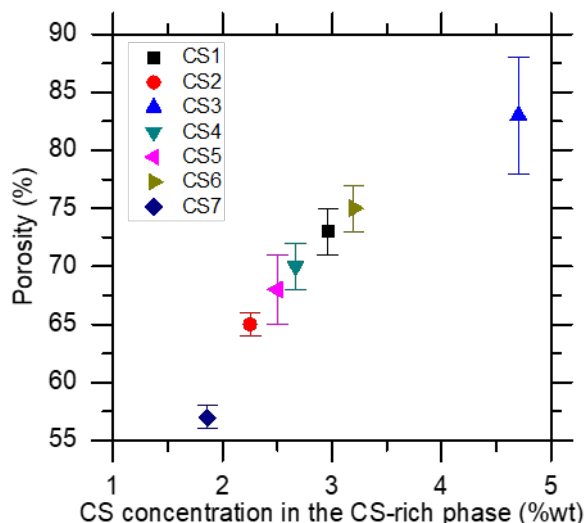


Figure IV - 12. Evolution of the porosity as a function of the concentration of CS in the CS-rich phase for hydrogels prepared with different CS grades at a fixed concentration of CS = 0.8 wt%.

CS3 is the only grade that is obtained from squid-derived chitin while the others are originated from shrimp-derived chitin. CS3 shows a particularly high porosity and pore size compared to other CS grades. It was previously reported in the literature that the crystallinity of CS varies in function of its origin.^{40,41} Chitin is essentially in the α phase in shrimp and crab shells while the β -chitin is usually found in squid pens. In α -chitin, there are two antiparallel molecules per unit cell while there is only one in β -chitin. Interchain hydrogen bonds were observed only for α conformation. Moreover, the crystal size was also found to depend on the origin of CS in this following order: shrimp > fungal ~ squid.⁴² Therefore, CS3 is expected to have a lower crystallinity in comparison with the other studied CS grades. This would make this grade more soluble than the others and the formation of CS aggregates would be less favorable. This specificity could explain the unexpectedly higher porosity and lower storage modulus of the CS3 hydrogel. Hence, the crystallinity level and the nature of the crystalline phase are also important parameters affecting the microstructure and the mechanical properties of the resulting hydrogel.

Interestingly, comparison of the different CS grades reveals a strong correlation of the elastic modulus, G' , with the effective volume fraction of the CS-rich phase, as shown in **Figure IV - 13a**. Here, the effective volume fraction, ϕ_{eff} , is defined as $(1-p)$ where p is the porosity. We find that G' scales with ϕ_{eff} following a power law, $G' \propto \phi_{\text{eff}}^m$ with $m = 4.8$ (**Figure IV - 13b**). Such a power law has been already interpreted for colloidal gels using the Ball and Brown's scaling theory.⁴³⁻⁴⁵ By assuming that the network consists of interconnected fractal clusters, the theory predicts that the elastic modulus of a colloidal gel scales with the colloid volume fraction as ϕ^m , with $m = 3.5 \pm 0.2$ for diffusion-limited

aggregation (DLA) and $m = 4.5 \pm 0.2$ for reaction-limited aggregation (RLA). On the one hand, DLA occurs when repulsive forces between the colloidal particles are negligible, so the aggregation rate is limited by the time for particles to diffuse and to encounter each other (strong-link type). On the other hand, RLA regime happens when particles need to encounter each other several times to form aggregates (weak-link type).⁴⁶ Such a power law and comparable exponents have been previously found for various colloidal gels.^{43,45,47–49} Here, for CS/ β GP/AHP hydrogels, the value of exponent $m = 4.8$ suggests that the aggregation would follow a RLA process. This result is in agreement with previous studies on CS/ β GP hydrogels that reported a fractal structure with fractal dimension around 2.3–2.5, which is close to the fractal dimension corresponding to RLA.^{28,50} Therefore, these results suggest that the interactions between CS colloidal-like particles in CS/salt mixtures are rather weak, which is similar to some protein-based colloidal gels.⁵¹

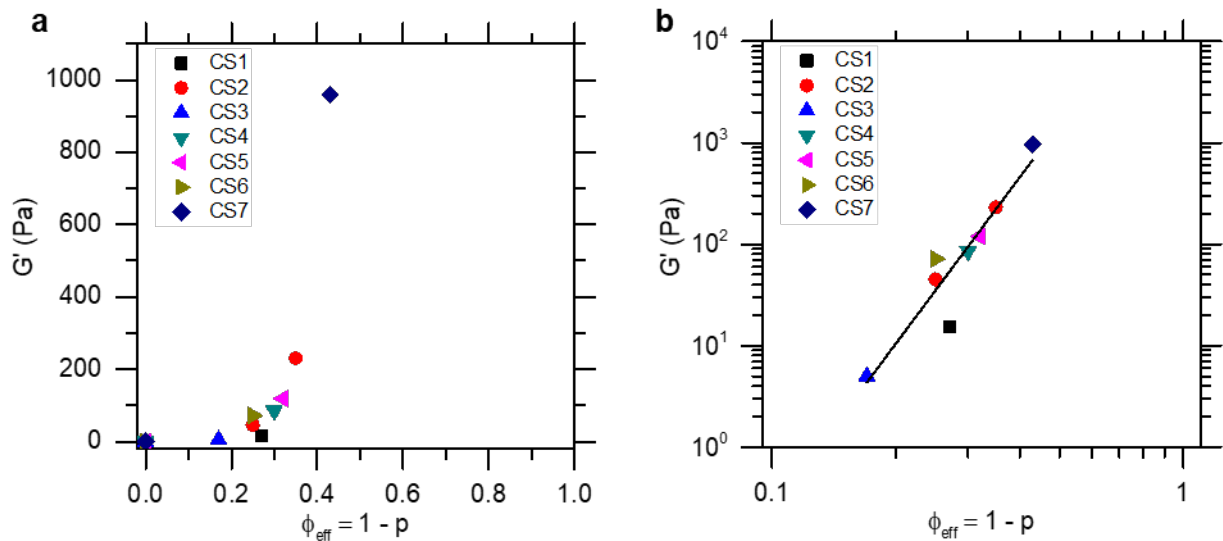


Figure IV - 13. Storage modulus, G' , of physiological CS/ β GP/AHP hydrogels (after 2 h at 37°C) at CS concentration of 0.8 wt% as a function of the effective volume fraction, ϕ_{eff} , for different CS grades: (a) lin-lin representation; (b) log-log representation, full line is a fit by a power law ϕ_{eff}^m with $m = 4.8$.

IV.4. Effect of the presence of cells on the microstructure of CS/ β GP/AHP hydrogels

This section focuses on exploring the incidence of the presence of cells on the microstructure of CS/ β GP/AHP hydrogels. The studied cell concentrations correspond to the ones classically found in cell-laden systems. For that, the microstructures of regular hydrogel (without cells) and hydrogels containing 10^6 and 5.10^6 cells.mL⁻¹ are quantitatively compared using the previously described method in section I.3. Both CS and cells are fluorescently labelled using different dye, allowing simultaneous observations by confocal microscopy.

This work was carried out in collaboration with Rémy Agniel and Dr. Carla Palomino-Durand (ERRMECe, CY Cergy Paris Université).

IV.4.1. Materials & Methods

4.1.a. Materials & Cells

In the following part, the study was performed with the same chitosan grade as in Chapter II also referred to as CS2 in the section IV.3. α -MEM phosphate buffer saline without calcium and magnesium (PBS) was purchased from Gibco. MemBright 560 nm was obtained from Idylle Labs. 4',6-diamidino-2-phenylindole (DAPI) and ProLong™ Gold was purchased from Thermo Fischer Scientific.

MC3T3-E1 pre-osteoblastic cells were obtained from ATCC®.

4.1.b. Experimental methods

Preparation and sterilization of reactants

The preparation and sterilization of reactants were realized as described in Chapter II.

Preparation of physiological CS/ β GP/AHP mixtures

All the study was carried out on the formulation with fixed CS concentration at 0.8 wt%, pH = 7.4 and 300 mOsm.kg⁻¹.

Cell membrane staining

The membrane of MC3T3-E1 cells was stained using recently reported fluorescent probe, MemBright.⁵² The excitation wavelength, 560 nm, was chosen to avoid overlap with the one corresponding to fluorescently-labelled CS, 488 nm. Parameters such as the concentration of the fluorescent probe and the incubation time were optimized for MC3T3-E1 cell line.

The protocol was as follows: 1) A stock solution of MB560 was previously prepared at 2 μ mol.L⁻¹ in DMSO; 2) Cells were trypsinized and re-suspended in serum-free media at 10^6 cells.mL⁻¹; 3) The stock solution of MB560 nm was added to the cell suspension at a final concentration of 50 nmol.L⁻¹; 4) The

mixture was then incubated at 37°C for 30 min; 5) At the end of the incubation period, the mixture was centrifugated and the cell pellet was resuspended in serum-free media.

For the verification of the staining of MC3T3-E1 cells using MB560, the stained cells were seeded onto glass coverslips. After 4 h, cells were fixed using paraformaldehyde at 4 wt% and the nuclei was stained using DAPI solution at 5 $\mu\text{g.mL}^{-1}$. The glass coverslips were then mounted using ProLon™ Gold and observed by confocal microscopy (LSM 710, Zeiss) using lasers at 405 nm and 561 nm. By simultaneously observing the signals from MB560 and from DAPI, we found that 100 % of the cell membrane was stained, as shown in **Figure IV - 14**. Thanks to this staining protocol, the plasma membrane of living cells can be observed, allowing to evaluate cellular behavior. At 4 h following staining by MB560, MC3T3-E1 cells showed signs of cellular adhesion, indicating a good cell viability and a normal cell behavior.

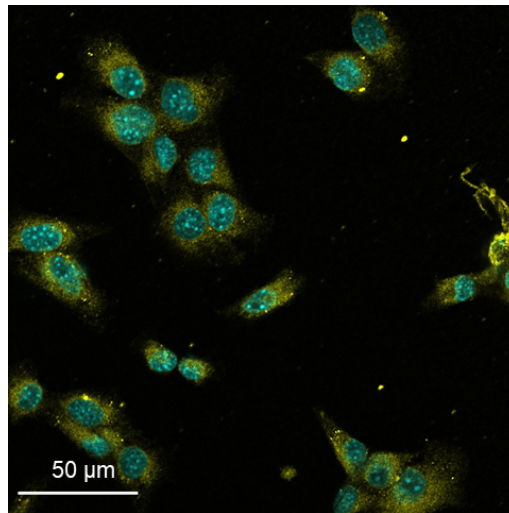


Figure IV - 14. Confocal micrograph of cells having membrane stained with MB 560 (yellow) and nuclei with DAPI (cyan).

The possibility of staining adherent cells was also investigated (see Appendix E for more details). We found that the cell density altered the staining efficiency. In particular, no staining could be achieved on adherent cells at confluence, indicating that high cell density is unfavorable for the interaction between the fluorescent probe and the plasma membrane. Therefore, the most convenient method is to carry out staining on cell suspensions which concentration can be easily controlled.

Cell encapsulation in CS/ β GP/AHP hydrogels

Cell encapsulation was performed at two concentrations: 10^6 and 5.10^6 cells.mL⁻¹. For both cell concentrations, the encapsulation protocol was as follows: (1) cells were previously stained with MB560 and re-suspended in serum-free media, then mixed gently with CS/ β GP/AHP solutions; (2) 300 μL of the mixture containing cells were dispensed into a 8-well culture plate (IBIDI) and incubated for 1 h at

37°C and 5% CO₂ to induce gelation; (3) 1 mL of culture medium supplemented with 10%v/v fetal calf serum and 1%v/v penicillin-streptomycin was added into each well. The cell suspensions were added to CS/βGP/AHP solutions at 1/9 vol/vol. The concentration of the cell suspension was 10⁷ and 5.10⁷ cells.mL⁻¹ for a final cell concentration in the cellularized solutions of 10⁶ and 5.10⁶ cells.mL⁻¹, respectively. Hydrogels without cells were also prepared by replacing the cell suspension by culture medium. Each formulation was realized in triplicate for observation at 1 h, 24 h and 72 h.

Confocal observation

The microstructure of hydrogels and cell-encapsulated hydrogels were observed at 1 h, 24 h and 72 h of incubation using confocal microscopy (LSM 710, Zeiss) using lasers at 488 nm and 561 nm. The image acquisition was performed respecting the protocol developed in section 0: for each sample, stacks of 10 images of (512 × 512 pixels, 225 μm × 225 μm) with an interval of 1 μm were recorded in eight random positions at 100 μm depth using oil immersion ×40 objective. One stack of 100 images of (512 × 512 pixels, 225 μm × 225 μm) with an interval of 1 μm was recorded for each sample using ×20 objective.

Quantitative image analysis

The porosity of the regular CS/βGP/AHP hydrogel was determined using *ImageJ* following the protocol described in section 0. For the hydrogels containing cells, the area fraction occupied by the CS-rich phase and the area fraction occupied by the cells were determined separately. For that, the channel corresponding to cells was analyzed using the *3D object counter* plugin,⁵³ following by thresholding by the Li's method and the pore fraction corresponding to the cells surface was calculated (**Figure IV - 15**).

The pore size distribution was determined by the morphological sieve method (section IV.2) using the channel corresponding to signal from fluorescently-labelled CS.

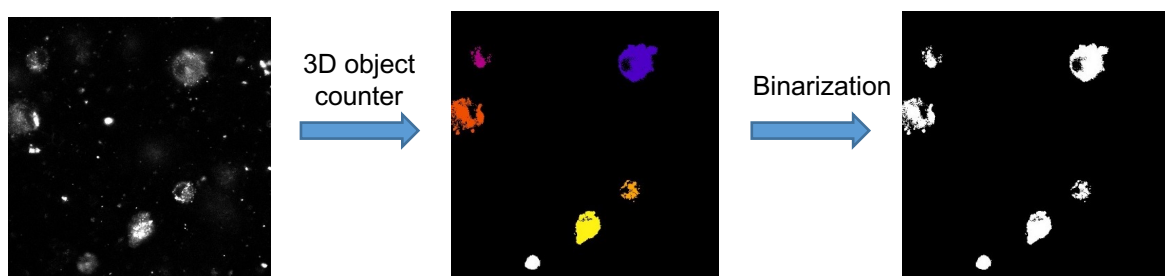


Figure IV - 15. Image processing of the channel corresponding to cells for calculating the pore fraction corresponding to the cells surface.

IV.4.2. Results and discussion

4.2.a. Cell distribution in hydrogels

MC3T3-E1 cells were encapsulated in physiological CS/ β GP/AHP hydrogel at CS 0.8 wt% at two different final cell concentrations: 10^6 or $5 \cdot 10^6$ cells.mL⁻¹. The distribution of encapsulated MC3T3-E1 cells within the hydrogels was observed using confocal microscopy at different incubation times (1 h, 24 h and 72 h). The staining by MB560 allows to localize cells within the hydrogel, and the microstructure of fluorescently-labelled CS/ β GP/AHP hydrogels and stained-cells were observed simultaneously, as shown in **Figure IV - 16a**.

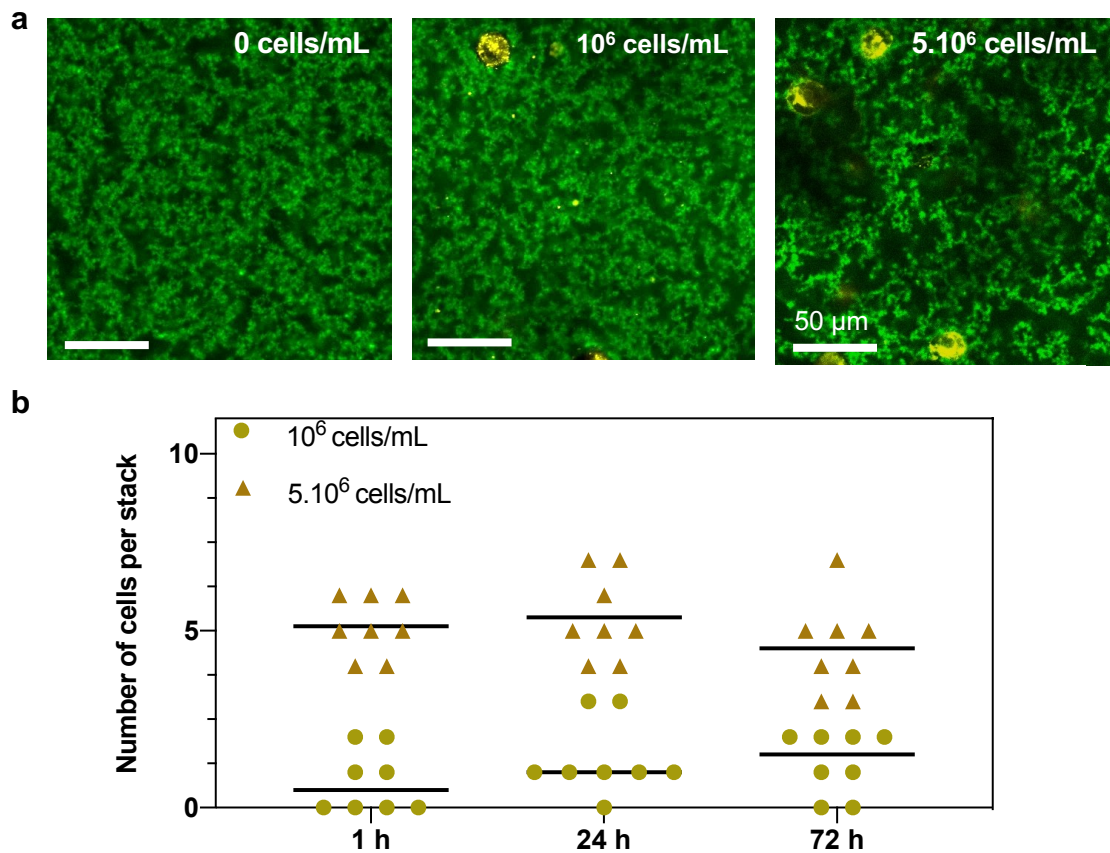


Figure IV - 16. a) Confocal micrographs of CS/ β GP/AHP hydrogels (CS 0.8 wt%) containing 10^6 cells.mL⁻¹ or $5 \cdot 10^6$ cells.mL⁻¹ at 24 h post-encapsulation of MC3T3-E1; **b)** Number of cells per stack for three incubation times.

Figure IV - 16b shows the number of MC3T3-E1 cells measured in 8 different locations at different incubation times for both cell concentrations. We found that the number of cells did not significantly change overtime, indicating that the staining of the plasma membrane was stable for 72 h. We counted between 0 and 3 cells per stack of images for the hydrogel containing 10^6 cells.mL⁻¹ and between 3 and

7 cells per stack for the hydrogel containing 5.10^6 cells.mL⁻¹. In average, we found 1 ± 1 cell per stack for the concentration of 10^6 cells.mL⁻¹ and 5 ± 1 cells per stack for the concentration of 5.10^6 cells.mL⁻¹. These numbers of cells per stack are consistent with the theoretical values: considering the volume of one stack, we should find 0.5 cell and 2.5 cells per stack for hydrogels containing 10^6 and 5.10^6 cells.mL⁻¹, respectively. Hence, we conclude that the cells can be homogeneously dispersed in CS/βGP/AHP hydrogels with concentrations up to 5.10^6 cells.mL⁻¹.

4.2.b. Effect of cells on the porosity and the pore size distribution

The microstructures of cell-laden hydrogels were compared to the one of the same hydrogel without cells. At 100 μm depth in the sample, confocal microscopy images over a $225 \mu\text{m} \times 225 \mu\text{m}$ area show a similar structure both for the hydrogel without cells and the hydrogel containing 10^6 cells.mL⁻¹. For the hydrogel containing 5.10^6 cells.mL⁻¹, the structure clearly looks more porous (**Figure IV - 16a**). The porosity was calculated for the hydrogel without cells and for the two cell-laden hydrogels by analyzing the signals from the fluorescently-labelled CS and from the stained cells. The results are shown in **Figure IV - 17a**. No significant difference was detected in the overall porosity between the hydrogel without cells and the hydrogels containing cells at both concentrations of 10^6 and 5.10^6 cells.mL⁻¹.

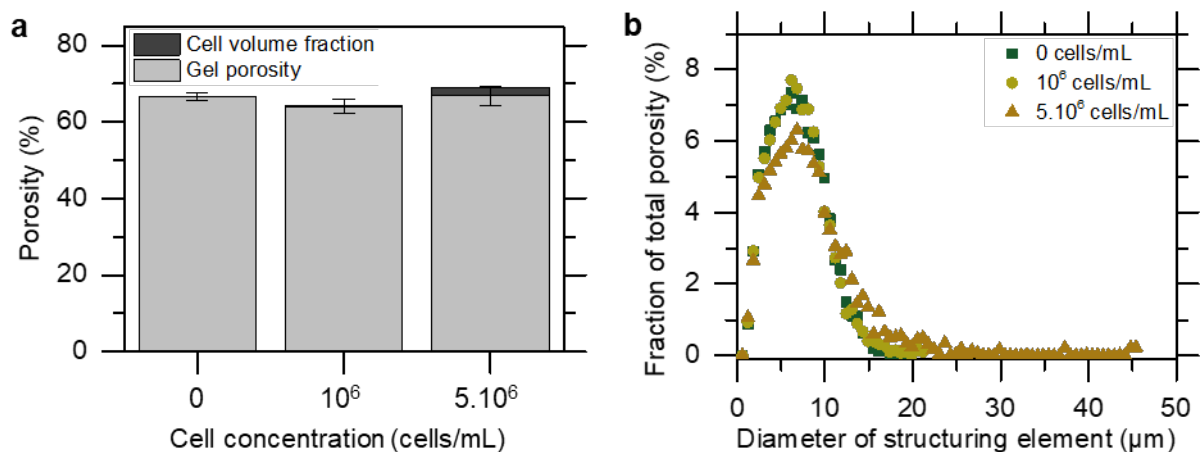


Figure IV - 17. Quantitative analysis of the microstructure for hydrogels containing different cell concentrations (0 , 10^6 and 5.10^6 cells.mL⁻¹) at 24 h post-encapsulation: overall porosity (**a**) and pore size distribution (**b**).

Concerning the pore size distribution, we observed in the confocal micrographs large pores up to 50 μm in the hydrogel containing 5.10^6 cells.mL⁻¹ (**Figure IV - 16a**). These observations were confirmed by quantitative analysis by the morphological sieve technique, as shown in **Figure IV - 17b**. At 10^6

cells.mL⁻¹, the pore size distribution barely changes compared to the regular hydrogel. At 5.10⁶ cells.mL⁻¹, macropores which size ranges from 15 to 45 μm are detected. These results clearly indicate that the presence of cells has an effect on the formation of the microstructure in CS/βGP/AHP hydrogels.

These observations and results were made on stacks of 10 images with an interval of 1 μm by assuming that the structure of the hydrogel is isotropic. Interestingly, observations of greater volumes from stacks of 100 images with an interval of 1 μm, indicate the presence of large elongated pores in the z-direction. Moreover, cells are observed at the bottom of each one of these pores, as shown in **Figure IV - 18**. Such elongated pores were observed on cellularized hydrogels for both cell concentrations, 10⁶ and 5.10⁶ cells.mL⁻¹. However, the difference in the pore size distribution between the hydrogel at 10⁶ cells.mL⁻¹ and the regular hydrogel is not significant (**Figure IV - 17a**). Since the number of these elongated pores are much less in the hydrogel with 10⁶ cells.mL⁻¹, the small stacks of 10 images analyzed by our protocol are not sufficient to capture this effect in this sample.

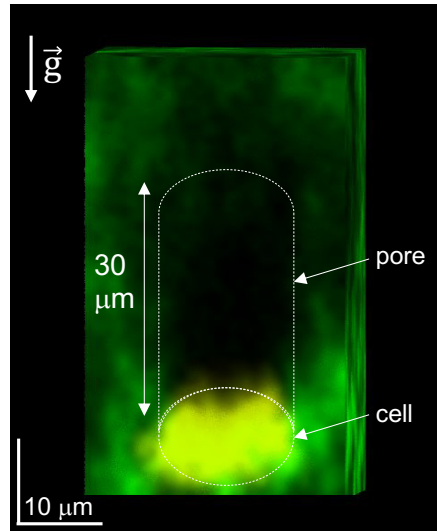


Figure IV - 18. 3D reconstruction from confocal micrographs for a region of 30 μm × 30 μm for hydrogel containing 5.10⁶ cells.mL⁻¹ at 72 h post-encapsulation.

We explain the formation of these large elongated macropores by the fact that cells undergo sedimentation during the sol/gel transition. By assimilating a cell to a particle having a defined density, the velocity at which the cell settles can be calculated following equation (IV - 3) defined by the Stokes law.⁵⁴

$$v = \frac{(\rho_{cell} - \rho_{medium}) \cdot g \cdot d^2}{18 \cdot \mu_{medium}} \quad (IV - 3)$$

where ρ_{cell} is the cell density estimated at 1050 kg.m⁻³,⁵⁵ ρ_{medium} is the formulation density estimated at 1000 kg.m⁻³ (water), g is the gravitational acceleration (9.8 m.s⁻²), d is the cell diameter approximated

to 10^{-6} m and μ_{medium} is the dynamic viscosity taken as $5 \cdot 10^{-3}$ Pa.s (value for a solution of CS at 1 wt%).

With those values, we estimate the velocity of a cell in the vicinity of $0.5 \mu\text{m}\cdot\text{s}^{-1}$. The typical duration of the gelation phase in our system is from 60 s to 120 s, therefore, the distance travelled by a cell is from 30 to 60 μm . This calculation is in perfect agreement with direct observations by confocal microscopy. The size of these elongated pores depends on the duration of the gelation phase and the sedimentation velocity. As shown in equation (IV - 3), the sedimentation velocity depends on several parameters depending on the characteristics of the cell type, and of the formulation. In particular, it is well known that the viscosity of polymer solutions changes significantly with the polymer concentration. Therefore, we expect that the formation of these elongated pores would be emphasized in formulations prepared with lower CS concentration. These results and observations were obtained from *in vitro* encapsulation in which the cellularized formulations were simply deposited into culture wells and incubated thereafter at 37°C. Even if the situation can be completely different for *in vivo* injections in which the cellularized formulations will be injected into biological media with much more complex fluid flows, one should keep in mind that the motion of cells during the gelation phase might contribute to the formation of pores within *in situ* forming hydrogels.

IV.5. Conclusions

In this chapter, the microstructure of CS/ β GP/AHP hydrogels was characterized quantitatively using our methods and tools based on the analysis of images acquired by confocal microscopy. From confocal microscopy images, the overall porosity and the pore size distribution were calculated. These methods and tools have proven to be performant for investigating the effect of the various characteristic and origins of CS and the presence of cells on the microstructure of these hydrogels.

Our results on seven CS grades suggested that the microstructural and mechanical properties of the hydrogel strongly depend on the characteristics and origin of CS. We showed that the microstructure of this system can be tuned using various CS grades. In particular, for a fixed concentration at 0.8 wt% of CS, a three-fold increase in the mean pore size going from $4.9 \pm 0.3 \mu\text{m}$ corresponding to a porosity of $57 \pm 1\%$ to $14.3 \pm 1.8 \mu\text{m}$ corresponding to a porosity of $83 \pm 1\%$ was obtained. We reported exciting findings about the power-law between the storage modulus and the effective volume fraction, similarly to colloidal gels. It would be interesting to further investigate the interparticle interactions because such understanding could provide ideas to control and tune the clustering process and the resulting gel microstructure.

We showed that cells can be homogeneously dispersed in CS/ β GP/AHP hydrogels up to $5.10^6 \text{ cells.mL}^{-1}$. An interesting effect of the presence of cells on the hydrogel microstructure was demonstrated: the sedimentation of cells during the gelation phase creates elongated pores which size goes up to tens of microns. This observation suggests that the hydrogel microstructure is not isotropic in the presence of cells. Therefore, it would be more adequate to develop tools for analyzing the porosity and the pore size distribution in 3D in further studies.

References

- (1) O'Brien, F. F. J.; Harley, B. B. A.; Waller, M. A.; Yannas, I. V.; Gibson, L. J.; Prendergast, P. J. The Effect of Pore Size on Permeability and Cell Attachment in Collagen Scaffolds for Tissue Engineering. *Technol. Heal. care* **2007**, *15* (1), 3–17. <https://doi.org/10.1016/j.biomaterials.2009.09.063>.
- (2) Bružauskaitė, I.; Bironaitė, D.; Bagdonas, E.; Bernotienė, E. Scaffolds and Cells for Tissue Regeneration: Different Scaffold Pore Sizes—Different Cell Effects. *Cytotechnology* **2016**, *68* (3), 355–369. <https://doi.org/10.1007/s10616-015-9895-4>.
- (3) Kaberova, Z.; Karpushkin, E.; Nevoralová, M.; Vetrík, M.; Šlouf, M.; Dušková-Smrčková, M. Microscopic Structure of Swollen Hydrogels by Scanning Electron and Light Microscopies: Artifacts and Reality. *Polymers (Basel)*. **2020**, *12* (3), 578. <https://doi.org/10.3390/polym12030578>.
- (4) Hirokawa, Y.; Jinnai, H.; Nishikawa, Y.; Okamoto, T.; Hashimoto, T. Direct Observation of Internal Structures in Poly(N-Isopropylacrylamide) Chemical Gels. *Macromolecules* **2002**, *32* (21), 7093–7099. <https://doi.org/10.1021/ma990437v>.
- (5) Luby-Phelps, K. Cytoarchitecture and Physical Properties of Cytoplasm: Volume, Viscosity, Diffusion, Intracellular Surface Area. *Int. Rev. Cytol.* **1999**, *192*, 189–221. [https://doi.org/10.1016/s0074-7696\(08\)60527-6](https://doi.org/10.1016/s0074-7696(08)60527-6).
- (6) Rossmann, K. Point Spread-Function, Line Spread-Function, and Modulation Transfer Function. Tools for the Study of Imaging Systems. *Radiology* **1969**, *93* (2), 257–272. <https://doi.org/10.1148/93.2.257>.
- (7) Swedlow, J. R. Quantitative Fluorescence Microscopy and Image Deconvolution. *Methods Cell Biol.* **2007**, *81* (06), 447–465. [https://doi.org/10.1016/S0091-679X\(06\)81021-6](https://doi.org/10.1016/S0091-679X(06)81021-6).
- (8) Gibson, S. F.; Lanni, F. Experimental Test of an Analytical Model of Aberration in an Oil-Immersion Objective Lens Used in Three-Dimensional Light Microscopy. *J. Opt. Soc. Am. A* **1992**, *9* (1), 154. <https://doi.org/10.1364/josaa.9.000154>.
- (9) Pawley, J. B. *Handbook of Biological Confocal Microscopy*; 2006.
- (10) Ahnesjö, A.; Andreo, P.; Brahme, A. Calculation and Application of Point Spread Functions for Treatment Planning with High Energy Photon Beams. *Acta Oncol. (Madr)*. **1987**, *26* (September 1986), 49–56.
- (11) Yoo, H.; Song, I.; Gweon, D. G. Measurement and Restoration of the Point Spread Function of Fluorescence Confocal Microscopy. *J. Microsc.* **2006**, *221* (3), 172–176. <https://doi.org/10.1111/j.1365-2818.2006.01556.x>.
- (12) Young, I. T. Quantitative Microscopy. *IEEE Eng. Med. Biol. Mag.* **1996**, *15* (1), 59–66. <https://doi.org/10.1109/51.482844>.
- (13) Young, I. T. Image Fidelity: Characterizing the Imaging Transfer Function. *Methods Cell Biol.* **1989**, *30* (C), 1–45. [https://doi.org/10.1016/S0091-679X\(08\)60974-7](https://doi.org/10.1016/S0091-679X(08)60974-7).
- (14) Shaw, P. J.; Rawlins, D. J. The Point-spread Function of a Confocal Microscope: Its Measurement and Use in Deconvolution of 3-D Data. *J. Microsc.* **1991**, *163* (2), 151–165. <https://doi.org/10.1111/j.1365-2818.1991.tb03168.x>.
- (15) Sarder, P.; Arye, N. Deconvolution Methods for 3-D Microscopy Images. *IEEE Signal Process. Mag.* **2006**, No. 2nd Edition, 32–45.
- (16) Shapiro, L.; Stockman, G. *Computer Vision*; Hall, P., Ed.; 2001.
- (17) Krishnaveni, A.; Shankar, R.; Duraisamy, S. A Review on Various Image Thresholding Methods for Mammogram Image Segmentation. *Compliance Eng. J.* **2020**, *11* (2), 414–426.
- (18) Pare, S.; Kumar, A.; Singh, G. K.; Bajaj, V. Image Segmentation Using Multilevel Thresholding: A Research Review. *Iran. J. Sci. Technol. - Trans. Electr. Eng.* **2020**, *44* (1). <https://doi.org/10.1007/s40998-019-00251-1>.
- (19) Otsu, N. A Threshold Selection Method from Gray-Level Histograms. *IEEE Trans. Syst. Man Cybern.* **1979**, *20* (1), 62–66.
- (20) Li, C. H.; Lee, C. K. Minimum Cross Entropy Thresholding. *Pattern Recognit.* **1993**, *26* (4), 617–625. [https://doi.org/10.1016/0031-3203\(93\)90115-D](https://doi.org/10.1016/0031-3203(93)90115-D).

- (21) Li, C. H.; Tam, P. K. S. An Iterative Algorithm for Minimum Cross Entropy Thresholding. *Pattern Recognit. Lett.* **1998**, *19* (8), 771–776. [https://doi.org/10.1016/S0167-8655\(98\)00057-9](https://doi.org/10.1016/S0167-8655(98)00057-9).
- (22) Matheron, G. *Random Sets and Integral Geometry*; Wiley, 1975.
- (23) Luengo Hendriks, C. L. *Structure Characterization Using Mathematical Morphology*, 2004.
- (24) Wu, Y. S.; van Vliet, L. J.; Frijlink, H. W.; van der Voort Maarschalk, K. Pore Size Distribution in Tablets Measured with a Morphological Sieve. *Int. J. Pharm.* **2007**, *342* (1–2), 176–183. <https://doi.org/10.1016/j.ijpharm.2007.05.011>.
- (25) Luengo Hendriks, C. L.; van Kempen, G. M. P.; van Vliet, L. J. Improving the Accuracy of Isotropic Granulometries. *Pattern Recognit. Lett.* **2007**, *28* (7), 865–872. <https://doi.org/10.1016/j.patrec.2006.12.001>.
- (26) Schneider, C. A.; Rasband, W. S.; Eliceiri, K. W. NIH Image to ImageJ: 25 Years of Image Analysis. *Nat. Methods* **2012**, *9* (7), 671–675. <https://doi.org/10.1038/nmeth.2089>.
- (27) Dougherty, R. P. Extensions of DAMAS and Benefits and Limitations of Deconvolution in Beamforming. *Collect. Tech. Pap. - 11th AIAA/CEAS Aeroacoustics Conf.* **2005**, *3* (May), 2036–2048. <https://doi.org/10.2514/6.2005-2961>.
- (28) Crompton, K. E.; Prankerd, R. J.; Paganin, D. M.; Scott, T. F.; Horne, M. K.; Finkelstein, D. I.; Gross, K. A.; Forsythe, J. S. Morphology and Gelation of Thermosensitive Chitosan Hydrogels. *Biophys. Chem.* **2006**, *121* (1), 14–20. <https://doi.org/10.1016/j.bpc.2005.12.005>.
- (29) Crompton, K. E.; Forsythe, J. S.; Horne, M. K.; Finkelstein, D. I.; Knott, R. B. Molecular Level and Microstructural Characterisation of Thermally Sensitive Chitosan Hydrogels. *Soft Matter* **2009**, *5* (23), 4704–4711. <https://doi.org/10.1039/b907593c>.
- (30) Kaivosoja, E.; Barreto, G.; Levón, K.; Virtanen, S.; Ainola, M.; Kontinen, Y. T. Chemical and Physical Properties of Regenerative Medicine Materials Controlling Stem Cell Fate. *Ann. Med.* **2012**, *44* (7), 635–650. <https://doi.org/10.3109/07853890.2011.573805>.
- (31) O'Brien, F. J.; Harley, B. A.; Yannas, I. V.; Gibson, L. J. The Effect of Pore Size on Cell Adhesion in Collagen-GAG Scaffolds. *Biomaterials* **2005**, *26* (4), 433–441. <https://doi.org/10.1016/j.biomaterials.2004.02.052>.
- (32) Chenite, A.; Chaput, C.; Wang, D.; Combes, C.; Buschmann, M. D.; Hoemann, C. D.; Leroux, J. C.; Atkinson, B. L.; Binette, F.; Selmani, A. Novel Injectable Neutral Solutions of Chitosan Form Biodegradable Gels in Situ. *Biomaterials* **2000**, *21* (21), 2155–2161. [https://doi.org/10.1016/S0142-9612\(00\)00116-2](https://doi.org/10.1016/S0142-9612(00)00116-2).
- (33) Zhou, H. Y.; Chen, X. G.; Kong, M.; Liu, C. S.; Cha, D. S.; Kennedy, J. F. Effect of Molecular Weight and Degree of Chitosan Deacetylation on the Preparation and Characteristics of Chitosan Thermosensitive Hydrogel as a Delivery System. *Carbohydr. Polym.* **2008**, *73* (2), 265–273. <https://doi.org/10.1016/j.carbpol.2007.11.026>.
- (34) Grigoriev, T. E.; Zagoskin, Y. D.; Belousov, S. I.; Vasilyev, A. V.; Bukharova, T. B.; Leonov, G. E.; Galitsyna, E. V.; Goldshtein, D. V.; Chvalun, S. N.; Kulakov, A. A.; Paltsev, M. A. Influence of Molecular Characteristics of Chitosan on Properties of In Situ Formed Scaffolds. *Bionanoscience* **2017**, *7* (3), 492–495. <https://doi.org/10.1007/s12668-017-0411-5>.
- (35) Kolawole, O. M.; Lau, W. M.; Khutoryanskiy, V. V. Chitosan/ β -Glycerophosphate in Situ Gelling Mucoadhesive Systems for Intravesical Delivery of Mitomycin-C. *Int. J. Pharm. X* **2019**, *1* (February), 100007. <https://doi.org/10.1016/j.ijpx.2019.100007>.
- (36) Rinaudo, M.; Milas, M.; Dung, P. Le. Characterization of Chitosan. Influence of Ionic Strength and Degree of Acetylation on Chain Expansion. *Int. J. Biol. Macromol.* **1993**, *15* (5), 281–285. [https://doi.org/10.1016/0141-8130\(93\)90027-J](https://doi.org/10.1016/0141-8130(93)90027-J).
- (37) Dang, P. A.; Palomino-Durand, C.; Elsafi Mabrouk, M.; Marquaille, P.; Odier, C.; Norvez, S.; Pauthe, E.; Corté, L. Rational Formulation Design of Injectable Thermosensitive Chitosan-Based Hydrogels for Cell Encapsulation and Delivery. *Carbohydr. Polym.* **2022**, *277*, 118836. <https://doi.org/10.1016/j.carbpol.2021.118836>.
- (38) Filion, D.; Lavertu, M.; Buschmann, M. D. Ionization and Solubility of Chitosan Solutions Related to

- Thermosensitive Chitosan/Glycerol-Phosphate Systems. *Biomacromolecules* **2007**, *8* (10), 3224–3234. <https://doi.org/10.1021/bm700520m>.
- (39) Lavertu, M.; Filion, D.; Buschmann, M. D. Heat-Induced Transfer of Protons from Chitosan to Glycerol Phosphate Produces Chitosan Precipitation and Gelation. *Biomacromolecules* **2008**, *9* (2), 640–650. <https://doi.org/10.1021/bm700745d>.
- (40) Gardner, K. H.; Blackwell, J. Refinement of the Structure of B-Chitin. **1975**, *14*, 1581–1595.
- (41) Minke, R.; Blackwell, J. The Structure of α -Chitin. *J. Mol. Biol.* **1978**, *120* (2), 167–181. [https://doi.org/10.1016/0022-2836\(78\)90063-3](https://doi.org/10.1016/0022-2836(78)90063-3).
- (42) Jaworska, M.; Sakurai, K.; Gaudon, P.; Guibal, E. Influence of Chitosan Characteristics on Polymer Properties. I: Crystallographic Properties. *Polym. Int.* **2003**, *52* (2), 198–205. <https://doi.org/10.1002/pi.1159>.
- (43) Buscall, R.; Mills, P. D. A.; Goodwin, J. W.; Lawson, D. W. Scaling Behaviour of the Rheology of Aggregate Networks Formed from Colloidal Particles. *J. Chem. Soc. Faraday Trans. 1 Phys. Chem. Condens. Phases* **1988**, *84* (12), 4249–4260. <https://doi.org/10.1039/F19888404249>.
- (44) Shih, W. H.; Shih, W. Y.; Kim, S. Il; Liu, J.; Aksay, I. A. Scaling Behavior of the Elastic Properties of Colloidal Gels. *Phys. Rev. A* **1990**, *42* (8), 4772–4779. <https://doi.org/10.1103/PhysRevA.42.4772>.
- (45) Mohraz, A. Interfacial Routes to Colloidal Gelation. *Curr. Opin. Colloid Interface Sci.* **2016**, *25*, 89–97. <https://doi.org/10.1016/j.cocis.2016.07.005>.
- (46) Lin, M. Y.; Lindsay, H. M.; Weitz, D. A.; Ballt, R. C.; Klein, R.; Meakin, P. Universality in Colloid Aggregation. *Nat.* **1989**, *339* (June), 360–362.
- (47) Grant, M. C.; Russel, W. B. Volume-Fraction Dependence of Elastic Moduli and Transition Temperatures for Colloidal Silica Gels. *Phys. Rev. E* **1993**, *47* (4), 2606–2614. <https://doi.org/10.1103/PhysRevE.47.2606>.
- (48) Awad, T. S.; Rogers, M. A.; Marangoni, A. G. Scaling Behavior of the Elastic Modulus in Colloidal Networks of Fat Crystals. *Fat Cryst. Networks* **2004**, 349–380. <https://doi.org/10.1201/9781420030549.ch10>.
- (49) Shih, W. Y.; Shih, W. H.; Aksay, I. A. Elastic and Yield Behavior of Strongly Flocculated Colloids. *J. Am. Ceram. Soc.* **1999**, *82* (3), 616–624. <https://doi.org/10.1111/j.1151-2916.1999.tb01809.x>.
- (50) Aliaghaei, M.; Mirzadeh, H.; Dashtimoghadam, E.; Taranejoo, S. Investigation of Gelation Mechanism of an Injectable Hydrogel Based on Chitosan by Rheological Measurements for a Drug Delivery Application. *Soft Matter* **2012**, *8* (27), 7128–7137. <https://doi.org/10.1039/c2sm25254f>.
- (51) Wu, H.; Morbidelli, M. Model Relating Structure of Colloidal Gels to Their Elastic Properties. *Langmuir* **2001**, *17* (4), 1030–1036. <https://doi.org/10.1021/la001121f>.
- (52) Collot, M.; Ashokkumar, P.; Anton, H.; Boutant, E.; Faklaris, O.; Galli, T.; Mély, Y.; Danglot, L.; Klymchenko, A. S. MemBright: A Family of Fluorescent Membrane Probes for Advanced Cellular Imaging and Neuroscience. *Cell Chem. Biol.* **2019**, *26* (4), 600–614.e7. <https://doi.org/10.1016/j.chembiol.2019.01.009>.
- (53) Bolte, S.; Cordelières, F. P. A Guided Tour into Subcellular Colocalization Analysis in Light Microscopy. *J. Microsc.* **2006**, *224* (3), 213–232. <https://doi.org/10.1111/j.1365-2818.2006.01706.x>.
- (54) Stokes, G. *On the Effect of Internal Friction of Fluids on the Motion of Pendulums*; Transactions of the Cambridge Philosophical Society, 1851.
- (55) Grover, W. H.; Bryan, A. K.; Diez-Silva, M.; Suresh, S.; Higgins, J. M.; Manalis, S. R. Measuring Single-Cell Density. *Proc. Natl. Acad. Sci. U. S. A.* **2011**, *108* (27), 10992–10996. <https://doi.org/10.1073/pnas.1104651108>.

CHAPTER V

BIO-FUNCTIONALIZATION OF CS/ β GP/AHP
HYDROGELS

TABLE OF CONTENTS

Résumé en français	201
V.1. Introduction.....	202
V.2. Encapsulation of MPNST cancer cells in CS/βGP/AHP hydrogels	203
V.2.1. Materials & Methods	203
2.1.a. Materials & cells	203
2.1.b. Experimental methods	204
V.2.2. Results & Discussion	205
2.2.a. The choice of CS/βGP/AHP formulations	205
2.2.b. 2D culture of MPNST cells on CS/βGP/AHP hydrogels.....	205
2.2.c. Encapsulation of MPNST cells in CS/βGP/AHP hydrogels.....	207
V.3. Bio-functionalization of CS/βGP/AHP hydrogels	210
Materials & methods	211
3.1.a. Materials & cells	211
3.1.b. Experimental methods	212
V.3.2. Results & discussion	214
3.2.a. Characterization of the bio-functionalization	214
3.2.b. Preliminary evaluation of the efficiency of bio-functionalization strategies	218
V.4. Conclusion.....	220
References	221

Résumé en français

Dans le Chapitre II, la cytocompatibilité des hydrogels CS/ β GP/AHP a été démontrée par l'encapsulation *in vitro* de deux types cellulaires : la lignée cellulaire pré-ostéoblastique MC3T3-E1 et les fibroblastes gingivaux humains (HGF). Cependant, la plupart des cellules présentaient une morphologie arrondie qui indique l'absence d'adhésion entre les cellules et la matrice de CS. Cette observation est en accord avec des études précédentes sur des hydrogels composés de CS et de sels. Il est bien connu que les interactions qui se produisent entre les cellules et leur environnement tissulaire local gouvernent l'activité cellulaire. Par conséquent, l'objectif de ce chapitre est, dans une première partie, de comprendre les raisons causant la morphologie arrondie des cellules lorsqu'elles sont encapsulées dans des hydrogels CS/ β GP/AHP. Deux hypothèses étaient : 1) l'inadéquation entre les propriétés mécaniques des hydrogels CS/ β GP/AHP et des tissus natifs de ces cellules ; et 2) l'absence de signaux biochimiques permettant l'adhésion cellulaire. Dans une seconde partie, des stratégies visant à améliorer l'activité des cellules encapsulées seront explorées.

Dans la première partie de ce chapitre (V.2), le comportement des cellules cancéreuses impliquées dans les tumeurs malignes de la gaine nerveuse périphérique (MPNST), en culture 2D ou 3D dans des hydrogels CS/ β GP/AHP, est étudié. Ces cellules se développent généralement dans des tissus mous dont les modules élastiques (10 - 1000 Pa) sont comparables à celles de nos hydrogels. Deux formulations physiologiques préparées à des concentrations de CS 0.5 ou 0.8 wt% ont été étudiées. Les résultats ont mis en évidence l'absence de cytotoxicité du système et sont très encourageants car presque toutes les cellules encapsulées dans l'hydrogel CS 0.5 wt% sont restées vivantes après 6 jours. Cependant, peu de signes d'adhérence cellulaire ont été observés dans les deux conditions (2D et 3D). Ces observations suggèrent que même lorsque les propriétés mécaniques globales des hydrogels correspondent au tissu natif, les signaux biochimiques sont cruciaux pour permettre l'adhésion cellulaire.

Par conséquent, dans la seconde partie (V.3), des stratégies pour incorporer dans des formulations CS/ β GP/AHP une séquence peptidique contenant du RGD ou de la fibronectine (FN) visant à améliorer l'activité cellulaire ont été explorées. La séquence peptidique a été greffée avec succès sur des chaînes CS et le greffage n'altère pas le processus de thermogélification. Cependant, les observations des cellules MC3T3-E1 ne montrent pas de signe d'adhésion sur l'hydrogel préparé avec du CS greffé RGD. Pour la FN, les observations et analyses ont montré que la protéine était effectivement incorporée dans les hydrogels CS/ β GP/AHP soit par un simple mélange soit par un greffage covalent sur des chaînes CS avant gélification. Pour les deux approches, la formulation résultante présentait une gélification rapide à 37°C. Cependant, l'adhésion de cellules n'étaient pas améliorée en présence de la FN, ce qui pourrait être expliqué par une distribution inhomogène et l'agrégation de la FN dans l'hydrogel. D'autres études seront nécessaires pour développer des stratégies permettant un meilleur contrôle à la fois de la distribution et de la conformation de la FN.

V.1. Introduction

In Chapter II, the cytocompatibility of CS/ β GP/AHP hydrogels was demonstrated by *in vitro* encapsulation of two cell types: MC3T3-E1 pre-osteoblastic cell line and primary human gingival fibroblasts (HGF). At a cell concentration of 10^6 cells.cm⁻³, both cell types showed good viability, at least 80%, at 24 h post-encapsulation. However, most of the cells presented rounded morphology, indicating a poor cellular adhesion to the CS matrix. This observation is in agreement with previous studies on CS/salt hydrogels.^{1,2} It is well known that the interactions that occur between cells and their local tissue environment guides physiological processes (Chapter I, section I.1.3). Hence, the goal of this chapter is firstly, to investigate on the possible reasons of the rounded morphology of cells when they are encapsulated within CS/ β GP/AHP hydrogels and secondly, to explore strategies aiming at improving the cellular activity.

Mechanical properties have been shown to have an important role in dictating cellular behavior. We suggest that the unusual morphology of encapsulated MC3T3-E1 and HGF cells in CS/ β GP/AHP hydrogels might be due to a mismatch between the stiffness of the hydrogel and the one of native tissues of these cells. Indeed, the storage modulus, G' , for a CS/ β GP/AHP hydrogel prepared with 0.8 wt% of CS is in the range of a few hundreds of Pa, which is very low compared to the natural environment of MC3T3-E1 and HGF cells, *i.e.* bone (\sim GPa) and gingiva (\sim MPa).^{3,4}

The biochemical properties of the scaffold surface are also crucial to cell adhesion and proliferation. It is well known that cell integrin binding plays a significant role in dictating cellular behavior. CS is not inherently cell adhesive because it does not possess cell binding moieties.⁵⁻⁸ Nevertheless, one might wonder if CS can promote cell adhesion thanks to the positively charged D-glucosamine monomers as the cell membrane is negatively charged.⁹ However, in the thermally-induced gelation in CS/salt mixtures, CS chains are neutralized.¹⁰ Therefore, the rounded cell phenotype might be partially explained by the lack of biochemical signals allowing cell attachment.

In this chapter, studies were carried out in order to better elucidate these two points. Firstly, in section V.2, the behavior of cancer cells involved in the malignant peripheral nerve sheath tumors (MPNST), which usually grow in soft tissue, in contact with CS/ β GP/AHP hydrogels is investigated. Secondly, in section V.3, strategies aiming to improve the bioactivity of the hydrogels by incorporating a small peptide sequence or a protein bearing cell binding sites are explored.

V.2. Encapsulation of MPNST cancer cells in CS/βGP/AHP hydrogels

In this section, we explore the behavior of cancer cells encapsulated within CS/βGP/AHP hydrogels. These cells are Schwann cells involved in the malignant peripheral nerve sheath tumors (MPNST) usually associated with neurofibromatosis type 1.¹¹ They grow in soft tissues such as fat, lymph and blood vessels, nerves, which elastic moduli are in the order of 10 – 1000 Pa.¹²⁻¹⁴ Today, there is still no treatment to prevent their malignant transformation and to inhibit the development of tumors.¹⁵ The research team of Dr. Piotr Topilko (Institut Mondor de Recherche Biomédicale) developed genetically engineered mouse models to study the origin and pathogenic mechanisms of MPNST.¹⁶ Schwann cells at different development stages can be isolated from the tumors.

The present study has therefore two aims. Firstly, there is now a need to have an *in vitro* model in order to investigate in depth the behavior of these cells alone or in co-culture with other nerve fiber elements. Our CS/βGP/AHP hydrogels can be good candidates as their soft nature could mimic the tissue on which MPNST cells like to grow. Secondly, this study would elucidate whether the previously observed rounded phenotype of MC3T3 and HGF is due to a mismatch in mechanical properties.

In this preliminary study we investigated the behavior of MPNST cells in contact with CS/βGP/AHP hydrogels. Two conditions were realized, 2D culture on preformed hydrogels or encapsulation within the hydrogels. Two physiological formulations at CS concentration of 0.8 wt% or 0.5 wt% (pH = 7.4 ± 0.05 and 300 ± 30 mOsm.L⁻¹) will be investigated.

This work was carried out in collaboration with Dr. Laure Lecerf and Dr. Piotr Topilko (Institut Mondor de Recherche Biomédicale).

V.2.1. Materials & Methods

2.1.a. Materials & cells

In this study, we used the same grade of chitosan CS as the one studied in Chapter II. It corresponds to a relative low molar mass (viscosity 30-100 cps) (CS2 in Chapter IV).

MPNST cells were isolated from tumors in genetically engineering mice. These mice were genetically modified allowing the expression of the Tomato fluorescent protein ($\lambda_{ex}/\lambda_{em} = 554/581$ nm). Cells of passage < 10 were used.

2.1.b. Experimental methods

Preparation of physiological formulations

Stock solutions of CS, β GP and AHP were prepared and sterilized according to protocol described in our previous study (Chapter II).¹⁷ Physiological CS/ β GP/AHP formulations ($\text{pH} = 7.4 \pm 0.05$ and $300 \pm 30 \text{ mOsm.L}^{-1}$) at CS concentration of 0.8 or 0.5 wt% were prepared following the formulations reported our previous study (Chapter II).¹⁷

2D culture of MPNST cells on CS/ β GP/AHP hydrogels

CS/ β GP/AHP hydrogels having thickness about 1.5 mm were prepared by pouring 300 μL of freshly prepared formulations into 24-well culture plate (polystyrene). The formulations were then incubated for 1 h at 37°C and 5% CO_2 to induce gelation. MPNST cells were trypsinized and resuspended in DMEM medium supplemented with 10 %v/v fetal calf serum and 1 %v/v penicillin-streptomycin. Cell suspension was added onto CS/ β GP/AHP hydrogels at a density of $15 \cdot 10^4 \text{ cells.cm}^{-2}$. The medium was changed after 3 days of incubation. Each formulation was realized in duplicate. For control, cells were seeded directly onto culture well at a density of $15 \cdot 10^4 \text{ cells.cm}^{-2}$.

Observations were made using fluorescence phase contrast microscope (Zeiss Axiovert 40 CFL) equipped with $\times 4$ and $\times 10$ objectives at different incubation times (1, 3, 6 days). Images of ($563 \mu\text{m} \times 422 \mu\text{m}$) were recorded at random positions in the hydrogel.

Encapsulation or 3D culture of MPNST cells in CS/ β GP/AHP hydrogels

Encapsulation for MPNST cells was carried out using the same protocol as for MC3T3-E1 and HGF cells (Chapter II). The final cell concentration was $10^6 \text{ cells.cm}^{-3}$. Hydrogels without cells were also prepared by replacing the cell suspension by culture medium. The medium was changed after 3 days of incubation. Each formulation was realized in triplicate.

Observations were made using fluorescence phase contrast microscope (Zeiss Axiovert 40 CFL) equipped with $\times 4$ and $\times 10$ objectives at different incubation times (1, 3, 6 days). Images of ($1408 \mu\text{m} \times 1056 \mu\text{m}$) and ($563 \mu\text{m} \times 422 \mu\text{m}$) were recorded at two z positions: at the bottom (close to the bottom of the culture well) and in the middle of the sample.

Evaluation of the cell viability: the cell viability at Day 6 was estimated using trypan blue dye exclusion test. 1 mL trypan blue solution at 50 %vol in DMEM was added into each well. Dead cells are stained by trypan blue and appear as dark point under white light source. Live cells show red fluorescence. The cell number was determined using the *Cell counter* plugin in ImageJ. The cell viability is determined as the ratio of live cells over the total number of cells and is averaged on six random areas of ($1408 \mu\text{m} \times 1056 \mu\text{m}$) sample for each formulation.

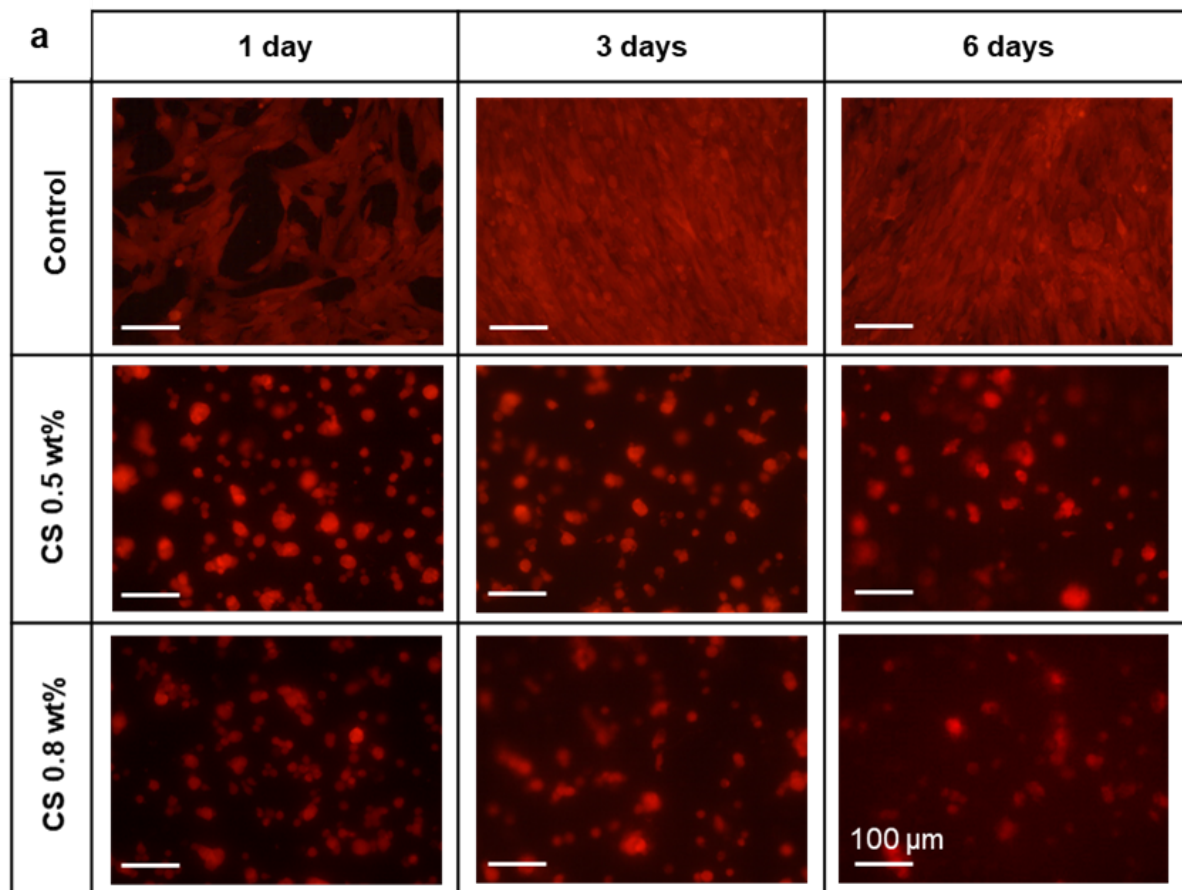
V.2.2. Results & Discussion

2.2.a. The choice of CS/βGP/AHP formulations

Two formulations at different CS concentrations (0.5 and 0.8 wt%) were studied in order to explore the effect of the mechanical properties and the microstructure on MPNST cells behavior. The hydrogel prepared with CS 0.5 wt% possesses lower storage modulus with higher porosity and larger pores than the CS 0.8 wt% hydrogel. The properties of these hydrogels were characterized in previous chapters. Briefly, the storage modulus G' , measured by rheology, reaches approximately 30 Pa for 0.5 wt% and 180 Pa for 0.8 wt% after 1 h of incubation. After 6 h, G' reaches 60 Pa for 0.5 wt% and 300 Pa for 0.8 wt%. The porosity was found to be $75 \pm 5\%$ for CS 0.5 wt% and $63 \pm 7\%$ for CS 0.8 wt%. Both hydrogels possess interconnected elongated pores which size can go up to 15 μm for CS 0.8 wt% and 30 μm for CS 0.5 wt%.

2.2.b. 2D culture of MPNST cells on CS/βGP/AHP hydrogels

MPNST were seeded at a density of $15 \cdot 10^4 \text{ cells.cm}^{-2}$ on preformed physiological CS/βGP/AHP hydrogels prepared with CS concentration at 0.5 or 0.8 wt% ($\text{pH} = 7.4 \pm 0.05$ and $300 \pm 30 \text{ mOsm.L}^{-1}$). Cells were directly seeded onto culture wells at the same density for control. **Figure V - 1a** shows images at different incubation times. For the control, cells showed a well spread morphology, which is the normal phenotype of MPNST cells, and good proliferation as the confluence was reached after 3 days. When being cultured on CS/βGP/AHP hydrogels, some cells exhibited a prolongation of the cytoplasm from Day 3 for both formulations, as shown in **Figure V - 1b**. However, most of the cells showed rounded morphology up to 6 days whatever the CS concentration. These observations suggest that the surface of CS/βGP/AHP hydrogels is not favorable for the adhesion of this cell type.



b

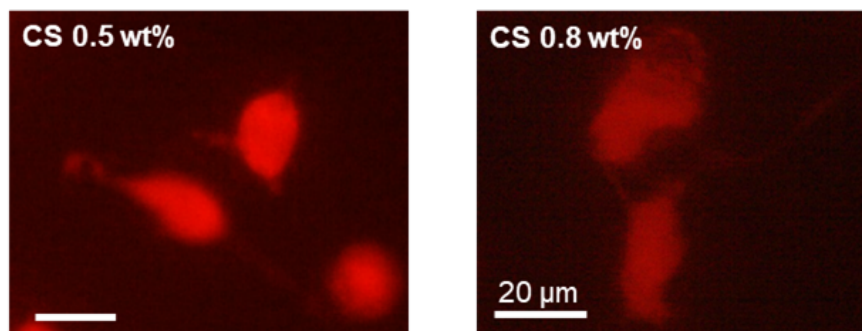


Figure V - 1. *2D culture of MPNST cells: a) Images of cells in control condition or on CS/ β GP/AHP hydrogels prepared at CS concentration of 0.5 or 0.8 wt% at Day 1, 3 and 6. b) Zoom on cells showing cytoplasmic extension at Day 3.*

2.2.c. Encapsulation of MPNST cells in CS/βGP/AHP hydrogels

MPNST cells were encapsulated at a concentration of 10^6 cells.cm⁻³ in two physiological CS/βGP/AHP hydrogels (pH = 7.4 ± 0.05 and 300 ± 30 mOsm.L⁻¹) prepared with a CS concentration of 0.5 or 0.8 wt%. **Figure V - 2** shows the microscopy images taken at two different focus showing cells at bottom or in the middle of the sample. For both formulations, cells at the bottom showed spread morphology after 1 day while those in the middle showed rounded morphology up to 6 days. More cells were found at the bottom position for CS 0.5 wt% than for CS 0.8 wt%. This might be explained by the fact that the hydrogel CS 0.5 wt% actually broke into pieces due to its very weak mechanical properties. This situation fosters cell motion to reach the tissue culture polystyrene surface. Thus, cells were found to be in the optimal cell culture condition at the bottom, therefore showed good proliferation. For CS 0.8 wt%, all sample remained macroscopically intact. Hence, cells remained embedded within the hydrogel.

In order to evaluate the viability of the encapsulated MPNST cells at Day 6, we used trypan blue dye exclusion test. The trypan blue molecule only passes through the membrane of dead cells and stain them in a distinctive dark blue color. The live cells do not absorb trypan blue but show red fluorescence as they express the Tomato protein. Typical images obtained after the trypan blue test are shown in **Figure V - 3a-b**. The homogeneity of the cell dispersion was verified by cell counting in six random areas for each position, at the bottom or in the middle of the sample, and for each formulation. Cell counting was not possible for the CS 0.5 wt% sample at the bottom position as the cells were well spread. **Figure V - 3c** shows the local cell concentration, which is in agreement with the initial concentration of encapsulated cells, 10^6 cells.cm⁻³.

Figure V - 3d shows the viability of encapsulated MPNST cells at Day 6 by averaging on six images of (1408×1056 μm) per position for each formulation. The viability of encapsulated MPNST was $51 \pm 7\%$ for CS 0.8 wt% (average for both positions) and $97 \pm 3\%$ for CS 0.5 wt% (middle position). The cell viability is significantly higher for CS 0.5 wt%, which have lower storage modulus and larger pore size than CS 0.8 wt%. These results suggest that the survival of MPNST cells is more favorable with lower CS concentration. However, despite encouraging cell survival (nearly all encapsulated cells in the CS 0.5 wt% hydrogel remained alive after 6 days), poor signs of cell adhesion were observed within the hydrogel.

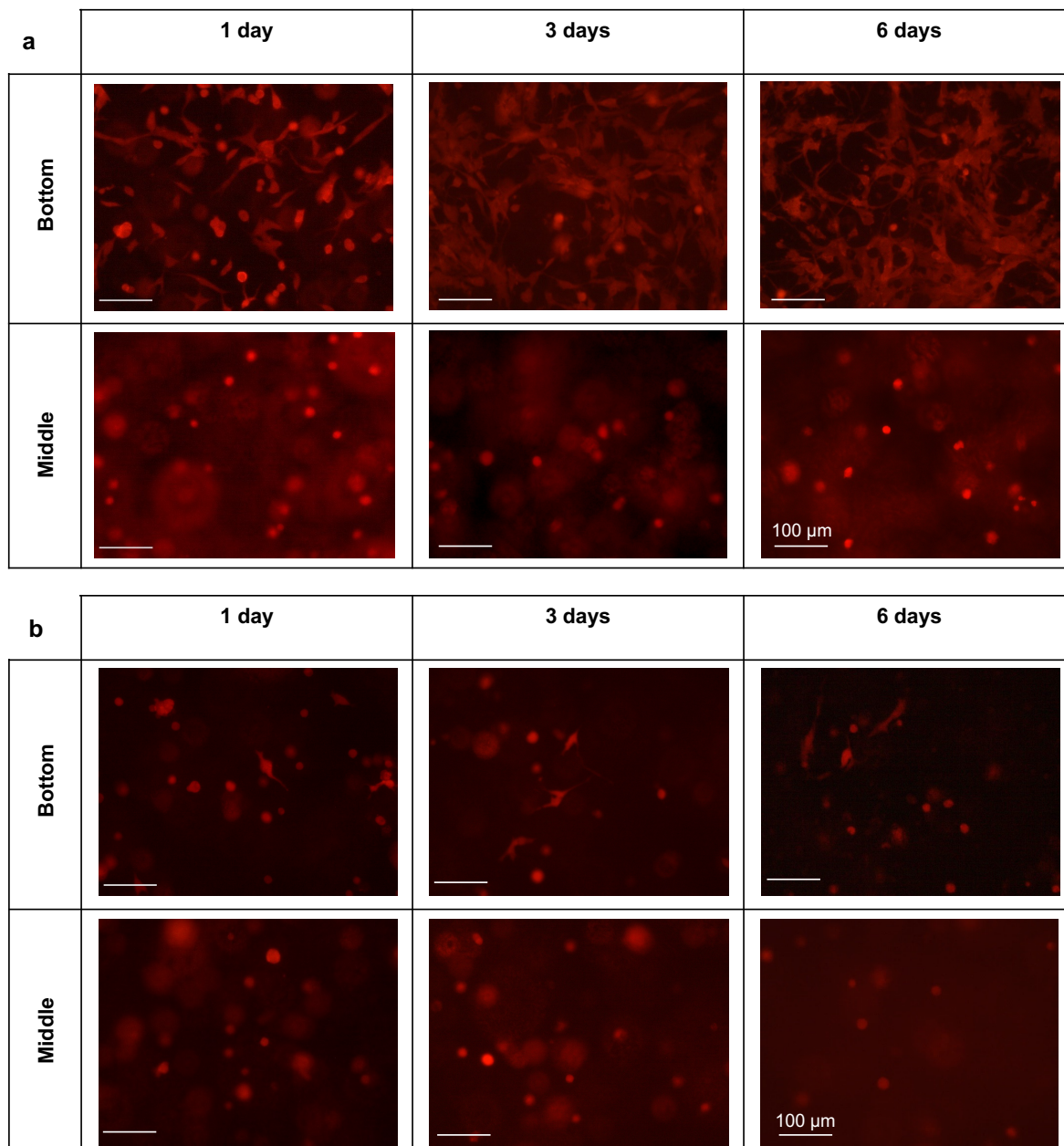


Figure V - 2. Images of encapsulated MPNST cells in CS/ β GP/AHP hydrogels prepared at a CS concentration of 0.5 wt% (a) or 0.8 wt% (b) at different incubation times.

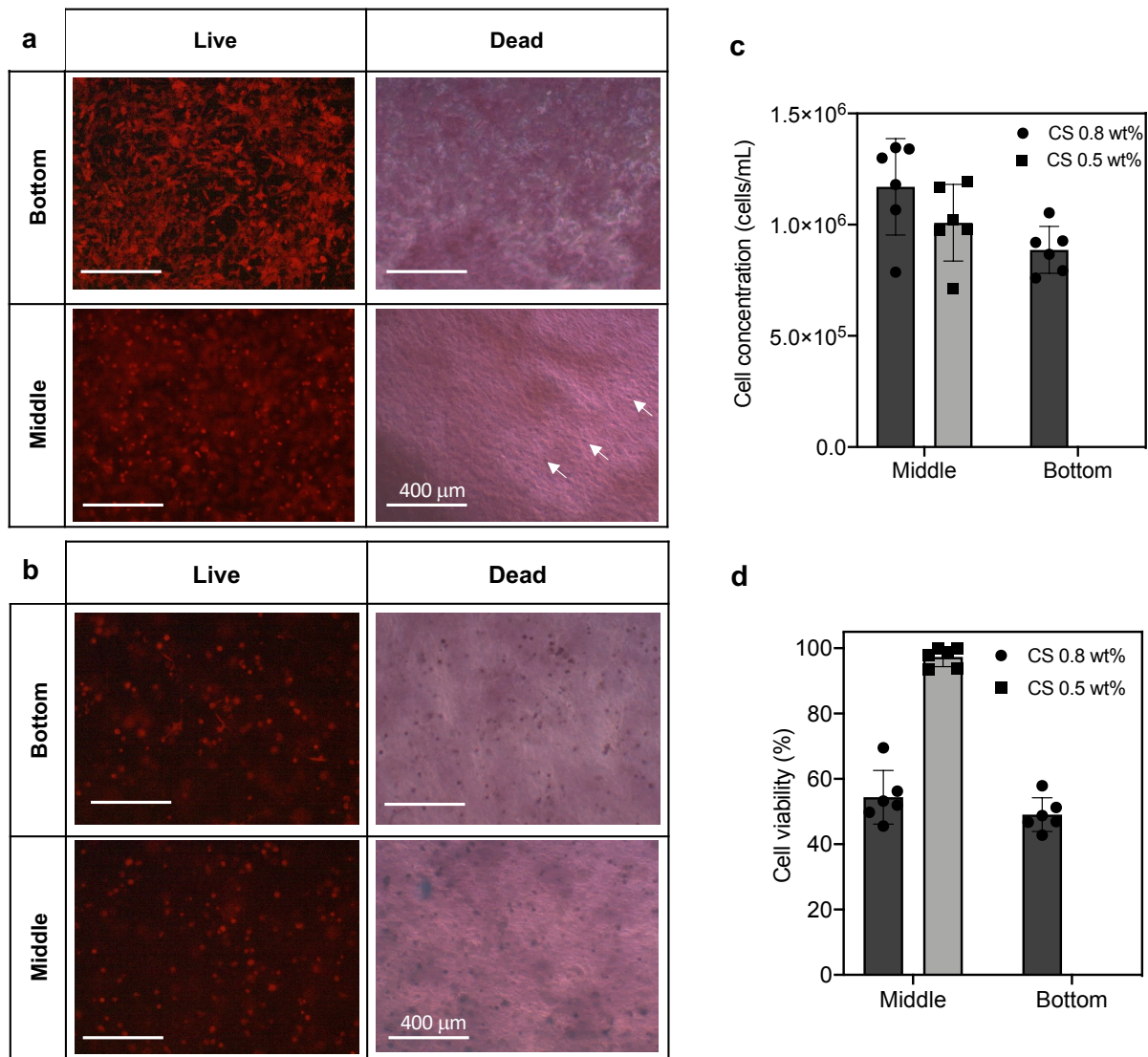


Figure V - 3. a-b) Red tomato expression and trypan blue staining on encapsulated MPNST cells in CS/ β GP/AHP hydrogels prepared with 0.5 wt% (a), white arrows indicate dead cells, or 0.8 wt% (b) of CS; **c)** Cell counting and **d)** Cell viability at Day 6.

through disulfide bonds near the C-terminal. Each subunit contains about 2500 amino acids.³⁹ FN can be recognized by a large number of integrins depending on its structural conformation.⁴⁰ Indeed, FN contains not only one RGD sequence per subunit but also others binding domains, as shown in **Figure V - 5**, thus offering multiple docking points for cells.⁴⁰ Moreover, synergistic effects on cell adhesion induced by the simultaneous presence of RGD and PHSRN sequences were previously reported.⁴¹ FN has been widely studied for improving the bioactivity of 2D or 3D cell scaffolds.⁴²⁻⁴⁸ In particular, it has been showed that covalently immobilized FN induced better cell adhesion than simply adsorbed FN.⁴² In this study, the incorporation of FN in CS/ β GP/AHP hydrogels *via* simple mixing or covalent grafting, was investigated.

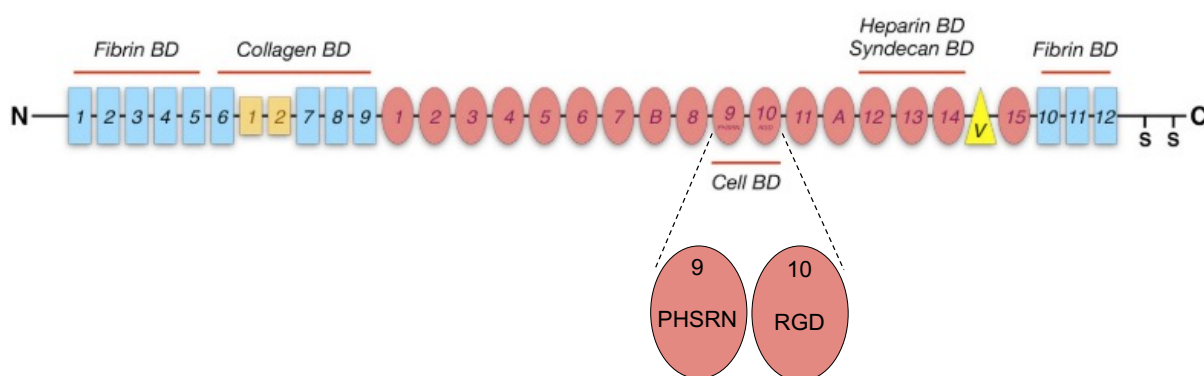


Figure V - 5. Structure of FN single subunit. Repeats and binding domains (BD) are indicated. Adapted from Parisi *et al.*⁴⁰

The efficiency of both strategies was assessed on the MC3T3-E1 cell line. These cells are able to interact with RGD through $\alpha_v\beta_v$, $\alpha_v\beta_5$ integrins and with FN through $\alpha_5\beta_1$, $\alpha_v\beta_5$ integrins.⁴⁹

This study was carried out in collaboration with Dr. Carla Palomino-Durand (ERRMECe, CY University).

V.3.1. Materials & methods

3.1.a. Materials & cells

In this study, we used the grade of chitosan corresponding to the low molar mass chitosan (viscosity 30-100 cps) studied in Chapter II (CS2 in Chapter IV). GRGDSPG₆ was purchased from Genscript[®]. Fibronectin was purified from human blood plasma following the protocol reported by Poulouin *et al.*⁵⁰ EDC and sulfo-NHS were purchased from Sigma Aldrich. The Live/Dead[™] kit and AlamarBlue[™] reagent were purchased from Invitrogen.

MC3T3-E1 pre-osteoblastic cells were obtained from ATCC[®].

3.1.b. Experimental methods

Grafting of GRGDSPG₆ onto CS

The GRGDSPG₆ sequence was covalently grafted onto CS chains using carbodiimide chemistry with a protocol adapted from Mansur *et al.*⁵¹ The reaction was carried out in sterile conditions. Briefly, stock solution of CS at 2 wt% was prepared using acetic acid, AcOH, at a molar ratio of [AcOH]/[NH₂] = 1. The pH of CS solution was then adjusted to 6.0 using NaOH 0.1 M in an ice bath (4°C). Aqueous solutions of EDC and sulfo-NHS were prepared at 1 wt% and 2.5 wt%, respectively. GRGDSPG₆ was dissolved in water at 2 mg.mL⁻¹. In an ice bath, EDC and sulfo-NHS were added into GRGDSPG₆ solution at a molar ratio of [EDC]:[NHS]:[GRGDSPG₆] = 0.5:1:1 and the mixture was stirred for 15 min for activation of G₆RGD. CS solution was added into the activated peptide at a molar ratio of [GRGDSPG₆]:[CS monomer] = 1:200 and the system was incubated under stirring at room temperature (21°C) for 1 h. The resulting solution, noted CS-RGD, was dialyzed using molecular weight cut-off membrane (4–6 kDa) during 4 days to eliminate excess reagents. The final CS-RGD solution having a CS concentration of 0.87 wt% was mixed with a regular CS stock solution at 2 wt% to obtain a stock solution at concentration of 1.33 wt%. Therefore, the theoretical grafting ratio decreased to [GRGDSPG₆]:[CS monomer] = 1:300.

Infrared spectroscopy characterization

Solutions of regular CS and peptide grafted CS, CS-G₆RGD, were analyzed using infrared spectroscopy. 0.5 g of each solution was dried at 40°C under vacuum during 4 h to obtain a thin film. The films were then analyzed by infrared spectroscopy using the ATR mode. Measurements were realized between 400 and 4000 cm⁻¹ using 32 scans and a resolution of 2 cm⁻¹.

Grafting of FN onto CS

The same protocol in sterile conditions as for the grafting of GRGDSPG₆ was applied to the grafting of FN. Pre-activated FN solution was added into CS solution which pH was adjusted to 6.0 at a molar ratio in monomer of [FN]:[CS] = 1:100. After dialysis, the final solution of functionalized CS, CS-FN, presented a concentration in CS of 0.94 wt%. This solution was then mixed with a regular CS stock solution at 2 wt% to obtain a stock solution of 1.33 wt% in CS. Therefore, the theoretical grafting ratio decreased to [FN]:[CS] = 1:140.

Preparation of bio-functionalized hydrogels

Thermosensitive hydrogels were prepared using functionalized CS, CS-RGD or CS-FN following the protocol described in Chapter II.

For formulations in which FN was incorporated by simple mixing, a small amount of culture medium in the formulation (5 %vol.) was substituted by stock solution of FN in HEPES buffer and was added to CS/ β GP/AHP mixture. The final concentration of FN in the hydrogel was 50 $\mu\text{g}\cdot\text{mL}^{-1}$.

Microstructure of CS-FN/ β GP/AHP and CS/ β GP/AHP/FN hydrogels

For confocal observations, CS was fluorescently labelled by AlexaFluor 488 and FN with AlexaFluor 568. The same protocol as described in Chapter III was used for labelling CS. A similar protocol was applied for labelling FN. The ratio of [Alexa Fluor 568]:[FN monomers] was 1:300.

For the simple mixing approach, fluorescently-labelled CS was added to regular CS (labelled CS/regular CS = 0.5 wt%) prior to mixing with the salts. For the covalently grafting approach, fluorescently-labelled FN was grafted onto mixtures of regular CS with fluorescently labelled CS (labelled CS/regular CS = 0.5 wt%).

The microstructure of the hydrogels and the distribution of FN was observed using confocal microscopy (LSM 710, Zeiss) using lasers at 488 nm and 561 nm. Each hydrogel sample was scanned from bottom to 300 μm depth at 8 random positions. Stacks of images were taken at $\times 10$ magnification and a 512×512 pixel resolution with the pinhole at 1 Airy unit and interval of 4 μm .

2D culture of MC3T3-E1 cells

2D cultures of MC3T3-E1 cells were carried out on preformed CS/ β GP/AHP and CS-RGD/ β GP/AHP hydrogels. Hydrogel having thickness about 1.5 mm were prepared by pouring 300 μL of freshly prepared formulations into 24-well culture plate. The formulations were incubated for 1 h at 37°C and 5% CO_2 to induce gelation. MC3T3-E1 cells were trypsinized and re-suspended in α MEM medium supplemented with 10 %v/v fetal calf serum and 1 %v/v penicillin-streptomycin. Cell suspension was added onto CS/ β GP/AHP or CS-RGD/ β GP/AHP hydrogels at a density of 10^4 cells. cm^{-2} . For control, cells were seeded directly onto culture well at a density of 10^4 cells. cm^{-2} .

Observations were made at 4 h and 24 h after cell seeding using phase-contrast microscopy.

Encapsulation of MC3T3-E1 cells and Live/Dead assay

Encapsulation of MC3T3-E1 cells in CS/ β GP/AHP, CS-FN/ β GP/AHP and CS/ β GP/AHP/FN hydrogels was carried out following the protocol described in Chapter II. The final cell concentration was fixed at 10^6 cells. cm^{-3} .

After 24 h, the encapsulated MC3T3-E1 cells were stained using Live/Dead assay following the protocol described in Chapter II. The distribution and the state of the cells were visualized using a laser scanning confocal microscope (LSM 710, Zeiss) using lasers at 488 nm and 561 nm. Each hydrogel sample was

scanned from bottom to 250 μm depth at the center of the sample. Stacks were taken at $\times 20$ magnification and a 512×512 pixel resolution with the pinhole at 1 Airy unit and interval of 4 μm .

V.3.2. Results & discussion

3.2.a. Characterization of the bio-functionalization

Bio-functionalization by RGD-containing peptide sequence

In this study, **GRGDSPG**₆ was grafted onto CS chains using the carbodiimide crosslinker chemistry involving EDC and sulfo-NHS. This reaction has been widely studied in bioconjugation of polymers by proteins or peptides.^{20,27,28,30,42,51–56} EDC reacts with carboxylic acid groups to form a highly reactive *O*-acylurea intermediate that can react with primary amine, leading to a stable amide bond. However, the reactive *O*-acylurea intermediate is very unstable and can easily undergo hydrolysis before reacting with the amine function. For this reason, sulfo-NHS is usually added to this coupling reaction to create an NHS ester that is considerably more stable than the *O*-acylurea intermediate. The NHS ester intermediate then forms amide bond by reacting with amine. Here, the $-\text{COOH}$ terminal in **GRGDSPG**₆ sequence was activated in the presence of EDC/sulfo-NHS, leading to the formation of a reactive intermediate that reacted with primary amine functions on CS. The grafting ratio, [**GRGDSPG**₆]:[CS monomer] = 1:200, was chosen according to previous studies in the literature, which reported a positive effect on the cell adhesion for [peptide]:[monomer] ranging from 1:10 to 1:600.^{34,51,57}

IR spectroscopy was performed to characterize the reaction between **GRGDSPG**₆ and CS. The typical region associated with amide bond for regular CS and peptide grafted CS (CS-RGD) is shown in **Figure V - 6**. The absorption peak at 1650 cm^{-1} corresponds to the C=O stretching of the secondary amides (amide I band).⁵⁸ The absorption peak around 1550 cm^{-1} comes from the N-H bending vibrations in the primary amine NH_2 and from the N-H bending and C-N stretching in secondary amides (amide II band).⁵⁸ While comparing the regular CS and CS-RGD, the ratio between the intensities of the 1650 cm^{-1} and 1550 cm^{-1} peaks clearly increases. These measurements indicate that the reaction between **GRGDSPG**₆ occurred and biofunctionalized CS-RGD was produced.

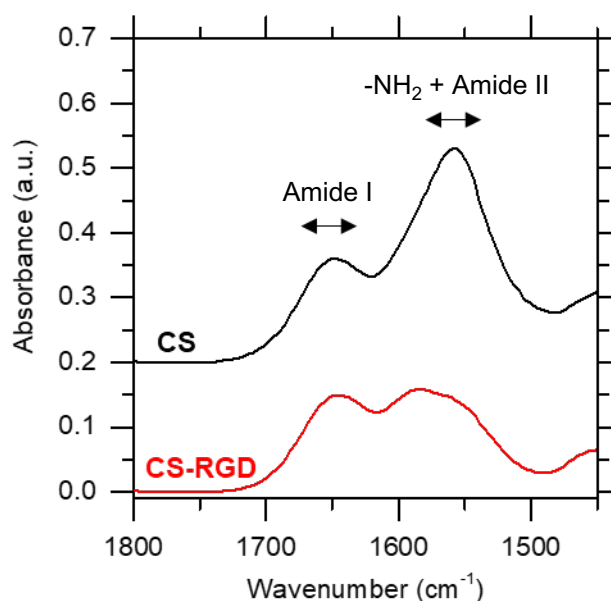


Figure V - 6. IR spectra of CS and CS-RGD films after drying at 40°C in vacuum for 4 h.

Due to the dialysis step that eliminates excess reactants, the obtained CS-RGD solution has a CS concentration of 0.87 wt%. This solution was mixed with a solution of regular CS at 2.0 wt% to obtain a stock solution of 1.33 wt% that was then used to prepare CS/ β GP/AHP mixtures at 0.8 wt% of CS. The final grafting ratio was [GRGDSPG₆]:[CS monomer] = 1:300. We verified that the mixture resulted in a transparent and liquid solution having a pH = 7.4 at 4°C. Upon heating to 37°C, this mixture turned into a gel within 2 min. Therefore, the presence of RGD moiety immobilized on CS chains does not alter the thermally-induced gelation process in CS/ β GP/AHP mixtures.

Bio-functionalization with FN

FN was incorporated to CS/ β GP/AHP formulations through two approaches: by simple mixing or by covalent conjugation using carbodiimide chemistry. For simple mixing, FN was added after the mixing of β GP and AHP to the CS solution to avoid precipitation and/or denaturation of FN due to the acidic pH of the CS stock solution. The final concentration of FN in the hydrogel was 50 $\mu\text{g}\cdot\text{mL}^{-1}$, which corresponds to a molar ratio in monomer of [FN]:[CS] = 1:100. FN was conjugated onto CS chains using the same protocol as for the conjugation of GRGDSPG₆ with the same targeted grafting ratio as for the simple mixing approach. The CS-FN solution after dialysis had a CS concentration of 0.92 wt%. The CS concentration was then adjusted to 1.33 wt% by adding of stock solution at 2.0 wt%. Therefore, the theoretical molar ratio in monomer was [FN]:[CS] = 1:140. We verified that mixtures prepared with CS-FN and phosphate salts presented pH = 7.4 at 4°C and turned into a gel within 2 min at 37°C.

The distribution of FN within the CS/ β GP/AHP mixtures as well as the efficiency of the conjugation reaction were evaluated using confocal microscopy using fluorescently-labelled FN and CS.

Confocal microscopy images of CS/ β GP/AHP, CS/ β GP/AHP/FN and CS-FN/ β GP/AHP hydrogels recorded using lasers 488 nm and 560 nm at a position of 100 μ m depth in the sample are shown in **Figure V - 7**. As expected, no signal of FN was observed in the CS/ β GP/AHP (**Figure V - 7a**). For CS/ β GP/AHP/FN hydrogel, a gradient concentration of FN is observed with higher concentration at the interface between the hydrogel and the medium (**Figure V - 7b, ii**). In CS-FN/ β GP/AHP hydrogel, red dots corresponding to the signal from FN are observed. We suggest that these points might be aggregates of FN. In the 3D reconstructed volumes from stacks of images, we observe that FN aggregates are distributed within the hydrogel, however, these are mostly on the interface between the hydrogel and the culture medium (**Figure V - 7c, ii**). It is worth to note that the distribution of these aggregates stayed unchanged even after rinsing by PBS (data not shown), suggesting that they were grafted onto CS. Although FN is not homogeneously distributed in the final CS/ β GP/AHP hydrogel in both strategies, signal from FN is clearly detected in the bulk of the hydrogel (**Figure V - 7b-c, i**).

From these observations, it seems that when FN is simply mixed with CS/ β GP/AHP mixtures, a phase separation occurs between FN and CS. Indeed, only a part of FN is distributed in the hydrogel but most of FN chains migrated or were expelled to the hydrogel edges. We assumed that by covalently grafting FN onto CS chains, this phenomenon could be avoided. Nevertheless, FN were found in an aggregated form. We hypothesize that the aggregation of FN might occur during the activation step by EDC/sulfo-NHS as both reactive functions, carboxylic acid and primary amine, are present in FN.

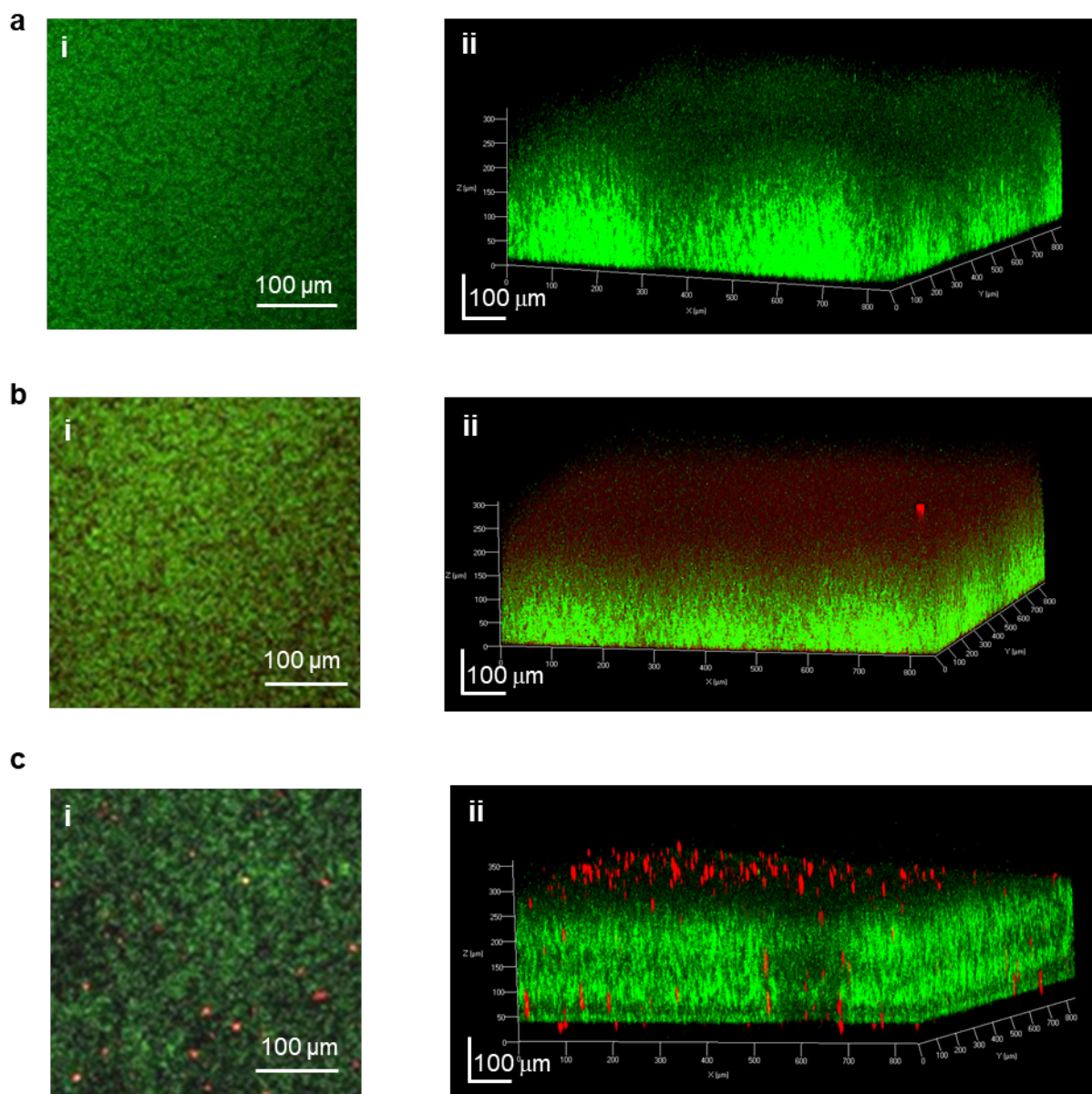


Figure V - 7. Confocal microscopy images taken at 100 μm depth inside the sample (i) and volumes reconstructed from stacks of images (ii) for regular CS/ β GP/AHP hydrogel (a), CS/ β GP/AHP/FN hydrogel (b) and CS-FN/ β GP/AHP hydrogel (c). CS concentration = 0.8 wt%, CS is labelled with AlexaFluor 488 and FN with AlexaFluor 568.

3.2.b. Preliminary evaluation of the efficiency of bio-functionalization strategies

In order to evaluate the efficiency of the studied bio-functionalization strategies, the behaviors of MC3T3-E1 cells in 2D or 3D culture either with the regular hydrogel or with bio-functionalized hydrogels were compared.

Bio-functionalization by RGD-containing peptide sequence

The efficiency was evaluated in an *in vitro* 2D culture of MC3T3-E1 on CS/ β GP/AHP hydrogels prepared with regular CS or RGD-grafted CS (CS-RGD). For control conditions, cells were directly seeded onto culture wells (polystyrene for tissue culture). Observations at two different incubations times, 4 h and 24 h, are shown in **Figure V - 8**.

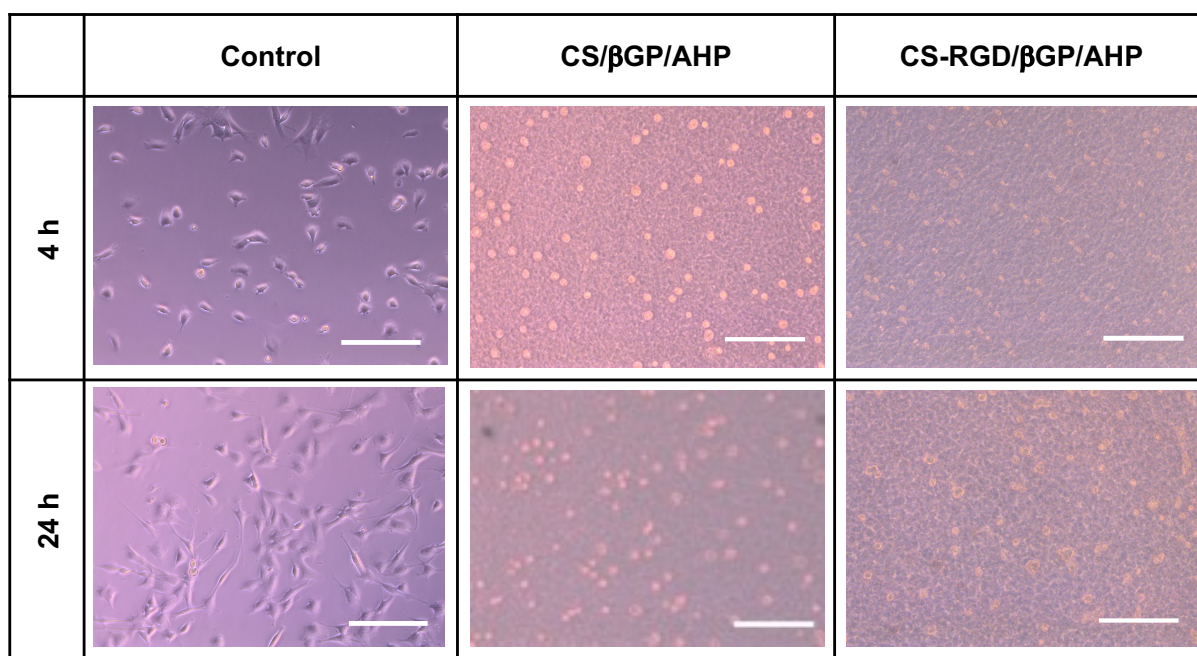


Figure V - 8. Microscope images of 2D cultures of MC3T3-E1 cells seeded on the culture wells (control), CS/ β GP/AHP or CS-RGD/ β GP/AHP hydrogels at 4 h or 24 h. Scale bar = 100 μ m.

In control conditions, MC3T3-E1 cells showed normal behavior. Cell spreading was observed at 4 h after seeding. At 24 h, all the cells showed a spread morphology and the proliferation was confirmed by a clear increase in the number of. For cells seeded on preformed CS/ β GP/AHP hydrogel, cells showed rounded morphology at 4 h. At 24 h, they remained rounded and no proliferation was observed. This observation is in agreement with previous studies that reported that no cell spreading was observed in 2D culture on CS films.⁵⁻⁸ For the hydrogel prepared with CS-RGD with a theoretical grafting ratio at [RGD]:[CS monomer] = 1:300, cells showed a similar behavior as for the regular hydrogel. These

unsatisfactory results might be explained by the insufficient peptide density that is available at the surface of the hydrogel, assuming CS-RGD chains homogeneously distributed in the hydrogel volume.

Bio-functionalization with FN

The efficiency of the incorporation of FN on the cellular behavior was evaluated by *in vitro* encapsulation of MC3T3-E1 cells. Cells were encapsulated into CS/ β GP/AHP hydrogels prepared with either regular or functionalized CS with FN, CS-FN, and the hydrogel in which FN was added by simple mixing. The concentration in CS was fixed at 0.8 wt% in all studied formulations. The viability and morphology of encapsulated cells were assessed using Live/Dead staining. Representative images recorded by confocal microscopy are shown in **Figure V - 9**. Although the cell viability was not quantified in this study, most of the encapsulated cells were alive at 24 h post-encapsulation. According to the results presented in Chapter II, the cell viability is expected to be around 80% at 24 h for the CS/ β GP/AHP formulation. Most of encapsulated cells exhibit a rounded morphology in the three hydrogels. However, some signs of cytoplasm extension were observed for cells encapsulated in the two bio-functionalized formulations, CS/ β GP/AHP/FN and CS-FN/ β GP/AHP, as indicated by white arrows in **Figure V - 9**.

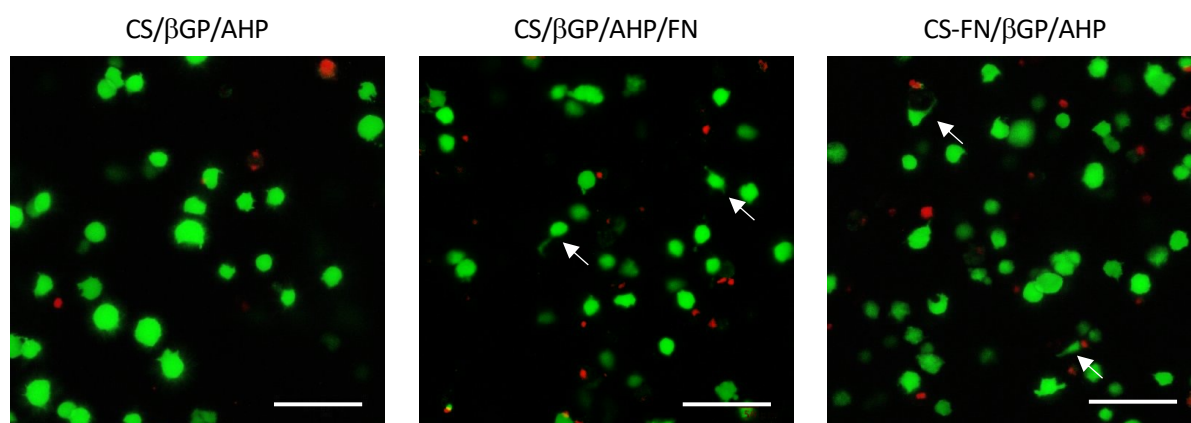


Figure V - 9. Confocal microscopy images of Live/Dead assays for MC3T3 cells encapsulated in the regular hydrogel, CS/ β GP/AHP, and in bio-functionalized hydrogels with FN, CS/ β GP/AHP/FN and CS-FN/ β GP/AHP at 24 h post-encapsulation. Images are obtained from the projection of 66 slices taken at a random position in the hydrogel with a field of $425 \times 425 \times 300 \mu\text{m}$. Scale bar = $100 \mu\text{m}$.

The observed cell behavior can be explained by the heterogeneous distribution of FN within the CS/ β GP/AHP hydrogel, as previously discussed. For the approach in which FN was simply mixed to the formulation after adding the salt, FN was observed in the bulk of the hydrogel, but most of FN signal was detected at the hydrogel edges. Therefore, the quantity of FN accessible to encapsulated cells might not be sufficient for enhancing cell attachment. For the approach in which FN was covalently grafted onto CS chains, FN was mostly found in an aggregated form. Hence, cell binding sites on FN might not

be correctly exposed and accessible to cells. Such issues related to the use of proteins was already reported in the literature.^{52,59,60} In particular, no cell attachment and spreading was observed when cells were seeded onto a surface coated with FN aggregates.⁶⁰ Therefore, in both functionalization approaches explored in this study, the distribution and the accessibility to cell binding sites on FN need to be better controlled in order to improve cell activity in CS/βGP/AHP hydrogels.

V.4. Conclusion

In this chapter, studies were carried out to investigate the origin of the rounded phenotype of encapsulated cells in CS/salt hydrogels. In the first study, the behavior of MPNST cells, which native tissues have a stiffness to that of CS/βGP/AHP hydrogels, was investigated in 2D or 3D cultures. The results clearly evidenced the absence of cytotoxicity and are very encouraging as nearly all encapsulated cells in the CS 0.5 wt% hydrogel remained alive after 6 days. Despite encouraging cell survival, poor signs of cell adhesion were observed. These results and observations suggest that even when the overall mechanical properties of the hydrogels match with the native tissues, biochemical signals are crucial for cell adhesion.

In the second study, we incorporated biochemical signals – RGD-containing peptide sequence or fibronectin (FN) – into the formulations to improve the cell activity in CS/βGP/AHP hydrogels. The peptide sequence was successfully grafted onto CS chains and the grafting did not alter the thermogelling process. However, the cellular response of MC3T3-E1 cells showed no signs of cellular adhesion, suggesting that further optimization is needed. For FN, the protein was incorporated into CS/βGP/AHP hydrogels either by a simple mixing or covalent grafting onto CS chains prior to gelation. In both approaches, the resulting formulations exhibited fast gelation at 37°C. However, the distribution and the conformation of FN in the hydrogel was not optimal for cell attachment. Formulation strategies are needed to better control the distribution and the conformation of FN within these hydrogels in order to efficiently favor cell attachment.

References

- (1) Nair, L. S.; Starnes, T.; Ko, J. W. K.; Laurencin, C. T. Development of Injectable Thermogelling Chitosan-Inorganic Phosphate Solutions for Biomedical Applications. *Biomacromolecules* **2007**, *8* (12), 3779–3785. <https://doi.org/10.1021/bm7006967>.
- (2) Ceccaldi, C.; Assaad, E.; Hui, E.; Buccionyte, M.; Adoungotchodo, A.; Lerouge, S. Optimization of Injectable Thermosensitive Scaffolds with Enhanced Mechanical Properties for Cell Therapy. *Macromol. Biosci.* **2017**, *17* (6), 1–10. <https://doi.org/10.1002/mabi.201600435>.
- (3) Guimarães, C. F.; Gasperini, L.; Marques, A. P.; Reis, R. L. The Stiffness of Living Tissues and Its Implications for Tissue Engineering. *Nat. Rev. Mater.* **2020**, *5* (5), 351–370. <https://doi.org/10.1038/s41578-019-0169-1>.
- (4) Goktas, S.; Dmytryk, J. J.; McFetridge, P. S. Biomechanical Behavior of Oral Soft Tissues. *J. Periodontol.* **2011**, *82* (8), 1178–1186. <https://doi.org/10.1902/jop.2011.100573>.
- (5) Aranaz, I.; Mengibar, M.; Harris, R.; Panos, I.; Miralles, B.; Acosta, N.; Galed, G.; Heras, A. Functional Characterization of Chitin and Chitosan. *Curr. Chem. Biol.* **2009**, *3* (2), 203–230. <https://doi.org/10.2174/187231309788166415>.
- (6) Carvalho, C. R.; López-Cebral, R.; Silva-Correia, J.; Silva, J. M.; Mano, J. F.; Silva, T. H.; Freier, T.; Reis, R. L.; Oliveira, J. M. Investigation of Cell Adhesion in Chitosan Membranes for Peripheral Nerve Regeneration. *Mater. Sci. Eng. C* **2017**, *71*, 1122–1134. <https://doi.org/10.1016/j.msec.2016.11.100>.
- (7) Luna, S. M.; Silva, S. S.; Gomes, M. E.; Mano, J. F.; Reis, R. L. Cell Adhesion and Proliferation onto Chitosan-Based Membranes Treated by Plasma Surface Modification. *J. Biomater. Appl.* **2011**, *26* (1), 101–116. <https://doi.org/10.1177/0885328210362924>.
- (8) Custodio, C.; Alves, C.; Reis, R.; Mano, J. Immobilization of Fibronectin in Chitosan Substrates Improves Cell Adhesion and Proliferation. *J. Tissue Eng. Regen. Med.* **2010**, *4* (7), 524–531. <https://doi.org/10.1002/term>.
- (9) Pekker, M.; Sneider, M. N. The Surface Charge of a Cell Lipid Membrane. *J. Phys. Chem. Biophys.* **2015**, *5* (2). <https://doi.org/10.4172/2161-0398.1000177>.
- (10) Fillion, D.; Lavertu, M.; Buschmann, M. D. Ionization and Solubility of Chitosan Solutions Related to Thermosensitive Chitosan/Glycerol-Phosphate Systems. *Biomacromolecules* **2007**, *8* (10), 3224–3234. <https://doi.org/10.1021/bm700520m>.
- (11) Zhu, Y.; Ghosh, P.; Charnay, P.; Burns, D. K.; Parada, L. F. Neurofibromas in NF1: Schwann Cell Origin and Role of Tumor Environment. *Science (80-.)*. **2002**, *296* (5569), 920–922. <https://doi.org/10.1126/science.1068452>.
- (12) Katz, D.; Lazar, A.; Lev, D. Malignant Peripheral Nerve Sheath Tumour (MPNST): The Clinical Implications of Cellular Signalling Pathways. *Expert Rev. Mol. Med.* **2009**, *11* (October), 1–23. <https://doi.org/10.1017/S1462399409001227>.
- (13) Guimarães, C. F.; Gasperini, L.; Marques, A. P.; Reis, R. L. The Stiffness of Living Tissues and Its Implications for Tissue Engineering. *Nat. Rev. Mater.* **2020**, *5* (5), 351–370. <https://doi.org/10.1038/s41578-019-0169-1>.
- (14) Rosso, G.; Guck, J. Mechanical Changes of Peripheral Nerve Tissue Microenvironment and Their Structural Basis during Development. *APL Bioeng.* **2019**, *3* (3), 1–12. <https://doi.org/10.1063/1.5108867>.
- (15) Al-Gahtany, M.; Midha, R.; Guha, A.; Jacobs, W. B. Malignant Peripheral Nerve Tumors. *Textb. Neuro-Oncology* **2005**, 564–571. <https://doi.org/10.1016/B978-0-7216-8148-1.50077-2>.
- (16) Radomska, K. J.; Couplier, F.; Gresset, A.; Schmitt, A.; Debbiche, A.; Lemoine, S.; Wolkenstein, P.; Vallat, J. M.; Charnay, P.; Topilko, P. Cellular Origin, Tumor Progression, and Pathogenic Mechanisms of Cutaneous Neurofibromas Revealed by Mice with Nf1 Knockout in Boundary Cap Cells. *Cancer Discov.* **2019**, *9* (1), 130–147. <https://doi.org/10.1158/2159-8290.CD-18-0156>.
- (17) Dang, P. A.; Palomino-Durand, C.; Elsafi Mabrouk, M.; Marquaille, P.; Odier, C.; Norvez, S.; Pauthe, E.;

- Corté, L. Rational Formulation Design of Injectable Thermosensitive Chitosan-Based Hydrogels for Cell Encapsulation and Delivery. *Carbohydr. Polym.* **2022**, *277*, 118836. <https://doi.org/10.1016/j.carbpol.2021.118836>.
- (18) Ruoslahti, E. Rgd and Other Recognition Sequences for Integrins. *Annu. Rev. Cell Dev. Biol.* **1996**, *12* (1), 697–715. <https://doi.org/10.1146/annurev.cellbio.12.1.697>.
 - (19) Alipour, M.; Baneshi, M.; Hosseinkhani, S.; Mahmoudi, R.; Jabari Arabzadeh, A.; Akrami, M.; Mehrzad, J.; Bardania, H. Recent Progress in Biomedical Applications of RGD-Based Ligand: From Precise Cancer Theranostics to Biomaterial Engineering: A Systematic Review. *J. Biomed. Mater. Res. - Part A* **2020**, *108* (4), 839–850. <https://doi.org/10.1002/jbm.a.36862>.
 - (20) Hersel, U.; Dahmen, C.; Kessler, H. RGD Modified Polymers: Biomaterials for Stimulated Cell Adhesion and Beyond. *Biomaterials* **2003**, *24* (24), 4385–4415. [https://doi.org/10.1016/S0142-9612\(03\)00343-0](https://doi.org/10.1016/S0142-9612(03)00343-0).
 - (21) Comisar, W. A.; Kazmers, N. H.; Mooney, D. J.; Linderman, J. J. Engineering RGD Nanopatterned Hydrogels to Control Preosteoblast Behavior: A Combined Computational and Experimental Approach. *Biomaterials* **2007**, *28* (30), 4409–4417. <https://doi.org/10.1016/j.biomaterials.2007.06.018>.
 - (22) Chen, L.; Li, B.; Xiao, X.; Meng, Q.; Li, W.; Yu, Q.; Bi, J.; Cheng, Y.; Qu, Z. Preparation and Evaluation of an Arg-Gly-Asp-Modified Chitosan/Hydroxyapatite Scaffold for Application in Bone Tissue Engineering. *Mol. Med. Rep.* **2015**, *12* (5), 7263–7270. <https://doi.org/10.3892/mmr.2015.4371>.
 - (23) Masuko, T.; Iwasaki, N.; Yamane, S.; Funakoshi, T.; Majima, T.; Minami, A.; Ohsuga, N.; Ohta, T.; Nishimura, S. I. Chitosan-RGDSSGC Conjugate as a Scaffold Material for Musculoskeletal Tissue Engineering. *Biomaterials* **2005**, *26* (26), 5339–5347. <https://doi.org/10.1016/j.biomaterials.2005.01.062>.
 - (24) Tiğli, R. S.; Gümüşdereliöğlü, M. Evaluation of RGD- or EGF-Immobilized Chitosan Scaffolds for Chondrogenic Activity. *Int. J. Biol. Macromol.* **2008**, *43* (2), 121–128. <https://doi.org/10.1016/j.ijbiomac.2008.04.003>.
 - (25) Schmidt, S.; Zeiser, M.; Hellweg, T.; Duschl, C.; Fery, A.; Möhwald, H. Adhesion and Mechanical Properties of PNIPAM Microgel Films and Their Potential Use as Switchable Cell Culture Substrates. *Adv. Funct. Mater.* **2010**, *20* (19), 3235–3243. <https://doi.org/10.1002/adfm.201000730>.
 - (26) Chung, T.; Lu, Y.; Wang, S.; Lin, Y.; Chu, S. Growth of Human Endothelial Cells on Photochemically Grafted Gly – Arg – Gly – Asp (GRGD) Chitosans. *Biomaterials* **2002**, *23*, 4803–4809.
 - (27) Park, K. H.; Kim, M. H.; Park, S. H.; Lee, H. J.; Kim, I. K.; Chung, H. M. Synthesis of Arg-Gly-Asp (RGD) Sequence Conjugated Thermo-Reversible Gel via the PEG Spacer Arm as an Extracellular Matrix for a Pheochromocytoma Cell (PC12) Culture. *Biosci. Biotechnol. Biochem.* **2004**, *68* (11), 2224–2229. <https://doi.org/10.1271/bbb.68.2224>.
 - (28) Mauri, E.; Sacchetti, A.; Vicario, N.; Peruzzotti-Jametti, L.; Rossi, F.; Pluchino, S. Evaluation of RGD Functionalization in Hybrid Hydrogels as 3D Neural Stem Cell Culture Systems. *Biomater. Sci.* **2018**, 501–510. <https://doi.org/10.1039/C7BM01056G>.
 - (29) Kudva, A. K.; Luyten, F. P.; Patterson, J. RGD-Functionalized Polyethylene Glycol Hydrogels Support Proliferation and in Vitro Chondrogenesis of Human Periosteum-Derived Cells. *J. Biomed. Mater. Res. - Part A* **2018**, *106* (1), 33–42. <https://doi.org/10.1002/jbm.a.36208>.
 - (30) Li, J.; Yun, H.; Gong, Y.; Zhao, N.; Zhang, X. Investigation of MC3T3-E1 Cell Behavior on the Surface of GRGDS-Coupled Chitosan. *Biomacromolecules* **2006**, *7* (4), 1112–1123. <https://doi.org/10.1021/bm050913r>.
 - (31) Massia, S. P.; Hubbell, J. A. Covalent Surface Immobilization of Arg-Gly-Asp- and Tyr-Ile-Gly-Ser-Arg-Containing Peptides to Obtain Well-Defined Cell-Adhesive Substrates. *Anal. Biochem.* **1990**, *187* (2), 292–301. [https://doi.org/10.1016/0003-2697\(90\)90459-M](https://doi.org/10.1016/0003-2697(90)90459-M).
 - (32) Bellis, S. L. Advantages of RGD Peptides for Directing Cell Association with Biomaterials. **2012**, *32* (18), 4205–4210. <https://doi.org/10.1016/j.biomaterials.2011.02.029>. Advantages.
 - (33) Hansson, A.; Hashom, N.; Falson, F.; Rousselle, P.; Jordan, O.; Borchard, G. In Vitro Evaluation of an RGD-Functionalized Chitosan Derivative for Enhanced Cell Adhesion. *Carbohydr. Polym.* **2012**, *90* (4),

- 1494–1500. <https://doi.org/10.1016/j.carbpol.2012.07.020>.
- (34) Kang, S. W.; Cha, B. H.; Park, H.; Park, K. S.; Lee, K. Y.; Lee, S. H. The Effect of Conjugating RGD into 3D Alginate Hydrogels on Adipogenic Differentiation of Human Adipose-Derived Stromal Cells. *Macromol. Biosci.* **2011**, *11* (5), 673–679. <https://doi.org/10.1002/mabi.201000479>.
- (35) Hsu, S. H.; Shu, W. W.; Hsieh, S. C.; Tsai, C. L.; Chen, D. C.; Tan, T. S. Evaluation of Chitosan-Alginate-Hyaluronate Complexes Modified by an RGD-Containing Protein as Tissue-Engineering Scaffolds for Cartilage Regeneration. *Artif. Organs* **2004**, *28* (8), 693–703. <https://doi.org/10.1111/j.1525-1594.2004.00046.x>.
- (36) Wang, Y. Y.; Lü, L. X.; Feng, Z. Q.; Xiao, Z. D.; Huang, N. P. Cellular Compatibility of RGD-Modified Chitosan Nanofibers with Aligned or Random Orientation. *Biomed. Mater.* **2010**, *5* (5). <https://doi.org/10.1088/1748-6041/5/5/054112>.
- (37) Lee, J. W.; Park, Y. J.; Lee, S. J.; Lee, S. K.; Lee, K. Y. The Effect of Spacer Arm Length of an Adhesion Ligand Coupled to an Alginate Gel on the Control of Fibroblast Phenotype. *Biomaterials* **2010**, *31* (21), 5545–5551. <https://doi.org/10.1016/j.biomaterials.2010.03.063>.
- (38) Lee, J. W.; Kim, H.; Lee, K. Y. Effect of Spacer Arm Length between Adhesion Ligand and Alginate Hydrogel on Stem Cell Differentiation. *Carbohydr. Polym.* **2016**, *139*, 82–89. <https://doi.org/10.1016/j.carbpol.2015.12.024>.
- (39) Pankov, R.; Yamada, K. M. Fibronectin at a Glance. *J. Cell Sci.* **2002**, *115* (20), 3861–3863. <https://doi.org/10.1242/jcs.00059>.
- (40) Parisi, L.; Toffoli, A.; Ghezzi, B.; Mozzoni, B.; Lumetti, S.; Macaluso, G. M. A Glance on the Role of Fibronectin in Controlling Cell Response at Biomaterial Interface. *Jpn. Dent. Sci. Rev.* **2020**, *56* (1), 50–55. <https://doi.org/10.1016/j.jdsr.2019.11.002>.
- (41) Mardon, H. J.; Grant, K. E. The Role of the Ninth and Tenth Type III Domains of Human Fibronectin in Cell Adhesion. *FEBS Lett.* **1994**, *340* (3), 197–201. [https://doi.org/10.1016/0014-5793\(94\)80137-1](https://doi.org/10.1016/0014-5793(94)80137-1).
- (42) Custodio, C.; Alves, C.; Reis, R.; Mano, J. Immobilization of Fibronectin in Chitosan Substrates Improves Cell Adhesion and Proliferation. *J. Tissue Eng. Regen. Med.* **2010**, No. 4, 316–323. <https://doi.org/10.1002/term>.
- (43) Seidlits, S. K.; Drinnan, C. T.; Petersen, R. R.; Shear, J. B.; Suggs, L. J.; Schmidt, C. E. Fibronectin-Hyaluronic Acid Composite Hydrogels for Three-Dimensional Endothelial Cell Culture. *Acta Biomater.* **2011**, *7* (6), 2401–2409. <https://doi.org/10.1016/j.actbio.2011.03.024>.
- (44) Jun, I.; Lee, Y. Bin; Choi, Y. S.; Engler, A. J.; Park, H.; Shin, H. Transfer Stamping of Human Mesenchymal Stem Cell Patches Using Thermally Expandable Hydrogels with Tunable Cell-Adhesive Properties. *Biomaterials* **2015**, *54*, 44–54. <https://doi.org/10.1016/j.biomaterials.2015.03.016>.
- (45) Schulte, A.; Alhusaini, Q. F. M.; Schönherr, H. Anodic Aluminum Oxide Nanopore Template-Assisted Fabrication of Nanostructured Poly(Vinyl Alcohol) Hydrogels for Cell Studies. *ACS Appl. Bio Mater.* **2020**, *3* (4), 2419–2427. <https://doi.org/10.1021/acsabm.0c00153>.
- (46) Trujillo, S.; Gonzalez-Garcia, C.; Rico, P.; Reid, A.; Windmill, J.; Dalby, M. J.; Salmeron-Sanchez, M. Engineered 3D Hydrogels with Full-Length Fibronectin That Sequester and Present Growth Factors. *Biomaterials* **2020**, *252* (November 2019). <https://doi.org/10.1016/j.biomaterials.2020.120104>.
- (47) Shinohara, S.; Kihara, T.; Sakai, S.; Matsusaki, M.; Akashi, M.; Taya, M.; Miyake, J. Fabrication of in Vitro Three-Dimensional Multilayered Blood Vessel Model Using Human Endothelial and Smooth Muscle Cells and High-Strength PEG Hydrogel. *J. Biosci. Bioeng.* **2013**, *116* (2), 231–234. <https://doi.org/10.1016/j.jbiosc.2013.02.013>.
- (48) Trujillo, S.; Vega, S. L.; Song, K. H.; San Félix, A.; Dalby, M. J.; Burdick, J. A.; Salmeron-Sanchez, M. Engineered Full-Length Fibronectin–Hyaluronic Acid Hydrogels for Stem Cell Engineering. *Adv. Healthc. Mater.* **2020**, *9* (21), 1–12. <https://doi.org/10.1002/adhm.202000989>.
- (49) Lee, M. H.; Adam, C. S.; Boettiger, D.; DeGrado, W. F.; Shapiro, I. M.; Composto, J. S.; Ducheyne, P. Adhesion of MC3T3-E1 Cells to RGD Peptides of Different Flanking Residues: Detachment Strength

- and Correlation with Long-Term Cellular Function Mark. *J. Biomed. Mater. Res. Part A* **2006**, *79* (4), 963–973. <https://doi.org/0.1002/jbm.a.31065>.
- (50) Poulouin, L.; Gallet, O.; Rouahi, M.; Imhoff, J. M. Plasma Fibronectin: Three Steps to Purification and Stability. *Protein Expr. Purif.* **1999**, *17* (1), 146–152. <https://doi.org/10.1006/prep.1999.1103>.
- (51) Mansur, A. A. P.; de Carvalho, S. M.; Mansur, H. S. Bioengineered Quantum Dot/Chitosan-Tripeptide Nanoconjugates for Targeting the Receptors of Cancer Cells. *Int. J. Biol. Macromol.* **2016**, *82*, 780–789. <https://doi.org/10.1016/j.ijbiomac.2015.10.047>.
- (52) Vallières, K.; Chevallier, P.; Sarra-Bournet, C.; Turgeon, S.; Laroche, G. AFM Imaging of Immobilized Fibronectin: Does the Surface Conjugation Scheme Affect the Protein Orientation/Conformation? *Langmuir* **2007**, *23* (19), 9745–9751. <https://doi.org/10.1021/la701323q>.
- (53) Tsai, W. B.; Chen, Y. R.; Li, W. T.; Lai, J. Y.; Liu, H. L. RGD-Conjugated UV-Crosslinked Chitosan Scaffolds Inoculated with Mesenchymal Stem Cells for Bone Tissue Engineering. *Carbohydr. Polym.* **2012**, *89* (2), 379–387. <https://doi.org/10.1016/j.carbpol.2012.03.017>.
- (54) Tsai, W. B.; Chen, Y. R.; Liu, H. L.; Lai, J. Y. Fabrication of UV-Crosslinked Chitosan Scaffolds with Conjugation of RGD Peptides for Bone Tissue Engineering. *Carbohydr. Polym.* **2011**, *85* (1), 129–137. <https://doi.org/10.1016/j.carbpol.2011.02.003>.
- (55) Kim, S.; Cui, Z. K.; Fan, J.; Fartash, A.; Aghaloo, T. L.; Lee, M. Photocrosslinkable Chitosan Hydrogels Functionalized with the RGD Peptide and Phosphoserine to Enhance Osteogenesis. *J. Mater. Chem. B* **2016**, *4* (31), 5289–5298. <https://doi.org/10.1039/c6tb01154c>.
- (56) Huang, Y. S.; Bertrand, V.; Bozukova, D.; Pagnouille, C.; Labrugère, C.; De Pauw, E.; De Pauw-Gillet, M. C.; Durrieu, M. C. RGD Surface Functionalization of the Hydrophilic Acrylic Intraocular Lens Material to Control Posterior Capsular Opacification. *PLoS One* **2014**, *9* (12), 1–32. <https://doi.org/10.1371/journal.pone.0114973>.
- (57) Patrulea, V.; Hirt-Burri, N.; Jeannerat, A.; Applegate, L. A.; Ostafe, V.; Jordan, O.; Borchard, G. Peptide-Decorated Chitosan Derivatives Enhance Fibroblast Adhesion and Proliferation in Wound Healing. *Carbohydr. Polym.* **2016**, *142*, 114–123. <https://doi.org/10.1016/j.carbpol.2016.01.045>.
- (58) Parker, F. S. *Applications of Infrared Spectroscopy in Biochemistry, Biology and Medicine*; A Division of Plenum Publishing Corporation: New York, 1971.
- (59) Kowalczyńska, H. M.; Nowak-Wyrzykowska, M.; Kołos, R.; Dobkowski, J.; Kamiński, J. Fibronectin Adsorption and Arrangement on Copolymer Surfaces and Their Significance in Cell Adhesion. *J. Biomed. Mater. Res. - Part A* **2005**, *72* (2), 228–236. <https://doi.org/10.1002/jbm.a.30238>.
- (60) Bascetin, R. Etude de l' Auto-Assemblage de La Fibronectine Plasmatique Humaine : Mécanismes et Réponses Cellulaires, Université de Cergy-Pontoise, 2015.

CONCLUSION

Along with the tremendous development of cell-based therapies, there is a growing need for injectable matrices able to support the retention and survival of injected cells. Based on the literature review presented in **Chapter I**, we identified that thermosensitive injectable hydrogels have a great potential for this application. Unfortunately, most of the proposed hydrogels consist in a macromolecular network having a submicron mesh size. Therefore, the macroporosity required for cell proliferation and migration is lacking. In this PhD thesis, I studied thermosensitive hydrogels in which macroporosity emerges from a phase separation between a polymer and water.

This thermosensitive system, which is composed of chitosan (CS) and phosphate salt(s), shows interesting features for use as a cell-laden hydrogel. These mixtures can remain liquid at neutral pHs at room temperature and turn into a gel within minutes at body temperature. Interestingly, the resulting hydrogels present a heterogeneous structure composed of interconnected CS-rich regions and water-rich regions (pores). **In this project, we proposed to take advantage of this peculiar process and hypothesized that thermosensitive cell-laden hydrogels having adequate macroporosity for cell survival and proliferation can be prepared by finely controlling the sol/gel transition. By gaining a deeper understanding of the physical-chemistry of this system, my goal was to design thermosensitive and injectable hydrogels based on CS/salt mixtures having tunable macroporosity for cell encapsulation and delivery.**

A major limitation of the CS/ β GP system, which have first been identified, is its cytotoxic osmolarity induced by the high β GP (β -glycerophosphate) concentrations required to reach physiological pHs. Strategies have been explored in the literature to improve this standard system, by partially or totally replacing β GP by other salts. Nevertheless, a rational platform was still lacking to prepare thermosensitive mixtures composed of CS and salts in which pH, osmolarity and therefore gelation kinetics and cytocompatibility can be controlled whatever the CS concentration. In **Chapter II**, we presented a rational formulation design by combining β GP with a second phosphate salt, AHP. With this third component, the pH and the osmolarity of the mixture can be adjusted finely and independently by playing with the ratios $[\text{salt}]/[\text{NH}_2]$, thus giving the possibility to prepare physiological formulations having tunable CS concentration. Injectable CS solutions having pH 7.4 at 4°C and an osmolarity of $300 \pm 30 \text{ mOsm.L}^{-1}$ were obtained for CS concentrations ranging from 0.4 to 0.9 wt%. We demonstrated the existence of a critical temperature above which the sol/gel transition occurs with a gelation kinetics following a power-law as a function of the temperature. Varying CS concentration allowed us to tune the microstructural and mechanical properties of these hydrogels. The cytocompatibility of the

CS/ β GP/AHP hydrogel prepared with 0.8 wt% of CS was demonstrated by *in vitro* encapsulation of two cell types. These results provided a proof-of-concept of the relevance of our platform allowing to formulate cell-laden thermosensitive CS solutions with two phosphate salts. This work was published in Carbohydrate Polymers.

In **Chapter III**, we investigated the molecular and microscopic mechanisms involved in the thermosensitivity of the CS/salt mixtures. At the molecular level, our results, combined with previous studies in the literature, showed that the sol/gel transition is due to the intrinsic temperature-dependence of the pK_a of the D-glucosamine monomers, regardless of the salt. We highlighted that in the presence of some specific salts, a hydration layer forms, providing a way to shift the sol/gel transition to higher temperature. We demonstrated that the presence of polyol moieties is not mandatory and that β GP can be replaced by other salts able to interact with both CS and water molecules. We identified MES as an interesting cytocompatible alternative to β GP. At the microscopic level, the dynamics of emergence of the macroporous structure in thermosensitive CS/ β GP/AHP hydrogels was observed *in situ* in real time and quantitatively characterized using original setups. From these results and observations, we proposed a molecular and microscopic picture explaining how this macroporous structure arises from the clustering and percolation of CS colloidal-like particles.

From the understanding on the mechanisms of the sol/gel transition, one might expect that the characteristics of CS (molar mass distribution, deacetylation degree, origin) and the presence of cells might have an effect on the hydrogel microstructure. This question was explored in **Chapter IV**. We firstly developed tools and methods to quantitatively characterize the microstructure of CS/ β GP/AHP hydrogels. Using these methods, we found that the porosity and the pore size can be tuned using CS having different characteristics while maintaining the physiological conditions. We showed that cells can be homogeneously encapsulated in our hydrogels up to a concentration of $5 \cdot 10^6$ cells.mL⁻¹, without having an effect on the matrix microstructure. We observed that, by a purely mechanical effect, cells create elongated large pores of tens of μ m by settling down during the gelation phase.

The behavior of different encapsulated cell types in CS/ β GP/AHP hydrogels indicated a need for a better cell-hydrogel adhesion, therefore a bio-functionalization of the matrix was investigated. Strategies incorporating either an RGD-containing peptide sequence or fibronectin (FN) into the formulations were explored in **Chapter V**. The peptide sequence was successfully grafted onto CS chains and the grafting did not alter the thermogelling process. However, no significant improvement in cellular adhesion was observed for MC3T3-E1. With FN, observations and analysis showed that the protein was effectively incorporated into CS/ β GP/AHP hydrogels, either by a simple mixing or by a covalent grafting onto CS chains prior to gelation. For both approaches, the resulting formulations exhibited a fast gelation at

37°C. However, the heterogeneous distribution and the aggregated conformation of FN in the hydrogels probably did not provide a good accessibility for cells to the protein binding sites.

To conclude, in this PhD project, I succeeded in designing a robust platform to prepare thermosensitive CS mixtures with phosphate salts, β GP and AHP, which are compatible with cell injection and survival. I demonstrated that this approach can be applied to functionalized CS or to CS having various molar mass and deacetylation degree. Such a general platform was lacking in the literature despite numerous studies on CS/salt mixtures. We reported interesting findings on the gelation kinetics with the existence of a critical temperature, and on the molecular mechanisms by elucidating the importance and the conditions of formation of a hydration layer ensuring the thermal stability of CS chains at low temperatures. These results open new routes to tune the thermal stability and the gelation kinetics of these systems. At the microscopic level, we highlighted the similar features between CS/salt gels and colloidal gels, which suggests ideas and strategies to adjust the sol/gel transition temperature and the microstructure of the gels. By developing tools and methods to process confocal microscopy images, we explored parameters affecting the hydrogel microstructure, such as the concentration and characteristics of CS, as well as the presence of cells. These methods can still be optimized to better analyze the 3D structure of the gels. Finally, several bio-functionalization strategies were explored in a preliminary study and are currently the object of further research.

Perspectives for further studies will be exposed in the following section.

PERSPECTIVES

Tuning of the thermal stability of CS/salt mixtures

In **Chapter III**, we identified that MES is an interesting candidate to formulate thermosensitive and cytocompatible CS solutions. The use of MES is biologically relevant as it is already widely used as a buffer in biology. The strength of the hydration layer induced by the salts directly governs the thermal stability of CS/salt mixture at neutral pHs. In particular, we showed that the thermal stability is greater in the presence of MES than in the presence of β GP. These results suggest that the thermal stability of CS/salt mixture can be finely tuned by controlling the energy of the interactions between the salts and water molecules. Therefore, it would be interesting to study the osmolarity, gelation kinetics, mechanical and microstructural properties as well as the cytocompatibility of CS/MES mixtures in further studies.

Understanding and tuning of the interparticle interactions

In **Chapter III**, we also showed that the macroporous structure in CS/salt mixtures emerges from the clustering and percolation of colloidal-like CS particles. This process was found to follow a reaction-limited aggregation (RLA) regime. In colloidal gels, it is well known that a network resulting from diffusion-limited aggregation (DLA) is more porous than the one from reaction-limited aggregation (RLA). The probability for two particles to bind together at contact is equal to 1 for DLA and less than 1 for RLA.¹ By making an analogy with colloidal gels, we can imagine to tune the interactions between CS particles as a way to switch from one regime to the other. For that, it is necessary to firstly gain a deeper understanding on the inter-particle interactions, then secondly to develop strategies to tune these interactions.

In that context, a quantitative analysis of the dynamics of the clustering and percolation process would be interesting. For this, image analysis of the direct observations by LSCM can be carried out. For tuning the interparticle interactions, one can imagine to chemically modify the CS structure. For example, introducing hydrophobic functions would be a way to strengthen the interactions which can be tuned by varying the size and the grafting density of these functions. However, this approach can be time-consuming and an optimization of the formulation design to prepare physiological mixtures might be needed. Other strategies inspired from previous studies on colloidal gels for tuning the interparticle interactions can be applied to our system.²⁻⁴ For example, one could study the possibility to induce extra attractive interactions between CS particles by adding a small amount of another polymer to create

depletion effects. By playing with the concentration of the added polymer, the interparticle interactions may be tuned, as well as the macroporosity and the mechanical properties.

In vitro injection model for investigating the microstructure

In **Chapter IV**, we showed that the presence of cells affected the microstructure. Encapsulated cells create elongated pores while settling under the effect of gravity during the short gelation phase. In our image analysis, the microstructure is assumed to be isotropic. This protocol would need to be revised to better account the anisotropic pores created by cells.

Moreover, it would be interesting to investigate the microstructure in a configuration which is closer to the reality of *in vivo* injections of the cell-laden formulation into a cavity filled with fluid. For that, in a preliminary study, a setup was realized to simulate such situations (**Figure P-1a**). Agarose hydrogel at 1 wt% was used as a tissue model. Then, cavities of controlled size were realized using cutters. Using a syringe-pump, the formulation was injected into the cavity which is immersed in PBS at 37°C. We found that the formulation turns into a gel quasi-instantaneously to fill in the cavity (**Figure P-1b**). For further studies, the microstructure of the hydrogel and the effect of various parameters, such as the injection rate and volume, the size and geometry of the cavity, will be investigated quantitatively using confocal microscopy and our image analysis protocol.

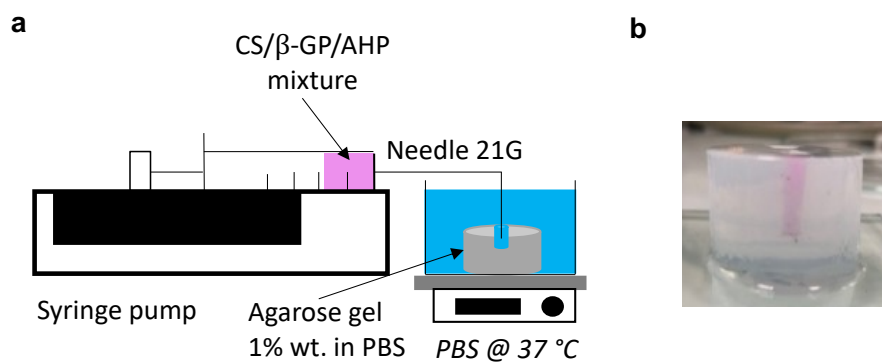


Figure P - 1. *In vitro* injection model: a) schematic illustration of the setup; b) photograph showing agarose hydrogel with filled cavity ($d = 6 \text{ mm}$, $h = 10 \text{ mm}$) by the CS/βGP/AHP hydrogel. Injection rate = $250 \mu\text{L}.\text{min}^{-1}$.

Optimization of the biofunctionalization

The biofunctionalization of CS/ β GP/AHP mixtures need to be further optimized to produce relevant materials for cell delivery or 3D culture. In **Chapter V**, two strategies consisting in incorporating either a RGD-containing peptide sequence or an ECM protein containing cell-binding sites were explored. Both strategies did not show satisfactory results concerning the behavior of encapsulated MC3T3 in biofunctionalized hydrogels. Therefore, potential approaches for better characterizing and improving these two strategies are exposed below.

Incorporation of RGD-containing peptide sequences:

Firstly, the distribution of the grafted RGD-containing peptide sequence in CS solutions and in CS/ β GP/AHP hydrogels needs to be better characterized. Indeed, grafting RGD-containing peptide sequences might affect the physico-chemical properties of CS chains, thus leading to a phase separation between grafted CS chains and regular CS chains. Thus, the grafted CS chains and the RGD-containing peptide sequences would not be homogeneously distributed within the hydrogels. To study this question, we could use a model system by grafting a fluorescent probe having a similar structure and molar mass to the targeted peptide sequence. LSCM observations would provide information about the distribution of the peptide sequence.

Secondly, our preliminary study was performed with a grafting ratio [peptide]:[CS monomer] = 1:200, which was chosen according to the values found in the literature, ranging from 1:10 to 1:1000. Our *in vitro* study suggests that this grafting ratio need to be optimized for specific cell types.

Incorporation of fibronectin or other ECM proteins:

We saw in **Chapter V** that the distribution and the conformation of fibronectin FN are crucial parameters for the efficiency of the biofunctionalization strategy. This should be considered when incorporating proteins in the system, either by simple mixing or covalent grafting. Hence, in further studies, there is a real need to firstly understand the origin of the aggregation of FN observed in the final hydrogel. Investigations should be carried out from the activation of FN by EDC/NHS, through the grafting reaction onto CS chains to the formation of the FN-grafted CS and salts mixture. For instance, confocal observations of systems containing fluorescently-labelled FN would provide a way to characterize systematically the conformation and the localization of FN in the hydrogel.

References

- (1) Poon, W. C. K.; Haw, M. D. Mesoscopic Structure Formation in Colloidal Aggregation and Gelation. *Adv. Colloid Interface Sci.* **1997**, *73*, 71–126. [https://doi.org/10.1016/S0001-8686\(97\)90003-8](https://doi.org/10.1016/S0001-8686(97)90003-8).
- (2) Ramakrishnan, S.; Chen, Y. L.; Schweizer, K. S.; Zukoski, C. F. Elasticity and Clustering in Concentrated Depletion Gels. *Phys. Rev. E - Stat. Physics, Plasmas, Fluids, Relat. Interdiscip. Top.* **2004**, *70* (4), 4. <https://doi.org/10.1103/PhysRevE.70.040401>.
- (3) Lu, P. J.; Zaccarelli, E.; Ciulla, F.; Schofield, A. B.; Sciortino, F.; Weitz, D. A. Gelation of Particles with Short-Range Attraction. *Nature* **2008**, *453* (7194), 499–503. <https://doi.org/10.1038/nature06931>.
- (4) Whitaker, K. A.; Varga, Z.; Hsiao, L. C.; Solomon, M. J.; Swan, J. W.; Furst, E. M. Colloidal Gel Elasticity Arises from the Packing of Locally Glassy Clusters. *Nat. Commun.* **2019**, *10* (1). <https://doi.org/10.1038/s41467-019-10039-w>.

APPENDICES

A. Determination of the dissociation constants of β GP and AHP

Dissociation constants of β GP and AHP were determined by classical pH titration experiments at 4°C and 25°C ($\pm 1^\circ\text{C}$). In brief, a solution of HCl at 1 mol.L⁻¹ was added to 15 mL of solutions of each salt at 0.1 mol.L⁻¹ under vigorous agitation and the pH was recorded as a function of the added volume of HCl. Solutions of salts were placed in an ice bath for measurements at 4°C. For pH ranging from 9 to 1, only one equilibrium was completely observed for both salts. Dissociation constants determined as pH at $\frac{1}{2}$ of the equivalent volume are $pK_{\text{AHP},2} = 6.7$, $pK_{\beta\text{GP},2} = 6.2$ and were not dependent on the temperature. For the present study, only these two values are needed as the pH of interest is near neutral. pH titration for β GP and AHP are shown in **Figure A-1**.

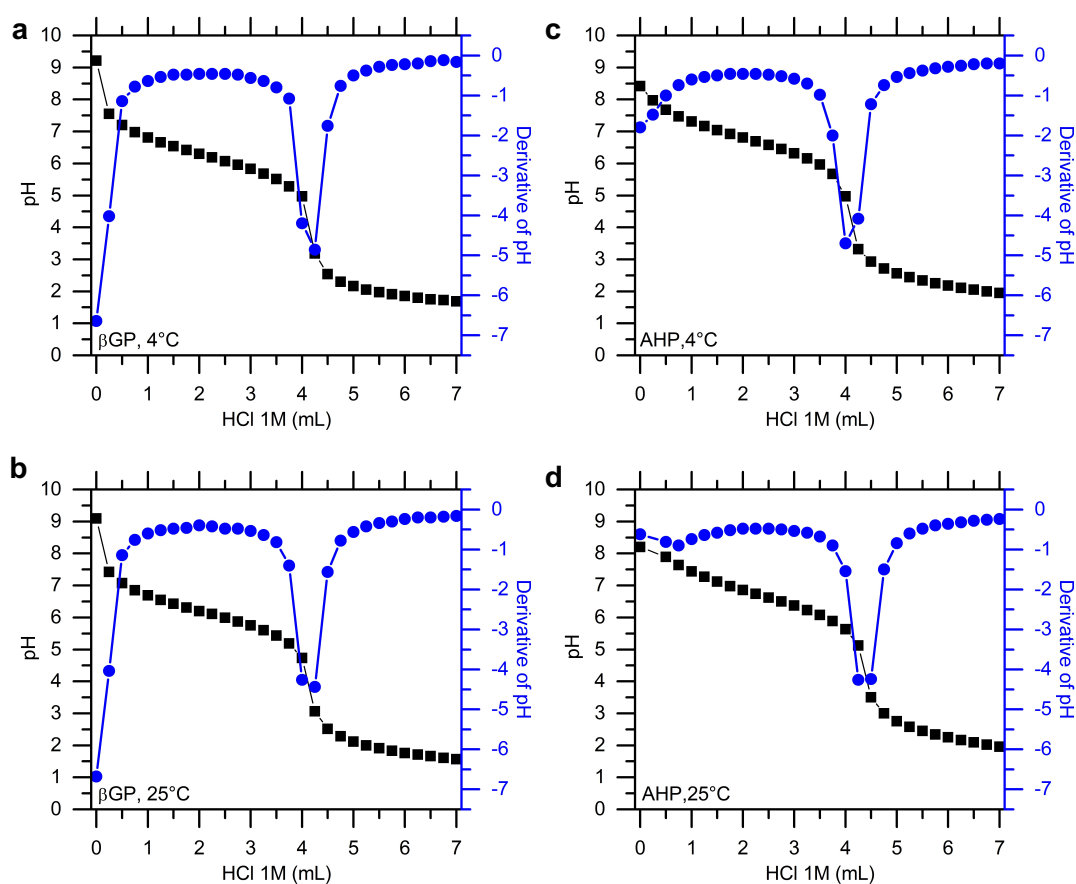


Figure A-1. pH-titration curves (squares) and their derivatives (circles) as a function of added HCl for β GP at 4°C (a) and 25°C (b), AHP at 4°C (c) and 25°C (d).

B. Viscometric study on various CS grades

The intrinsic viscosities, $[\eta]$, and the overlap concentrations, c^* , six CS grades, having the same origin from shrimp, were determined using viscometry.

These measurements have been realized in collaboration with Sonia Ortega and Prof. Rachel Auzély-Velty (CERMAV, CNRS).

For estimating c^* , the dynamic viscosity, η_{dyn} , of solutions of CS in AcOH 0.2M/AcONH₄ 0.15M (the same solvent as for GPC measurements) having concentrations ranging from 0.1 to 0.4 g.mL⁻¹ was measured using capillary viscometer. Measurements were duplicated for each CS grade.

The intrinsic viscosity, $[\eta]$, was determined according to the Huggins equation (B-1).

$$\frac{\eta_{sp}}{c} = [\eta] + k_H [\eta]^2 c \quad (B-1)$$

where η_{sp} is the specific viscosity and $\eta_{sp} = \frac{\eta_{dyn} - \eta_0}{\eta_0}$ with η_0 the viscosity of the solvent; c the concentration of CS solutions and k_H the Huggins parameter depending on the quality of the solvent.

Figure B-1 shows the Huggins plot for the six studied CS grades. From these plots, $[\eta]$ and c^* were determined and the results are shown in **Table B-1**.

Table B-1. Intrinsic viscosity, $[\eta]$, and overlap concentration, c^* , as determined by viscometry for the six studied CS grades.

CS grade	$[\eta]$ (mL/g)	c^* (%wt)
CS1	158 ± 8	0.63 ± 0.03
CS2	555 ± 10	0.18 ± 0.03
CS4	594 ± 30	0.17 ± 0.08
CS5	1220 ± 10	0.082 ± 0.006
CS6	1470 ± 75	0.068 ± 0.003
CS7	1750 ± 73	0.057 ± 0.002

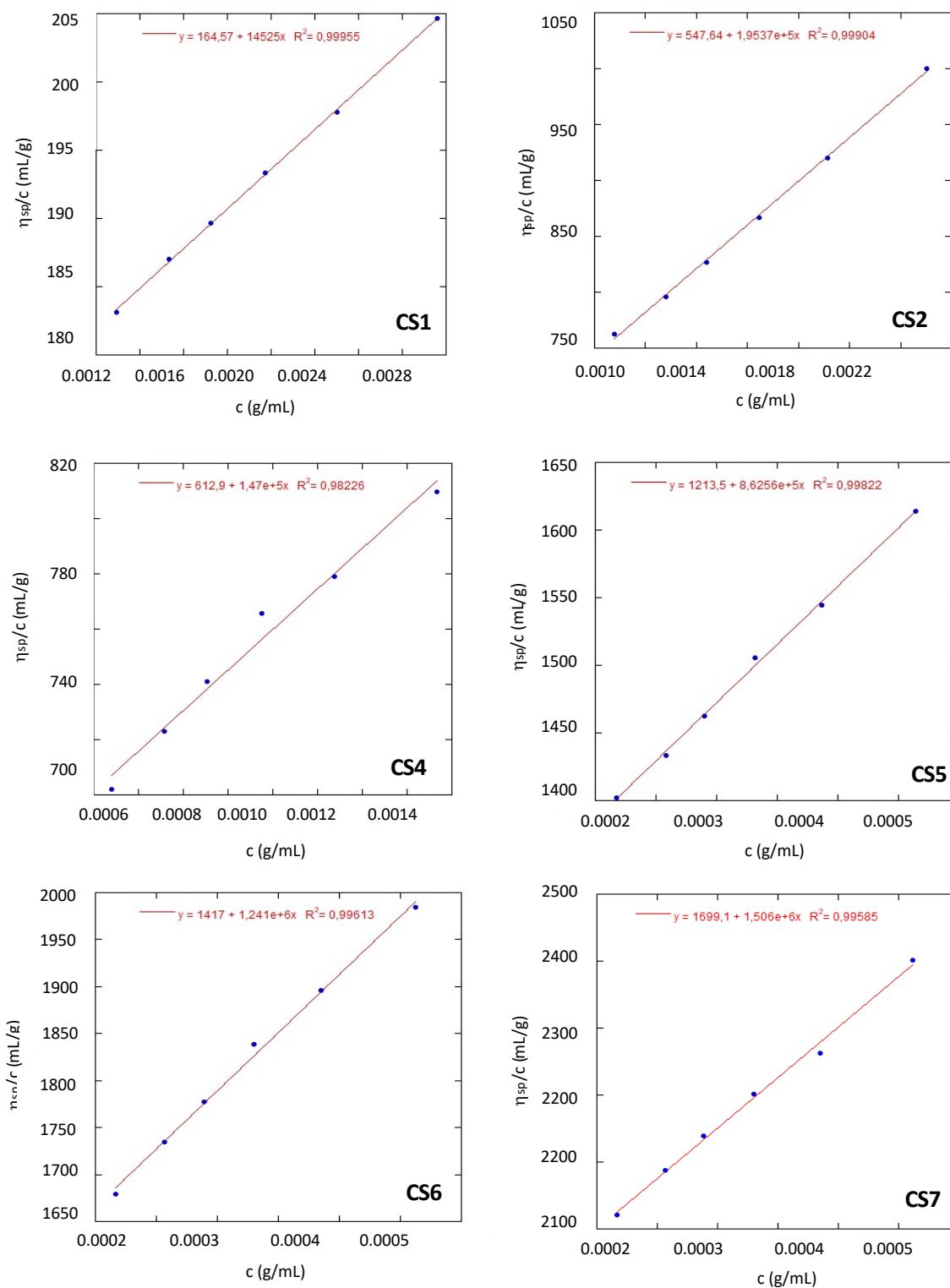


Figure B-1. Huggins plots for the six studied CS grades. $T = 20^\circ\text{C}$.

The weight average molar mass, M_w , determined by GPC shows good correlation with the intrinsic viscosity, as shown in **Figure B-2**.

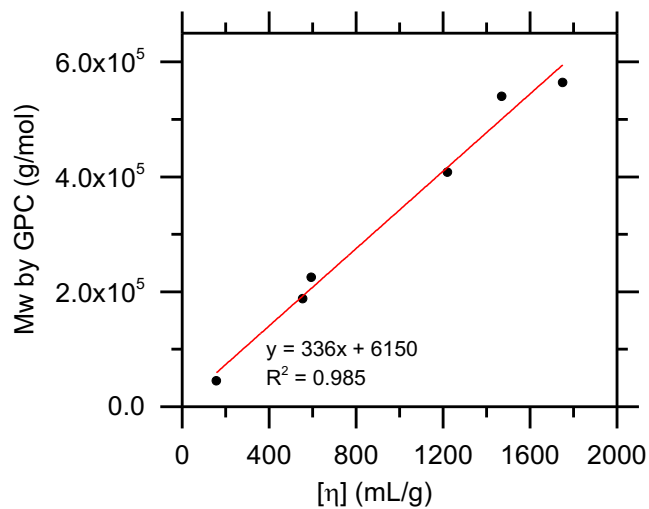


Figure B-2. M_w , determined by GPC, as a function of $[\eta]$, determined by viscometry.

C. DLS measurements

The raw data for the DLS measurements previously presented in **Chapter III, section 3.2.a** are shown in **Figure C-1**.

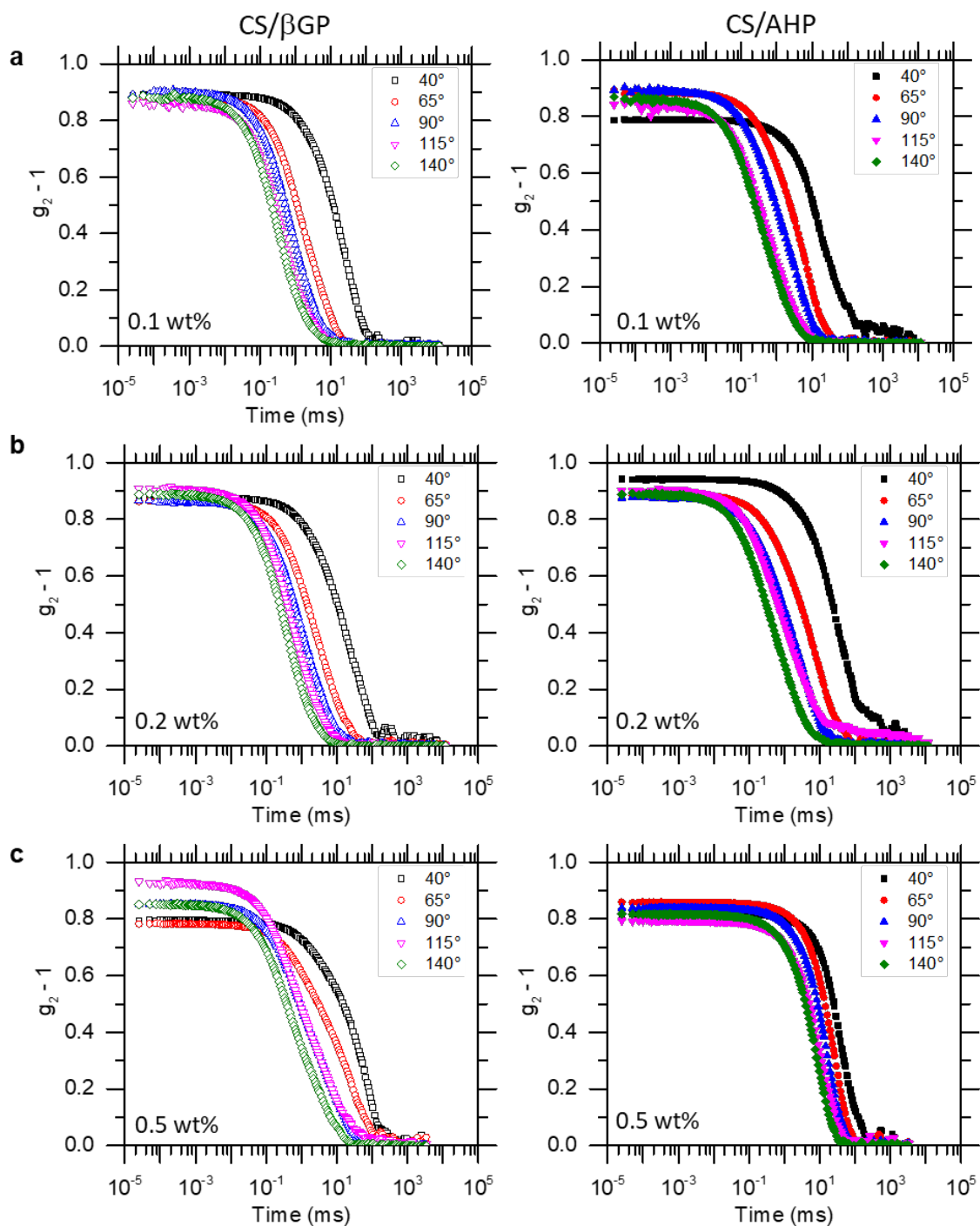


Figure C-1. Raw intensity correlation function, $g_2 - 1$, measured at various angles after 15 min at 4°C for CS/βGP and CS/AHP mixtures having pH = 7.4 prepared at various CS concentrations: 0.1 wt% (a), 0.2 wt% (b) and 0.5 wt% (c).

D. Effect of various characteristics of CS on the microstructural and mechanical properties of CS/ β GP/AHP hydrogels

D.1. Microstructural structure

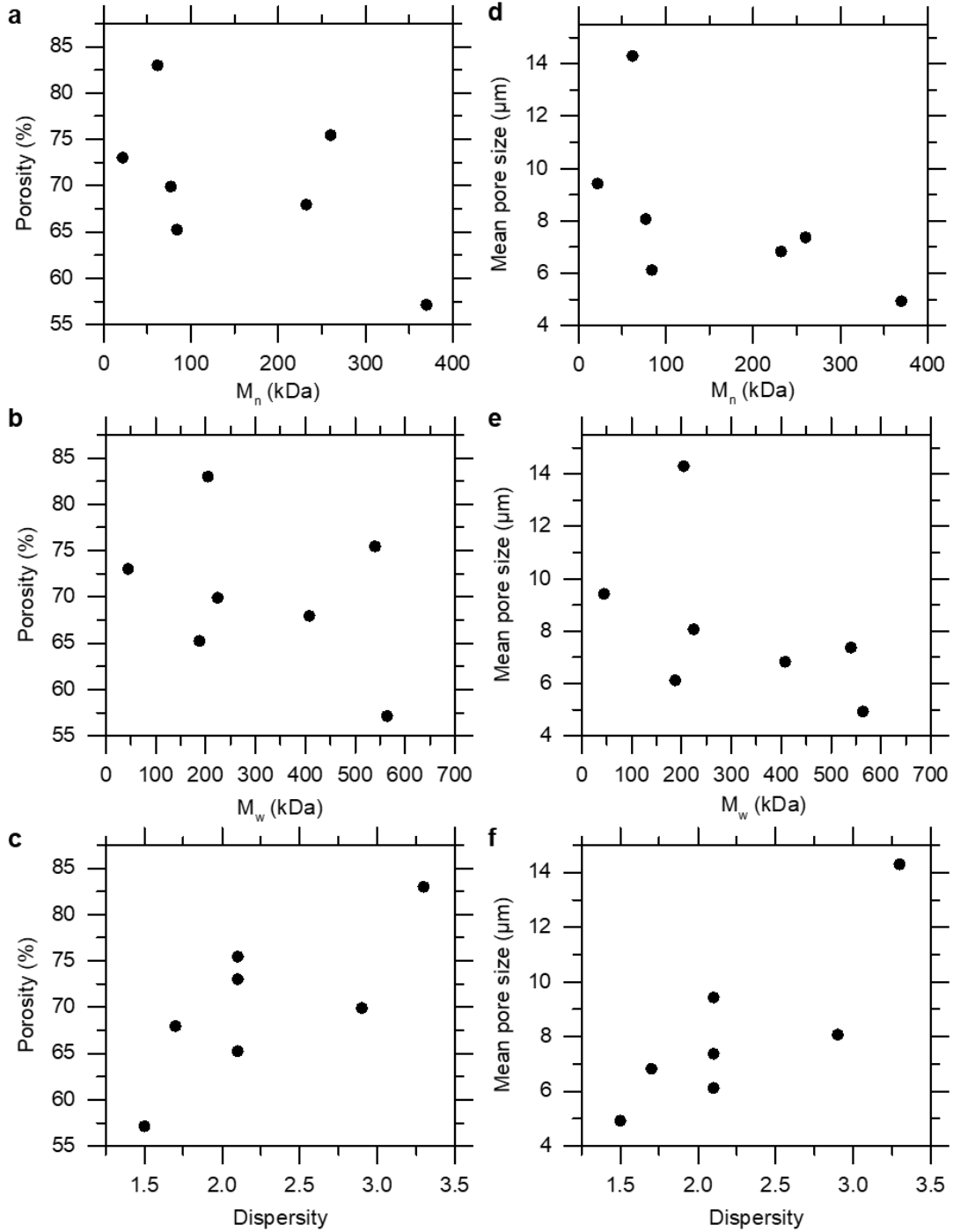


Figure D-1. Evolution of the overall porosity as a function of M_n (a), M_w (b), dispersity (c) and of the mean pore size as a function M_n (d), M_w (e), dispersity (f) for CS/ β GP/AHP hydrogels prepared with different CS grades after 2 h at 37°C. CS 0.8 wt%, pH = 7.4 \pm 0.05 at 4°C.

D.2. Mechanical properties

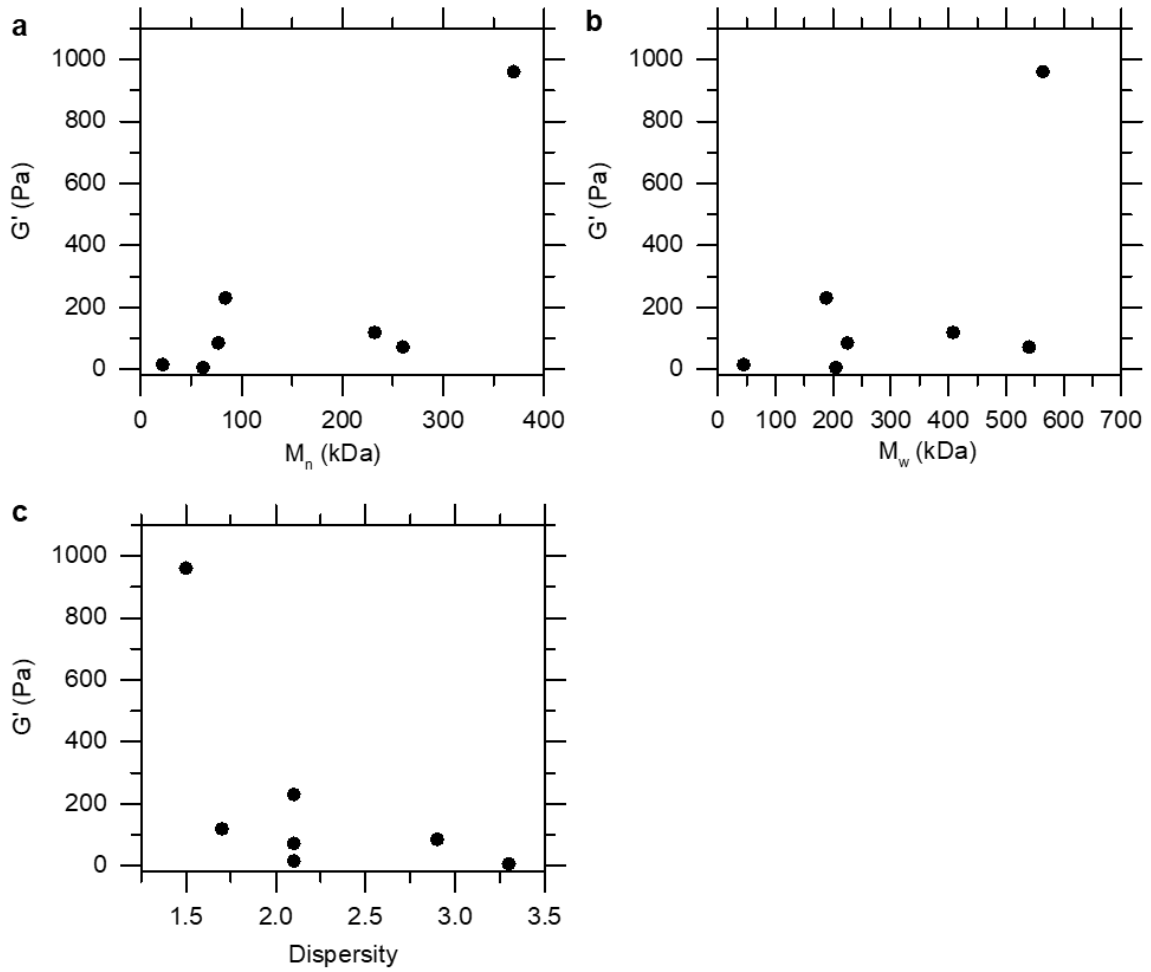


Figure D-2. Evolution of the storage modulus, G' , as a function of M_n (a), M_w (b), dispersity (c) for CS/ β GP/AHP hydrogels prepared with different CS grades after 2 h at 37°C. CS 0.8 wt%, pH = 7.4 \pm 0.05 at 4°C.

E. Staining of cell membrane by Membright 560 (MB560)

The possibility of staining adherent MC3T3-E1 cells by MB560 was investigated. For that, MC3T3-E1 cells were seeded at 10^4 cells. cm^{-2} onto 24-well plate. After incubation time $t = 1$ night or 6 days (confluence), the cells were stained using the protocol described in Chapter IV, section IV.4.1. Cells were fixed using paraformaldehyde and the nuclei was stained using DAPI solution.

Figure E-1 shows confocal microscopy image of simultaneous signals from MB560 and from DAPI. We observed that adherent cells were efficiently stained for $t = 1$ night but no cell was stained for $t = 6$ days.

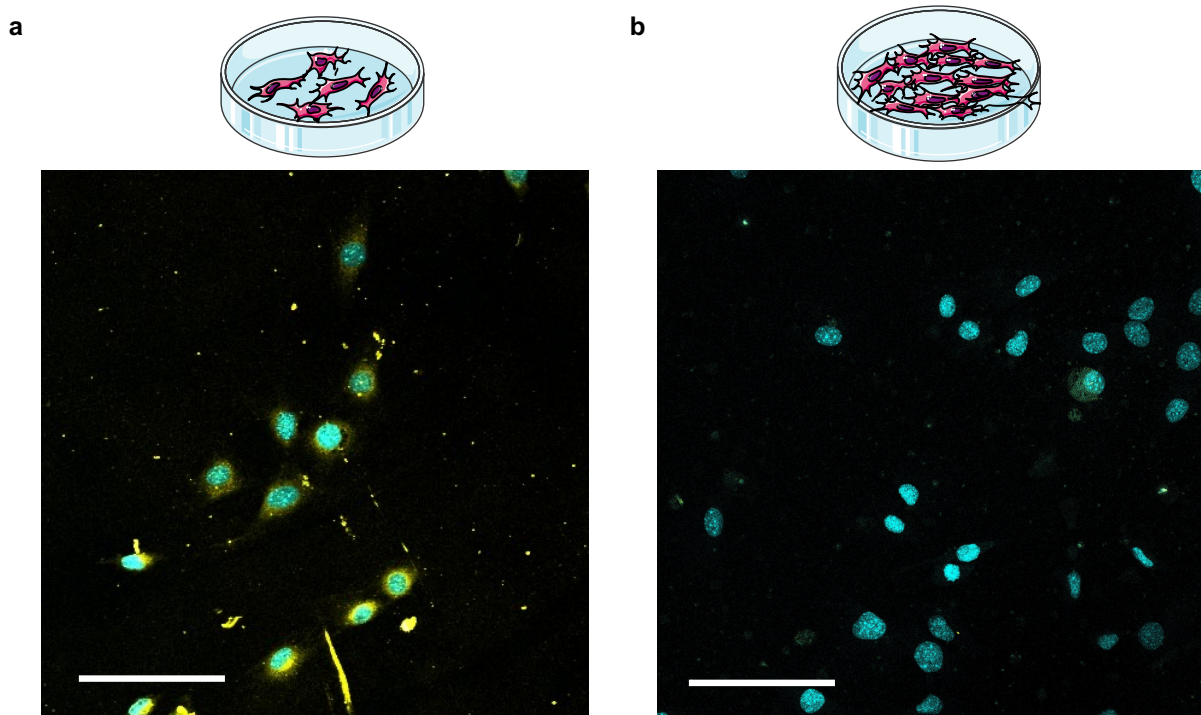


Figure E-1. Confocal micrographs of adherent MC3T3-E1 cells which membrane is stained with MB560 at $t = 1$ night (a) or $t = 6$ days (b) after seeding. Yellow = MB560 (membrane), cyan = DAPI (nuclei). Scale bar = $50 \mu\text{m}$.

RÉSUMÉ

Les hydrogels thermosensibles sont des matériaux prometteurs pour l'encapsulation et la délivrance de cellules. Notre approche est basée sur un système thermosensible dans lequel la transition sol/gel est induite par une séparation de phase dans des solutions aqueuses de chitosan et de sels phosphates. Ces mélanges peuvent être maintenus liquides à température ambiante à des pH physiologiques, et possèdent une transition sol/gel rapide à 37°C pour former un hydrogel macroporeux. Dans un premier temps, nous avons développé une approche rationnelle pour préparer des mélanges thermosensibles dans lequel les paramètres cruciaux, pH, osmolarité, cinétique de gélification, sont finement contrôlés indépendamment. La cytocompatibilité de ces systèmes est démontrée. Les mécanismes de la transition sol/gel, tant au niveau moléculaire que microscopique, ont été étudiés en profondeur. En particulier, nous avons réalisé des observations directes et indirectes résolues en temps permettant de suivre l'émergence de la microstructure macroporeuse. L'influence de diverses caractéristiques du chitosan, ainsi que l'effet de la présence de cellules sur les propriétés de l'hydrogel, ont été étudiés. Enfin, des stratégies de biofonctionnalisation visant à améliorer l'activité des cellules encapsulées ont été explorées.

MOTS CLÉS

hydrogel thermosensible, matrice injectable, délivrance de cellules, encapsulation de cellules, chitosan, macroporosité, hydrogel à séparation de phase

ABSTRACT

Thermosensitive hydrogels are highly valuable matrices for cell encapsulation and delivery. Here, our approach is based on a thermosensitive system in which the sol/gel transition is induced by a phase separation in aqueous mixtures of chitosan and phosphate salts. These mixtures can be held liquid at physiological pHs and room temperature while exhibiting a quick sol/gel transition at 37°C to form a macroporous hydrogel. Firstly, we developed a rational formulation design to prepare thermosensitive mixtures in which crucial parameters, like pH, osmolarity, gelation kinetics, can be precisely and independently controlled. The cytocompatibility of these finely adjusted physiological systems was demonstrated. The mechanisms of the sol/gel transition, both at molecular and microscopic levels, were investigated in depth. In particular, we were able to capture using time-resolved direct and indirect observations the emergence of the macroporous microstructure throughout phase separation. Influence of various characteristics of chitosan as well as effect of the presence of cells on hydrogel formation and properties were investigated. Finally, biofunctionalization strategies aiming at improving the activity of encapsulated cells were explored.

KEYWORDS

thermosensitive hydrogel, injectable vehicle, cell delivery, cell encapsulation, chitosan, macroporosity, phase-separated hydrogel